Carrier profiling of ZnO nanowire structures by scanning capacitance microscopy and scanning spreading resistance microscopy

Lin Wang

N° d'ordre : 2016LYSEI031

THESE de DOCTORAT DE L'UNIVERSITE DE LYON

préparée au sein de

l'INSA LYON

Ecole Doctorale: ED34
École doctorale matériaux de Lyon

Spécialité de doctorat : Matériaux Semiconducteurs
Discipline : Matériaux

Soutenue publiquement le 28/04/2016, par :

Lin WANG

Carrier profiling of ZnO nanowire structures by scanning capacitance microscopy and scanning spreading resistance microscopy

---

Devant le jury composé de :

M. Brice GAUTIER	Professeur des Universités	INSA LYON	Président
M. François BERTIN	Docteur, HDR	CEA-Leti	Rapporteur
M. Pierre EYBEN	Docteur, Senior Scientist	IMEC	Rapporteur
M. Daniel ALQUIER	Professeur des Universités	Université de Tours	Examinateur
M. Vincent SALLET	Docteur, Chargé de recherche	CNRS-UVSQ	Examinateur
M. Georges BREMOND	Professeur des Universités	INSA LYON	Directeur de thèse

Cette thèse a été préparée à l'Institut des Nanotechnologies de Lyon de l'INSA LYON

Acknowledgement

With this doctoral thesis finished, the part of my life as a PhD student, which began in September 2012 and lasted three years and a half, comes to its end. When I look back, I find myself fortunate to have such a journey in INL, in Lyon, in France, and to have so many people along the way without whose help, support and encouragements this thesis work would not have been possible.

First of all, I sincerely thank M. Prof. Georges Bremond, not only for giving me the opportunity to enter the nano-world and work in the field of characterization on nano-objects under his supervision, for helping me on a lot of administrative procedures, for his patient guidance, valuable discussions, and enthusiastic encouragement during the research work, but also for his kindness and continued care on my daily life outside the lab.

Most of the work in the thesis has been done in Lyon Institute of Nanotechnology (INSA LYON). So I would like to express my gratitude to this lab which is filled with so many kind people and experimental facilities which together have created a good environment for me to conduct the research.

I am thankful to M. Prof. Bruno Masenelli, head of the "Spectroscopy and Nanomaterials" group which I belonged to, for his assistance on the experiments and the discussions with him which have broadened my knowledge. More importantly, it was really a pleasure to be a member of such an active and energetic scientific group. Thanks to all the group members.

I am deeply grateful to Brice Gautier, David Albertini and Armel Descamps-Mandine for their teaching and guidance on the AFM system. On my way of learning the techniques and during the frequent and numerous AFM measurements, they have always been helpful and available whenever I was faced with problems. In particular, I would like to thank Brice Gautier for fruitful discussions and valuable advices on the SCM and SSRM experiments.

I want to thank Justine Laurent and Andrei Sabac for having worked together with me and for their help during the research work. I thank Bruno Canut and Cécile Jamois for teaching me SEM, Erwann Fourmond for teaching me Ellipsometry.

This work has been a part of the ANR project MADFIZ, in which groups from different labs (INL, GEMAC, GPM, Institut Néel, CEA-LETI and CEA-DEN) have taken part in. Here I would like to thank all my colleagues in this project for their helpful discussions and communications. Especially, I am extremely thankful to Vincent Sallet at GEMAC, Jean-Michel Chauveau at CRHEA and Sophie Guillemin at INL (also LMGP) for their supply of various ZnO samples as well as their communications and suggestions which have helped me so much in completing this work. Also, I want to thank Roger Brenier in ILM for his help

in the dip-coating work and Frédéric Godoy in SGM for his help in the polishing work.
I wish to express my special thanks to all the technicians and administrators in INL for their support and assistance in the laboratory. Secretaries and Virginie Lagarde have helped me a lot on the administrative procedure. Philippe Girard has always been so kind and helped me on many things. Joëlle Grégoire and Khaled Ayadi from NanoLyon platform have offered me patient trainings in the chemistry room and helped me a lot on the experiments.
I am grateful to all my colleagues in the same office and in the same lab for their kind help and encouragements, with honorable mentions of Roman Anufriev, Mouhannad Massoud, Hajjaji Hamza, Trung-hieu Nguyen, HU Xuan, LIU Huanhuan, Zhu Yao, Liu Jia, Ma Yue, Martin Pouzet, Daniel Thomas, Mohamed-Khairy Hamza and Mariam El-khatiball.
Particularly, I would like to thank François BERTIN and Pierre EYBEN for having been reviewers, Brice GAUTIER, Daniel ALQUIER and Vincent SALLET for having been examiners of my thesis. Thanks for their opinions, comments as well as the communication with them.
I always appreciate the great times I spent with all my friends in Lyon, especially those who came together with me to France, Xie Zhongjian, Zhang Biao, Yao lan, Liang Biao, Wang Lin, Zuo Wei, Li Xiubin and Cui jin.
I greatly appreciate the care and encouragements provided by my friends in China, especially Zhang Yanjun, Wang Qinggong, Du Pengfei, Zhang Junfei and so on.
I would like to express my appreciation to my girlfriend Yang Jing for always supporting me and being with me with her companion and help.
Finally, I am forever indebted to my family for their everlasting understanding and support.

April, 2016

Lin WANG

A mes quatre années à lyon, France.

Le changement est inévitable et le changement est pour le mieux.

Abstract: Carrier profiling of ZnO nanowire structures by scanning capacitance microscopy and scanning spreading resistance microscopy

The continuously decreasing feature size of semiconductor devices and structures towards nanometer scale has significantly stimulated the development of characterization tools for mapping their local electrical properties with ultra-high spatial resolution. In this regard, two scanning probe microscopy (SPM) techniques, i.e. scanning capacitance microscopy (SCM) and scanning spreading resistance microscopy (SSRM), have emerged as powerful techniques. After demonstrating their potentials and abilities on Si for the purpose of two dimensional (2D) carrier/dopant profiling at the nanometer scale, their use has been extended to other semiconductor materials (including Ge, SiC, GaAs, InP, GaN) and related electrical characterization on various nanoscaled devices and structures. However, as an important semiconductor having shown significant potential applications in electronic and optoelectronic fields, ZnO structures have rarely been studied by these tools. Besides, the applications of conventional characterization techniques are largely limited on characterizing semiconductor nanowires (NWs) structure, which has been of intense interest because of their potential as building blocks for diverse future devices.

This thesis work has focused on the application of SCM and SSRM to electrical characterization of ZnO-based nanostructures (specifically ZnO NWs) in terms of carrier profiling in the effort of their *p*-type doping. To this end, in the first step, the residual carrier concentrations in non-intentionally doped (nid) NWs grown by chemical bath deposition (CBD) and metal organic chemical vapor deposition (MOCVD) have been investigated. In order to perform SPM measurements on the NWs structure, a planarization process has been developed based on dip-coating of SiO_2 sol-gel solution. While NWs can be readily detected in the SiO_2 matrix, calibration method was utilized for quantitative analysis with two homo-epitaxially molecular beam epitaxy (MBE) grown ZnO:Ga multilayer staircase structures containing Ga density levels from 1.7×10^{17} to 3×10^{20} cm^{-3} serving as calibration samples. Cross sectional measurements on the staircase structures have evidenced a monotonic dependence of SCM and SSRM signals on the Ga doping concentration and allowed to construct SCM and SSRM calibration curves separately. As results, residual carrier concentrations around 3×10^{18} and 2×10^{18} cm^{-3} were estimated for the CBD and MOCVD ZnO NWs, respectively. These high values of residual doping level can help explain the difficulty on ZnO NWs *p*-type doping.

Besides microscopic electrical characterization of the NWs by SCM and SSRM, conventional macroscopic techniques have been used to characterize the assembly of ZnO NWs. Schottky contacts were fabricated by electron beam deposition of Pt. From capacitance-voltage (C-V)

characteristics, carrier concentrations at the level of 7×10^{16} cm^{-3} and 4×10^{16} cm^{-3} were revealed for the CBD and MOCVD ZnO NWs, respectively. A discussion has been made on the difference between results from C-V and SPM analysis which was related to the effective ZnO area in C-V measurement being influenced by both sample preparation process and NWs surface depletion effect.

With the first objective of this thesis work being the detection and determination of *p*-type conductivity in ZnO NWs, we have studied the effect of *ex situ* doping of phosphorus (P) by spin-on dopant approach and *in situ* doping of antimony (Sb) by MOCVD growth. The main results were obtained on the Sb doped samples, including ZnO:Sb film and ZnO/ZnO:Sb core-shell NWs. Although no *p*-type ZnO was detected, compensation effect of the residual *n*-type conduction has been observed for which a reasonable explanation is the formation of Sb-related acceptors. Finally, the possibility that ZnMgO should be easier to be doped into *p*-type than ZnO led us to characterize ZnO/ZnMgO heterostructures. Measurements on a 3-period ZnO/ZnMgO core-multishell coaxial NWs structure showed that the different layers can be well detected by both SCM and SSRM with a high spatial resolution as a result of different electrical properties of ZnO and ZnMgO, indicating their applicability in the characterization of future ZnO/ZnMgO heterojunction devices.

In conclusion, the investigation of SCM and SSRM applications on characterizing ZnO NWs has demonstrated the two as suitable electrical characterization techniques on ZnO-related nanomaterials. The methodology in this study can be further developed and extended to other NWs materials such as GaN and InP.

Résumé: Caractérisation électrique des nanofils de ZnO par Scanning capacitance microscopy et scanning spreading resistance microscopy

La diminution des dimensions géométriques des dispositifs et des structures semi-conductrices jusqu'à des échelles très fortement submicroniques a considérablement stimulé le développement des outils de caractérisation pour la cartographie de leurs propriétés électriques locales avec une résolution spatiale nanométrique. A cet égard, deux microscopies à sonde locale (Scanning Probe Microscopy en anglais) à savoir la Scanning Capacitance Microscopy (SCM) et la Scanning Spreading Resistance Microscopy (SSRM), ont émergé en tant que techniques performantes pour la mesure de dopage. Après avoir démontré toute leur potentialité à déterminer des profils 2D de dopage sur Si à l'échelle du nanomètre, leur utilisation a été étendue à d'autres matériaux semi-conducteurs (Ge, SiC, GaAs, InP, GaN) et la caractérisation électrique connexe de divers dispositifs et structures de dimension réduite. Bien que semi-conducteur aux propriétés électroniques et optoélectroniques potentiellement très séduisantes, le ZnO a très rarement été étudiés à l'aide de ces techniques SPM. De plus, la mesure des propriétés électriques directement sur des nanofils reste un défi majeur qui pourrait limiter le développement de ces technologies.

Ce travail de thèse porte sur l'application des techniques SCM et SSRM pour la caractérisation électrique de nanofils de ZnO avec l'objectif d'en déterminer le dopage par profilage des porteurs libres suite à des essais de dopage de type p. Dans le but de caractériser le dopage intrinsèque des nanofils, première étape importante pour analyser une tentative de dopage p, les premières études sont menées sur des nanofils de ZnO non-intentionnellement dopé obtenus par dépôt en bain chimique (Chemical Bath Deposition-CBD) ou par épitaxie en phase vapeur aux organométalliques (Metal Organic Chemical Vapor Deposition-MOCVD). Afin de pouvoir utiliser un référentiel planaire nécessaire à ces mesures par sonde locale, un procédé de remplissage par dip-coating et de polissage a été spécialement développé sur des champs de nanofils quasi-verticaux. De plus, dans le but de parvenir à un étalonnage des mesures SCM et SSRM, nous avons conçu et fait fabriquer des échantillons étalons de dopage de type n. Il s'agit de structures multicouches de ZnO:Ga épitaxies par jet moléculaire (Molecular Beam Epitaxy) contenant des niveaux de Ga en escalier de densité variable de 2×10^{17} à 3×10^{20} cm^{-3}. Les mesures sur des coupes transversales de ces deux de structures multicouches ont permis, pour la première fois sur ZnO d'établir un étalonnage des mesures SCM et SSRM et de déterminer le dopage intrinsèque électriquement actif de couches 2D nanométriques, résultat difficilement atteignable par d'autres techniques d'analyse. Des résultats inattendus de concentration résiduelle de porteur de l'ordre de 2×10^{18} et 3×10^{18} cm^{-3} ont été trouvés sur les nanofils de ZnO crus par MOCVD et par CBD respectivement. Ces

valeurs importantes de porteurs résiduels pourraient expliquer la difficulté à transformer en type *p* le dopage des nanofils de ZnO.

Outre la caractérisation électrique microscopique des nanofils par SCM et SSRM, des techniques macroscopiques classiques ont été utilisées pour caractériser des assemblées importantes de nanofils de ZnO. Les barrières de Schottky ont été formées par dépôt de Pt par faisceau d'électrons sur les échantillons de champs de nanofils « planarisés ». Une valeur brute de la concentration de porteurs intrinsèque de 7×10^{16} cm^{-3} et de 4×10^{16} cm^{-3} a été obtenue par des mesures capacitives (C-V profiling) sur l'échantillon de CBD et MOCVD nanofils, respectivement. Un modèle très simple appréciant la surface effective de ZnO en prenant en compte la déplétion radiale des nanofils a été élaboré, permettant une concordance nano-macro des niveaux de concentration de dopage.

L'objectif premier de la thèse étant axé sur la recherche et la détermination du dopage de type *p* dans les nanofils de ZnO, nous avons étudié les effets des dopages *ex situ* par diffusion du phosphore (procédé SOD) et des dopages *in situ* par incorporation d'antimoine (Sb) pendant la croissance MOCVD. Les résultats majeurs sont obtenus pour l'antimoine, en utilisant des couches ZnO: Sb 2D et des nanofils cœur-coquille ZnO/ZnO: Sb, ou l'hypothèse d'une compensation partielle du dopage n résiduel par un centre accepteur créé par le dopage Sb semble pouvoir être établie raisonnablement. La possibilité de convertir plus facilement en dopage de type *p* le ZnMgO nous a amené à caractériser par SCM et SSRM des nanofils cœur-coquille en multicouches contenant 3 périodes d'hétérostructure ZnO/ZnMgO. Les résultats décisifs obtenus par les mesures SCM et SSRM montrent que les différentes couches sont bien détectées avec une résolution spatiale élevée en raison des différences de propriétés électriques entre ZnO et ZnMgO. C'est une première approche importante vers la réalisation d'hétérojonction sur ZnO, ouvrant la voie vers des applications optoélectronique futures.

En conclusion, ce travail très méthodique sur la caractérisation par SCM et SSRM des dopages de nanofils de ZnO doit pouvoir être poursuivi et accentuer non seulement dans la filière ZnO et ses hétérostructures potentielles d'application, mais aussi sur d'autres filières de matériaux comme GaN ou InP.

List of acronyms

1D	One-Dimensional
2D	Two-Dimensional
AC	Alternating Current
AFM	Atomic Force Microscopy
APT	Atom Probe Tomography
C-AFM	Conductive-AFM
CBD	Chemical Bath Deposition
CMP	Chemical-Mechanical Polishing
C-V	Capacitance-Voltage
DC	Direct Current
DLTS	Deep-Level Transient Spectroscopy
EBIC	Electron Beam Induced Current
FET	Field-Effect Transistors
I-V	Current-Voltage
LED	Light Emitting Diodes
MBE	Molecular Beam Epitaxy
MIS	Metal-Insulator-Semiconductor
MOCVD	Metal Organic Chemical Vapor Deposition
nid	Non-intentionally Doped
NWs	Nanowires
PL	Photoluminescence
RIE	Reactive-Ion Etching
SCM	Scanning Capacitance Microscopy
SCS	Scanning Capacitance Spectroscopy
SE	Secondary Electrons
SEM	Scanning Electron Microscopy
SIMS	Two-Dimensional Secondary Ion Mass Spectroscopy
SPM	Scanning Probe Microscopy
SRP	Spreading Resistance Profiling
SSRM	Scanning Spreading Resistance Microscopy
UV	Ultraviolet

Contents

Chapter 1 Introduction.....1
1.1 Background.....1
1.2 2D carrier/dopant profiling techniques.....3
1.2.1 2D techniques based on 1D techniques.....3
1.2.2 Electron Microscopy based techniques.....4
1.2.3 Atom Probe Tomography.....6
1.2.4 Scanning probe microscopy based techniques.....6
1.3 Objective of this study.....11
1.4 Outline of this work.....11
Chapter 2 ZnO properties, characterization techniques and samples preparation.....17
2.1 Introduction of ZnO.....17
2.1.1 ZnO basic properties.....17
2.1.2 Doping of ZnO.....21
2.1.3 ZnO NWs.....22
2.2 AFM-based scanning probe microscopy.....23
2.2.1 Atomic force microscopy (AFM).....24
2.2.2 Scanning capacitance microscopy (SCM).....26
2.2.3 Scanning spreading resistance microscopy (SSRM).....30
2.2.4 Conductive atomic force microscopy (C-AFM).....31
2.2.5 Probes for electrical scanning probe microscopy.....32
2.3 Macroscopic characterization.....34
2.3.1 Metal-semiconductor contact.....34
2.3.2 Current-voltage (I-V) characteristics.....37
2.3.3 Capacitance-voltage (C-V) characteristics.....38
2.4 Planarization process for SPM measurements.....40
2.4.1 NWs samples.....41
2.4.2 Dip-coating of SiO_2.....41
2.4.3 Polishing and cleaning.....43
2.5 Conclusion.....45
Chapter 3 Carrier profiling on ZnO NWs by SCM.....55
3.1 Introduction.....55
3.2 SCM measurement on ZnO NWs.....56
3.2.1 CBD grown NWs.....56

3.2.2 MOCVD grown NWs..... 58
3.2.3 Quantification analysis for SCM measurement..... 60
3.3 SCM on ZnO:Ga staircase structures.....61
3.3.1 Choice of Ga as dopant in ZnO.....61
3.3.2 An investigation of tip depletion effect.....63
3.3.3 SCM on ZnO:Ga staircase samples..... 69
3.4 Determination of carrier concentration in NWs.....74
3.4.1 Requirements for calibration analysis: methodology for calibration.....74
3.4.2 Calibration for NWs by SCM..... 77
3.4.3 Calibration for NWs by SCS.....82
3.5 Conclusion..... 86
Chapter 4 Carrier profiling on ZnO NWs by SSRM..... 93
4.1 Introduction.....93
4.2 Tip-ZnO contact characteristics..... 95
4.2.1 Determination of tip force.....95
4.2.2 Resistance-force curve.....96
4.2.3 I-V characteristic at different tip forces..... 98
4.3 SSRM on ZnO NWs..... 99
4.3.1 CBD grown NWs.....99
4.3.2 MOCVD grown NWs..... 101
4.3.3 Quantification of SSRM measurement..... 102
4.4 SSRM on ZnO:Ga staircase structures..... 104
4.5 Determination of carrier concentration in NWs.....106
4.6 Conclusion..... 110
Chapter 5 Macroscopic characterization of collective ZnO NWs..... 117
5.1 Sample preparation..... 117
5.2 I-V characteristics..... 119
5.3 C-V characteristics and carrier profiling.....121
5.4 Discussion of C-V profiling on collective NWs..... 122
5.4.1 Influence of R_s..... 123
5.4.2 Influence of SiO_2 capacitance.....124
5.5 Discussion on the difference between microscopic and macroscopic results.....126
5.6 Conclusion..... 128
Chapter 6 Related applications of SCM/SSRM on ZnO based nanostructures..... 131
6.1 SCM/SSRM on ZnO:Sb film..... 131
6.2 SCM/SSRM on ZnO-based NWs--attempt of *p*-type doping..... 136

6.2.1 *Ex situ* doping: P doped ZnO NWs.....138
6.2.2 *In situ* doping: ZnO/ZnO:Sb core-shell NWs.....138
6.3 SCM/SSRM on ZnO/ZnMgO core-multishell coaxial structures.....143
6.4 Conclusion.....148
Chapter 7 General conclusion.....153

Chapter 1

Introduction

1.1 Background

Zinc oxide (ZnO), a II-VI compound semiconductor, has been under intensive and extensive study since the last decade of 20th century. As a matter of fact, the research work on this material dates back to 1930s [1], from when its lattice parameter, vibrational properties, optical properties have been investigated. Then from 1990s, the renewed interest on ZnO semiconductor properties was triggered by the commercial success of GaN-based optoelectronic and electronic devices. Compared with GaN, ZnO has a variety of advantageous properties making it even more suitable for optoelectronic device technology, especially its direct band gap (3.37 eV at 300K) and its high exciton binding energy at room temperature (60 meV, compared to ~24 meV for GaN), accompanied by the simpler crystal-growth technology, availability of large single crystal, better radiation resistance, biocompatibility and possible band gap engineering (3~4.5 eV) by doping with Cd or Mg. Owning to these advantages, ZnO has been considered as a good candidate in optoelectronics and significant research interests and efforts have been attracted on the realization of ZnO devices [2-5], although efficient *p*-type doping still represents a major obstacle on the way to the ultimate success [3].

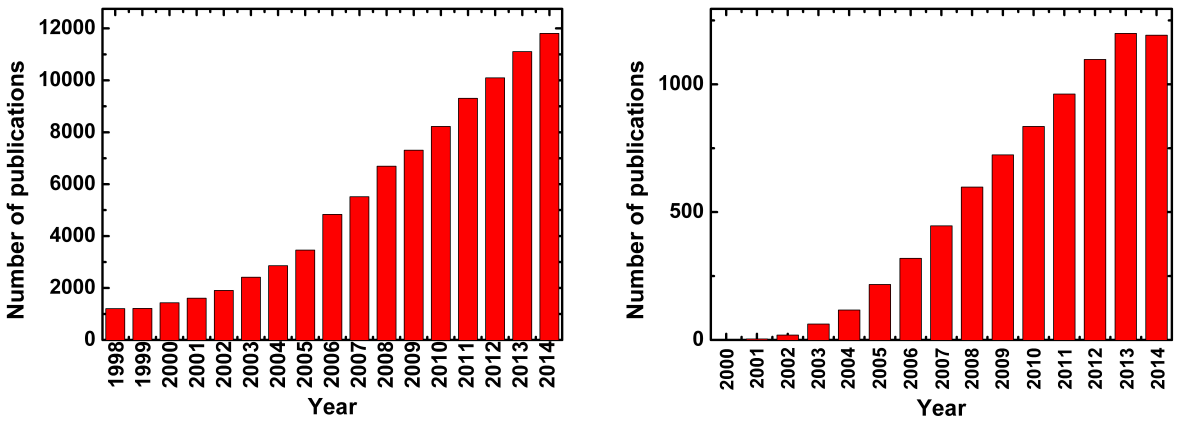

(a) (b)

Figure 1.1: (a) Number of publications on ZnO from 1998 to 2014. Source ISI Web of Science (search: Topic=ZnO or zinc oxide). (b) Number of publications on ZnO nanowires. Source ISI Web of Science (search: Topic=ZnO/zinc oxide nanowire/nanorod)

Recently, with the improvements in crystal growth at the nanometer scale, nanomaterials,

including 0-dimensional (0D), 1-dimensional (1D), and 2-dimensional (2D) nanostructures, have drawn considerable attention due to their unique physical properties arising from quantum confinement such as electronic quantum transport, enhanced radiative recombination of carriers, and noticeable performance in electronics, optics and photonics. Furthermore, 1D semiconductor nanowires (NWs) have been of intense interest in both academic research and industrial applications because of their potential as building blocks for the future generation of electronics, photonics, sensors, actuators, energy, and medical applications. Among 1D semiconductor materials, ZnO NWs are one of the most actively studied in nanoscience and nanotechnology (Figure 1.1). 1D ZnO nanostructures can be synthesized by a wide range of techniques [6], such as chemical bath deposition (CBD), physical vapor deposition, metal-organic chemical vapor deposition (MOCVD), molecular beam epitaxy (MBE), pulsed laser deposition (PLD), sputtering, flux methods, electrospinning, and even top-down approaches by etching. Their applications such as ultraviolet (UV) lasers [7], light emitting diodes (LED) [8], field-effect transistors (FET) [9], solar cells [10], nanogenerators [11], gas sensors [12], photodetectors [13], and photocatalysts [14] have been demonstrated in different groups. Moreover, the reduction in ZnO material dimension is thought to be beneficial for the realization of its *p*-type conduction [15].

To finally realize applications of ZnO NWs in electronic/optoelectronic field requires a good understanding of their electrical properties, including a proper control of their doping and its characterization. For this purpose, two kinds of approaches for investigation are usually used. One is to study the NWs at a collective scale. In this case, the conventional techniques for characterization on massive structures of the material are transferred for investigating the general electrical properties of collective nanostructures. For example, the current-voltage (I-V) and capacitance-voltage (C-V) methods allow for investigating charge transport and distribution and obtaining general information on the material. Deep-level transient spectroscopy (DLTS) and related methods, based on the analysis of capacitance or conductivity transients, can detect and characterize the electrical activity of defects. However, the electrical properties of NWs at a macroscopic level can significantly differ from that at a microscopic level, i.e. the nanometer level. Another is to study a single NW. Typically, ohmic contact and/or Schottky contact are formed by photolithography or electron-beam lithography approaches at the two ends of the NW to investigate it by performing analysis like I-V and electron beam induced current (EBIC). Furthermore, FET configuration on an individual NW can be constructed to examine the carrier mobility and carrier density inside the NW [16]. Nevertheless, these techniques have the disadvantages of complexity and generally do not allow the characterization of the radial difference of the NW since they are strictly not tools allowing 2D characterization, thus suffer a lack of exactly local electrical characterization .

1.2 2D carrier/dopant profiling techniques

As the feature size of semiconductor structures and devices enters nanometer scale, 2D electrical characterization tools with a high spatial resolution have been demanded to obtain important information on carrier/dopant distributions and are indispensable for a successful development of semiconductor technology. Primarily driven by the silicon technology in terms of reduced device feature size and increasing device functionalities, numerous 2D (or 3D) electrical characterization methods for carrier/dopant profiling have been developed. They can principally be divided into four categories [17]: (i) 2D techniques based on 1D techniques, (ii) Electron microscopy-based techniques, (iii) the lately emerging atom probe tomography (APT) technique and (iv) scanning probe microscopy (SPM) based techniques.

1.2.1 2D techniques based on 1D techniques

Two-dimensional Secondary Ion Mass Spectroscopy (SIMS)

SIMS is a technique used to analyze the composition of solid surfaces and thin films by sputtering the surface of the specimen with a focused primary ion beam and collecting and analyzing ejected secondary ions. It is one of the most powerful techniques for 1D dopant profiling in semiconductors owning to its good sensitivity (<ppm), high dynamic range (10^{14}-10^{21} cm^{-3}) and proper depth resolution (2-5 nm). It makes use of an ion beam with high energy (1-30 keV) to bombard the sample, resulting in the ejection or sputtering of atoms from the sample material. A small percentage of these ejected atoms are either positively or negatively charged and are referred to as “secondary ions”. They can be detected and analyzed by a mass-to-charge spectrometry, enabling us to obtain the information on the elements composition of the sample. Quantitative data on the sample’s composition can be obtained with the help of standard sample by counting the number of secondary ions and depth profiling is realized by monitoring the evolution of secondary ion emission with sputtering time. The yield of secondary ions relies on the specimen’s material, the specimen’s crystallographic orientation, and the nature, energy and incidence angle of the primary beam of ions. Oxygen atoms are usually used for sputtering electropositive elements or those with low ionization potential such as Na, B, and Al. Cesium atoms, on the other hand, show a better performance on sputtering negative ions from electronegative elements such as C, O, and As.

The extension of SIMS to 2D analysis involves scanning laterally the primary ion beam. However, the spatial resolution of the technique is considerably limited by the large ion beam diameter (>100 nm) for practical applications. The use of a different ion source (Ga+ or In+) have been proposed to improve the lateral spatial resolution (down to 20 nm) at the expense

of a significant decrease in the sensitivity in the measurement. A second approach makes use of specially designed test structures to improve the spatial resolution with an acceptable degree of sensitivity (~10^{17} cm^{-3}) [18]. However, this approach depends on the production of dedicated samples and cannot be used for realistic devices. Recently, protocols have been developed to obtain 2D SIMS depth profiles of repetitive 3D structures with high depth resolution (< 4 nm/decade), which may be adapted to analyze new generation semiconductor devices with 3D architecture [19-20].

1.2.2 Electron Microscopy based techniques

Field-Emission Scanning Electron Microscopy (SEM)

The principle of dopant profiling using SEM is that the intensity of secondary electrons (SE) collected in an SEM is very sensitive to the dopant density levels in a semiconductor specimen, with *p*- and *n*-type doped regions showing contrast in the SE image under certain conditions [21]. The enhancement or reduction of the SE emission is a consequence of the different electric field produced by the different dopant concentration and distribution in the material. It has been shown that the intensity contrast is related to ionized dopants, rather than the total number of dopant atoms [22].

This method in most cases involves very simple sample preparation, where a cross section obtained from cleaving is sufficient. The limiting factors in the lateral resolution are the Debye length (L_D) (for lightly doped material with large L_D) and the electron beam diameter (for highly doped material with small L_D) used for the analysis. Lateral resolution as small as 13-19 nm has been reported [23]. Regarding dopant concentration sensitivity, SEM has been successfully used to image *p*-type silicon with a concentration as low as 8×10^{15} cm^{-3} [24]. A weak point of the technique for dopant profiling is that the mechanism of the dopant contrast has not been completely understood, hindering the application of SEM for quantitative dopant profiling analysis. Also, a better understanding on the influence of the surface states in the measured contrast is needed.

Electron holography

Electron holography (Figure 1.2) makes use of a transmission electron microscope with a coherent source divided into two different beams. It measures the phase shift of an electron wave affected by a local electric or magnetic field. When the electrons pass through a semiconductor sample, the different potentials as a result of different dopant distribution are translated into different phase shifts of the electrons and the potential contours can be easily measured. In this way, electron holography can be used to map the electric fields in *p*-*n* junctions and the 2D electrostatic potential distributions in transistors. The method is

quantitative with a precision of 0.1 V and a spatial resolution better than 10 nm [25]. One practical limitation of the technique is that the best spatial resolution is achieved at the expense of a small field of view. This necessitates that several micrographs have to be made to have a complete measurement of the total carrier distribution of a device where a good spatial resolution is expected. Another limitation is the great phase shift sensitivity to variation in film thickness, which makes the technique very sensitive to sample preparation [25]. Finally, this technique is very sensitive to the doping fluctuation in case of low doping.

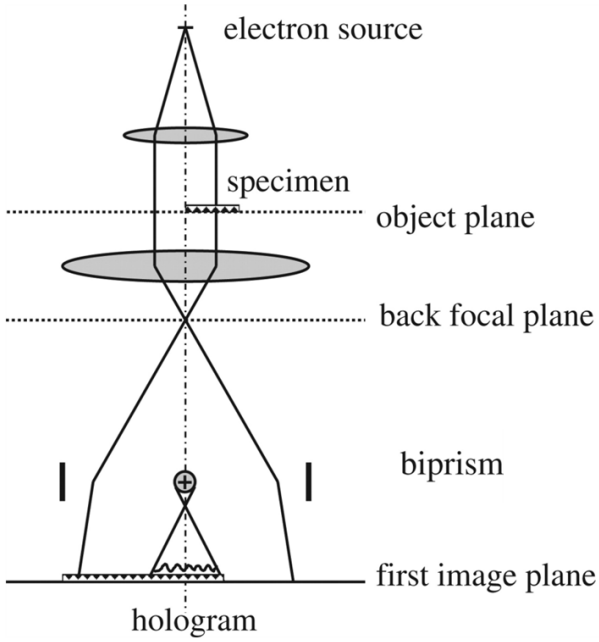

Figure 1.2: Setup for recording image-plane off-axis holograms. The object covering only half the object plane and the adjacent empty area are illuminated coherently. The object plane is imaged in the first image plane. By means of the electron biprism, the image wave and the adjacent empty wave are superimposed at an angle ('off-axis'). In the image plane, an interference pattern ('hologram') arises, consisting of parallel fringes modulated in contrast and fringe spacing by image amplitude and phase, respectively. Adapted from Ref [26].

Cathodoluminescence (CL)

Cathodoluminescence (CL) nanospectroscopy can also be used for the local carrier concentration determination. Its principle lies in the fact that the band-edge emission energy of a heavily doped semiconductor experiences a redshift depending on the carrier concentration due to its band-gap shrinkage or band-tailing [27-28]. Therefore, from the emission peak in the CL spectrum corresponding to the radiative recombination of free excitons, the carrier concentration of the semiconductor can be determined. CL nanospectroscopy is thought to be promising owning to its high sensitivity (~10^{15} cm^{-3}) of shallow level point-defects and nanometric resolution achievable by low-energy electron beam probe [29]. A recent work has reported a spatial resolution of 60 nm on the study of

ZnO nanorods [28]. Besides its relatively weak spatial resolution than expected, another disadvantage of this technique is that the redshift of band-edge emission peak is very small for relatively low carrier concentration, impeding its accuracy in this range.

1.2.3 Atom Probe Tomography

Atom probe tomography is a powerful emerging technique which is able to provide direct information about the chemical composition of elements together with a 3D map of position of each atom from a specimen at atomic scale [30]. It is based on a fabrication of a needle shaped sample submitted to a strong electric field which yields the field evaporation and ionization of the atoms at the probe apex. The resulting ions are sorted by time of fly and detected by a position sensitive detector, allowing the reconstruction of the whole volume of the tip in terms of atoms types as well as their positions. In the past, this technique was limited to metallic material. Since the introduction of the laser assisted atom probe in 2006 [31], where a laser pulse is added to the voltage pulse allowing for a well controlled field evaporation of the atoms from a non-conductive surface (so-called LA-APT), it has become possible to perform APT analyses on semiconductors and insulating materials [32]. However, complex field evaporation behaviors may differ from a material to another due to the existence of different physical mechanisms, which are not fully understood and can lead to an erroneous measurement of the elemental composition [33]. Also, the analyzed volume of the sample by this technique is largely limited and concentrations lower than 10^{18} cm^{-3} cannot be easily detected yet. Finally, although atom probe tomography is capable of mapping dopant atoms in nanoscale objects in 3D with high spatial resolution as SIMS, it does not reveal any information about their electrical activation.

1.2.4 Scanning probe microscopy based techniques

The development of atomic force microscopy (AFM) which makes use of a nanometer-sized probe tip at the end of a cantilever has open a new way to conduct study in atomic level. 2D carrier/dopant profiling SPM techniques have been developed on the base of AFM to measure the local properties of sample surfaces. In the measurement, the tip is scanned in both *x* and *y* directions and the electrical results at each position on the sample surface are recorded to reconstruct a 2D image of the sample's corresponding properties.

Kelvin probe force microscopy (KPFM)

KPFM can be used to measure the local electric surface potential distribution on the sample. When an AFM tip is brought close to the sample surface, an electrical force is generated between the tip and sample surface, due to the differences in their Fermi energy levels. By

applying an alternating current (AC) voltage (V_{ac}) plus an adjustable direct current (DC) voltage (V_{dc}) to the AFM tip, which generates oscillating electrical forces between the AFM tip and sample surface, and nullifies the oscillating electrical forces, respectively, KPFM measures the work function of the sample [34]. The measured electrochemical potential difference between the probe tip and the sample surface depends on their work-function difference related to the sample's carrier concentration, and can thus be used as a measure for the local doping concentration. KPFM has shown sensitivity to dopant density change from 10^{15} to 10^{20} cm^{-3} and has been applied successfully for qualitative two-dimensional carrier profiling of cross-sectioned Si structures [34]. Its application to more quantitative doping profiling is limited by the presence of surface charges on the sample surface. Its spatial resolution is one order of magnitude higher than SCM. An improved spatial resolution of the technique can be obtained by performing the measurements in vacuum.

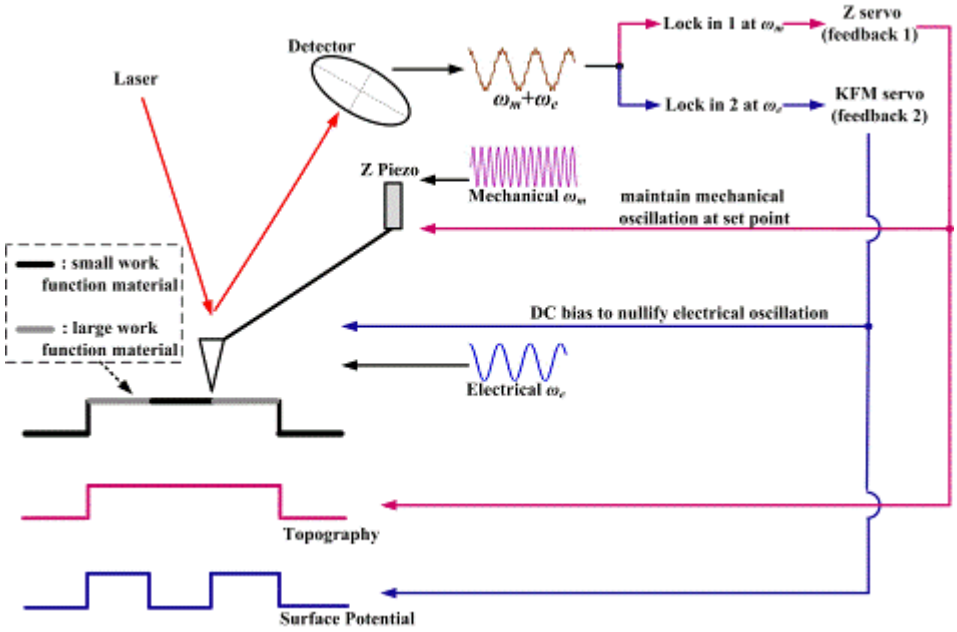

Figure 1.3: Working principles of KPFM [35].

Dopant-selective etching

Dopant-selective etching [36] is based on the fact that certain chemical solutions (mostly based on a mixture of HF, HNO_3, and either H_2O or CH_3COOH) preferentially etch doped silicon over undoped silicon. The sample topography after the etching step reflects the 2D carrier profile information and can be imaged using Transmission Electron Microscopy (TEM), SEM, Scanning Tunneling Microscope (STM), or AFM, to convert the topography profiles to electrical carrier distributions. The applicability of this method to 2D carrier profiling is limited because of (i) poor understanding of the etching process, (ii) poor control of the etching conditions, (iii) lack of a good quantification procedure and (iv) the fact it is a destructive technique.

Scanning microwave microscopy (SMM)

SMM combines the capability of outstanding local resolution of an AFM with with microwave signal compatibility [37]. It can be regarded as a kind of "next-generation scanning capacitance microscopy" (SCM, which will be introduced later) [38]. When a metal probe is in contact with a silicon surface, a metal-oxide-semiconductor (SCM) capacitor is formed whose total capacitance, in the simplified 1D model, is determined by the contributions of two capacitors connected in series: the surface oxide dielectric layer with a fixed capacitance and the underneath depletion layer in the substrate with a variable capacitance. The capacitance variation of the depletion layer in response to an applied ac bias is determined by the depletion depth, which is in turn largely affected by the local dopant/carrier concentration. Therefore by measuring the capacitance change induced by the applied ac bias, or dC/dV, the dopant concentration at each contact point can be mapped.

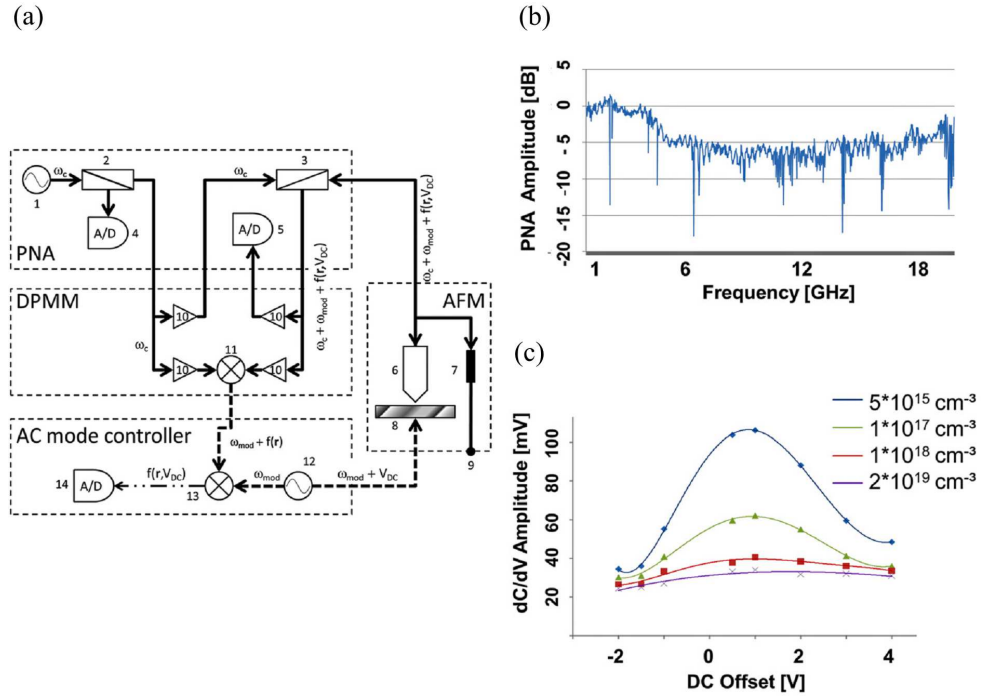

Figure 1.4: The principle of dopant profiling with scanning microwave microscopy. (a) The signal pathway for dC/dV imaging using the DPMM (dopant profiling measurement module) and the AC mode controller. 1: Microwave source, 2: directional coupler for power reference, 3: directional coupler for reflected signal power, 4: data acquisition for power reference, 5: data acquisition for reflected signal power, 6: AFM scanner and tip, 7: 50Ω load in resonator setup with AFM tip, 8: sample, 9: signal ground, 10: MW amplifiers, 11 MW mixer for demodulation, 12: low frequency oscillator, 13: low frequency mixer for demodulating the ω_{mod} signal, 14: dC/dV data acquisition; (b) PNA amplitude reflection (in Decibel dB) vs signal frequency from 1 to 20 GHz. (c) Spectroscopy curves showing dC/dV amplitude vs DC tip bias on differently doped regions of an *n*-type semiconductor. The doping levels range from 10^{15} to 10^{19} cm^{-3}. After Ref [39]

A schematic of dopant profiling with SMM is shown in Figure 1.4 [39]. Typically, a vector network analyzer (VNA) sends a continuous microwave (MW) signal to the conductive tip of an AFM. Depending on the impedance of the tip-sample interface, part of the microwave signal is reflected and measured by the PNA as the scattering S11 reflection signal. By measuring this signal, the capacitance/impedance at the contact position is obtained from the network analyzer. In practice, the mapped signals are the logarithm of the reflection coefficient amplitude, labeled as VNA amplitude, and the VNA phase. From the VNA amplitude and phase values, the contact capacitance/impedance can be derived after proper calibration.

The possible measurable range of doping concentrations in SMM has been demonstrated to be 10^{15}-10^{20} cm^3 in the case of Si [40]. The maximum lateral resolution has not yet been determined, which has been shown to be at least below 100 nm and determined by the tip radius as well as the local dopant density [39].

Scanning capacitance microscopy (SCM)/Scanning spreading resistance microscopy (SSRM)

SCM and SSRM represent two most extensively studied techniques for the purpose of 2D carrier/dopant profiling with nanometer scale resolution in semiconductors [41-43]. SCM measures the V_{ac}-induced capacitance variation of the tip/sample system, which depends on the carrier concentration underneath the tip, while in SSRM, by applying a V_{dc}, the local spreading resistance under the tip is measured (in an ideal case) which is intimately linked to the local resistivity of the sample. A spatial resolution of better than 10 nm and down to 1 nm (both dependent on used tips as well as measurement condition) has been previously demonstrated for SCM [44] and SSRM [45-46], respectively. These two techniques have proved their potential and wide applications in the area of 2D carrier/dopant profiling in materials such as Si, Ge, SiC, InP, GaN and GaAs. However, ZnO nanostructures have rarely been investigated, with only few studies on reporting the detection of local *p*-type ZnO. In terms of NWs structure, while another SPM technique, conductive-AFM (C-AFM) has been used for the study of electrical characterization on ZnO NWs [47], report of SCM and SSRM application is scarce.

A general comparison of different mentioned techniques for dopant/carrier profiling purpose is given in Table 1.1 in terms of their features such as detection type, spatial resolution, quantification possibility and ease of use.

Table 1.1: A general comparison of different dopant/carrier profiling techniques.

Techni-ques / Features	SIMS	SEM	Electron holography	CL	Atom probe tomography	Dopant-selective etching	KPFM	SMM	SCM	SSRM
Detection type	atoms 1D	carriers 2D	atoms 2D	carriers 2D	atoms 3D	/	carriers 2D	carriers 2D	carriers 2D	carriers 2D
Spatial resolution	1.5 nm	19 nm	5 nm	60 nm [28]	1 nm	/	atomic	< 100 nm	sub 10 nm	1 nm (in vacuum)
Quantifi-cation	calibration	no	no	yes	yes	no	difficult	calibration	calibration difficult	calibration
Ease of use	yes	yes	no, sample lamella	yes	very compli-cated	yes	yes	yes	yes	yes

1.3 Objective of this study

This thesis work aims to investigate the new applications of SCM and SSRM techniques to the electrical characterization of 2D doping profile in ZnO-related nanomaterials, with a particular focus on the quantitative determination of residual carrier concentrations inside non-intentionally doped (nid) ZnO NWs structure, which is considered being able to provide useful information on the way of *p*-type ZnO implementation. A strong effort is dedicated to the quantification analysis of the results on ZnO NWs by using calibration approach with the help of ZnO:Ga multilayer staircase structures and the comparison of the microscopic (SCM/SSRM) and macroscopic (conventional C-V measurement) characterization techniques. Then since *p*-type ZnO remains a tough challenge to overcome, great efforts have been made in the project to tackle this problem by doping ZnO NWs through both *ex situ* and *in situ* approaches. So another aspect of this work is to investigate the electrical properties of the doped ZnO NWs by SCM and SSRM in order to detect possible *p*-type ZnO. Furthermore, applications of the two techniques to characterizing ZnO-related nanostructures such as ZnO:Sb films and ZnO/ZnMgO coaxial NWs heterostructures are explored.

This thesis work is a part of the ANR MAD-FIZ (maîtrise du dopage des nanofils semiconducteurs : cas de l'oxyde de zinc) project which aims at understanding the complex relations between doping, size reduction, surface effects and transport properties in ZnO material with an ambitious objective of the realization of electroluminescent radial and/or axial ZnO NW *p-n* junctions and the observation of near UV electroluminescence. Six partners have taken part in this project including GEMAC (Groupe d'Etude de la Matière Condensée, GPM (Groupe de Physique des Matériaux), INL (Institut des Nanotechnologies de Lyon), Institut Néel, CEA-LETI (Commissariat à l'Energie Atomique et aux énergies alternatives-Laboratoire d'Electronique et des Technologies de l'Informatique) and CEA-DEN (Direction de l'Energie Nucléaire).

1.4 Outline of this work

This thesis is organized as follows:

After this introducing chapter (Chapter 1), Chapter 2 provides an introduction of ZnO basic properties and its *p*-type doing challenges, followed by an overview on the working principles of relevant techniques used in this work, including SCM, SSRM and C-AFM. Besides these techniques at microscopic scale, macroscopic characterization techniques such as I-V and C-V on metal-semiconductor Schottky contact are also described. At the end of this chapter, the developed planarization process based on dip-coating of SiO_2 for the studied ZnO NWs samples in order to obtain proper samples surfaces for consequent electrical characterization

measurements is presented.

Chapter 3 reports the application of SCM to characterizing ZnO NWs structures. Two NWs samples without intentional doping are studied, i.e. CBD grown and MOCVD grown NWs. Calibration method will be used for the purpose of quantitative analysis. Additionally, during the work of this chapter, the phenomenon of SCM data polarity inversion due to tip depletion effect in SCM measurements is investigated with the help of an *n*-type Si staircase structure.

In Chapter 4, the results of SSRM application on the same samples as in Chapter 3 are given. First the conductive diamond coated tip/sample contact characteristics are studied depending on the tip force. Then based on the SSRM results on ZnO NWs and on calibration structure under same condition, residual carrier concentrations for the ZnO NWs will be evaluated.

Chapter 5 presents characterization of collective ZnO NWs by employing conventional I-V and C-V techniques. Carrier concentration at a macroscopic level is determined from C-V analysis and the impact of the NWs field structure on the measurement result is investigated. Finally, a discussion is made on the difference of C-V characterization results from those in SCM/SSRM analysis.

In Chapter 6, related applications of SCM and SSRM on ZnO-based nanostructures are investigated with the main focus on the search and determination for *p*-type doping on ZnO NWs. *Ex situ* doping (by phosphorus-P) and *in situ* doping (by antimony-Sb) are studied. Main results are shown on Sb-doping samples including ZnO:Sb 2D film and ZnO/ZnO:Sb core-shell NWs structure in the attempt of attaining *p*-type in ZnO. Finally, considering the possibility to process easily *p*-type doping in ZnMgO, SCM and SSRM are used to characterize ZnO/ZnMgO core-multishell coaxial NWs heterostructures.

In the end, general conclusions and perspectives are given in Chapter 7.

References:

[1] Bunn, C. W. (1935). The lattice-dimensions of zinc oxide. Proceedings of the Physical Society, 47(5), 835.

[2] Look, D. C. (2001). Recent advances in ZnO materials and devices. Materials Science and Engineering: B, 80(1), 383-387.

[3] Özgür, Ü., Alivov, Y. I., Liu, C., Teke, A., Reshchikov, M., Doğan, S., ... & Morkoc, H. (2005). A comprehensive review of ZnO materials and devices. Journal of applied physics, 98(4), 041301.

[4] Janotti, A., & Van de Walle, C. G. (2009). Fundamentals of zinc oxide as a semiconductor. Reports on Progress in Physics, 72(12), 126501.

[5] Jagadish, C., & Pearton, S. J. (Eds.). (2011). Zinc oxide bulk, thin films and nanostructures: processing, properties, and applications. Elsevier.

[6] Xu, S., & Wang, Z. L. (2011). One-dimensional ZnO nanostructures: solution growth and functional properties. Nano Research, 4(11), 1013-1098.

[7] Huang, M. H., Mao, S., Feick, H., Yan, H., Wu, Y., Kind, H., ... & Yang, P. (2001). Room-temperature ultraviolet nanowire nanolasers. Science, 292(5523), 1897-1899.

[8] Könenkamp, R., Word, R. C., & Schlegel, C. (2004). Vertical nanowire light-emitting diode. Applied Physics Letters, 85(24), 6004-6006.

[9] Goldberger, J., Sirbuly, D. J., Law, M., & Yang, P. (2005). ZnO nanowire transistors. The Journal of Physical Chemistry B, 109(1), 9-14.

[10] Law, M., Greene, L. E., Johnson, J. C., Saykally, R., & Yang, P. (2005). Nanowire dye-sensitized solar cells. Nature materials, 4(6), 455-459.

[11] Wang, Z. L., & Song, J. (2006). Piezoelectric nanogenerators based on zinc oxide nanowire arrays. Science, 312(5771), 242-246.

[12] Fan, Z., & Lu, J. G. (2006). Chemical sensing with ZnO nanowire field-effect transistor. Nanotechnology, IEEE Transactions on, 5(4), 393-396.

[13] Soci, C., Zhang, A., Xiang, B., Dayeh, S. A., Aplin, D. P. R., Park, J., ... & Wang, D. (2007). ZnO nanowire UV photodetectors with high internal gain. Nano letters, 7(4), 1003-1009.

[14] Kuo, T. J., Lin, C. N., Kuo, C. L., & Huang, M. H. (2007). Growth of ultralong ZnO nanowires on silicon substrates by vapor transport and their use as recyclable photocatalysts. Chemistry of Materials, 19(21), 5143-5147.

[15] Yuan, G. D., Zhang, W. J., Jie, J. S., Fan, X., Zapien, J. A., Leung, Y. H., ... & Lee, S. T. (2008). p-type ZnO nanowire arrays. Nano Letters, 8(8), 2591-2597.

[16] Fan, Z., Wang, D., Chang, P. C., Tseng, W. Y., & Lu, J. G. (2004). ZnO nanowire field-effect transistor and oxygen sensing property. Applied Physics Letters, 85(24),

5923-5925.

[17] De Wolf, P., Stephenson, R., Trenkler, T., Clarysse, T., Hantschel, T., & Vandervorst, W. (2000). Status and review of two-dimensional carrier and dopant profiling using scanning probe microscopy. Journal of Vacuum Science & Technology B, 18(1), 361-368.

[18] Goodwin‐Johansson, S. H., Ray, M., Kim, Y., & Massoud, H. Z. (1992). Reconstructed two-dimensional doping profiles from multiple one-dimensional secondary ion mass spectrometry measurements. Journal of Vacuum Science & Technology B, 10(1), 369-379.

[19] Gorbenko, V., Grenier, A., Audoit, G., Cipro, R., Martin, M., David, S., ... & Barnes, J. P. (2015). Chemical characterization of III-V heterostructures in 3D architecture. Microelectronic Engineering, 147, 219-222.

[20] Gorbenko, V., Bassani, F., Merkulov, A., Baron, T., Martin, M., David, S., & Barnes, J. P. (2016). SIMS depth profiling and topography studies of repetitive III–V trenches under low energy oxygen ion beam sputtering. Journal of Vacuum Science & Technology B, 34(3), 03H131.

[21] Elliott, S. L., Broom, R. F., & Humphreys, C. J. (2002). Dopant profiling with the scanning electron microscope-A study of Si. Journal of applied physics, 91(11), 9116-9122.

[22] Turan, R., Perovic, D. D., & Houghton, D. C. (1996). Mapping electrically active dopant profiles by field‐emission scanning electron microscopy. Applied physics letters, 69(11), 1593-1595.

[23] Venables, D., Jain, H., & Collins, D. C. (1998). Secondary electron imaging as a two-dimensional dopant profiling technique: Review and update. Journal of Vacuum Science & Technology B, 16(1), 362-366.

[24] Elliott, S. L., Broom, R. F., & Humphreys, C. J. (2002). Dopant profiling with the scanning electron microscope-A study of Si. Journal of applied physics, 91(11), 9116-9122.

[25] Rau, W. D., Schwander, P., Baumann, F. H., Höppner, W., & Ourmazd, A. (1999). Two-dimensional mapping of the electrostatic potential in transistors by electron holography. Physical Review Letters, 82(12), 2614.

[26] Lichte, H., Geiger, D., & Linck, M. (2009). Off-axis electron holography in an aberration-corrected transmission electron microscope. Philosophical Transactions of the Royal Society of London A: Mathematical, Physical and Engineering Sciences, 367(1903), 3773-3793.

[27] Giles, N. C., Xu, C., Callahan, M. J., Wang, B., Neal, J. S., & Boatner, L. A. (2006). Effects of phonon coupling and free carriers on band-edge emission at room temperature in n-type ZnO crystals. Applied Physics Letters, 89(25), 251906.

[28] Watanabe, K., Nagata, T., Oh, S., Wakayama, Y., Sekiguchi, T., Volk, J., & Nakamura, Y. (2016). Arbitrary cross-section SEM-cathodoluminescence imaging of growth sectors and

local carrier concentrations within micro-sampled semiconductor nanorods. Nature communications, 7:10609, 1-9.

[29] Watanabe, K., Nakamura, Y., & Ichikawa, M. (2008). Spatial resolution of imaging contaminations on the GaAs surface by scanning tunneling microscope-cathodoluminescence spectroscopy. Applied Surface Science, 254(23), 7737-7741.

[30] Perea, D. E., Allen, J. E., May, S. J., Wessels, B. W., Seidman, D. N., & Lauhon, L. J. (2006). Three-dimensional nanoscale composition mapping of semiconductor nanowires. Nano letters, 6(2), 181-185.

[31] Gault, B., Vurpillot, F., Vella, A., Gilbert, M., Menand, A., Blavette, D., & Deconihout, B. (2006). Design of a femtosecond laser assisted tomographic atom probe. Review of Scientific Instruments, 77(4), 043705.

[32] Amirifar, N., Lardé, R., Talbot, E., Pareige, P., Rigutti, L., Mancini, L., ... & Hassani, S. (2015). Quantitative analysis of doped/undoped ZnO nanomaterials using laser assisted atom probe tomography: Influence of the analysis parameters. Journal of Applied Physics, 118(21), 215703.

[33] Saxey, D. W. (2011). Correlated ion analysis and the interpretation of atom probe mass spectra. Ultramicroscopy, 111(6), 473-479.

[34] Henning, A. K., Hochwitz, T., Slinkman, J., Never, J., Hoffmann, S., Kaszuba, P., & Daghlian, C. (1995). Two-dimensional surface dopant profiling in silicon using scanning Kelvin probe microscopy. Journal of applied physics, 77(5), 1888-1896.

[35] http://www.corpe.et.aau.dk/research/pcc

[36] Turner, D. R. (1960). On the mechanism of chemically etching germanium and silicon. Journal of the electrochemical Society, 107(10), 810-816.

[37] Smoliner, J., Huber, H. P., Hochleitner, M., Moertelmaier, M., & Kienberger, F. (2010). Scanning microwave microscopy/spectroscopy on metal-oxide-semiconductor systems. Journal of Applied Physics, 108(6), 064315.

[38] Humer, I., Huber, H. P., Kienberger, F., Danzberger, J., & Smoliner, J. (2012). Phase and amplitude sensitive scanning microwave microscopy/spectroscopy on metal-oxide-semiconductor systems. Journal of Applied Physics, 111(7), 074313.

[39] Huber, H. P., Humer, I., Hochleitner, M., Fenner, M., Moertelmaier, M., Rankl, C., ... & Kabos, P. (2012). Calibrated nanoscale dopant profiling using a scanning microwave microscope. Journal of Applied Physics, 111(1), 014301.

[40] Torigoe, K., Arita, M., & Motooka, T. (2012). Sensitivity analysis of scanning microwave microscopy for nano-scale dopant measurements in Si. Journal of Applied Physics, 112(10), 104325.

[41] Williams, C. C. (1999). Two-dimensional dopant profiling by scanning capacitance

microscopy. Annual review of materials science, 29(1), 471-504.

[42] Giannazzo, F., Musumeci, P., Calcagno, L., Makhtari, A., & Raineri, V. (2001). Carrier concentration profiles in 6H-SiC by scanning capacitance microscopy. Materials Science in Semiconductor Processing, 4(1), 195-199.

[43] Eyben, P., Xu, M., Duhayon, N., Clarysse, T., Callewaert, S., & Vandervorst, W. (2002). Scanning spreading resistance microscopy and spectroscopy for routine and quantitative two-dimensional carrier profiling. Journal of Vacuum Science & Technology B, 20(1), 471-478.

[44] Bussmann, E., & Williams, C. C. (2004). Sub-10 nm lateral spatial resolution in scanning capacitance microscopy achieved with solid platinum probes. Review of scientific instruments, 75(2), 422-425.

[45] Douheret, O., Bonsels, S., & Anand, S. (2005). Determination of spatial resolution in atomic-force-microscopy-based electrical characterization techniques using quantum well structures. Journal of Vacuum Science & Technology B, 23(1), 61-65.

[46] Zhang, L., Tanimoto, H., Adachi, K., & Nishiyama, A. (2008). 1-nm spatial resolution in carrier profiling of ultrashallow junctions by scanning spreading resistance microscopy. Electron Device Letters, IEEE, 29(7), 799-801.

[47] Beinik, I., Kratzer, M., Wachauer, A., Wang, L., Lechner, R. T., Teichert, C., ... & Hsu, X. Y. (2011). Electrical properties of ZnO nanorods studied by conductive atomic force microscopy. Journal of Applied Physics, 110(5), 052005.

Chapter 2

ZnO properties, characterization techniques and samples preparation

In this chapter, first the basic properties of ZnO material is described with a special focus on ZnO NWs and ZnO *p*-type doping problem. Then, the scanning probe microscopy (SPM) techniques used in this work are introduced, including scanning capacitance microscopy (SCM), scanning spreading resistance microscopy (SSRM) and conductive atomic force microscopy (C-AFM). The probes employed for these techniques are also treated. The next section deals with conventional macroscopic electrical techniques for characterizing metal-semiconductor structure, i.e. current-voltage (I-V) and capacitance-voltage (C-V) techniques, which have been used for the characterization of collective ZnO NWs in this work. In the end, the developed planarization process on the studied ZnO NWs structure for future electrical SPM measurements is presented.

2.1 Introduction of ZnO

2.1.1 ZnO basic properties

2.1.1.1 Crystal structure

ZnO is a II-VI compound semiconductor whose ionicity resides at the borderline between the covalent and ionic semiconductors. The crystal structures shared by ZnO are wurtzite (*B4*), zinc blende (*B3*), and rocksalt (*B1*) as schematically shown in Figure 2.1 [1]. Among them, the wurtzite structure, which belongs to the space group $P6_3mc$, is thermodynamically stable under ambient conditions thus the most popular form of ZnO. The wurtzite structure has a hexagonal unit cell with two lattice parameters *a* and *c* in the ratio of $c/a=(8/3)^{1/2}=1.633$ (in an ideal wurtzite structure) and belongs to the space group $P6_3mc$ in the Hermann-Mauguin notation. The structure is composed of two interpenetrating hexagonal close-packed (hcp) sublattices, each of which consists of one type of atom displaced with respect to each other along the threefold *c*-axis by the amount of $u=3/8=0.375$ (in an ideal wurtzite structure) in fractional coordinates. The internal parameter *u* is defined as the length of the bond parallel to the *c*-axis (anion-cation bond length or the nearest-neighbor distance) divided by the *c* lattice parameter. In a real ZnO crystal, the wurtzite structure slightly deviates from the ideal arran-

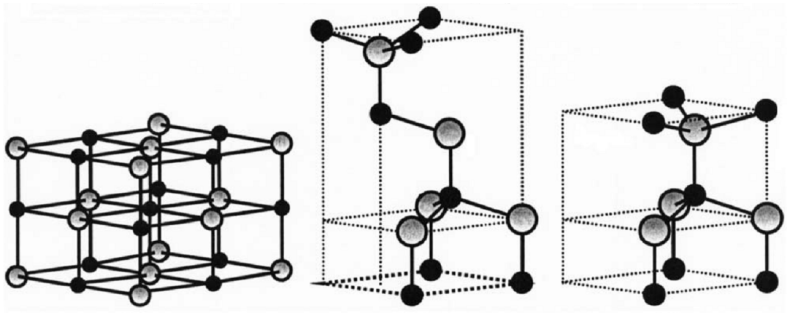

(a) (b) (c)

Figure 2.1: Stick and ball representation of ZnO crystal structures: (a) cubic rocksalt, (b) cubic zinc blende and (c) hexagonal wurtzite. The shaded gray and black spheres denote Zn and O atoms, respectively. (after reference [1])

gement, by changing the *c/a* ratio or the *u* value in such a way that the four tetrahedral distances are kept roughly constant through a distortion of tetrahedral angles due to long-range polar interactions.

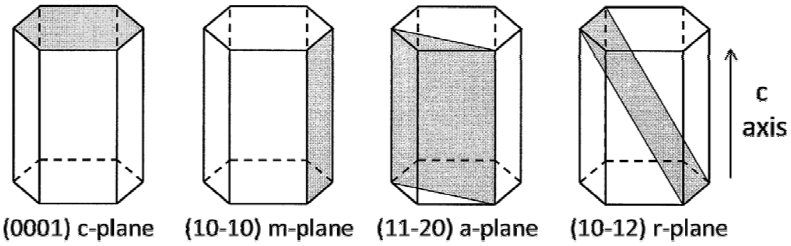

Figure 2.2: Illustration of typical wurtzite surfaces defined by four-vectors [2].

The surfaces in wurtzite structure are typically described by four vectors - three in the *xy*-plane defining the hexagonal geometry and one along the *z* axis (known as *c* axis). The four most common face terminations of wurtzite ZnO are (0001), (000-1), the non-polar (11-20) and (10-10) (Figure 2.2). The (0001) and (000-1) surfaces are perpendicular to the *c* axis. They are terminated by either a layer of zinc or a layer of oxygen, making them polar and possess different chemical and physical properties. (11-20) and (10-10) facets contain equal numbers of Zn and O atoms thus being non-polar.

2.1.1.2 Lattice parameters

Lattice parameters of ZnO have been investigated over many decades. The lattice parameters of a semiconductor usually depend on the following factors: (i) free electron concentration acting via deformation potential of a conduction band minimum occupied by these electrons, (ii) concentration of foreign atoms and defects and their difference of ionic radii with respect to the substituted matrix ion, (iii) external strains (e.g. those induced by substrate), and (iv) temperature. The room-temperature lattice constants determined by various experimental

Table 2.1: Measured and calculated lattice constants and the *u* parameter of ZnO in the literature.

a(Å)	*c*(Å)	*c/a*	*u*	Reference
		1.593	0.3856	[3] (ab initio calculation)
3.286	5.241	1.595	0.383	[4] (ab initio calculation)
3.2501	5.2071	1.6021	0.3817	[5] (*x*-ray diffraction measurement)
3.2496	5.2042	1.6018	0.3819	[6] (*x*-ray diffraction measurement)

measurements and theoretical calculations for the wurtzite ZnO are in good agreement with each other. The lattice constants mostly range from 3.2475 to 3.2501Å for the *a*-parameter and from 5.2042 to 5.2075Å for the *c*-parameter. The *c/a* ratio and *u* parameter vary in a slightly wider range, from 1.593 to 1.6035 and 0.383 to 0.3856, respectively. The deviation from that of the ideal wurtzite crystal is probably due to lattice stability and ionicity. It has been reported that free charge is the dominant factor responsible for expanding the lattice proportional to the deformation potential of the conduction band minimum and inversely proportional to the carrier density and bulk modulus. The point defects such as zinc antisites, oxygen vacancies, and extended defects, such as threading dislocations, also increase the lattice constant, albeit to a lesser extent in the heteroepitaxial layers.

2.1.1.3 Electrical characteristics

An accurate knowledge of a semiconductor's band structure is of vital importance when it is considered for potential applications. Experimental techniques can be used to investigate the band structure of the electronic states of wurtzite ZnO, including *x*-ray/UV reflection/absorption/emission techniques and angle-resolved photoelectron spectroscopy (ARPES). Besides, different theoretical approaches of varying degrees of complexity have been employed to calculate the band structure of ZnO.

One of the currently most reliable approaches to computation of electronic structure for semiconductors is a two-step procedure [8]: first, energy eigenvalues and eigenfunctions of a gKS (generalized Kohn-Sham) equation are computed using the HSE03 (Heyd, Scuseria, and Ernzerhof) [9] hybrid functional as zeroth approximation to the XC (exchange and correlation) self-energy. Then, by applying Hedin's GW approximation [10] for the self-energy, QP energies are computed with an accuracy of about 0.1 eV. This HSE03 +GW approach has proven its reliability yielding results in good agreement with measurements for ZnO [11].

The calculated quasiparticle (QP) band structures and densities of states (DOS) for wurtzite-ZnO, obtained from the HSE03+GW (as well as the GGA+U+Δ approach) (from reference [7]), are shown in Figure 2.3. The DOSs from this result show a good agreement

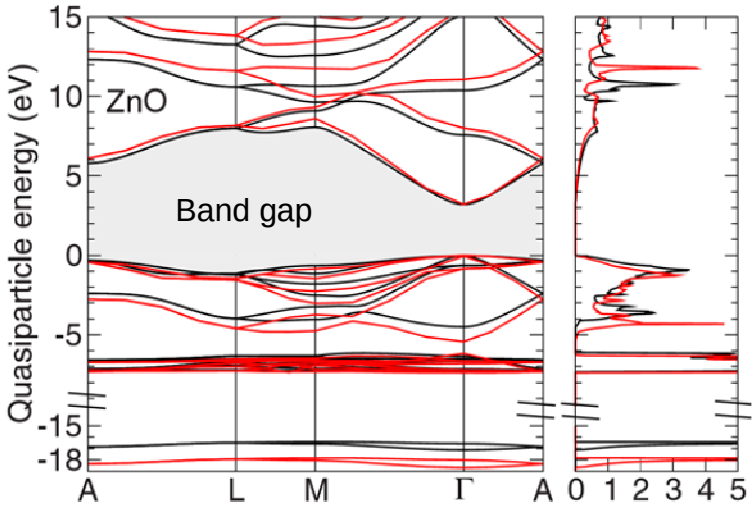

Figure 2.3: Quasiparticle band structures and densities of states of wurtzite-ZnO calculated within the GGA+U+Δ approach (black solid lines) and the HSE03+GW approach (red/bright solid lines). The valence band (VB) maximum has been used as energy zero and the fundamental gap region is shaded. (after [7])

with spectra from photoemission spectroscopy, *x*-ray absorption, and resonant *x*-ray emission spectroscopy [11]. The calculated fundamental gaps E_g is 3.21 eV (for wurtzite-ZnO). This value is slightly smaller than the experimental value (3.37 eV at room temperature [12]). One reason for the observed deviation is the atomic geometry obtained from the DFT-GGA (Density functional theory- Generalized gradient approximation) approach, which tends to overestimate the lattice constants slightly and, hence, gives too small gaps.

The two most famous electrical properties of ZnO are its direct wide band gap and large exciton binding energy. The band gap of ZnO is 3.44 eV at low temperatures and 3.37 eV at room temperature [12]. For comparison, the respective values for wurtzite GaN are 3.50 eV and 3.44 eV [13]. This enables applications of ZnO in optoelectronics in the blue/UV region, including light-emitting diodes, laser diodes and photodetector [14-16]. Reports on *p*-*n* homojunctions have also appeared in the literature [17], despite that stability and reproducibility have not been fully established. Furthermore, band-gap engineering in ZnO can be achieved by alloying with MgO and/or CdO (Cd doping can decrease the band gap, whereas Mg doping can increase the band gap). It is possible to provide a wide range of band gaps (3-4.5 eV) and band offsets for practical device applications [18]. The free-exciton binding energy in ZnO is 60 meV [19], compared with 25 meV in GaN [13]. This large exciton binding energy implies that efficient excitonic emission in ZnO can persist at room temperature and even higher [19]. Since the oscillator strength of excitons is typically much larger than that of direct electron-hole transitions in direct gap semiconductors [20], the large exciton binding energy makes ZnO a promising material for optical devices based on

excitonic effects. The electron effective mass for ZnO is 0.24 m_0, and the hole effective mass is 0.59 m_0. The corresponding electron Hall mobility at 300K is μ= 200 $cm^2/V•s$ for a low *n*-type conductivity, and the value for the hole is 5-50 $cm^2/V•s$ for a low p-type conductivity. The basic physical properties of ZnO are summarized and given in Table 2.2.

Table 2.2: Some basic properties of ZnO single crystal [18].

Property	**Value**
Density	5.606 g/cm^3
Atoms density	8.4×10^{22} $/cm^3$
Electrons density	3.36×10^{23} $/cm^3$
Stable phase at 300 K	wurtzite
Melting point	1975 °C
Thermal conductivity	0.6, 1-1.2 W/cm•K
Linear expansion coefficient (/°C)	a_0: 6.5×10^{-6} , c_0: 3.0×10^{-6}
Static dielectric constant	8.5
Refractive index	2.008, 2.029
Energy gap	3.37 eV (direct)
Intrinsic carrier concentration	$<10^6$ $/cm^3$
Exciton binding energy	60 meV
Electron effective mass	0.24 m_0
Electron Hall mobility at 300 K for low *n*-type conductivity	200 cm^2 /V•s
Hole effective mass	0.59 m_0
Hole Hall mobility at 300 K for low p-type conductivity	5-50 cm^2 /V•s

2.1.2 Doping of ZnO

Ambipolar doping is the main problem on the way of the application of ZnO as a material for electro-optic devices. Non-intentionally doped (nid) ZnO normally shows *n*-type conduction characteristics with residual carrier concentrations usually higher than 10^{17} cm^{-3} due to the presence of native donor defects (such as oxygen vacancies and zinc interstitials) [21-23], hydrogen atoms [24-25] and other possible impurities introduced during the growth process [26].

n-type doping of ZnO is easily to be realized. Group-III elements Al, Ga, and In as substitutional elements for Zn and group-VII elements Cl and I as substitutional elements for O can readily be used as *n*-type dopants [27]. For example, ZnO doping with Al, Ga, and In

has been attempted by many groups, leading to highly conductive *n*-type ZnO films [28-30]. Myong *et al*. grew Al-doped ZnO films by photo-assisted MOCVD method and obtained highly conductive films with a minimum resistivity of 6.2×10^{-4} Ω·cm [28]. Ataev *et al*. reported Ga-doped ZnO films grown by chemical-vapor deposition with resistivities as low as 1.2×10^{-4} Ω·cm [29]. Ko *et al*. succeeded in Ga doping of ZnO films grown on GaN templates by plasma-assisted MBE [30]. Thus, *n*-type doping of ZnO has been developed very well and is successfully used in various applications as *n*-type layers in light-emitting diodes as well as transparent ohmic contacts.

In contrast, reliable and stable *p*-type ZnO doping still remains a primary challenge for ZnO homojunction fabrication and related applications. The compensating effects of the donor-type defects and the low solubility of *p*-type dopants are both considered to be responsible for the difficulty in fabricating *p*-type ZnO [31-32]. In the research studies around the world, great efforts have been devoted to the realization of *p*-type ZnO as well as the understanding of origins of difficulties, in terms of both theoretical and experimental studies. *p*-type doping in ZnO may be possible by substituting either group-I elements (Li, Na, and K) for Zn sites or group-V elements (N, P, As and Sb) for O sites. From a theoretical point of view, group-I elements as *p*-type dopants in ZnO are better than group-V elements. However, the doping efficiency for them is usually limited by the formation of compensating interstitial [18]. Regarding group-V elements such as P, As and Sb, first-principles calculations shows that X_O (P_O, As_O and Sb_O) are deep acceptors and have high acceptor-ionization energies, owing to their large ionic radii as compared to O, which make it impossible for X_O to efficiently dope ZnO into *p*-type [26]. However, recent experiments showed that *p*-type ZnO could be prepared by doping with X. Then based on first-principle calculation, Limpijumnong *et al*. proposed X_{Zn}-$2V_{Zn}$ acceptor model about the large-size-mismatched impurities in ZnO [33]. In this model, X atom occupies Zn antisite instead of O sites to form X_{Zn}-$2V_{Zn}$ complex which is able to act as an acceptor.

Up to now, various approaches using group-IB, group-I, and group-V elements as potential acceptor dopants have been experimentally demonstrated for the synthesis of *p*-type ZnO using both *ex situ* and *in situ* doping processes [34-35]. Co-doping method (for example, III-N co-doping with III being In, Al or Ga) has also be proposed to attain *p*-type ZnO [36]. Nevertheless, although a lot of progress has been made in this field, there is still a long distance to the eventual success.

2.1.3 ZnO NWs

ZnO is easy to grow with rich morphologies and properties by a variety of economic processes. Among various nanostructures under investigation, ZnO nanowires (NWs) have

attracted significant attention over the last decade not only for their remarkable chemical and physical properties, but also for their diverse current and future technological applications [37]. Due to their remarkable performance in electronics, optics, and photonics, ZnO NWs are attractive candidates for many applications such as ultraviolet (UV) lasers [38-39], light emitting diodes (LED) [40-41], field-effect transistors (FET) [42-44], solar cells [45-46], nanogenerators [47], gas sensors [48], photodetectors [49], and photocatalysts [50].

ZnO NWs can be synthesized by a variety of techniques, which can be classified into two categories: (high temperature) vapor phase synthesis and (low temperature) solution phase synthesis.

A typical vapor phase synthesis method takes place in a closed chamber with a gaseous environment. First vapor species are produced by evaporation, chemical reduction, and gaseous reaction. Then, the species are transferred and condensed onto the surface of a solid substrate. Generally, the vapor phase synthesis process is carried out at high temperatures from 500 ^{o}C to 1500 ^{o}C and is able to produce high-quality NWs. Typical vapor phase synthesis techniques include vapor liquid solid (VLS) growth, chemical vapor deposition (CVD), metal organic chemical vapor deposition (MOCVD), physical vapor deposition (PVD), molecular beam epitaxy (MBE), pulsed laser deposition (PLD) and metal organic vapor phase epitaxy (MOVPE). Among them, VLS and MOCVD are two of the most important techniques for the ZnO NWs synthesis.

Solution phase synthesis has many advantages in comparison to vapor phase synthesis, such as low cost, low temperature, scalability, and ease of handling. Generally, solution phase reactions occur at relatively low temperatures (<200 ^{o}C) with respect to vapor phase synthesis processes. Thus, solution synthesis methods allow for a greater choice of substrates from inorganic to organic substrates. Besides, in solution phase synthesis, the growth process could be realized in either an aqueous or organic solution or a mixture of the two.

Semiconducting properties of ZnO NWs such as carrier concentration, conductivity, and mobility are often measured by a typical configuration of FET structure with a back gate [51]. The NW FET configuration is usually fabricated on highly doped Si substrates (back gate) with a SiO_2 layer of 100-500 nm (dielectric) to measure the conductivity type of the NWs, in which case the conduction type of the NWs can be determined by its responses to the applied gate voltage [52].

2.2 AFM-based scanning probe microscopy

Since its invention by Binnig *et al* [53], AFM has proved enormously adaptable and has been used to investigate not only the topography of nanostructured samples but also a diverse range of other properties: mechanical, magnetic and electrical. Along with the development of

techniques to explore the 'nanoworld', the continuous shrinkage of electronic devices has pushed their critical dimensions down to the nanometer level making necessary electrical characterization of semiconductor structures and devices at the corresponding scale. AFM has found extensive applications in electrical characterization to extend various conventional techniques into nanometer scale, showing prospect of being good candidates to meeting the demands of novel techniques for characterizing semiconductor devices involving nanostructures. Typical SPM techniques for electrical characterization on the base of AFM include SCM, SSRM, C-AFM, TUNA (tunneling atomic force microscopy), KPFM (kelvin probe force microscopy) and EFM (electrostatic force microscopy). This section will describe those having been employed in the work of this dissertation, i.e. SCM, SSRM, C-AFM.

2.2.1 Atomic force microscopy (AFM)

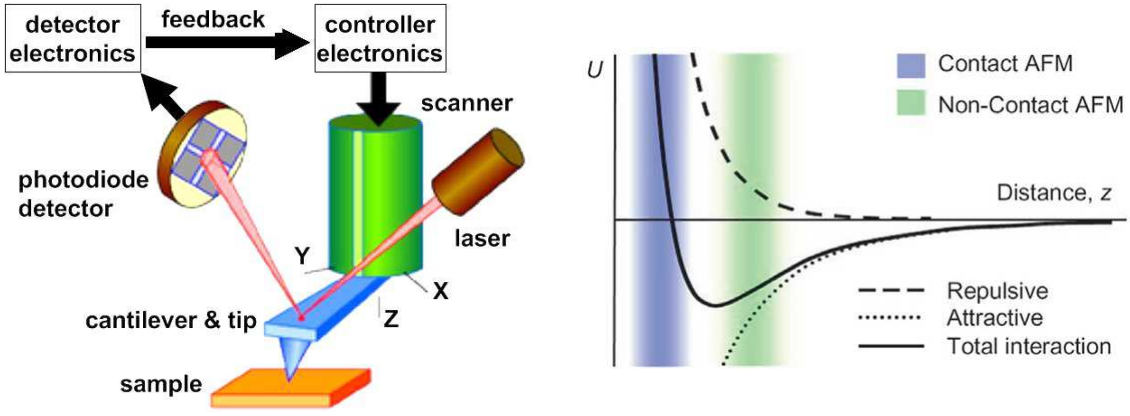

(a) (b)

Figure 2.4: (a) Schematic view of AFM operation [55]. (b) Plot of force against distance [56].

In AFM, an ultrasharp tip, which is mounted on a very small cantilever (typically a few 100 µm long and a few tens of µm wide) is positioned very close to the sample surface. In operation, the probe (cantilever + tip) is scanned over the surface of the sample and the deflection of the cantilever is measured, which reflects the topography change at each point, allowing one to reconstruct the scanned area with topography information. In most cases, the measurement of the cantilever deflection is done through monitoring the deviation of a laser beam reflected from the cantilever backside using a 4-sector photodetector. The key to the success of scanning probe techniques is the probe being positioned with extremely high precision and this is usually achieved using piezo-electric actuators [54]. A schematic view of AFM principle is presented in Figure 2.4.

Three basic AFM operation modes exist: contact mode, non-contact mode and intermittent contact mode. Among them, the first two are the most popularly used. In contact mode, as indicated by its name, the AFM tip is scanned in constant contact with the sample and the

change of cantilever deflection is monitored. A feedback loop used to control the voltage applied to the relevant piezo-element, and hence to maintain a constant cantilever deflection by vertically moving the scanner at each (*x*, *y*) data point to maintain a "setpoint" deflection. The distance that the scanner moves vertically at each data point is stored by the computer to form the topographic image of the sample surface. This allows the user to control the force acting on the sample, maintaining a low value even for significant changes in sample height, and thus preventing damage to both tip and sample.

Table 2.3: Comparison of the three AFM working modes [57].

	Advantage	Disadvantage
Contact Mode	● High scan speeds ● Rough samples with extreme changes in vertical topography can sometimes be scanned more easily	● Lateral (shear) forces may distort features in the image ● In ambient conditions may get strong capillary forces due to adsorbed fluid layer ● Combination of lateral and strong normal forces reduce resolution and mean that the tip may damage the sample, or vice versa
Tapping Mode	● Lateral forces almost eliminated ● Higher lateral resolution on most samples ● Lower forces so less damage to soft samples or tips	● Slower scan speed than in contact mode
Non-contact Mode	● Both normal and lateral forces are minimized, so good for measurement of very soft samples ● Can get atomic resolution in a UHV environment	● In ambient conditions the adsorbed fluid layer may be too thick for effective measurements ● Slower scan speed than tapping and contact modes to avoid contacting the adsorbed fluid layer

In non-contact mode, the cantilever is oscillated at a frequency slightly above the cantilever's resonance frequency typically with an amplitude of a few nanometers (<10 nm), in order to obtain an AC signal from the cantilever. The tip does not contact the sample surface, but oscillates above the adsorbed fluid layer on the surface during scanning. The cantilever's resonant frequency is decreased by the van der Waals forces, which extend from 1nm to 10nm above the adsorbed fluid layer, and by other long range forces which extend above the surface. The decrease in resonant frequency causes the amplitude of oscillation to decrease. The feedback loop maintains a constant oscillation amplitude or frequency by vertically moving the scanner at each (*x*, *y*) data point until a "setpoint" amplitude or frequency is reached. Finally, the vertically moving distance of the scanner at each (*x*, *y*) data point is stored by the

computer to produce the topographic image of the sample surface.

In intermittent contact mode, also referred to as “tapping mode”, a small piezo-electric element is used to vibrate the cantilever at, or close to, its resonant frequency. As the tip is brought towards the sample, the interaction between the tip and the sample leads to a force gradient which modifies the cantilever resonant frequency, so that for a fixed drive frequency, the cantilever’s amplitude of vibration decreases. Additionally, for typical tapping mode conditions, the tip makes contact with the surface at the bottom of each oscillation, resulting in a damping of the cantilever oscillation amplitude. In this case the feedback circuit is employed to maintain a constant cantilever oscillation amplitude rather than a constant cantilever deflection. The major advantage of this approach over contact mode is that since the probe only lightly “taps” on the sample surface during scanning, at the bottom of its swing, lateral (friction) forces between tip and sample are minimized, reducing the chance of damaging samples. A comparison of different AFM operation modes is presented in Table 2.3.

In this work, tapping mode is used when only the examination of topography is of interest, for example, to check the sample surface during sample preparation process, while electrical modes such as SCM, SSRM and C-AFM all operate in contact mode.

2.2.2 Scanning capacitance microscopy (SCM)

SCM has been developed and identified as a powerful tool for imaging two-dimensional carrier profiles in semiconductor devices and materials, with a nanometer spatial resolution [58-64]. Operating in contact mode and with a V_{dc} and a V_{ac} applied between the tip and sample, it measures the V_{ac}-induced capacitance variation of the metal-insulator-semiconductor (MIS) capacitor formed by the tip and sample. Due to the dependence of the depletion response of the semiconductor material on its local free carrier concentration, this information, at each position, is reflected by the capacitance variation signal.

SCM physical principle

The basic principle of SCM can be explained from the 1D MIS capacitor (Figure 2.5) [59], which consists of a dielectric layer sandwiched between a metal electrode (called gate) and a semiconducting substrate. An important feature of this structure is that the capacitance between the semiconductor (back contact) and the metal electrode is voltage-dependent. The equivalent circuit is simply composed of two capacitances: a capacitance in accumulation defined by the oxide thickness (C_{ox}), and a doping-dependent capacitance of the semiconductor (C_s). For an *n*-type semiconductor, when a positive bias is applied to the metal electrode, carriers will accumulate at the semiconductor/oxide interface. In this case, the

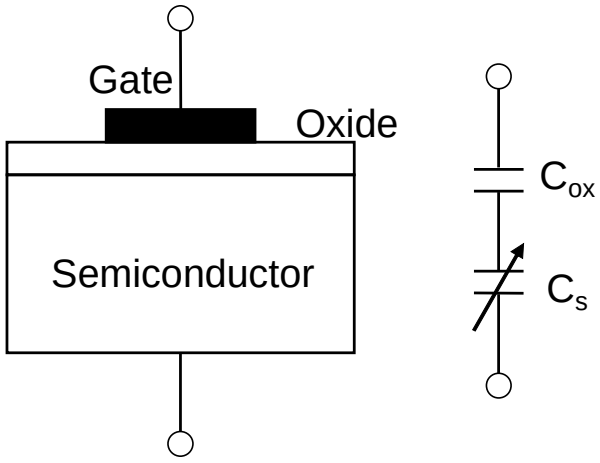

Figure 2.5: One-dimensional (1D) metal-insulator-semiconductor (MIS) capacitor for illustration of the tip-sample configuration in SCM measurement.

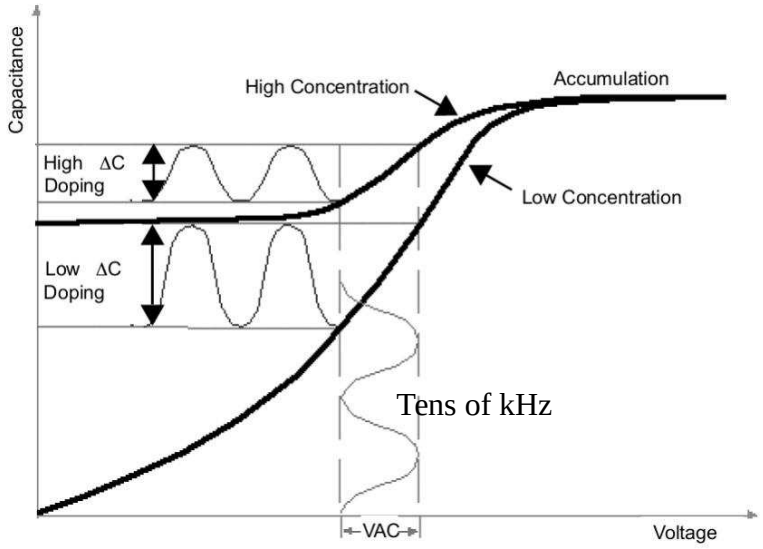

Figure 2.6: Illustration of SCM principle from C-V curves. C-V curve for a higher carrier concentration has a larger slope in the depletion region and a larger capacitance difference between the accumulation and deep depletion regime. The same V_{ac} applied on two materials with different carrier concentrations produces different ΔC signal.

measured capacitance (the accumulation capacitance) depends solely on the properties of the oxide layer. If a negative bias is applied, carriers will be repelled from the semiconductor-oxide interface, creating a depletion layer which acts as an additional dielectric layer in series with the oxide layer, decreasing the capacitance of the system. If the applied bias slowly becomes more negative, a minority carrier inversion layer will be generated at the semiconductor surface and hence the capacitance returns to its original value. However, if the bias is swept quickly, there is no time for an inversion layer to develop, and the capacitance will continue to drop (referred to as deep depletion [65]) until the breakdown field is reached.

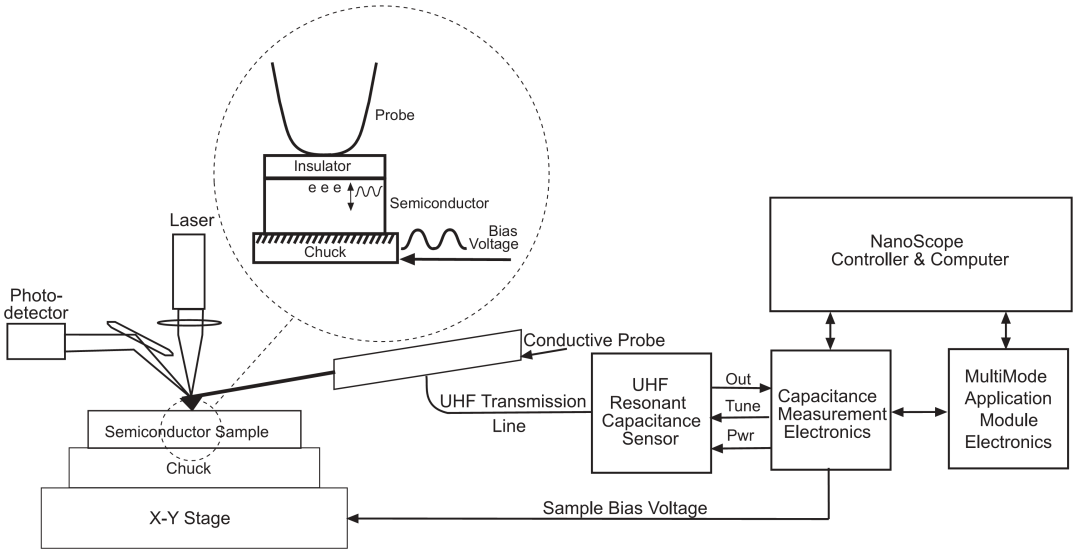

Figure 2.7: Diagram of SCM. Two main parts are presented: tip-sample system and the capacitance detection system [67].

In SCM, a kilohertz (kHz) frequency (5~100 kHz range with typical value of 90 kHz) V_{ac} is applied to the tip to induce capacitance changes. Hence, inversion is avoided, as there is no enough time for minority carrier diffusion to occur, and the system operates in the deep depletion regime.

Besides the voltage dependence of the system capacitance, the form of the C-V curve is also dependent on the carrier concentration in the sample. Material with fewer carriers depletes more easily, resulting in increases in the difference in capacitance (ΔC) between the accumulation and deep depletion regimes, and in the slope in the depletion regime. This is the very reason why SCM is able to probe the information of local carrier density (Figure 2.6).

In reality, in order to achieve high spatial resolution, the metal gate is replaced by an ultra-sharp conductive probe tip, thus the SCM measurement system can be represented by a 3D MIS capacitor. In this circumstance, the tip-sample capacitance should be in the order of attofarad (10^{-18} farad). Such a small static capacitance is far smaller than the system stray counterpart (cantilever/sample capacitance) and is extremely difficult to be measured, so modulation method has been introduced while measuring a dynamic change in capacitance at this scale is possible. This is implemented by the use of an ultra-high frequency (~1 GHz) capacitance sensor in combination with a lock-in amplifier, whose details can be easily found in the literature such as ref [66]. A diagram of SCM system is given in Figure 2.7.

Depending on using the feedback control or not, two modes are possible in SCM operation, named open loop SCM (without feedback) and closed loop SCM (with feedback). In open loop SCM, a V_{ac} with constant amplitude is applied during the scan, resulting in a corresponding change in capacitance, which may be detected by the capacitance sensor. As

the tip moves from a region with a high carrier density to one with a lower carrier density, the output from the lock-in amplifier increases due to the steeper slope of the C-V curve. This output is commonly described as the d*C*/d*V* amplitude signal. It is also possible to detect whether the slope of the curve is positive or negative, hence distinguishing between *n* and *p*-type material. The sign of the slope is given by the dC/dV phase signal. This mode is also called 'ΔV mode'.

In closed loop SCM, also referred as 'ΔC mode', the d*C*/d*V* value is kept constant by adjusting the amplitude of the V_{ac} through a feedback system. It means that the depletion region underneath the tip remains unchanged during the measurement. In this case the V_{ac} amplitude at each point in order to keep d*C*/d*V* at a given setpoint is measured. For higher carrier concentrations higher voltage amplitudes are needed. This mode offers a better resolution, since the depletion region is fixed, but has certain disadvantages such as the larger noise due to the electronic feedback or being much slower since the feedback control takes a certain time. All the SCM measurements presented in this work were done in open loop mode.

Scanning capacitance spectroscopy (SCS)

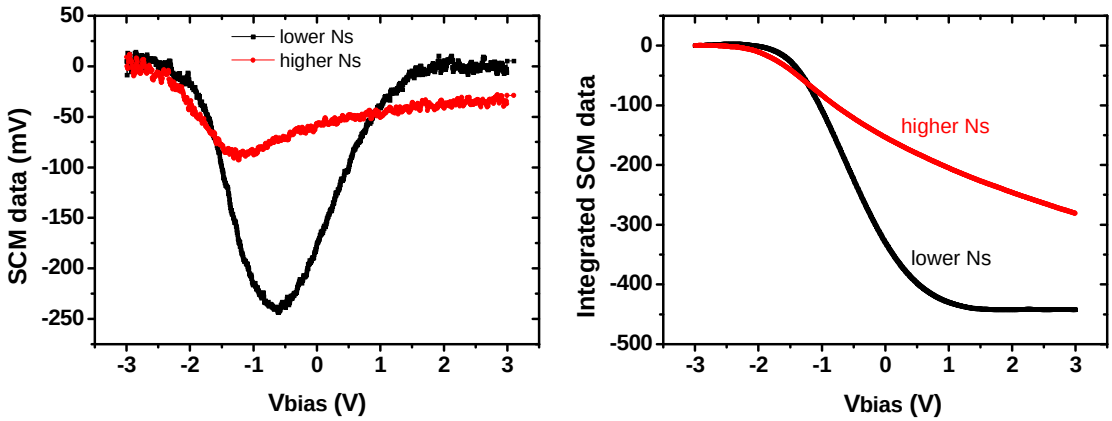

(a) (b)

Figure 2.8: (a) SCS curves on two semiconductor layers with different doping concentrations. (b) Integration of SCS results in (a) showing C-V like curves with difference of slope and of capacitance between the accumulation and deep depletion regimes. Higher N_s is around 10^{19} cm^{-3} and the lower N_s about mid 10^{16} cm^{-3}.

SCS (also known as d*C*/d*V* spectroscopy) is a variant of SCM [68]. Normally in SCM, under a fixed V_{dc} and V_{ac}, the probe tip is scanned over a certain area and the d*C*/d*V* signal is recorded for each pixel in this area, giving rise to a 2D d*C*/d*V* image. SCS extends SCM technique by ramping the applied V_{dc} with the tip at a specific location on the sample, so that a complete d*C*/d*V* curve can be obtained in function of the ramped V_{dc} [69]. Since the d*C*/d*V* signal is to some extent the deviation of the C-V curve of the tip-sample structure, the integration of SCS curves usually yield C-V-like curves. What's more, it is easy to understand

that the d*C*/d*V* signal for a lower carrier concentration region should have a larger maximum absolute value corresponding to the larger slope in the C-V curve. An example of the SCS curves on two regions with different carrier concentrations and their integrations is shown in Figure 2.8.

2.2.3 Scanning spreading resistance microscopy (SSRM)

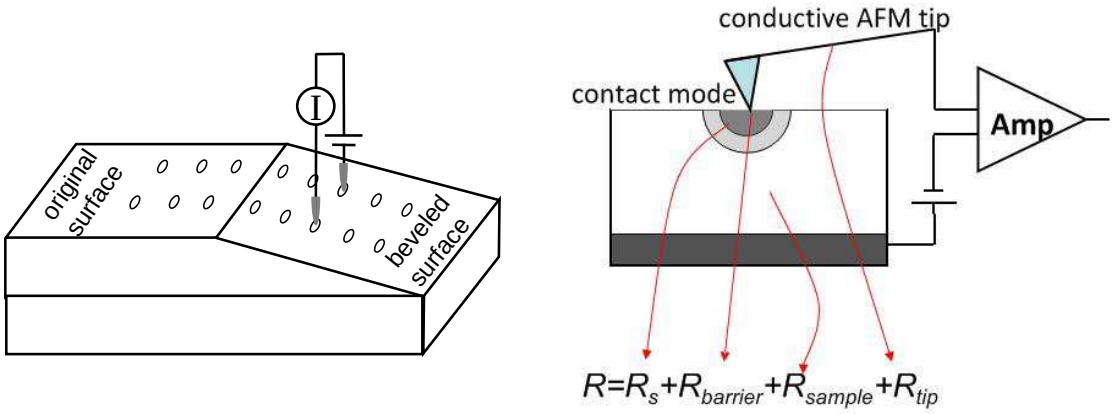

(a) (b)

Figure 2.9: (a) Illustration of SRP measurement. (b) Principle/Modeling of SSRM technique.

SSRM is another important SPM technique for 2D carrier profiling in semiconductors which shares similar popularity to SCM [70-75]. It was developed from the more mature technology of SRP in combination of AFM by De Wolf, P. *et al* [70]. It has a higher spatial resolution than SRP, while its essential principle is the resistance measurement, similar to that of SRP.

In order to establish a good electrical contact between the tip and sample, an electrically conductive probe tip is employed in contact mode with a relatively large tip force (µN order) on the sample. The tip force required depends on the studied material. Typically for Si, a tip force higher than 13 µN is needed to penetrate the thin native oxide layer on the surface [74-77]. With a constant voltage (V_{dc}) applied to the tip-sample system, the current is measured and the corresponding resistance is calculated for each point during the tip scan. The measured resistance is composed of several parts in series and can be written as $R=R_s+R_{barrier}+R_{bulk}+R_{tip}$, where R_s, $R_{barrier}$, R_{bulk} and R_{tip} represent local spreading resistance (which is of interest for carrier/dopant profiling), barrier resistance between the tip and the sample, bulk resistance of the sample and the resistance of the tip, respectively.

Among them, in the ideal case of ohmic contact, R_s dominates the total resistance with a relatively large tip force applied and is directly related to local resistivity through the equation $R_s=\rho/4a$ [78], where a is the radius of the electrical contact and ρ the resistivity determined by

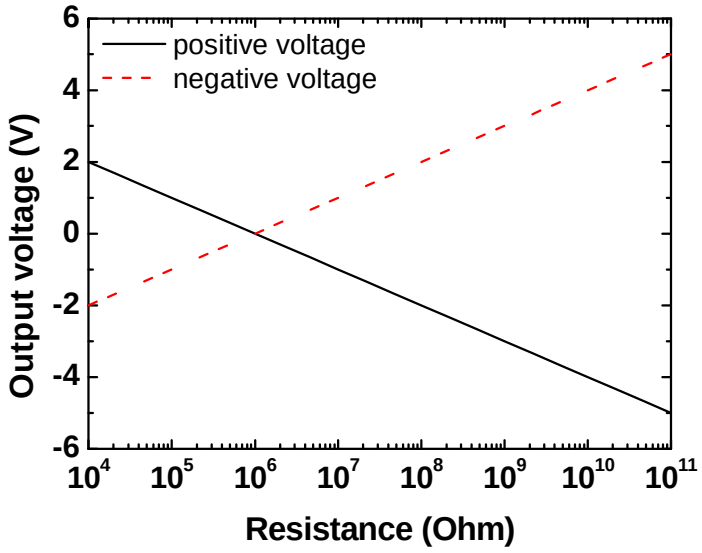

Figure 2.10: Transfer curve of the SSRM logarithmic current amplifier.

$1/(qn\mu_n+qp\mu_p)$, with μ being the carrier mobility and n and p being the carrier concentration for holes and electrons, respectively.

The current sensor in SSRM is a logarithmic current amplifier which is sensitive to a current range from 10 pA to 0.1 mA. The output signal indicating the resistance is given in Volt, whereby a change of 1 V corresponds to a change in resistance of one order of magnitude. The relation between the input current and output voltage is expressed by

$$V_{out} = +\log\left(\frac{I*10^6}{V_{dc}}\right) \quad \text{if } V_{dc} > 0; \tag{2-1}$$

$$V_{out} = -\log\left(\frac{I*10^6}{V_{dc}}\right) \quad \text{if } V_{dc} < 0. \tag{2-2}$$

Typically, a 0 V output signal corresponds to a resistance of 1 MΩ. The transfer curve relating the voltage scale to the resistance scale is represented in Figure 2.10.

2.2.4 Conductive atomic force microscopy (C-AFM)

C-AFM is another current-sensitive mode of atomic force microscopy in which a conductive tip is scanned in contact with the sample surface, while a voltage is applied between the tip and the sample, generating a current image. A primary difference of C-AFM from SSRM is the current sensor. In SSRM, a logarithmic current amplifier is employed in order to cover a wide range of current with similar sensitivity for its application to carrier profiling. On the contrast, in C-AFM, a linear current amplifier is in use to detect in most cases smaller current

through the sample. Strictly, two kinds of conductive AFM are referred to for regular use, TUNA and C-AFM, although the two terms are used somewhat interchangeably in the literature. Instrumentally, C-AFM employs a linear current amplifier with a range 2 pA~1 μA, whereas TUNA makes use of a more sensitive linear current amplifier with a range from 50 fA to 120 pA [79].

TUNA is especially useful for evaluating dielectric films subject to breakdown, such as silicon dioxide, SiO_2, and transistor gate oxide [80]. Tip/sample tunneling current depends on film thickness, leakage paths, possibly caused by defects, charge traps and tip geometry. While TUNA specializes in very small currents, C-AFM is suitable for imaging samples spanning a wide range of conductivity, particularly, the more conductive. For both, by maintaining a constant force between tip and sample, while the topography is acquired using the deflection signal of the cantilever, the current at each point is measured through an electric current amplifier, enabling the direct correlation of local topography with electrical properties.

Besides obtaining 2D current images under a certain bias voltage, one can also move the tip to a specific desired location to ramp the voltage while the current is measured to generate local current-voltage (I-V) curves.

In this thesis work, extended TUNA mode, which combines the sensitive current range of TUNA and C-AFM have been used.

2.2.5 Probes for electrical scanning probe microscopy

In basic modes for topography investigation such as contact mode and tapping mode, normal probes made of Si or Si_3N_4 without any coating layer on the tip can be employed. However, for almost all SPM modes for electrical characterization, the employment of a conductive probe connected to an external source is required. While probes and cantilevers used in different electrical techniques mentioned before may require particular characteristics, some requirements are of common interest since they are all scanning probe techniques in contact mode with a high resolution [81]:

- The tip should be as sharp as possible because the smaller the radius of curvature, the smaller the feature that can be resolved. In fact, the size of the probe apex is one of the components that determine the ultimate resolution of the techniques. In practice, it is possible to fabricate probes with a radius of curvature of about ten nanometers.
- A second important requirement is the hardness. For contact techniques, the rupture during scanning has to be avoided since it may reduce the sensitivity of the tip and the control of the measurements. If the tip is coated, a hard coating layer prevents the wear or detachment of the conducting outer layer.
- The electrical conductivity of the probe has to be high, preferably similar to the

conductivity of a metal.

- A good reflectivity of the top surface of the cantilever is also necessary for the photo-detection laser system.

All these characteristics above are essential for SCM, SSRM and C-AFM. However, each of them separately requires some other different features.

For SCM, the tip scanning involves a soft contact and the tip forces applied to the cantilever is on the order of nN. Commercial probes for SCM usually are made of etched Si in combination of a metal coating (like Pt/Ir, Co/Cr) at the tip end and the stiffness of cantilever is typically in the range of 0.1-5 N/m. These kinds of tips have the serious wear problem on the metal coating due to lateral forces experienced by the tip as it scans repeatedly across the sample. Hence, alternative coating materials such as tungsten [82] and TiN [83] are being examined. An alternative approach is the fabrication of all-metal tips (or all metal probes) so that wear of the tip does not result in a loss of conductivity, but merely a change in probe shape. However, these probes are not yet commercially available. For the SCM measurements in this work, Pt/Ir coated Si tip, Co/Cr coated tip and etched Si tip have been used. They typically have tip radii ~20 nm.

SSRM necessitates a hard tip contact on the material to make sure of a stable electrical contact in order that the measured resistance be dominated by local spreading resistance. Therefore, on one side, the cantilever must be stiff (20-100 N/m) because of the required large tip force on the sample, which is also dependent on the hardness of the material under measurement. On the other side, tip wear is a more particular concern compared with SCM. For these reasons, in the development of SSRM, the use of conductive diamond-based probes has been well established, since, for measurements on silicon, a very hard tip is needed to penetrate the surface oxide and establish a stable electrical contact [84]. Nevertheless, this is not the case for all SSRM experiments. For example, InP may be successfully imaged using metallic probes [71]. Both diamond-coated and all-diamond probes for AFM applications were initially developed by Niedermann *et al* [84]. Their initial diamond-coated probes exhibited a microstructure which persists in today's commercial probes; Hantschel *et al* [85] combined highly doped-diamond tips with silicon cantilevers. The resulting probes achieved a very broad dynamic range (approximately 5×10^{14} -5×10^{20} cm^{-3} for doping in *n*- and *p*-type silicon) [85], and an excellent spatial resolution [86] of around 5 nm. Note that this kind of probe can also be used in SCM measurements. Meantime, efforts have been made to integrate all-diamond tips with metallic cantilevers [87]. All-diamond tips represent a very promising solution for routine and accurate SSRM measurements and have recently already been commercially available from IMEC [88]. Tips used for SSRM experiments in this work are

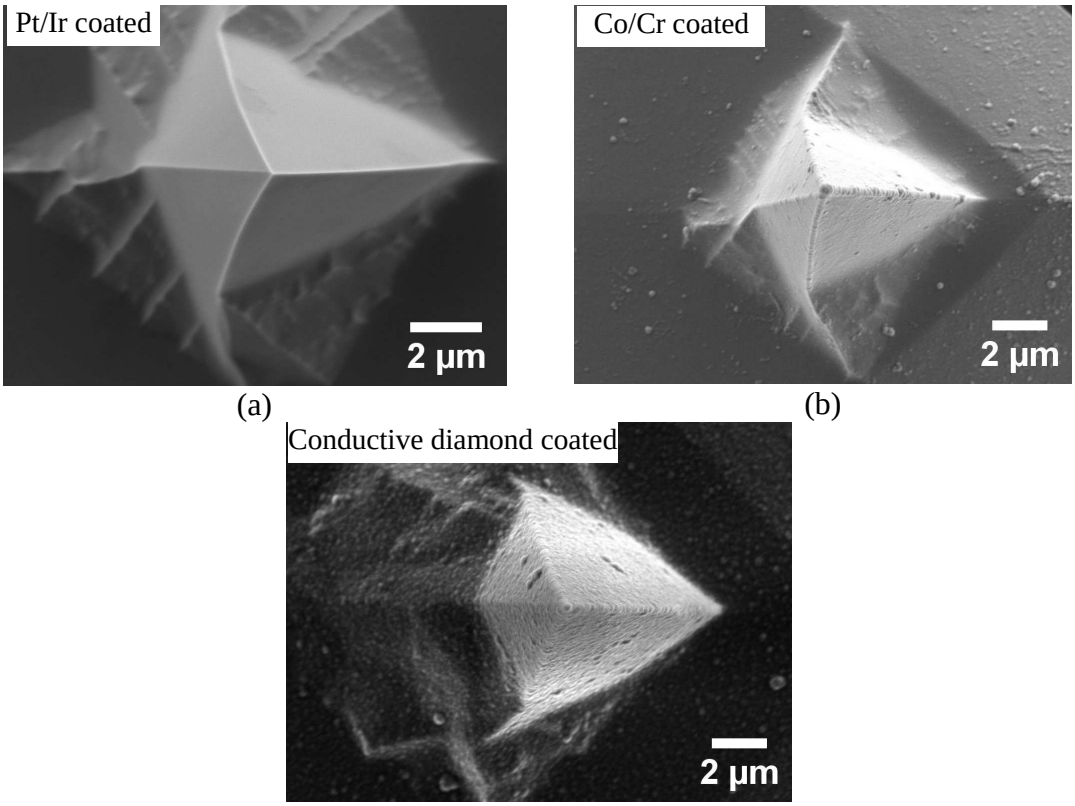

Figure 2.11: Typical SEM images of (a) Pt/Ir coated tip, (b) Co/Cr coated tip and (c) conductive diamond coated tip.

etched Si tips coated with 100 nm boron-doped conductive diamond layer. Typical tip radius is 100~150 nm as a result of the conformal coating.

2.3 Macroscopic characterization

2.3.1 Metal-semiconductor contact

Metal-semiconductor contact is an indispensable part in the microelectronics industry and for the proper function of almost any devices based on semiconductor. The quality of a metal-semiconductor contact is determined by a number of factors, including the mismatch between the Fermi-energies of the metal and the semiconductor, the semiconductor processing steps (cleaning and annealing) prior to contact fabrication as well as the contact fabrication technique. The contact is considered to be ohmic or rectifying (Schottky) according to its response to an applied external bias.

Ohmic contact

From the I-V characteristic point of view, an ohmic contact can simply be defined as having a linear and symmetric I-V relationship for both positive and negative voltages. Ohmic contact is important for carrying electrical current into and out of the semiconductor. In an ideal

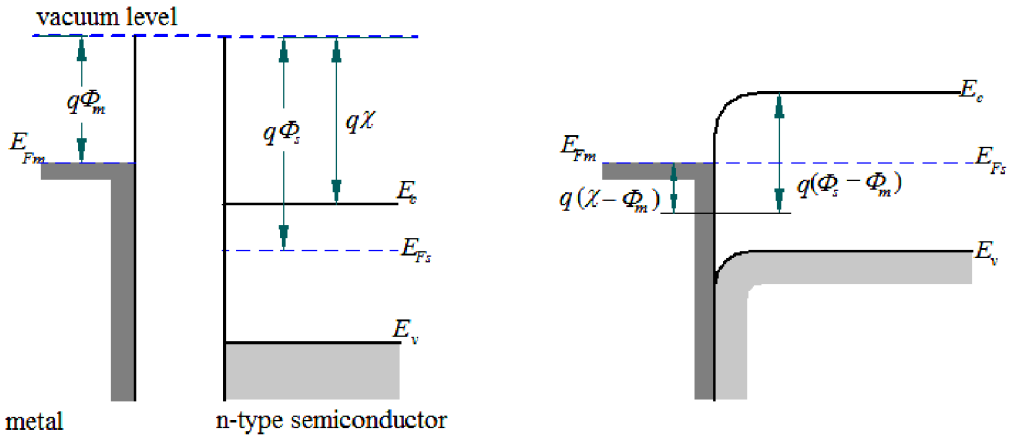

Figure 2.12: Ohmic contact to *n*-type semiconductor $\Phi_M < \Phi_S$ (a) before contact, (b) equilibrium band diagram for the contact. (Adopted from [89])

ohmic contact, no barrier to the carrier flow is observed in either the positive or the negative direction. Thus, charge carriers are free to move in either direction across the contact with minimal or no resistance.

When a metal and a semiconductor (ideally with no surface states) are brought in contact and equilibrium is maintained, their Fermi levels will align. To fabricate an ohmic contact on an *n*-type semiconductor, it requires that the metal work function be closer to or smaller than the semiconductor electron affinity. Formation of such a contact is illustrated in Figure 2.12. Bringing the metal into intimate contact with the semiconductor will cause a transfer of electrons from the metal to the semiconductor to reach Fermi-level alignment (Figure 2.12b). This process raises electron energies in the semiconductor relative to the metal thus reducing the barrier to electron flow between the two. Similarly, for *p*-type semiconductors, the metal work function should be greater than the electron affinity of the semiconductor such that, charge carriers are transferred from the semiconductor to the metal for equilibrium.

Regarding ZnO, formation of ohmic contacts to ZnO with low contact resistivity can be realized by reducing the barrier height to increase thermionic emission, or/and increasing the ZnO surface doping density to narrowing the barrier width for carriers to tunnel through field emission process. ZnO has an electron affinity ~4.2-4.35 eV. Therefore, Al and Ti can be used for ohmic contacts to *n*-ZnO as their work functions are 4.28 and 4.33 eV, respectively [90-91]. In reality, the barrier height is influenced by many factors, including crystal quality, defects, and surface conditions. For the work in this thesis, Ag paste has been used to form ohmic contact with ZnO thin films and ZnO NWs field [92].

Schottky contact

A metal-semiconductor contact is referred to as a Schottky contact if it can rectify current in

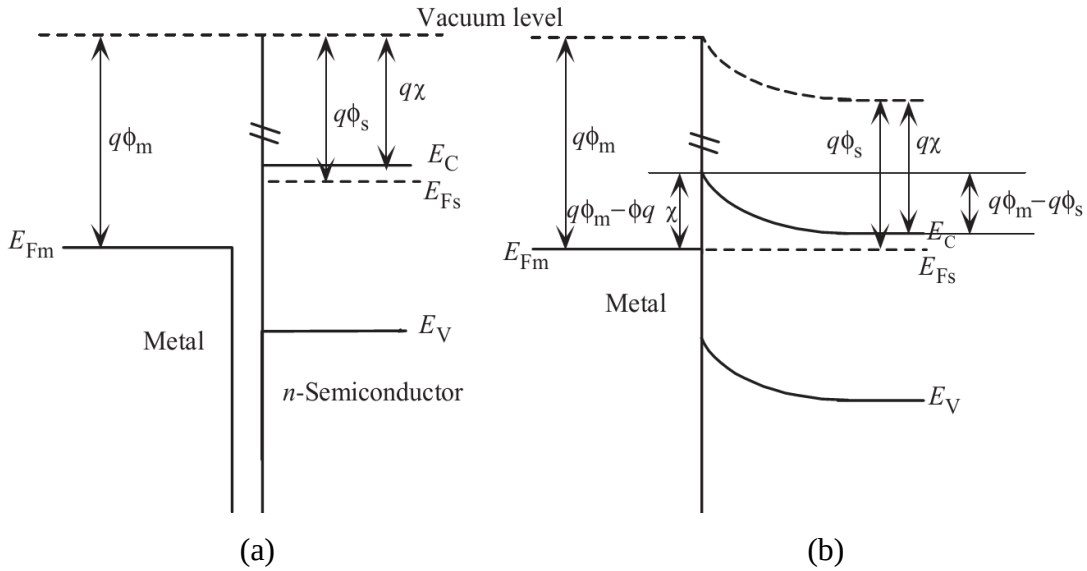

Figure 2.13: Band diagrams for Schottky contact on n-semiconductor $\Phi_M > \Phi_S$ (a) before contact, (b) after contact in equilibrium [93].

the forward biased mode and allows negligible or no current to flow in the reverse direction. Ideal Schottky contacts are formed when a difference in potential exists between the Fermi level of the metal and the band edge where majority charge carriers reside in the semiconductor (ignoring the effects of surface and interface states). The formation of a Schottky contact is illustrated in Figure 2.13. The difference in potential between the Fermi-energy of the metal and semiconductor gives the barrier height, Φ_B. For an *n*-type semiconductor, the barrier height is given theoretically as [94]

$$\Phi_B = \Phi_M - \chi_S \tag{2-3}$$

where Φ_M is the metal work function, χ_s is the electron affinity of the semiconductor. In real Schottky contacts, the barrier height is affected by interfacial layers, surface states, defects and chemical reactions which also determine the quality of the contacts.

In the case of ZnO, the understanding and control of Schottky contacts represent still a considerable challenge, as evidenced by the wide and variable range of barrier heights measured from the same metal on a given ZnO surface. Various metals can be used to form Schottky contact with ZnO, including Al, Ti, Ir, Pt, Pd, Au, Ag, while the quality of Schottky barriers has been observed to be dependent on factors such as crystal quality, impurities and defects, as well as surface treatment prior to metal deposition. This is not the focus of this thesis work, and details can be found in the review of Leonard J. Brillson [95] and the references therein. For information, in this work, Schottky contact with ZnO is realized by electron beam evaporation of Pt after ATMA (acetone, trichloroethylene, methanol and air-exposed) surface treatment [96].

2.3.2 Current-voltage (I-V) characteristics

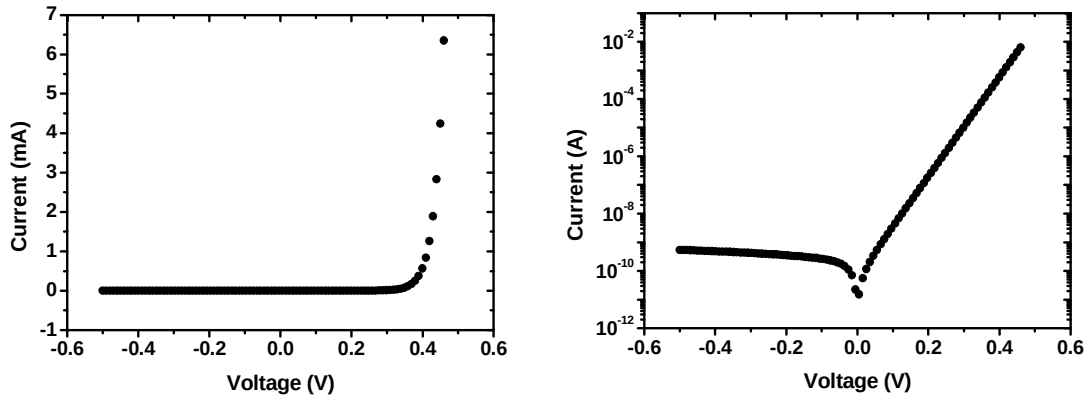

(a) (b)

Figure 2.14: Simulation of I-V curve for ideal Schottky contact. (a) Linear axis scale. (b) Semi-log axis scale.

A popular method to evaluate a Schottky contact and determine the barrier height is to measure its I-V characteristics. At room temperature, under the assumption that thermionic emission is the only mechanism responsible for the flow of electrons across the potential barrier, I-V characteristics across the metal-semiconductor interface follow the thermionic emission relation. Taking *n*-type semiconductor for example, in thermal equilibrium and assuming $\Phi_B >> kT/q$, the thermionic emission of electrons in either direction is expressed as [97],

$$J_{TE} = A^* T^2 \exp(-\frac{q\Phi_B}{kT}) \tag{2-4}$$

where J_{TE} is the current density, A^* the Richardson constant, k the Boltzmann constant, and T the semiconductor temperature. When a forward bias V is applied on the Schottky contact, the barrier potential is lowered to Φ_B-V. Then the electrons flow from the semiconductor to the metal increases and

$$J_{fwd} = A^* T^2 \exp\left[-\frac{q(\Phi_B - V)}{kT}\right] \tag{2-5}$$

The current density flowing in the reverse direction is independent of the applied bias voltage and is known as the saturation current density J_0 where,

$$J_0 = A^* T^2 \exp(-\frac{q\Phi_B}{kT}) \tag{2-6}$$

Thus, the net current flowing across the Schottky contact is

$$J = J_{fwd} - J_0 = J_0\left[\exp\left(\frac{qV}{kT}\right) - 1\right] \tag{2-7}$$

For applied bias voltages $V >> kT/q$, the -1 term is negligible and the current density should increase exponentially with V.

When the Schottky contact is reversed biased, the barrier potential increases to Φ_B+V which makes $J_{fwd} << J_0$ and the net current density is equal to the saturation current density J_0 independent of V.

Equation (2-7) represents the ideal case of pure thermionic emission over a homogeneous, defect free, Schottky barrier with no interface states. Typical I-V characteristics of this kind of Schottky contact are shown in Figure 2.14. For the analysis of real I-V characteristics an ideality factor η is introduced giving,

$$J = J_0\left[\exp\left(\frac{qV}{\eta kT}\right) - 1\right] \tag{2-8}$$

I-V characteristics are usually plotted as ln$J$ versus V from which η can be obtained from the slope of the linear part of forward bias region, provided $V >> kT/q$,

$$\eta = \frac{q}{kT}\ln\left(\frac{d\ln J}{dV}\right)^{-1} \tag{2-9}$$

The effective barrier height Φ_B can be deduced by extrapolating the same linear part to V=0 V to find the saturation current density J_0 from which,

$$\Phi_B = -\frac{q}{kT}\ln\left(\frac{J_0}{A^*T^2}\right) \tag{2-10}$$

Values of η greater than unity are caused by non-ideal behaviors which cause the Schottky contact to deviate from pure thermionic transport, most common types of which are image force lowering, field emission and contact inhomogeneity.

2.3.3 Capacitance-voltage (C-V) characteristics

An alternative method of measuring the barrier height of the Schottky contact is the C-V technique. However, another important application of this technique is to obtain the depth profile of the effective carrier concentration of the semiconductor [96], which is essential in the fabrication of semiconductor devices and also a part of the work in this thesis.

In the case of bulk material, under reverse bias conditions, the region of the semiconductor underneath the metal is depleted and the width of the depletion region of the

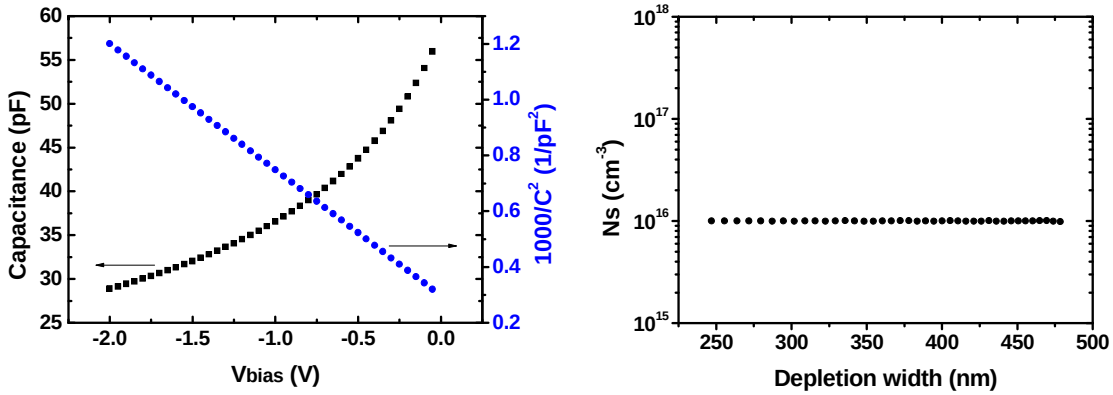

(a) (b)

Figure 2.15: Simulation of (a) C-V curve and (b) calculated depth profile for a uniform doping concentration of 10^{16} cm^{-3}.

metal/semiconductor junction depends on the applied voltage. Under the depletion width approximation [97], this depleted region can be considered as nature dielectric thus form a "parallel plate" capacitor with the metal and the undepleted bulk of the semiconductor being "plates". Under an applied bias V, the depletion width W_d can be expressed as

$$W_d = \sqrt{\frac{2\varepsilon_s\varepsilon_0}{qN_s}\left(V_{bi} - \frac{kT}{q} - V\right)} \tag{2-11}$$

Where ε_s is the dielectric constant of the semiconductor, ε_0 the vacuum permittivity, N_s the effective carrier density, V_{bi} the built-in voltage in the form of $V_{bi}=\Phi_B-\xi$, with ξ being the energy difference between the bottom of the conduction band and the Fermi level (for n-type semiconductor).

The total space charge Q_{sc} in the depletion region is

$$Q_{sc} = qN_sW_dA \tag{2-12}$$

where A is the area of the contact. The small signal capacitance of the Schottky junction $C=\mathrm{d}Q/\mathrm{d}V$ is given by

$$C = A\sqrt{\frac{q\varepsilon_s\varepsilon_0N_s}{2(V_{bi} - kT/q - V)}} \tag{2-13}$$

So we have

$$\frac{1}{C^2} = \frac{2}{q\varepsilon_s\varepsilon_0N_sA^2}\left(V_{bi} - \frac{kT}{q} - V\right) \tag{2-14}$$

In C-V characterization, $1/C^2$ is measured as a function of the applied bias voltage by

applying a small V_{ac} (typical frequency between 10 kHz and 1 MHz). The effective carrier concentration can be obtained from the slope of the $1/C^2$ versus V plot (example in Figure 2.15),

$$N_s = -\frac{2}{q\varepsilon_s\varepsilon_0 A^2}\left[\frac{d(1/C^2)}{dV}\right]^{-1} \tag{2-15}$$

while V_{bi} can be obtained from the intercept of the slope with the $1/C^2$ axis.
By varying the depletion region width through scanning the applied voltage and measuring the capacitance, the doping profile of the semiconductor can be obtained. A simulation example of this analysis is given in Figure 2.15.

2.4 Planarization process for SPM measurements

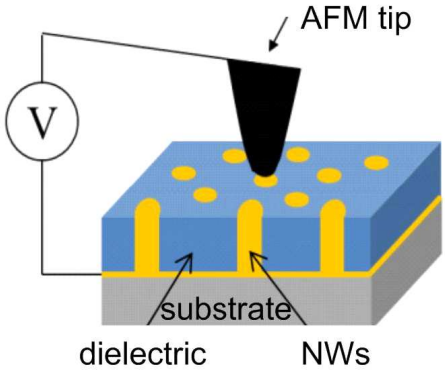

Figure 2.16: Illustration of SCM/SSRM measurements on NWs field structure.

In most cases, as-grown NWs structure is suitable for neither direct device fabrication nor their electrical characterization due to the air gap between the NWs, which necessitates integration processes. One integration method is to disperse the NWs in solution phase [98] and deposit them on another substrate, for example Si substrate with a top SiO_2 insulating layer [99-101]. Then macroscopic metal contacts can be deposited so that they intersect one end of some of the NWs for subsequent characterizations [102-104]. Another method called vertical integration involves filling with a dielectric material to consolidate the NWs and provide insulation between them [105-107]. For SCM/SSRM in this work, we want to characterize the NWs from the top of them and the tip is supposed to scan in a relatively flat 2D area (Figure 2.16). Therefore, at the first place, a planarization process has been developed for the NWs structure. In principle, the process includes two steps: dip-coating of SiO_2 to encapsulate the NWs and chemical mechanical polishing (CMP) to expose the NWs as well as to obtain a flat sample surface (Figure 2.17).

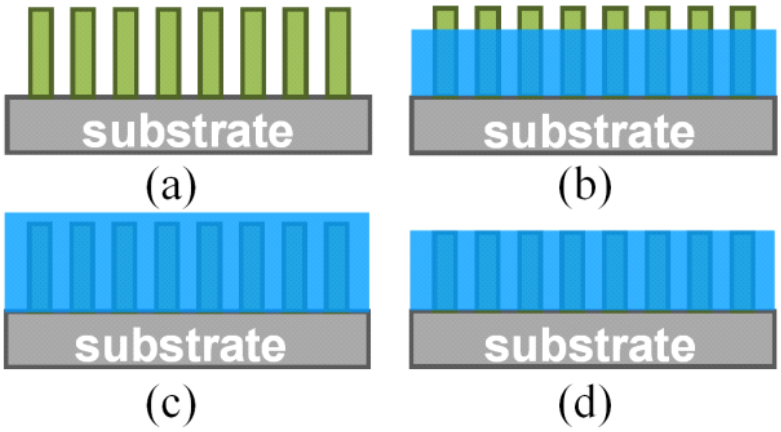

Figure 2.17: Illustration of planarization process of NWs sample used in this work for SCM/SSRM measurements. (a) As-grown NWs. (b) Dip-coating of SiO_2 dielectric. (c) Continue of dip-coating of SiO_2 dielectric to embed and consolidate the NWs. (d) Polishing and cleaning to expose the NWs and reach a flat clean sample surface.

2.4.1 NWs samples

Here two NWs samples are introduced. One was provided by our colleagues in GEMAC. The ZnO NWs were grown on a-plane sapphire substrate by MOCVD in a horizontal reactor operating at 60 torr. Diethyl-zinc (DEZn) and nitrous oxide (N_2O) have been used as zinc and oxygen precursors, respectively. Helium was used as the carrier gas. Substrate temperature was 900 °C and an oxygen/zinc molar ratio of 800 was used to ensure the growth of one-dimensional nanostructures. The growth has led to ZnO NWs exhibiting a mean length around 1.3 µm, and NW diameters in the range of 110~160 nm.

Another ZnO NWs sample, provided by Sophie Guillemin from LMGP&INL, was grown by chemical bath deposition (CBD) method. A highly doped *n*-type Si was used as the substrate. The growth process can be described as following: first a ZnO seed layer composed of ZnO nanoparticles is deposited on the substrate by dip-coating process to furnish nucleation site for the subsequent growth of NWs, then the sample is immersed for 3 hours in a solution ($Zn(NO_3)_2 \cdot 6H_2O$ and Hexamethylenetetramine HMTA in deionized water) at 90 °C for growth process. Grown NWs have typical diameters between 40 and 60 nm and lengths about 2 µm.

2.4.2 Dip-coating of SiO_2

The dip-coating process consists of dipping the sample into and pulling it out from the SiO_2 sol at a constant speed. The SiO_2 sol in this work was prepared by using TEOS (tetraethylorthosilicate), HCl (0.022 N) and ethanol in the proportion of 5 mL, 2 mL and 37.7 mL. It was stirred for at least 5 hours before its use for dip-coating. The dip-coating process

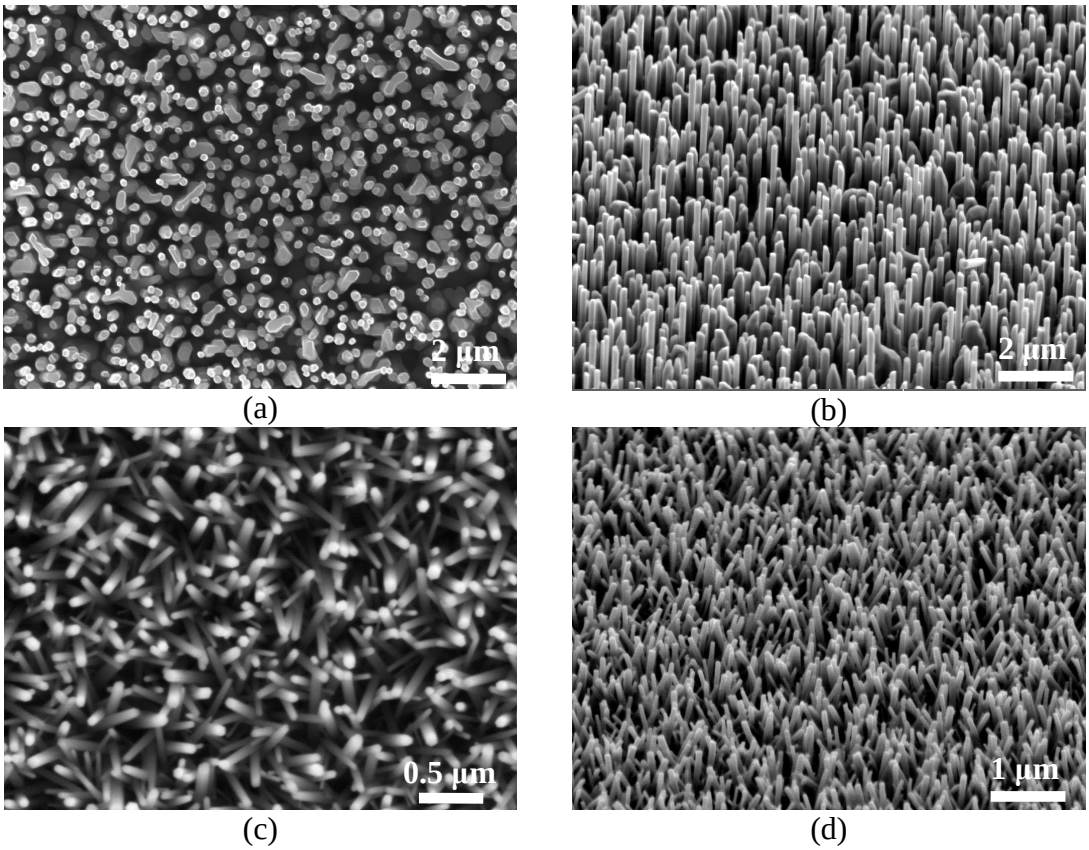

Figure 2.18: SEM images of MOCVD grown ZnO NWs (a) top view, (b) tilt view and CBD grown ZnO NWs (c) top view, (d) tilt view in this work.

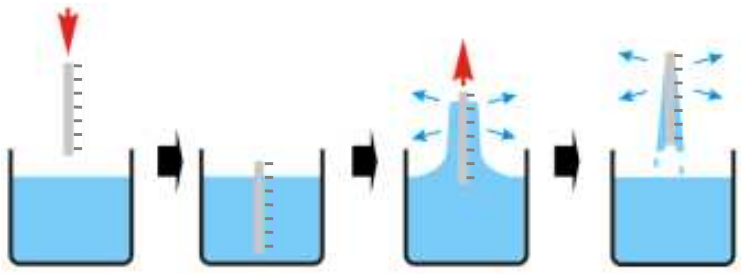

Figure 2.19: Illustration of dip-coating of SiO_2 on NWs field.

was done by employing a home-made dip-coater equipped with a hanger attached to a motor. The hanger helps the sample be pinched while the motor enables the movement of the sample with different velocity. Typical important velocities are V4, V5, V6 corresponding to 4, 8, 20 cm/min respectively. After pulling out the sample, it is left to dry for a few minutes followed by an annealing process as follows:

First, the sample is put in normal atmosphere for 15 minutes at 100 °C to evaporate the solvent. Then it is moved to O_2 atmosphere for another 15 minutes at ambient temperature before the temperature is increased to 600 °C for 30 minutes. Finally, the sample is cooled down during 15 minutes still under O_2 atmosphere. This annealing process is supposed to consolidate the coated matrix and reduce the possible defects that arise during the dip-coating of SiO_2.

A reference sample, simply Si substrate, was used to check the effect of SiO_2 dip-coating. It was found that a process at speed *V4* (4 cm/min) and *V6* (20 cm/min) gives a SiO_2 layer about ~60 nm and ~106 nm thick, respectively, as measured by ellipsometry method. However, due to the high-density NWs existence on the NWs sample, the SiO_2 layer thickness from a similar process is likely to have a larger value that for the Si substrate. For example, it was noticed that 6 processes at speed *V4* would yield a SiO_2 layer thickness about 1 μm. In contrast, the speed *V6* was found to bring about cracks or detach the seed layer of the NWs forest during the annealing process. This is probably due to the internal stress of the SiO_2 layer since a higher speed leads to a thicker layer of SiO_2. So in this work, we have used mainly the speed *V4* for the NWs samples.

The progress of dip-coating was monitored by several tools, including particularly optical microscope, SEM and ellipsometry. Although ellipsometry worked well for the Si substrate samples, it was difficult to perform good measurement for the NWs samples simply because of their huge roughness during the planarization process (proper working of ellipsometry needs enough reflection of the used light).

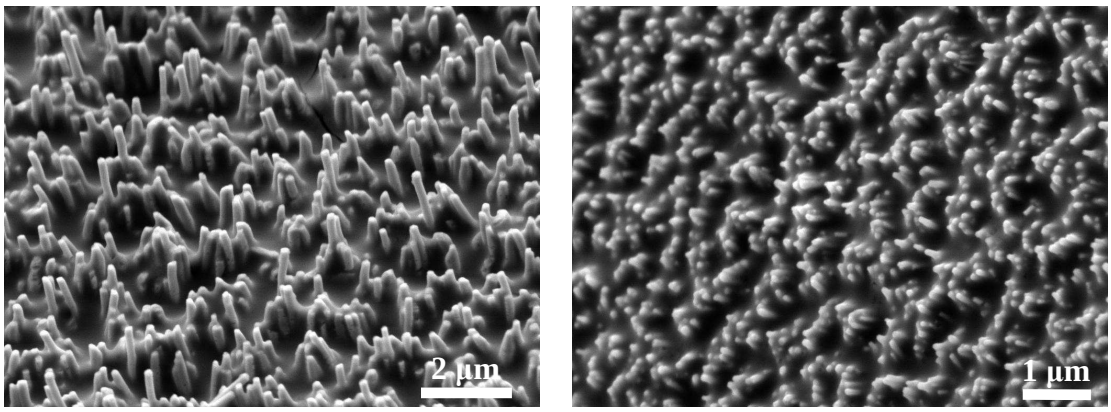

(a) (b)

Figure 2.20: (a) MOCVD NWs sample and (b) CBD NWs sample after the dip-coating process.

SEM images of the two samples during the preparation process are shown in Figure 2.20. The process of dip-coating is finished when the NWs are all buried in the resulted SiO_2 dielectric matrix. In certain cases, where the NWs are very long, the dip-coating process can also be stopped once the desired thickness of SiO_2 is reached.

2.4.3 Polishing and cleaning

The NWs are encapsulated by SiO_2 matrix after the dip-coating process. However, they are still far from being proper for SCM/SSRM measurement considering the unsatisfactory roughness situation. Also, the part of SiO_2 at the top of NWs needs to be removed for performing electrical measurement. At first we tried reactive-ion etching (RIE) to do this job but it was difficult to control the etching process and to effectively flatten the sample surface

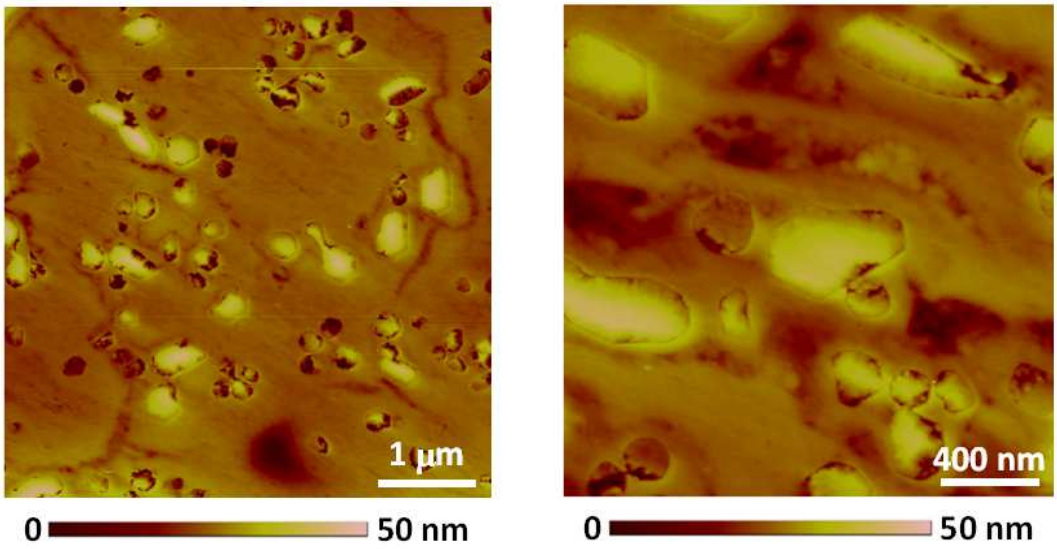

(a) (b)

Figure 2.21: Tapping AFM on the MOCVD NWs sample after polishing process. (a) 5×5 µm^2 area, roughness RMS value=5 nm, height range=105 nm. (b) 2×2 µm^2, roughness RMS value=5.68 nm, height range=79.4 nm.

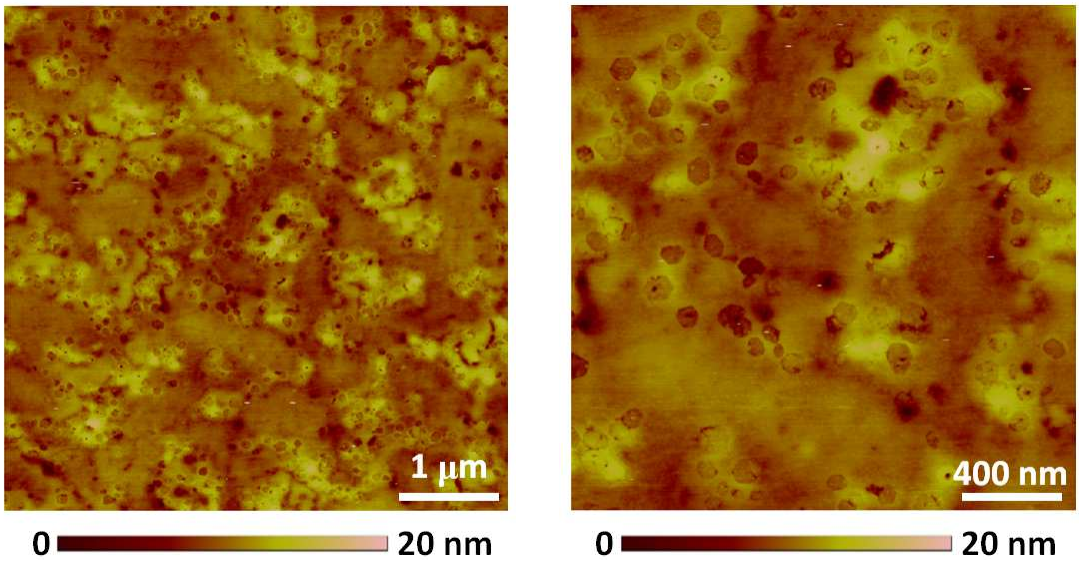

(a) (b)

Figure 2.22: (a) Tapping AFM on CBD NWs after polishing process. (a) 5×5 µm^2 area, roughness RMS value=1.69 nm, height range=40.3 nm. (b) 2×2 µm^2, roughness RMS value=1.72 nm, height range=40.8 nm.

to a small roughness. So we turned to chemical-mechanical polishing (CMP). For this purpose, a colloidal suspension containing 50 nm-diameter SiO_2 nanoparticles was regularly used to ensure an acceptable surface roughness in the end for subsequent electrical characterization.

After each polishing process, undesired SiO_2 nanoparticles usually remain on the sample surface. It is important to clean the sample thoroughly. This was done by using a cotton swab under running deionized water. Also, ultrasonic bath has been used to better complete this task.

The ultrasonic bath has as parameters the time, the power (from 10% to 100 %) and the frequency (37 or 80 kHz). After several trials, a combination of the power 70%, the frequency 80 kHz and a duration of 3 minutes were decided for future use.

Monitoring of the polishing and cleaning process was carried out by performing tapping AFM on the sample surface after each step. Typically a surface roughness of less than 6 nm was achieved for an area of 2×2 μm^2 when the polishing process came to an end (Figure 2.21 and Figure 2.22). This result, if not perfect, is already suitable for the SCM/SSRM characterization after the backside metal contact is made to the samples. Throughout this thesis, large area Ag paint on the substrate and/or on the side of the sample has been utilized for forming backside metal contact for NWs samples.

2.5 Conclusion

This chapter provides an introduction of the electrical characterization techniques that have been employed in this work. SPM tools based on AFM including SCM, SSRM and C-AFM were introduced. Among them, SCM and SSRM have the ability to probe two dimensional carriers distribution at a nanometer scale. Principle of SCM is the detection of local tip-sample capacitance variation excited by a V_{ac} of tens of kHz frequency, while SSRM senses the carrier information through the local spreading resistance by measuring the current flowing through the sample, which in most cases requires a relatively large tip force on the sample. Both SCM and SSRM will be used in the following for carrier density investigation in ZnO material. In contrast to the logarithmic current amplifier used in SSRM, C-AFM makes use of a linear current amplifier with a dynamic detect range from to sub pA to 1 μA. It is used to study the tip-sample contact I-V characteristics. In addition to SPM techniques, macroscopic tools including I-V and C-V measurements were also introduced for their employment in the electrical characterization of collective ZnO NWs. In the last section, the developed planarization process for the as-grown NWs structure was reported. As results, after the preparation procedure, the NWs samples have relatively smooth surfaces which are suitable for following electrical mode SPM measurements.

References:

[1] Morkoç, H., & Özgür, Ü. (2008). Zinc oxide: fundamentals, materials and device technology. John Wiley & Sons.

[2] Iwanaga, J., Yokogawa, T., & Yamada, A. (2013). U.S. Patent No. 8,421,054. Washington, DC: U.S. Patent and Trademark Office.

[3] Jaffe, J. E., & Hess, A. C. (1993). Hartree-Fock study of phase changes in ZnO at high pressure. Physical Review B, 48(11), 7903.

[4] Catti, M., Noel, Y., & Dovesi, R. (2003). Full piezoelectric tensors of wurtzite and zinc blende ZnO and ZnS by first-principles calculations. Journal of Physics and Chemistry of Solids, 64(11), 2183-2190.

[5] Kisi, E. H., & Elcombe, M. M. (1989). u parameters for the wurtzite structure of ZnS and ZnO using powder neutron diffraction. Acta Crystallographica Section C: Crystal Structure Communications, 45(12), 1867-1870.

[6] Karzel, H., Potzel, W., Köfferlein, M., Schiessl, W., Steiner, M., Hiller, U., ... & Schwarz, K. (1996). Lattice dynamics and hyperfine interactions in ZnO and ZnSe at high external pressures. Physical Review B, 53(17), 11425.

[7] Schleife, A., Rödl, C., Fuchs, F., Furthmüller, J., & Bechstedt, F. (2009). Optical and energy-loss spectra of MgO, ZnO, and CdO from ab initio many-body calculations. Physical Review B, 80(3), 035112.

[8] Fuchs, F., Furthmüller, J., Bechstedt, F., Shishkin, M., & Kresse, G. (2007). Quasiparticle band structure based on a generalized Kohn-Sham scheme. Physical Review B, 76(11), 115109.

[9] Heyd, J., Scuseria, G. E., & Ernzerhof, M. (2003). Hybrid functionals based on a screened Coulomb potential. The Journal of Chemical Physics, 118(18), 8207-8215.

[10] Hedin, L. (1965). New method for calculating the one-particle Green's function with application to the electron-gas problem.Physical Review, 139(3A), A796.

[11] Preston, A. R. H., Ruck, B. J., Piper, L. F. J., DeMasi, A., Smith, K. E., Schleife, A., ... & Durbin, S. M. (2008). Band structure of ZnO from resonant x-ray emission spectroscopy. Physical Review B, 78(15), 155114.

[12] Mang, A., & Reimann, K. (1995). Band gaps, crystal-field splitting, spin-orbit coupling, and exciton binding energies in ZnO under hydrostatic pressure. Solid state communications, 94(4), 251-254.

[13] Madelung, O. (2012). Semiconductors: data handbook. (Netherlands: Springer)

[14] Look, D. C. (2001). Recent advances in ZnO materials and devices. Materials Science and Engineering: B, 80(1), 383-387.

[15] Nickel, N. H., & Terukov, E. (Eds.). (2006). Zinc Oxide-A Material for Micro-and

Optoelectronic Applications. (Netherlands: Springer)

[16] Jagadish, C., & Pearton, S. J. (Eds.). (2011). Zinc oxide bulk, thin films and nanostructures: processing, properties, and applications. (New York: Elsevier.)

[17] Tsukazaki, A., Ohtomo, A., Onuma, T., Ohtani, M., Makino, T., Sumiya, M., ... & Ohno, H. (2005). Repeated temperature modulation epitaxy for p-type doping and light-emitting diode based on ZnO. Nature materials, 4(1), 42-46.

[18] Fan, J. C., Sreekanth, K. M., Xie, Z., Chang, S. L., & Rao, K. V. (2013). p-Type ZnO materials: theory, growth, properties and devices. Progress in Materials Science, 58(6), 874-985.

[19] Reynolds, D. C., Look, D. C., & Jogai, B. (1996). Optically pumped ultraviolet lasing from ZnO. Solid State Communications, 99(12), 873-875.

[20] Yu, P. Y., & Cardona, M. (2005). Fundamentals of Semiconductors. Physics and Materials Properties, 3rd edn. (Berlin: Springer)

[21] Kohan, A. F., Ceder, G., Morgan, D., & Van de Walle, C. G. (2000). First-principles study of native point defects in ZnO. Physical Review B, 61(22), 15019.

[22] Zhang, S. B., Wei, S. H., & Zunger, A. (2001). Intrinsic n-type versus p-type doping asymmetry and the defect physics of ZnO. Physical Review B, 63(7), 075205.

[23] Look, D. C., Farlow, G. C., Reunchan, P., Limpijumnong, S., Zhang, S. B., & Nordlund, K. (2005). Evidence for native-defect donors in n-type ZnO. Physical review letters, 95(22), 225502.

[24] Van de Walle, C. G. (2000). Hydrogen as a cause of doping in zinc oxide. Physical Review Letters, 85(5), 1012.

[25] Hofmann, D. M., Hofstaetter, A., Leiter, F., Zhou, H., Henecker, F., Meyer, B. K., ... & Baranov, P. G. (2002). Hydrogen: a relevant shallow donor in zinc oxide. Physical Review Letters, 88(4), 045504.

[26] Park, C. H., Zhang, S. B., & Wei, S. H. (2002). Origin of p-type doping difficulty in ZnO: The impurity perspective. Physical Review B, 66(7), 073202.

[27] Kato, H., Sano, M., Miyamoto, K., & Yao, T. (2002). Growth and characterization of Ga-doped ZnO layers on a-plane sapphire substrates grown by molecular beam epitaxy. Journal of Crystal Growth, 237, 538-543.

[28] Myong, S. Y., Baik, S. J., Lee, C. H., Cho, W. Y., & Lim, K. S. (1997). Extremely transparent and conductive ZnO: Al thin films prepared by photo-assisted metalorganic chemical vapor deposition (photo-MOCVD) using AlCl3 (6H2O) as new doping material. Japanese journal of applied physics, 36(8B), L1078.

[29] Ataev, B. M., Bagamadova, A. M., Djabrailov, A. M., Mamedov, V. V., & Rabadanov, R. A. (1995). Highly conductive and transparent Ga-doped epitaxial ZnO films on sapphire by

CVD. Thin solid films, 260(1), 19-20.

[30] Ko, H. J., Chen, Y. F., Hong, S. K., Wenisch, H., Yao, T., & Look, D. C. (2000). Ga-doped ZnO films grown on GaN templates by plasma-assisted molecular-beam epitaxy. Applied Physics Letters, 77(23), 3761-3763.

[31] Park, C. H., Zhang, S. B., & Wei, S. H. (2002). Origin of p-type doping difficulty in ZnO: The impurity perspective. Physical Review B, 66(7), 073202.

[32] Lee, W. J., Kang, J., & Chang, K. J. (2006). Defect properties and p-type doping efficiency in phosphorus-doped ZnO. Physical Review B, 73(2), 024117.

[33] Limpijumnong, S., Zhang, S. B., Wei, S. H., & Park, C. H. (2004). Doping by large-size-mismatched impurities: the microscopic origin of arsenic-or antimony-doped p-type zinc oxide. Physical review letters, 92(15), 155504.

[34] Lu, M. P., Lu, M. Y., & Chen, L. J. (2012). p-Type ZnO nanowires: From synthesis to nanoenergy. Nano Energy, 1(2), 247-258.

[35] Özgür, Ü., Alivov, Y. I., Liu, C., Teke, A., Reshchikov, M., Doğan, S., ... & Morkoc, H. (2005). A comprehensive review of ZnO materials and devices. Journal of applied physics, 98(4), 041301.

[36] Yamamoto, T., & Katayama-Yoshida, H. (1999). Solution using a codoping method to unipolarity for the fabrication of p-type ZnO. Japanese Journal of Applied Physics, 38(2B), L166.

[37] Cui, J. (2012). Zinc oxide nanowires. Materials Characterization, 64, 43-52.

[38] Huang, M. H., Mao, S., Feick, H., Yan, H., Wu, Y., Kind, H., ... & Yang, P. (2001). Room-temperature ultraviolet nanowire nanolasers. Science, 292(5523), 1897-1899.

[39] Vanmaekelbergh, D., & Van Vugt, L. K. (2011). ZnO nanowire lasers. Nanoscale, 3(7), 2783-2800.

[40] Chen, M. T., Lu, M. P., Wu, Y. J., Song, J., Lee, C. Y., Lu, M. Y., ... & Chen, L. J. (2010). Near UV LEDs made with in situ doped pn homojunction ZnO nanowire arrays. Nano letters, 10(11), 4387-4393.

[41] Könenkamp, R., Word, R. C., & Schlegel, C. (2004). Vertical nanowire light-emitting diode. Applied Physics Letters, 85(24), 6004-6006.

[42] Goldberger, J., Sirbuly, D. J., Law, M., & Yang, P. (2005). ZnO nanowire transistors. The Journal of Physical Chemistry B, 109(1), 9-14.

[43] Fan, Z., Wang, D., Chang, P. C., Tseng, W. Y., & Lu, J. G. (2004). ZnO nanowire field-effect transistor and oxygen sensing property. Applied Physics Letters, 85(24), 5923-5925.

[44] Chang, P. C., Fan, Z., Chien, C. J., Stichtenoth, D., Ronning, C., & Lu, J. G. (2006). High-performance ZnO nanowire field effect transistors. Applied physics letters, 89(13),

133113.

[45] Law, M., Greene, L. E., Johnson, J. C., Saykally, R., & Yang, P. (2005). Nanowire dye-sensitized solar cells. Nature materials, 4(6), 455-459.

[46] Baxter, J. B., & Aydil, E. S. (2005). Nanowire-based dye-sensitized solar cells. Applied Physics Letters, 86(5), 053114.

[47] Wang, Z. L., & Song, J. (2006). Piezoelectric nanogenerators based on zinc oxide nanowire arrays. Science, 312(5771), 242-246.

[48] Fan, Z., & Lu, J. G. (2006). Chemical sensing with ZnO nanowire field-effect transistor. Nanotechnology, IEEE Transactions on, 5(4), 393-396.

[49] Soci, C., Zhang, A., Xiang, B., Dayeh, S. A., Aplin, D. P. R., Park, J., ... & Wang, D. (2007). ZnO nanowire UV photodetectors with high internal gain. Nano letters, 7(4), 1003-1009.

[50] Kuo, T. J., Lin, C. N., Kuo, C. L., & Huang, M. H. (2007). Growth of ultralong ZnO nanowires on silicon substrates by vapor transport and their use as recyclable photocatalysts. Chemistry of Materials, 19(21), 5143-5147.

[51] Fan, Z., Wang, D., Chang, P. C., Tseng, W. Y., & Lu, J. G. (2004). ZnO nanowire field-effect transistor and oxygen sensing property. Applied Physics Letters, 85(24), 5923-5925.

[52] Fan, Z., Wang, D., Chang, P. C., Tseng, W. Y., & Lu, J. G. (2004). ZnO nanowire field-effect transistor and oxygen sensing property. Applied Physics Letters, 85(24), 5923-5925.

[53] Binnig, G., Quate, C. F., & Gerber, C. (1986). Atomic force microscope. Physical review letters, 56(9), 930.

[54] Edward, T. Y. (1996). Nanoscale characterization of semiconductor materials and devices using scanning probe techniques. Materials Science and Engineering: R: Reports, 17(4), 147-206.

[55] http://www.cds.caltech.edu/

[56] http://www.parkafm.com/

[57] http://www.doitpoms.ac.uk/tlplib/afm/

[58] Williams, C. C., Slinkman, J., Hough, W. P., & Wickramasinghe, H. K. (1989). Lateral dopant profiling with 200 nm resolution by scanning capacitance microscopy. Applied Physics Letters, 55(16), 1662-1664.

[59] Williams, C. C. (1999). Two-dimensional dopant profiling by scanning capacitance microscopy. Annual review of materials science, 29(1), 471-504.

[60] Sumner, J., Oliver, R. A., Kappers, M. J., & Humphreys, C. J. (2008). Assessment of the performance of scanning capacitance microscopy for n-type gallium nitride. Journal of

Vacuum Science & Technology B, 26(2), 611-617.

[61] Bowallius, O., Anand, S., Nordell, N., Landgren, G., & Karlsson, S. (2001). Scanning capacitance microscopy investigations of SiC structures. Materials Science in Semiconductor Processing, 4(1), 209-211.

[62] Duhayon, N., Clarysse, T., Eyben, P., Vandervorst, W., & Hellemans, L. (2002). Detailed study of scanning capacitance microscopy on cross-sectional and beveled junctions. Journal of Vacuum Science & Technology B, 20(2), 741-746.

[63] Douheret, O., Maknys, K., & Anand, S. (2004). Scanning capacitance microscopy investigations of InGaAs/InP quantum wells. Thin solid films, 459(1), 67-70.

[64] Giannazzo, F., Musumeci, P., Calcagno, L., Makhtari, A., & Raineri, V. (2001). Carrier concentration profiles in 6H-SiC by scanning capacitance microscopy. Materials Science in Semiconductor Processing, 4(1), 195-199.

[65] S. M. Sze (1981) Physics of semiconductor devices, 2nd edn. Wiley, New York, 371–373.

[66] Buh, G. H., Tran, C., & Kopanski, J. J. (2004). PSPICE analysis of a scanning capacitance microscope sensor. Journal of Vacuum Science & Technology B, 22(1), 417-421.

[67] Veeco Instruments Inc. (2003). Application Modules: Dimension and MultiMode Manual: Rev. D. 7-10.

[68] Edwards, H., McGlothlin, R., San Martin, R., Elisa, U., Gribelyuk, M., Mahaffy, R, Shih C K, List R S and Ukraintsev V A. (1998). Scanning capacitance spectroscopy: An analytical technique for pn-junction delineation in Si devices. Applied physics letters, 72(6), 698-700.

[69] Schaadt, D. M., Miller, E. J., Edward, T. Y., & Redwing, J. M. (2001). Lateral variations in threshold voltage of an AlxGa1− xN/GaN heterostructure field-effect transistor measured by scanning capacitance spectroscopy. Applied Physics Letters, 78(1), 88-90.

[70] De Wolf, P., Clarysse, T., Vandervorst, W., Snauwaert, J., & Hellemans, L. (1996). One- and two- dimensional carrier profiling in semiconductors by nanospreading resistance profiling. Journal of Vacuum Science & Technology B, 14(1), 380-385.

[71] De Wolf, P., Geva, M., Reynolds, C. L., Hantschel, T., Vandervorst, W., & Bylsma, R. B. (1999). Two-dimensional carrier profiling of InP-based structures using scanning spreading resistance microscopy. Journal of Vacuum Science & Technology A, 17(4), 1285-1288.

[72] Eyben, P., Xu, M., Duhayon, N., Clarysse, T., Callewaert, S., & Vandervorst, W. (2002). Scanning spreading resistance microscopy and spectroscopy for routine and quantitative two-dimensional carrier profiling. Journal of Vacuum Science & Technology B, 20(1), 471-478.

[73] Fraser, I. S., Oliver, R. A., Sumner, J., McAleese, C., Kappers, M. J., & Humphreys, C. J. (2007). Compositional contrast in AlxGa1-xN/GaN heterostructures using scanning spreading

resistance microscopy. Applied surface science, 253(8), 3937-3944.

[74] Schulze, A., Verhulst, A. S., Nazir, A., Hantschel, T., Eyben, P., & Vandervorst, W. (2013). A comprehensive model for the electrical nanocontact on germanium for scanning spreading resistance microscopy applications. Journal of Applied Physics, 113(11), 114310.

[75] Lu, R. P., Kavanagh, K. L., St J, D. W., Kuhl, A., SpringThorpe, A. J., Griswold, *et al*. (2001). Calibrated scanning spreading resistance microscopy profiling of carriers in III–V structures. Journal of Vacuum Science & Technology B, 19(4), 1662-1670.

[76] Hantschel, T., Niedermann, P., Trenkler, T., & Vandervorst, W. (2000). Highly conductive diamond probes for scanning spreading resistance microscopy. Applied Physics Letters, 76(12), 1603-1605.

[77] Eyben, P., Mody, J., Vemula, S. C., & Vandervorst, W. (2008). Impact of the environmental conditions on the electrical characteristics of scanning spreading resistance microscopy.Journal of Vacuum Science & Technology B, 26(1), 338-341.

[78] De Wolf, P., Clarysse, T., & Vandervorst, W. (1998). Quantification of nanospreading resistance profiling data. Journal of Vacuum Science & Technology B, 16(1), 320-326.

[79] De Wolf, P., Brazel, E., & Erickson, A. (2001). Electrical characterization of semiconductor materials and devices using scanning probe microscopy. Materials Science in Semiconductor Processing, 4(1), 71-76.

[80] Murrell, M. P., Welland, M. E., O'Shea, S. J., Wong, T. M. H., Barnes, J. R., McKinnon, A. W., *et al*. (1993). Spatially resolved electrical measurements of SiO_2 gate oxides using atomic force microscopy. Applied physics letters, 62(7), 786-788.

[81] Fouchier, M., Eyben, P., Alvarez, D., Duhayon, N., Xu, M., Brongersma, S., *et al*. (2003, April). Fabrication of conductive atomic force microscope probes and their evaluation for carrier mapping. In Microtechnologies for the New Millennium (pp. 607-616). International Society for Optics and Photonics.

[82] Huang, H. S., Cheng, H. M., & Lin, L. J. (2005). Coating tips used in electrical scanning probe microscopy with W and AuPd. Applied surface science, 252(5), 2085-2091.

[83] Wiederhold, K. P., Yamaguchi, Y., Ayala, A., Matheaus, M., Gutierrez, C. J., & Galloway, H. C. (2000). Ti/TiN coatings for microfabricated cantilevers used in atomic force microscopy.Journal of Vacuum Science & Technology B, 18(3), 1182-1186.

[84] Niedermann, P., Hänni, W., Blanc, N., Christoph, R., & Burger, J. (1996). Chemical vapor deposition diamond for tips in nanoprobe experiments. Journal of Vacuum Science & Technology A, 14(3), 1233-1236.

[85] Hantschel, T., Niedermann, P., Trenkler, T., & Vandervorst, W. (2000). Highly conductive diamond probes for scanning spreading resistance microscopy. Applied Physics Letters, 76(12), 1603-1605.

[86] Alvarez, D., Hartwich, J., Fouchier, M., Eyben, P., & Vandervorst, W. (2003). Sub-5-nm-spatial resolution in scanning spreading resistance microscopy using full-diamond tips. Applied physics letters, 82(11), 1724-1726.

[87] Álvarez, D., Fouchier, M., Kretz, J., Hartwich, J., Schoemann, S., & Vandervorst, W. (2004). Fabrication and characterization of full diamond tips for scanning spreading-resistance microscopy.Microelectronic engineering, 73, 910-915.

[88] http://www2.imec.be/be_en/services-and-solutions/cams/products/full-diamond-probes.html

[89] W. Mtangi, MSc Dissertation, University of Pretoria 2009 Electrical characterization of ZnO and metal ZnO contacts.

[90] Kim, H. K., Han, S. H., Seong, T. Y., & Choi, W. K. (2001). Electrical and Structural Properties of Ti/Au Ohmic Contacts to n ZnO. Journal of The Electrochemical Society, 148(3), G114-G117.

[91] Park, J. H., Kim, T. H., Chang, N. Y., Kim, J. S., Kim, G. H., & Lee, B. T. (2010). Microstructural investigation of Ti/Au ohmic contacts on Ga doped single crystalline n-ZnO films. Materials Science and Engineering: B, 167(1), 51-54.

[92] Wang, Z. L., & Song, J. (2006). Piezoelectric nanogenerators based on zinc oxide nanowire arrays. Science, 312(5771), 242-246.

[93] Morkoç, H., & Özgür, Ü. (2008). Zinc oxide: fundamentals, materials and device technology. John Wiley & Sons, 388-390.

[94] S. M. Sze (1981) Physics of semiconductor devices, 2nd edn. Wiley, New York, 255-258.

[95] Brillson, L. J., & Lu, Y. (2011). ZnO Schottky barriers and Ohmic contacts. Journal of Applied Physics, 109(12), 121301.

[96] Oh, M. S., Hwang, D. K., Lim, J. H., Choi, Y. S., & Park, S. J. (2007). Improvement of Pt Schottky contacts to n-type ZnO by KrF excimer laser irradiation. Applied Physics Letters, 91(4), 042109.

[97] Blood, P., & Orton, J. W. (1992). The electrical characterization of semiconductors: majority carriers and electron states (Vol. 2). Academic Press, 234-235.

[98] Kang, J., Myung, S., Kim, B., Oh, D., Kim, G. T., & Hong, S. (2008). Massive assembly of ZnO nanowire-based integrated devices. Nanotechnology, 19(9), 095303.

[99] Huang, Y., Duan, X., Wei, Q., & Lieber, C. M. (2001). Directed assembly of one-dimensional nanostructures into functional networks. Science, 291(5504), 630-633.

[100] Whang, D., Jin, S., Wu, Y., & Lieber, C. M. (2003). Large-scale hierarchical organization of nanowire arrays for integrated nanosystems. Nano letters, 3(9), 1255-1259.

[101] Zhou, X., Dayeh, S. A., Aplin, D., Wang, D., & Yu, E. T. (2006). Direct observation of

ballistic and drift carrier transport regimes in InAs nanowires. Applied physics letters, 89(5), 053113.

[102] Li, Q. H., Liang, Y. X., Wan, Q., & Wang, T. H. (2004). Oxygen sensing characteristics of individual ZnO nanowire transistors. Applied Physics Letters, 85(26), 6389-6391.

[103] Fan, Z., Wang, D., Chang, P. C., Tseng, W. Y., & Lu, J. G. (2004). ZnO nanowire field-effect transistor and oxygen sensing property. Applied Physics Letters, 85(24), 5923-5925.

[104] Goldberger, J., Sirbuly, D. J., Law, M., & Yang, P. (2005). ZnO nanowire transistors. The Journal of Physical Chemistry B, 109(1), 9-14.

[105] Luo, L., Zhang, Y., Mao, S. S., & Lin, L. (2006). Fabrication and characterization of ZnO nanowires based UV photodiodes.Sensors and Actuators A: Physical, 127(2), 201-206.

[106] Nguyen, P., Ng, H. T., Yamada, T., Smith, M. K., Li, J., Han, J., & Meyyappan, M. (2004). Direct integration of metal oxide nanowire in vertical field-effect transistor. Nano Letters, 4(4), 651-657.

[107] Latu-Romain, E., Gilet, P., Noel, P., Garcia, J., Ferret, P., Rosina, M., ... & Chelnokov, A. (2008). A generic approach for vertical integration of nanowires. Nanotechnology, 19(34), 345304.

Chapter 3

Carrier profiling on ZnO NWs by SCM

In the previous part of this thesis, the characterization techniques employed in this thesis work and the NWs sample preparation processes have been described. The following two chapters deal with the application of the introduced SPM techniques to characterizing ZnO NWs, with the aim of performing carrier profiling on such quasi-1D structure. This chapter reports the results and discussions related to SCM. First, SCM measurements on well-prepared NWs sample are done to demonstrate its capability of detecting the ZnO NWs embedded in SiO_2 matrix. However, the results themselves are qualitative in respect of the tip-sample capacitance variation thus do not allow quantitative analysis. To tackle this problem, i.e. to quantitatively obtain the carrier concentration information inside the NWs, calibration method is employed. Two multi-layer staircase structures of Ga doped ZnO were grown by MBE, which cover a Ga dopant density range from 1.7×10^{17} to 1.2×10^{19} and from 1.7×10^{18} to 3×10^{20} cm^{-3}, separately. They are used for producing the calibration dataset (calibration curve) of SCM data versus carrier concentration. Finally, from SCM/SCS measurements on ZnO NWs and ZnO:Ga samples under the same conditions and the calibration analysis, the carrier concentrations for the NWs were extracted. It needs to point out that the non-intentionally doped (nid) ZnO NWs are of *n*-type, so *n*-type ZnO multilayer structure for calibration purpose is used. And since stable *p*-type ZnO is still an unsolved problem, no quantitative carrier profiling is performed. However, an effort to obtain *p*-type conduction in ZnO NWs will be addressed in Chapter 6.

3.1 Introduction

Scanning capacitance microscopy (SCM) has been developed to meet the demands of determination of two dimensional (2D) carrier/dopant profiles with a nanoscale resolution in semiconductor materials [1]. It is widely studied and used as it gives information of not only the dopant/carrier concentration, but also the conduction type (*p* or *n*) [2-5]. Its typical spatial resolution is around 20 nm which is ultimately limited by the tip radius and can be improved by imaging on beveled structures [6, 7]. This technique has been first demonstrated and extensively employed in Si-based structures/devices [1-2, 4-6], and then extended to the study of some other semiconductor materials such as InP, GaN, SiC, SiGe [8-13]. However, ZnO, as a significant wide band gap semiconductor with lots of potential applications [14], has rarely been investigated with this tool, with only three studies reporting local surface-induced or

grain boundary related *p*-type ZnO [15-17]. In this chapter, the use of SCM is explored for 2D dopant/carrier profiling in ZnO by performing SCM measurements on ZnO multi-layer structures with varying Ga dopant concentrations. For quantitative application, carrier concentrations inside ZnO NWs are assessed using calibration method.

3.2 SCM measurement on ZnO NWs

After the NWs samples being prepared as described in Chapter 2, SCM measurements were carried out to check the capability of SCM to examine the NWs. The two samples, i.e. CBD grown and MOCVD grown ZnO NWs introduced before, were studied. For clarity, for all the measurements in this work, the voltage is applied on the sample instead of the probe.

3.2.1 CBD grown NWs

Figure 3.1 shows an SCM result on the CBD grown ZnO NWs. From the electrical channels (SCM data channel and d*C*/d*V* phase channel), it can be noticed that the ZnO NWs are well detected showing contrast with the SiO_2 matrix. The NWs give stronger SCM data signals as a result of the response of electrons depletion effect inside, while the SiO_2 dielectric produces weaker (near zero) SCM data signal in absence of free carriers. Regarding the d*C*/d*V* phase signal, after adjusting the lock-in phase parameter, its polarity can be used to indicate the conduction type of the carriers underneath the tip with *n*-type and *p*-type corresponding to opposite d*C*/d*V* polarities. Here, the lock-in phase was set in such a way that a positive value of d*C*/d*V* phase around $\pi/2$ indicates *n*-type conduction of the sample and a negative value suggests *p*-type. So as can be seen from the line profile in Figure 3.1(d), while the NWs are detected to be of *n*-type, d*C*/d*V* signal for the SiO_2 matrix appears as just noise indicating no detection of regular capacitance variation, thus no free carriers.

In the SCM result, the hexagonal form of the NWs was not clearly observed mainly because of their very small diameters and their poor vertical alignment. It needs to keep in mind that SCM response of semiconductors is sensitive to the choice of V_{dc} since a V_{dc} far from the 'flat-band' voltage may produce not enough capacitance variation for detection. The optimized V_{dc} may depend on the surface treatment as well as the doping level of the sample and the knowledge of it could be useful for normal SCM measurements. A good way to have an idea about the dependence of SCM data on V_{dc} is perform SCS measurement. A typical SCS curve with the tip on a ZnO NW of the sample is shown in Figure 3.2. It can be observed that the optimized V_{dc} for obtaining the largest SCM data signal is around -1.2 V.

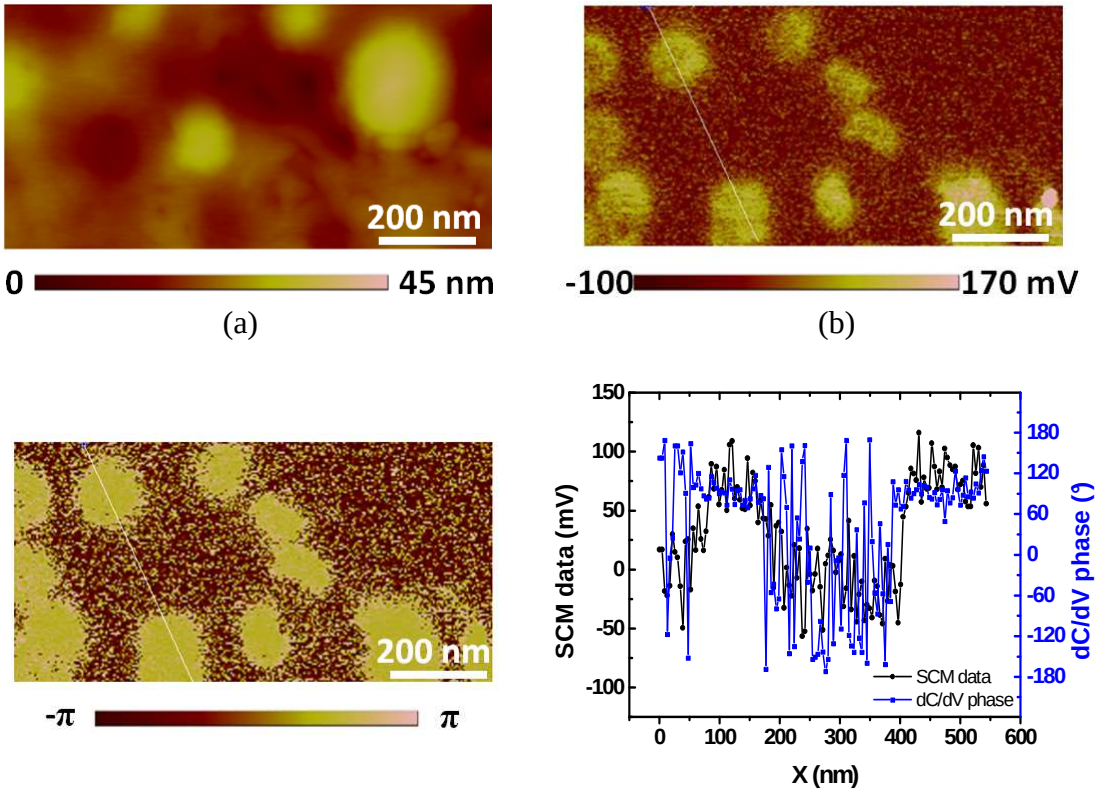

Figure 3.1: SCM on CBD grown NWs sample. (a) Topography image of the 1 μm×0.5 μm scanned area. (b) SCM data image. (c) d*C*/d*V* phase image. (d) Line profile of SCM data and d*C*/d*V* phase as indicated by the line in (b) and (c). Apparently, ZnO NWs are well detected giving larger SCM data than the SiO_2 matrix and d*C*/d*V* phase difference is recorded. Notice that SiO_2 matrix gives only noise regardless of topography change. Measurement condition: Pt/Ir coated tip was used. V_{dc}=-1 V and V_{ac}=500 mV were applied.

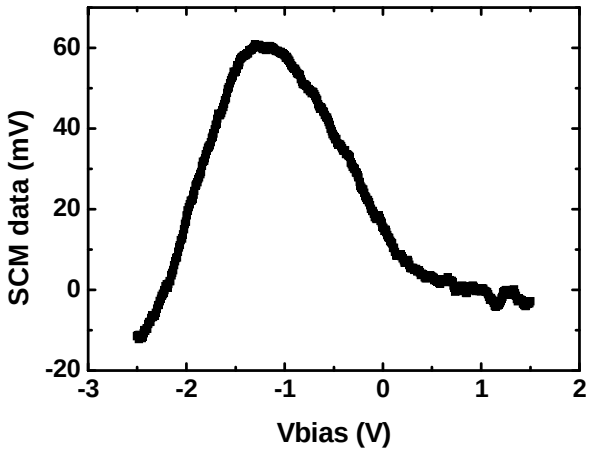

Figure 3.2: SCS curve with the tip on contact with a ZnO NW. V_{dc} for the maximum value of SCM data can be identified near -1.2 V. Measurement condition: Pt/Ir coated tip was used and V_{ac}=500 mV was applied.

3.2.2 MOCVD grown NWs

Figure 3.3 shows an SCM result on the MOCVD grown ZnO NWs sample. Similar to the case of CBD grown sample, the NWs and the SiO_2 matrix are in both electrical channels well distinguished due to their different properties (semiconductor versus dielectric). Moreover, the hexagonal shape for certain NWs is apparently visible. However, a core-shell contrast is observed for a large mount of NWs. To investigate this phenomenon, we compared in detail its correspondence with topography features.

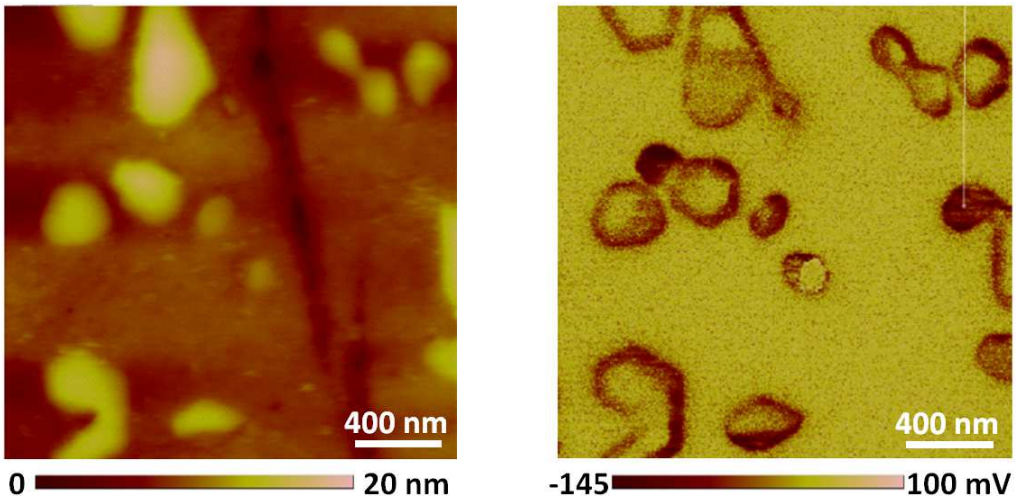

(a) (b)

Figure 3.3: SCM on MOCVD grown NWs sample. (a) Topography image of the 2 μm×2 μm scanned area. Roughness RMS value=3.61 nm, height range=32.4 nm. (b) SCM data image. The NWs and the SiO_2 matrix are distinguished in both electrical channels. Besides, core-shell contrast is observed for NWs. Measurement condition: Pt/Ir coated tip was used. V_{dc}=0 V and V_{ac}=2000 mV were applied.

Comparing the topography image with the SCM data one, it is noticed that the core-shell contrast can be correlated to the topography change, which occurs near the NWs location during the tip scan. For some areas where no significant topography change is experienced (as indicated in the two circles in Figure 3.3), the SCM data signal appears more homogeneous. Another example indicating the impact of topography variation is presented in Figure 3.4. This allows us to conclude that the core-shell contrast existence for NWs is, if not wholly, partly due to the topography features. When the tip scans at a lower position on the sample surface, for instance, the edge of the NWs, a larger contact area occurs between the tip and the sample, which is likely to bring about a larger capacitance variation, leading to a larger SCM data. This effect also underlines the importance of a suitable sample surface in terms of flatness. Another possible reason for the core-shell contrast is surface induced depletion effect, which reduces the carrier concentration near NWs surface (interface between NWs and SiO_2), causing a larger SCM signal.

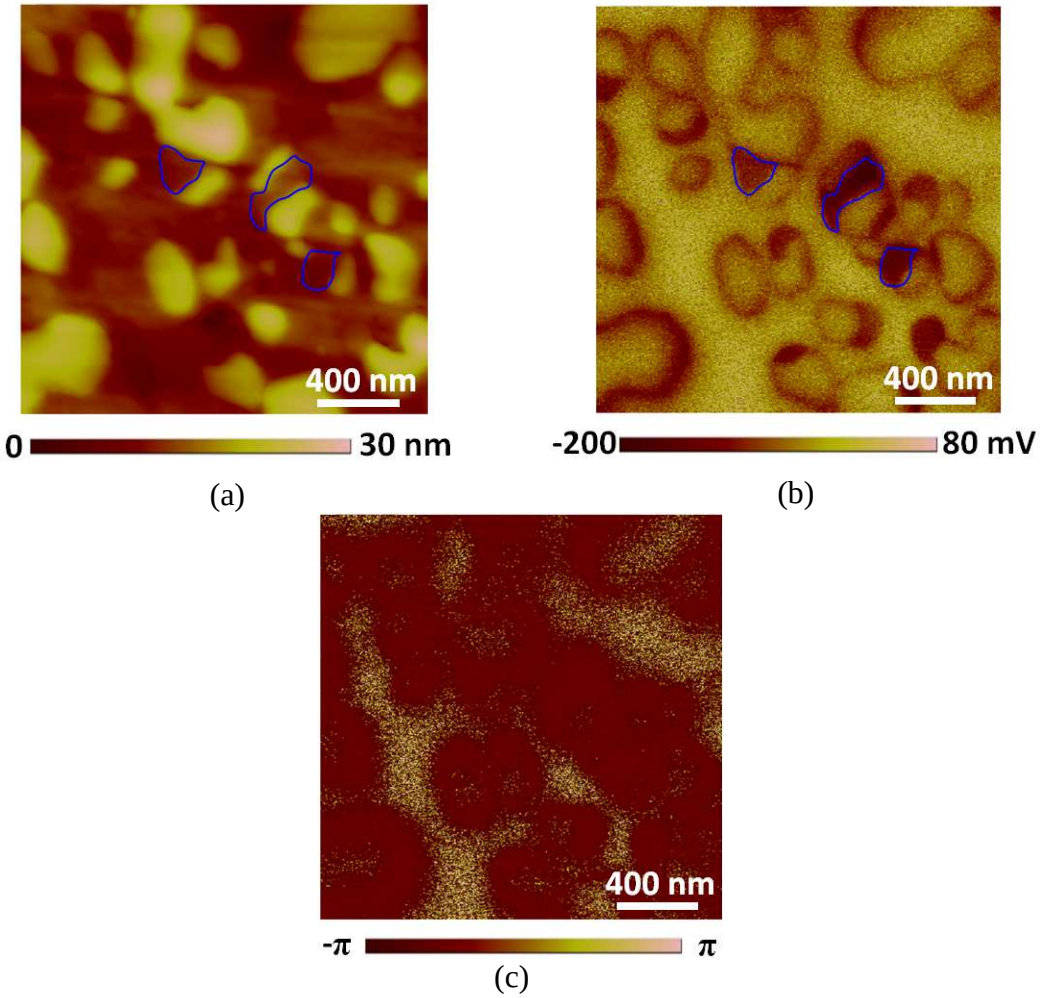

Figure 3.4: SCM on MOCVD grown NWs sample. (a) Topography AFM image. (b) SCM data image collected simultaneously. (c) dC/dV phase image. Correlation can be noticed between topography features and SCM data core-shell contrast for NWs.

This core-shell contrast was also observed by Latu-Romain *et al* [15] in SCM on NWs grown under similar conditions. In their case, they encapsulated the NWs by spin coating of polymer and took use of oxygen plasma etching to expose the top of them. This preparation process can lead to a more significant topography feature of the sample surface. For the analysis of the core-shell contrast, they ascribed it to surface-induced *p*-type conductivity and estimated a 90 nm *p*-type ZnO shell [15].

In our case, the NWs including their shells are identified to be of *n*-type. Since the sample preparation process is different from that in ref [15], it is difficult to compare the two results. Concerning the CBD ZnO NWs, no core-shell contrast was observed. One possible explanation is the better surface flatness which decreases the impact of topographical changes. Another is that the CBD NWs have smaller diameters making it hard to resolve the spatial carrier density difference.

3.2.3 Quantification analysis for SCM measurement

As expected, the ZnO NWs are well detected in SCM measurements. From the obtained results, it is possible to extract the SCM data values for the NWs. However, the results on the NWs alone do not allow one to extract any quantitative information about the carrier density inside them and quantitative analysis of SPM measurement has been from the start a challenging problem.

Many SCM studies aim to convert an SCM signal profile into an accurate dopant/carrier profile. For Si, it has been shown that when the dopant density only varies gently over a length scale of a few Debye lengths (13 nm for a dopant concentration of 10^{17} cm^{-3} and 0.4 nm for a concentration of 10^{20} cm^{-3}), the carrier density is a reasonable measure of the activated dopant density. Huang *et al* [18] made one of the first comparisons between dopant densities extracted from SCM and SIMS data. They applied a quasi- 1D model to extract a dopant profile from the measured SCM data and found good agreement with both SIMS and SRP profiles over a dopant density range of 10^{17} cm^{-3} to 10^{20} cm^{-3}. Below 10^{17} cm^{-3}, the error between SCM and SIMS or SRP profiles becomes larger since the Debye length at these dopant densities becomes comparable to the tip size, and the quasi-1D approximation breaks down.

Kopanski *et al* [19] developed a slightly more sophisticated model of SCM, achieving a numerical solution of a nonlinear Poisson's equation in three dimensions. Then Huang *et al* [20] went further by developing an inversion routine based on their quasi-1D model which would allow the automatic extraction of dopant concentrations from SCM results. McMurray *et al* [6] improved the accuracy of the 1D model and extended it to 2D, and developed a faster version of the inversion algorithm. However, all these developments encountered the problem of a broad range of unknown input parameters, including the tip size, the thickness and dielectric constant of the surface oxide, which are required but not necessarily well known in an experimental situation. Also, to calibrate the model, the dopant density at (at least) one point in the SCM scan must be known.

In this work, we don't focus on a specific model for conversion of SCM data to dopant/carrier profile. Instead, direct calibration method is adopted for the quantitative analysis of SCM (also SSRM). The idea is to obtain a calibration curve (dataset) of SCM data versus carrier concentration on the base of staircase structure containing a series of carrier concentrations. The dopant concentration profile can be revealed by conventional SIMS technique. Then, through calibration process, the SCM data results for the NWs can be converted into quantitative carrier density.

3.3 SCM on ZnO:Ga staircase structures

3.3.1 Choice of Ga as dopant in ZnO

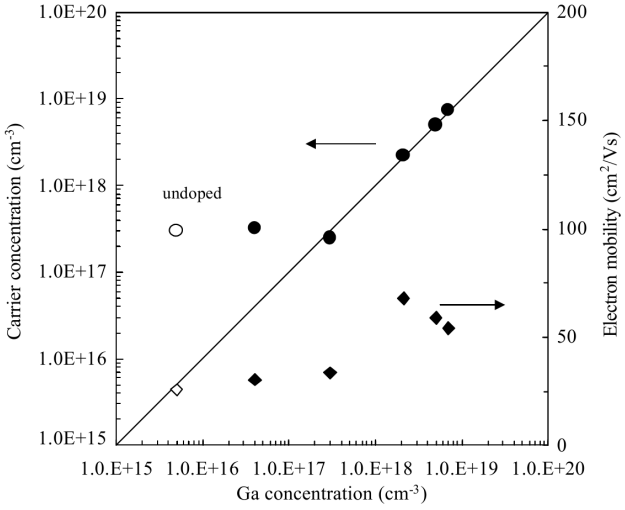

Figure 3.5: Dependence of carrier concentration and electron mobility on Ga concentration in ZnO epitaxial layers. Solid line shows that the activation ratio of Ga is unity. [23]

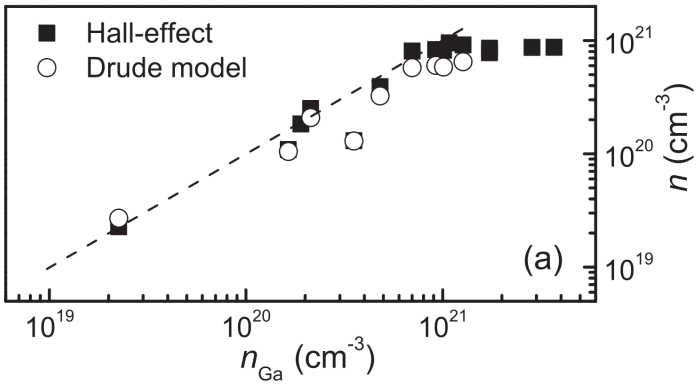

Figure 3.6: Concentration of free electrons obtained from Hall measurements (filled squares) and from optical spectra within the Drude model (open circles) versus Ga concentration. The dashed curve represents the line $n=n_{Ga}$. [24]

It is well known that Ga acts as an effective donor in ZnO. First, Ga is less reactive and more resistive to oxidation, compared to another dopant (Al for instance) [21]. Second, the ionic radius and the covalent radius of Ga are 0.62 and 1.26 Å, respectively, which are similar to those of Zn (0.74, 1.31 Å), as compared with Al (0.50, 1.26 Å) and In (0.81, 1.44 Å) [22]. In fact, the effectiveness of *n*-type doping for ZnO by Ga dopant has been demonstrated by Kato, H. *et al* [23], Ko H. *et al* [21]and Sadofev S. *et al* [24], in whose work the near-unity activation ratio of Ga was described for Ga concentration exceeding 3×10^{17} cm^{-3} (Figure 3.5), from 1.33×10^{18} to 10^{20} cm^{-3} and from 2×10^{19} to until 10^{21} (Figure 3.6) in MBE grown ZnO:Ga layers, respectively. So in this work, we have chosen Ga as the dopant for the ZnO structure

for calibration purpose and it is considered that a majority part of Ga impurity are contributing to the free carrier concentration in the doped range > 10^{17} cm^{-3}.

Two non-polar multi-layer staircase structures were developed by MBE (Jean-Michel Chauveau in CRHEA). MBE growth was chosen because it allowed a better control of the structure's quality, especially that it is possible to reduce the residual carrier density for nid ZnO layers to a low level (~10^{14} cm^{-3} level was achieved in ref [25]). The structures were grown on 10×20 mm^2 m-plane (10-10) ZnO substrates in a Riber Epineat MBE system equipped with conventional effusion cells for elemental Zn and Ga. The growth of the ZnO:Ga/ZnO heterostructures was performed at 500 °C under zinc-rich conditions with a growth rate of 0.3 µm/h. The Ga concentration was controlled by adjusting the temperature of the Ga cell.

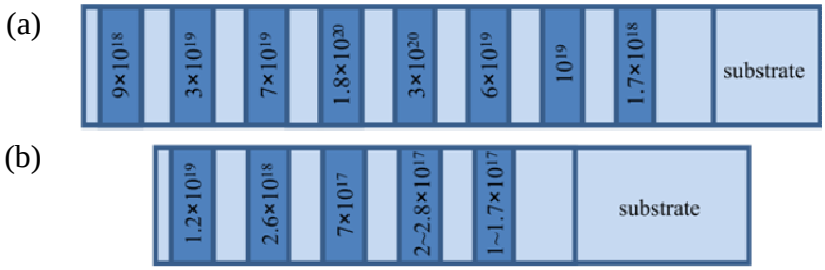

Figure 3.7: Schematic view of (a) sample A and (b) sample B. Dark stripes correspond to ZnO:Ga layers while bright ones indicate nid ZnO layers and ZnO substrate at right side. Sample A has a layer thickness of ~200 nm with a ~400 nm buffer layer. Sample B has layer thickness of ~140 nm with a ~261 nm buffer layer. Ga density values from SIMS are given for each layer (unit: cm^{-3}).

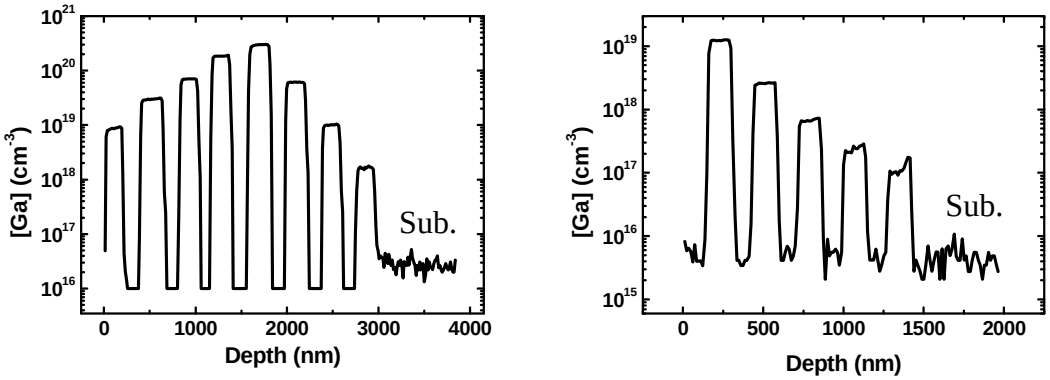

Figure 3.8: Ga density profile revealed by SIMS of (a) sample A and (b) B. Surface is to the left for both.

Sample A consists of eight ZnO:Ga layers of ~200 nm thickness with Ga concentration ranging from 1.7×10^{18} to 3×10^{20} cm^{-3} (Figure 3.7(a)), while sample B has five ZnO:Ga layers ~140 nm thick with various Ga concentration between 1.7×10^{17} and 1.2×10^{19} cm^{-3} (Figure 3.7(b)), as detected by SIMS (results in Figure 3.6). For both samples, a buffer layer of ZnO (thickness of 400 nm for sample A and 261 nm for sample B) was grown before growth of

ZnO:Ga layers. All doped layers are separated by nid layers of similar thickness.

3.3.2 An investigation of tip depletion effect

The Ga doped ZnO layers in the staircase samples are of *n*-type. Besides, nid ZnO layers nominally exhibit *n*-type conductivity. According to the principle of SCM, all the layers, being of same-type conductivity, should yield SCM data of same polarity. However, sometimes in our SCM measurements, opposite signs are observed specially for the most heavily doped and non-doped layers (an example in Figure 3.9 (a)). This phenomenon was also noticed in the literature for other materials like GaN (Figure 3.9(b)) [26]. Since in both cases, results like this should not be considered as proof of existence of two types of carriers, this phenomenon was first investigated with help of a Si multilayer structure and was eventually ascribed to the tip depletion effect.

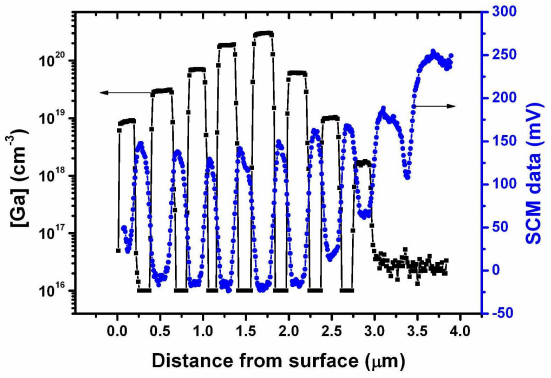

(a)

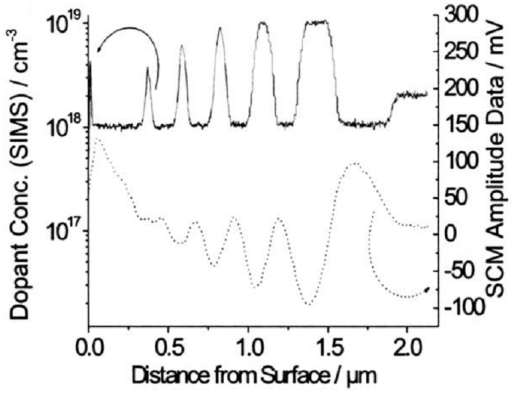

(b)

Figure 3.9: (a) An SCM data profile is plotted with Ga density profile from SIMS. For the 5 most heavily doped layers, SCM data values are observed negative instead of positive as other layers. (b) Processed SCM data (dotted) is plotted with SIMS data (solid) for a GaN-based structure [26]. Negative SCM data for some layers can be seen.

As a matter of fact, during the development and application of SCM, factors influencing the capacitance-voltage characteristics of the tip-sample system in SCM measurement have also been extensively investigated [27-32] such as choice of V_{dc} [29], stray laser light [27] and modulation voltage V_{ac} [30]. One special factor is the tip depletion, which signifies the possible participation of the tip itself in the SCM signal in consequence of its response to V_{ac}. After etched tungsten wire as probe tip, metal coated (for instance Pt/Ir and Co/Cr coating) Si cantilever/tip combinations have been in regular use for SCM. This kind of tip does not deplete under voltage bias during SCM measurements. Nevertheless, the serious tip wear problem is encountered concerning the very thin metallic coating, whose loss can cause an exposure of the material used inside (Si for instance in the case of electrical tip). V. V. Zavyalov [31] compared the quality of heavily doped Si tips with Co/Cr coated tips and

investigated related tip depletion phenomenon, pointing out that this phenomenon arising for Si tips can distort SCM data and thus impact unfavorably quantitative dopant profiling. M. L. O'Malley [32] simulated SCM imaging of Si *p*-*n* junction using semiconductor probe tips, revealing the interaction between the tip and studied sample, in which the contribution of the tip dC/dV to the overall dC/dV is most significant when the tip concentration is on the order of or less than that of the sample. Also, simulations results showed that a tip of same conduction type as the sample may produce SCM signal of opposite sign for a certain high sample carrier concentration [32].

To address this issue, we performed SCM measurement using three types of tips (a commercial Pt/Ir coated Si tip (SCM-PIC type from Bruker) used for the first time that we call "fresh tip", a worn tip where Pt/Ir coating at tip apex is lost after some previous measurements, exposing the Si inside, and a tip without metal coating on front side but just etched Si (ESP type from Bruker)) on a phosphorus doped multilayer structure of Si to investigate the effect of tip depletion in real cases. The Si material in all tips here is doped by antimony (*n*-type dopant) and possesses a resistivity of 0.01~0.025 Ω•cm [33], which should correspond to a dopant concentration of ~5×10^{18} cm^{-3}, close to the doping range of the analyzed sample. The sample in study is phosphorus doped *n*-type Si multilayer structure. It consists of 5 regions with varying doping concentrations between 2×10^{17} and 2×10^{19} cm^{-3} (covering the dopant concentration of the tip Si) on a p-type substrate with a hole density ~10^{15} cm^{-3} (SIMS profile in Figure 3.10(b)). It shows that although SCM can help recognizing local carrier type, loss of tip metal coating can produce misleading results for the identification of carrier type in heavily *n*-type doped material.

Simple cleavage was conducted to obtain its cross section and native oxide layer was used as insulating layer in SCM measurements. For information, since laser-induced photoelectronic generation may distort the Si sample response in SCM [27], this laser effect has been avoided by displacing the laser spot relatively far from the tip end. For clarity, in this work, lock-in phase was set in such a way that positive SCM data (positive d*C*/d*V* phase) would correspond to *n*-type and negative SCM data (negative d*C*/d*V* phase) corresponds to *p*-type.

Figure 3.10(a) shows an original SCM image of the sample using the new Pt/Ir coated tip. The contrast between layers with various doping concentrations is clearly visible. Figure 3.10(b) presents a comparison of its averaged SCM data profile with [P] profile from SIMS. It is seen that results from the two techniques agree well with each other in a way that an increase in doping concentration producing a reduction in SCM data amplitude. Here, a proper V_{dc} not far from 0 V has been chosen for SCM for reasonable monotonic SCM behavior with doping concentration [29]. Along with the agreement between SCM and SIMS, all the SCM data for the doped layers are positive and have a positive and stable phase, which indicates a correct

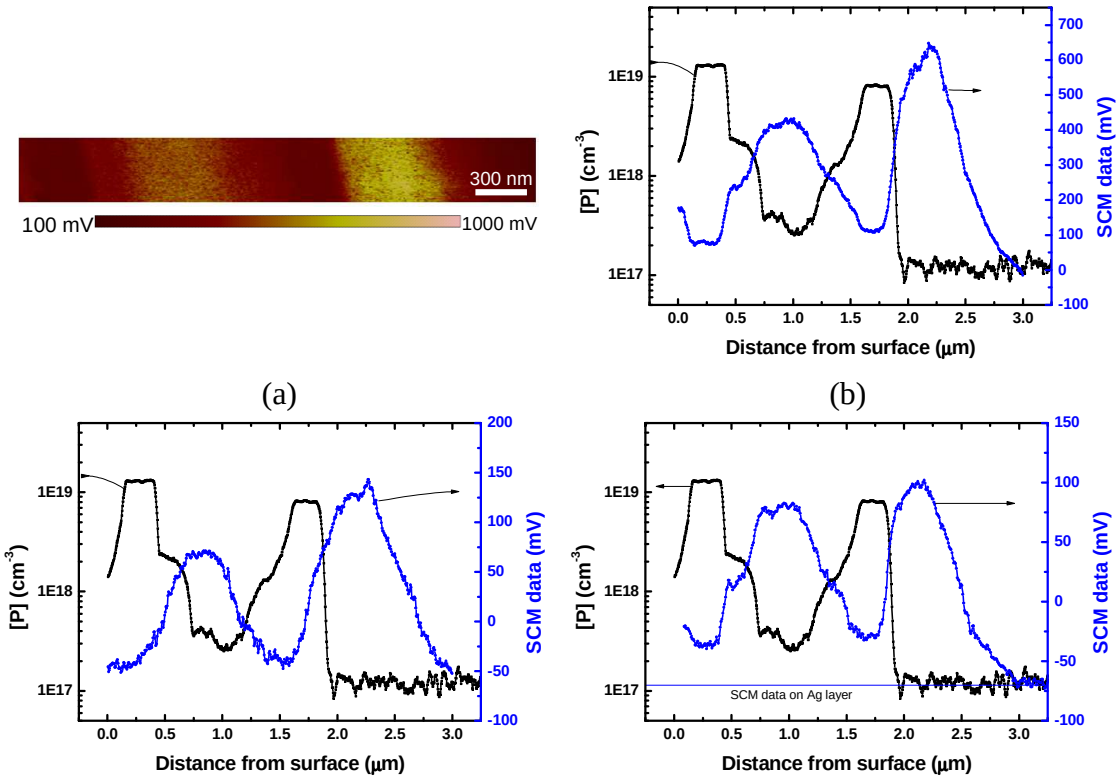

Figure 3.10: (a) Original SCM image using a new Pt/Ir coated tip. (b) Averaged SCM profile of (a) plotted with SIMS result. (c) SIMS and SCM profile using a worn SCM-PIC tip. (d) SIMS and SCM profile for an ESP tip. The line at SCM data= -70 mV implies SCM data with measurement on Ag metal demonstrating tip depletion effect. Measurement conditions: V_{dc}= -1 V, V_{ac}= 1000 mV for new Pt/Ir coated tip and ESP tip. V_{dc}= -1 V, V_{ac}= 2000 mV for worn Pt/Ir coated tip. Sample surface is to the left (same for other Figures).

recognition of SCM signal for all the layers as *n*-type.

The SCM profile obtained with the worn Pt/Ir coated tip and its comparison with SIMS are shown in Figure 3.10(c). The opposite sign of SCM data can be noticed for the two most heavily doped layers, i.e. the 8×10^{18} and 2×10^{19} cm^{-3} layers. It indicates that using this tip, the two most heavily doped layers have both negative SCM data values instead of positive ones, which, according to the way we have set lock-in phase, should correspond to *p*-type carriers. This means SCM in this case fails to successfully recognize the carrier type for the two regions. This error of SCM data polarity is related to the tip depletion originated from the wear of the tip. In the tip wear process, the metal coating on it is gradually removed and the Si inside is exposed thus tip depletion in response to V_{ac} occurs. Since the material of Si tip has a carrier density around 5×10^{18} cm^{-3}, for carriers concentration lower than this value, the worn tip could still perform well as gate and does not cause a reversal of SCM phase, but for carrier density higher than this value, the tip depletion effect might not be negligible or even can dominate the overall SCM signal response, resulting in a misleading result. For clearness, the

negative SCM data signal at the end of each SCM data profile is related to the *p*-type substrate. And the differences in position of SCM data crossing zero is a consequence of both the applied voltage and the tip depletion contribution during SCM measurement. A study on the dependence of *p-n* junction shift on the V_{bias} can be found in [34].

SCM measurements were also done using another kind of no-metal coated tip. No metal coating is at the tip end which results in a direct contact of the Si tip on the sample and a coexistence of depletions inside the tip and sample. Obtained SCM profile is shown in Figure 3.10(d). Apparently SCM profile shows a behavior similar to that of the worn tip. The additional line indicates the SCM data with the tip scanning on Ag metal surface. No SCM signal is supposed to be detected in SCM on a metal layer when a metal or metal-coated tip is used. However, the SCM measurement of this tip on Ag layer gives an SCM signal slightly larger in amplitude than that of the heavily doped semiconducting layers. Moreover, the layer with highest dopant concentration (2×10^{19} cm^{-3}) presents an SCM data closer to the line for Ag layer than the layer with second highest doping concentration (8×10^{18} cm^{-3}).

Figure 3.11(a) and Figure 3.11(b) show profiles of SCM measurements at different V_{dc} using the new Pt/Ir coated tip and the non-metal coated tip, respectively. For the former, the change in V_{dc} can hardly reverse the sign of SCM data which only show a dependence of amplitude on V_{dc}. This is related to the flat-band voltage differences for layers which has been well studied before and is not the focus of our work here. For the tip without metal coating, by varying V_{dc} the most heavily doped layer i.e. 2×10^{19} cm^{-3} layer tends more easily to undergo SCM data polarity reversal then the 8×10^{18} cm^{-3} layer. It is because tip depletion accounts for a larger part of overall signal as a result of the larger difference in carrier concentration between the tip and the doped layer. In this way, it would not be unreasonable to claim more

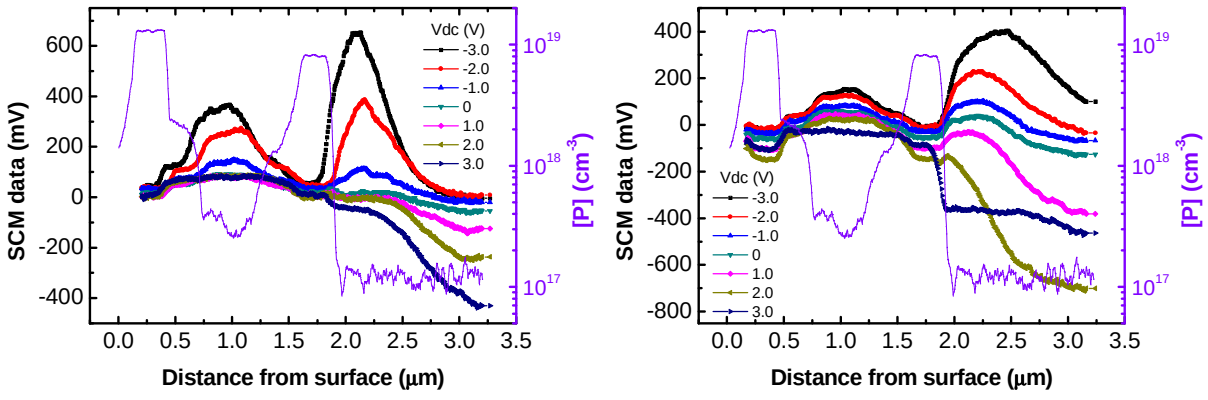

Figure 3.11: SCM data profiles on studied sample under various V_{dc} using (a) a new Pt/Ir coated Si tip (b) no-metal coated Si tip. The new Pt/Ir coated tip gives positive SCM data for all *n* doped regions under all used V_{dc} while negative SCM data appear for two regions with highest dopant concentration under certain V_{dc} in the case of no-metal coated tip. V_{ac}= 1000 mV was used for modulation.

chances for a higher *n*-type carrier concentration than 2×10^{19} cm^{-3} to cause a negative SCM signal during the tip wear process. It is worth noting that for the same kind of tip, we didn't observe this SCM phase reversal phenomenon for layers with holes concentrations higher than 10^{19} cm^{-3} in a *p*-type Si multilayer structure. It is easy to understand considering opposite type of carriers in the tip and sample because the depletion of the tip enhance the system capacitance change yielding a larger SCM signal than that only taking into account the sample depletion, as has been analyzed by M. L. O'Malley [32].

Although for no-metal coated tip and the worn tip in this work, the sign of SCM signal (or dC/dV phase) no longer reflects correctly the local carrier type, it is still possible to observe a consistence between SCM signal and the doping concentration, by introducing a new baseline instead of zero of SCM signal amplitude to relieve from errors induced by tip depletion effect. This can be the case for some well-known semiconductor structures in SCM analysis [26, 35]. Nevertheless, it should be underlined that this can be done only if we have enough information of the carriers in the sample. Otherwise, adequate attention should be appreciated before a correct conclusion is made, especially in the case where unknown or unexpected carrier type is involved.

The tip wear is still an unsolved problem in SCM measurement. The tip fragility, together with the fact the Si material for SCM tip fabrication has a certain carrier concentration (around 5×10^{18} cm^{-3} for most widely used Pt/Ir coated tip) may cause a fatal error for the carrier type identification in SCM. The sensitive range of carrier density for this problem may cover all the carrier concentrations higher than that of the Si-based tip. As additional information, even the tip end runs out of metal coating, it can still be possible to acquire a reasonable topography image, increasing the difficulty to have intention to replace it by another new tip. What's more, for scans of tip on cross sections or other area with considerable topography changes, tip wear can take place really fast [1].

A comparison of scanning capacitance spectroscopy (SCS) [36] on different layers using the new Pt/Ir tip and the worn one is shown in Figure 3.12. For the former, SCS signal keeps positive in the scan range and exhibits a dependence on V_{dc}. Besides, SCM data peak value decreases with increasing dopant concentration as expected. In contrast, for the worn tip, while the two lightly doped layers are still well distinguished and give positive SCM values, the two layers with dopant concentrations of 8×10^{18} and 2×10^{19} cm^{-3} are mistaken producing negative SCM data. And SCS with the tip on Ag layer yields more negative SCM data, indicating the existence of tip depletion effect.

Metal-coated Si tips do not deplete at first. However, loss of metal coating can potentially play a role preventing from obtain correct results. As SCM is preferably used for the finding and recognition of certain local type carriers at nanometer scale, for well-known samples, it is

not a crucial problem for the interpretation of results as long as we keep in mind the possibility of tip depletion. But for not fully known samples, where analysis of SCM signal polarity matters a lot for result interpretation, this kind of tip may induce unwanted mistake while still give acceptable topography information. As shown before, commercial etched *n*-type Si based metal-coated tip may fail to discern a heavily doped *n*-type material from a *p*-type material.

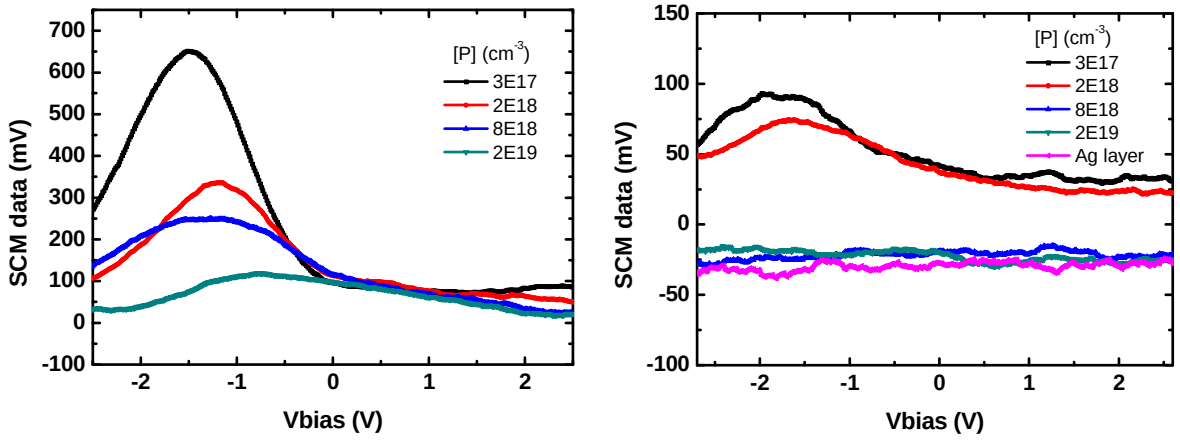

(a) (b)

Figure 3.12: (a) SCS spectra for different layers on the sample using (a) the new Pt/Ir coated tip and (b) the worn tip. The new tip with Pt/Ir coating discerns all *n*-type layers correctly while the SCM peak value shows dependence on dopant density (decrease with increasing dopant density). The worn tip identifies correctly the two layers with lower carrier concentrations but mistakes the type of the other two layers yielding negative SCM signal values. In (b), negative SCM data from SCS on Ag indicates effect of tip depletion.

To sum up this part, cross-sectional SCM was performed on a multilayer structure of *n*-type Si with phosphorus dopant density ranging from 2×10^{17} to 2×10^{19} cm^{-3} using three types of tips. The results show that use of a new metal coated tip is able to produce SCM profile in good agreements with SIMS result, together with correct identification of carrier type. However, a worn tip in loss of metal coating can bring about a misleading SCM signal polarity depending on the local carrier density of the sample as a result of tip depletion. This indicates the possibility of errors in determination of carrier type by SCM for carrier (of same conduction type as the tip, *n* or *p*) concentrations similar and higher than that of Si tip. Actually, the contribution of tip depletion is likely to depend on the nature of the tip (even the extent of the metal coating loss) as well as on the V_{dc}, since it can determine the work point in the C-V curve. Therefore, it is strongly suggested that sufficient carefulness accompany the interpretation of SCM profile, especially where sample is not fully known and SCM data polarity is of significant importance for analysis.

The ZnO staircase structures in this work have some layers with very high dopant concentrations (until 3×10^{20} cm^{-3}). The study above explains well the possible SCM data sign

reversal for them. Keeping this in mind, it would no longer be a problem for the interpretation of our obtained SCM profiles.

3.3.3 SCM on ZnO:Ga staircase samples

Although the primary purpose of employing the staircase samples is to obtain the calibration curve for determination of carrier concentration in ZnO NWs, in fact, SCM (also for SSRM) has never been formally investigated for ZnO on such dedicated structure. So before extracting any calibration curves for analysis on NWs, the staircase samples were studied separately.

Topography and SCM data are collected simultaneously in SCM measurements. Efforts were done to find out a relatively flat area on the cross-section for SCM measurements in order to avoid significant unwanted alteration/variation of SCM signal due to large topographical changes [5]. For the results presented here, the root mean square roughness of the area under investigation is 7.2 nm and 0.9 nm for sample A (topography image in Figure 3.13(a)) and B (Figure 3.14(a)), respectively.

In SCM, capacitance variation due to V_{ac} is detected. Material with fewer carriers depletes more easily and thus will result in a larger capacitance variation/SCM signal. Therefore, a higher Ga concentration should yield a smaller SCM data amplitude. Figure 3.13(b) shows the original SCM data image of the first staircase structure. It can be seen clearly that the doped layers are strongly distinguished from the undoped layers. As the latter result in higher SCM data amplitudes due to their lower carrier concentrations, they thus appear as brighter stripes. Averaged SCM profile of sample A is plotted in Figure4.13(c). On the same graph, the result from the well-established one dimensional dopant profiling technique - SIMS is shown. Comparing the plots of the two techniques, as can be expected, the SCM amplitude experiences a general trend of increase with decreasing Ga density in the doped regions, especially for the first four grown doped layers. This consistency between results from the two techniques demonstrates SCM being able to detect dopant levels as well as their difference in the range from 1.7×10^{18} to 3×10^{20} cm^{-3}. Another point to be noticed is that SCM amplitude profile presents smoother in comparison with abrupt profile of Ga concentration given by SIMS, a phenomenon also arising for SCM on other materials [3, 26]. There can be two reasons. One is related to tip-average effect which is a fundamental spatial resolution limit in cross sectional SCM (typical tip radius for Pt/Ir coated tip is 20~25 nm) [6]. The other corresponds to difference between carrier profile and that of Ga concentration as a result of carrier distribution near the interface of doped and non-intentionally doped layers and the fact that SCM is sensitive to carrier profile rather than dopant profile. The spatial resolution limited by these factors could be largely improved by angle-beveling the sample as demons-

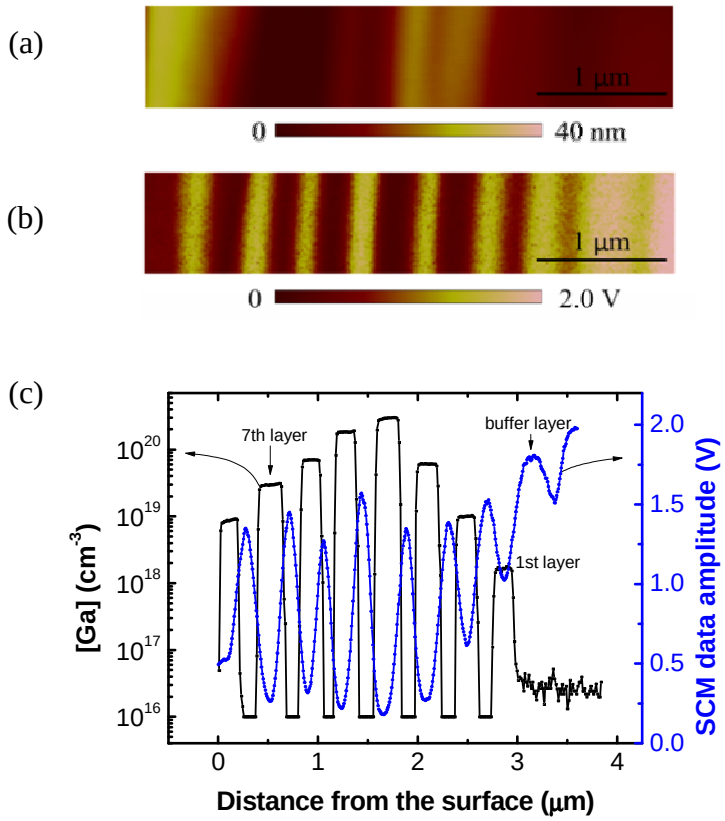

Figure 3.13: (a) Topography image of the area for measurement on sample A. RMS roughness of the area is 7.2 nm. (b) Raw SCM amplitude image of sample A with V_{dc}=0 V, V_{ac}=1000 mV. The top surface is to the left. The dark vertical stripes correspond to doped layers. (c) Processed SCM amplitude data plotted with SIMS data for sample A. Layer with higher Ga concentration yields smaller SCM amplitude.

trated from SCM measurements on ultra-narrow doping profiles and their simulations [7, 37]. The discrepancy of SCM amplitude for the 7th doped layer (as marked in Figure 3.13(c)) can be explained by a smaller contact area of the tip and the sample surface in consequence of a relatively large topography change. Regarding the nid layers, they produce higher SCM amplitudes than all the doped layers, as expected, as a result of their lower carrier concentration which is unknown for exact values but still falls into the dynamic range of SCM. The stripe at about 3.2 μm from the top surface corresponds to the buffer layer with higher SCM amplitude. Besides, the interface between substrate and buffer layer (at the onset of the MBE growth) can be identified by the valley of SCM amplitude profile at 3.38 μm. Unlike those Ga doped layers, this additional decrease of SCM amplitude, indicating an increase of local carrier density, can not be ascribed to Ga donors since SIMS did not detect an obvious increase of Ga impurity. This highly conductive interface is caused by an impurity segregation result at the interface involving donor impurities including Al and Si, which have been revealed by SIMS.

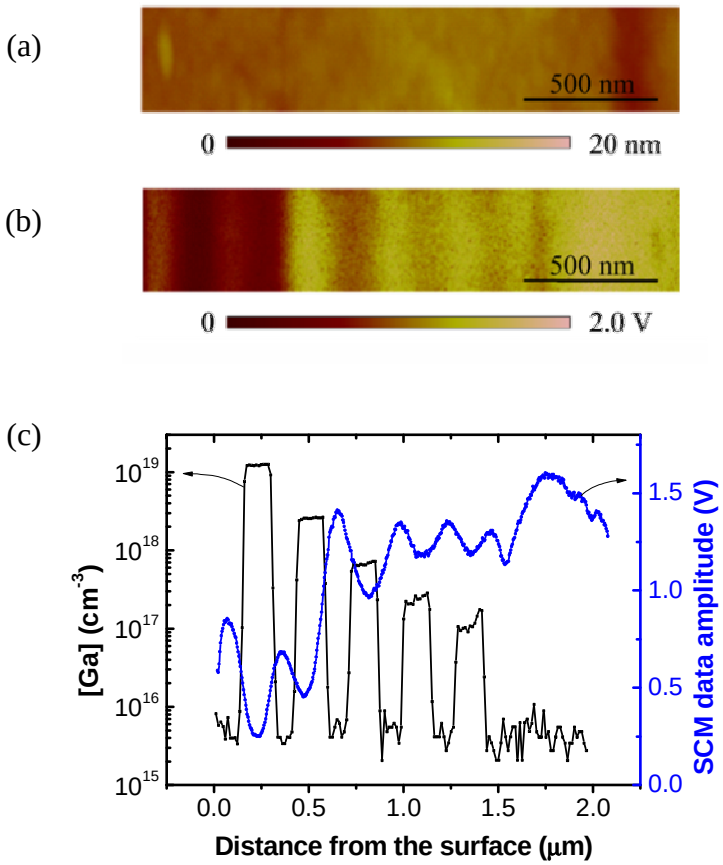

Figure 3.14: (a) Topography image of the area for measurement on sample B. RMS roughness of the area 0.9 nm. (b) Raw SCM amplitude data image of sample B with V_{dc}=0 V, V_{ac}=1000 mV. The top surface is to the left. The relatively dark vertical stripes correspond to doped layers. (c) Processed SCM amplitude data plotted with SIMS data for sample B.

The second staircase structure covers a Ga dopant range between 1.7×10^{17} and 1.2×10^{19} cm^{-3}. The SCM data image is shown in Figure 3.14(b) corresponding to topography area in Figure 3.14(a). The contrast between the doped and nid layers is not as visible as the first structure. There are two reasons: one is that this sample has smaller layer thickness (~140 nm) than that of the previous one (200 nm), this enhances tip-average effect in a visual way making it more difficult to have similar apparent contrasts; Another is that doped layers in this sample have in general lower Ga concentrations compared with the first one, which indicates a smaller difference of carrier concentration with nid layers thus yields a weaker contrast.

Comparison of SCM result with [Ga] profile is shown in Figure 3.14(c), differences between doped layers are still well presented in a way that a higher Ga dopant level causes a lower SCM amplitude for the whole doping range, indicating SCM being able to distinguish doping levels from 1.7×10^{17} to 1.2×10^{19} cm^{-3} for ZnO.

SCS allows detecting capacitance variations with the tip at specific locations on the sample and yields SCM data versus V_{dc} curve. Figure 3.15(a) shows typical SCS curves for the undoped buffer layer and first four grown doped layers in sample A. Layers with fewer Ga

dopants result in larger peak values of the SCM amplitude due to their easier depletion and the undoped buffer layer gives a signal of highest peak of SCM amplitude. SCM data reflect the capacitance variation (d*C*/d*V*) of the tip-sample system, thus integration of SCS result should produce a capacitance-voltage-like curve. This is shown in Figure 3.15(b). The differences in Ga density are also demonstrated by the difference in capacitance between accumulation and deep depletion regimes as well as the slope in depletion regime. What's more, the difference in bias voltage for absolute maximum SCM data, i.e. SCM data peak position, is related to the different flat-band voltages for layers with varying Ga density. This

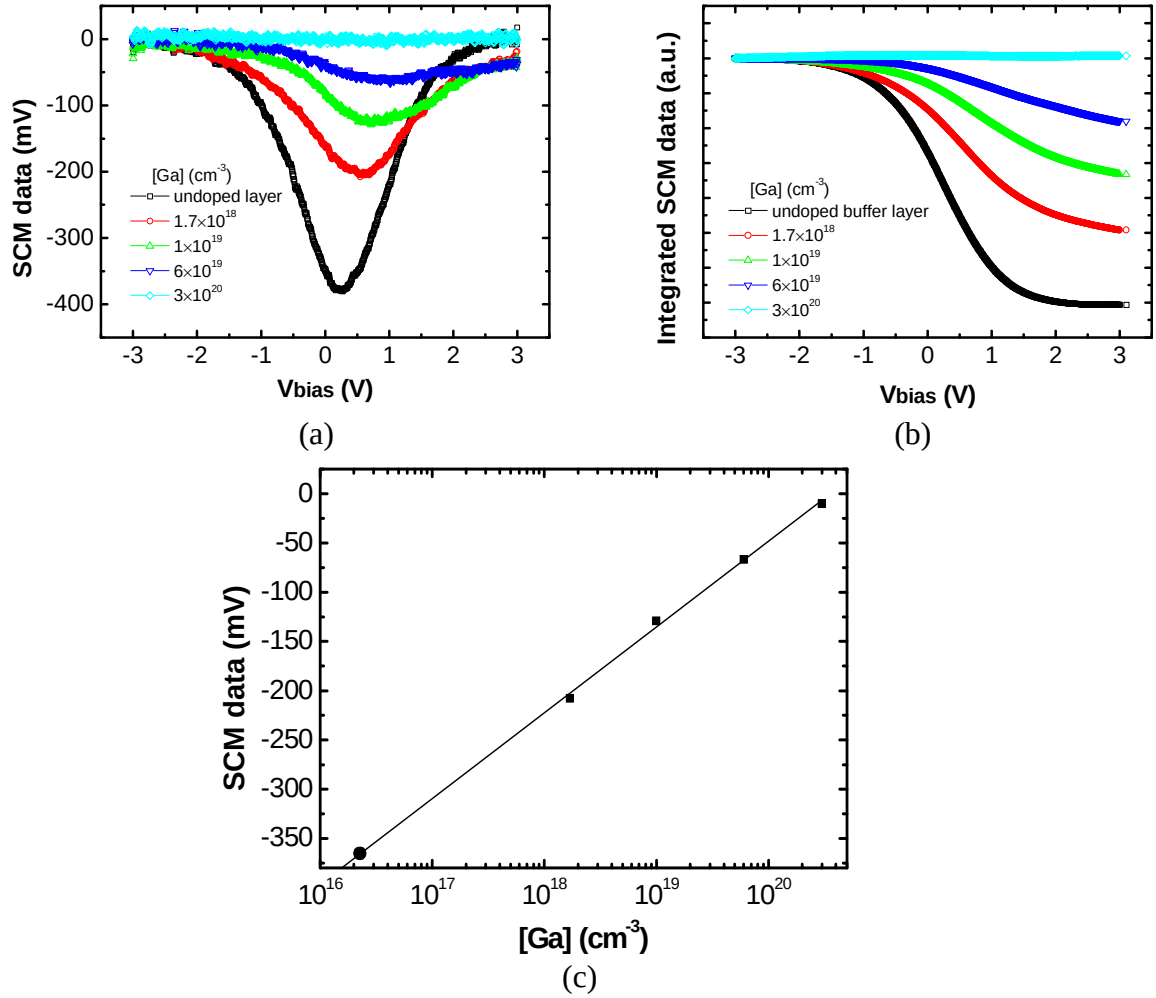

Figure 3.15: (a) Typical SCS curves and (b) their integrations for the first 4 doped layers and undoped buffer layer in sample A. (c) The estimation of residual carrier concentration for buffer layer in sample A. A lower Ga density produces a higher SCM data peak. Also, change of bias voltage for SCM data peak implies flat-band voltage difference among them, which is shown clearly in (b). Notice: for clearness, negative SCM curves are shown to produce integration C-V curves.

fact implies the importance of V_{dc} choice in order to obtain reasonable monotonic SCM data versus carrier concentration behaviour as an improper V_{dc} can lead to unwanted contrast reversal phenomenon [4].

Another fact concerning the integration of SCS curves is their resemblance to that expected for metal-insulator-semiconductor (MIS) configuration instead of Schottky contact. This can be explained by a combination of two factors: first is a thin water film inevitably present on the sample surface and possible $Zn(OH)_2$ formation [38]. This causes that ZnO (and ZnO:Ga) surface remains insulating until a relatively high voltage (>10 V) is used to temporarily remove the surface water layer at the tip-sample junction [39, 40]. Another is that here probe tip of small spring constant (typically 0.2 N/m) was used and the interaction force between the tip and sample was minimized as usually adjusted in SCM measurement to protect probe tip. These facts, together with the amplitude of V_{dc} (less than 2 V) and V_{ac} (1 V) is unlikely to desorb the water layer and possible $Zn(OH)_2$ on the sample surface. So, the surface thin water layer and possible $Zn(OH)_2$ play the role of insulating part in the measurements.

The results above together demonstrate the ability of SCM to detect and distinguish the dopant/carrier densities ranging from 1.7×10^{17} to higher than 10^{20} cm^{-3}, allowing us to draw a conclusion that SCM potentially can be used as an effective tool to quantitatively characterize ZnO based material. To this end, calibration method can be used for fast and easy analysis. This is accomplished by extracting the SCM amplitude~dopant density curves on the basis of SCM results. Two extracted curves for sample A and B are shown in Figure 3.16(a) and 4.16(b), respectively. They are obtained on the basis of SCM results under a series of V_{dc} and extracting the largest SCM amplitude value for each layer.

p-type doping of ZnO has been from the start an intractable challenge to overcome to fundamentally realize its application in (opto-)electronic area [41]. A main step towards *p*-type ZnO is to suppress meaningfully *n* carrier existence usually arising in its non-doped structures. So it is important to have an access to residual carrier concentration of nid ZnO layers. As a first quantitative application of the SCM in this thesis work, we were able to estimate its value for the nid layers of our sample. The SCM amplitude for nid buffer layer is about 1.8 V (in Figure 3.13(c)), this value is out of the calibration curve due to the lower concentration of the buffer layer. Based on a linear fitting of the curve (inset in Figure 3.16(a)), the residual carrier concentration is estimated to be around 10^{16} cm^{-3}. The same analysis can be done using the SCS result of sample A as well as SCM result of sample B, a similar value of residual carrier density is found for the buffer layer (10^{16} and 4×10^{16} cm^{-3} for SCS result of sample A (Figure 3.15(a)) and SCM result of sample B (Figure 3.16(b)), respectively). These results are comparable to that obtained from C-V analysis on an undoped 1 μm thick film grown under same conditions around the same period. This illustrates another advantage of SCM in comparison with conventional C-V measurement for dopant/carrier profiling where a film thick enough is needed to avoid effect of substrate in studying the residual carrier density.

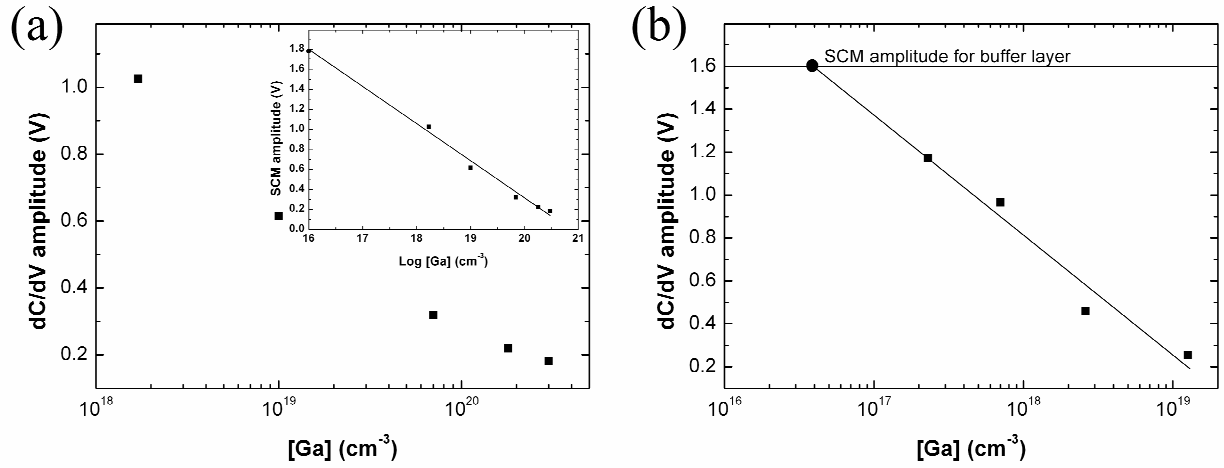

Figure 3.16: Calibration data of SCM amplitude with regards to Ga dopant density established from SCM results of (a) sample A and (b) sample B. Inset in (a) shows estimation of the residual carrier concentration for nid buffer layer in sample A (SCM amplitude being 1.8 V) to be about 10^{16} cm^{-3}. Black solid circle in (b) indicates SCM amplitude value for buffer layer of sample B and its residual carrier concentration is estimated to be around 4×10^{16} cm^{-3}.

For summary of this section, cross-sectional SCM measurements have been performed on ZnO:Ga staircase structures with various Ga concentration from 2×10^{17} to 3×10^{20} cm^{-3}. The consistency between results from SCM and SIMS demonstrates the ability of SCM to distinguish reliably between differently doped layers in ZnO for levels between 1.7×10^{17} cm^{-3} and 3×10^{20} cm^{-3}. Calibration curves are extracted based on SCM results under different V_{dc} and residual *n*-type carrier concentration for the nid buffer layer was estimated to be around 10^{16} cm^{-3}. This study demonstrates the potential of SCM for dopant/carrier characterization for ZnO nanostructures and devices.

3.4 Determination of carrier concentration in NWs

Nid ZnO NWs normally display *n*-type conduction behavior as a result of donors such as zinc interstitials, oxygen vacancies [42], interstitial hydrogen [43], and some other impurities [44]. For the realization of *p*-type doping of ZnO NWs, it is of significant importance to know the residual carrier concentration inside nid grown NWs. In this section, the values of residual carrier densities for the CBD and MOCVD grown NWs are determined through calibration method.

3.4.1 Requirements for calibration analysis: methodology for calibration

The ability of SCM to characterize ZnO NWs in SiO_2 matrix has been demonstrated in section 3.2, where the NWs were well detected and corresponding SCM data signal can be obtained.

For quantitative analysis, calibration dataset is required. To this end, two ZnO:Ga staircase structures have been developed and SCM investigation on them has shown a monotonic dependence of SCM signal on the dopant concentration, indicating that they can serve as calibration samples for the quantitative determination of the carrier concentration for the NWs. However, there are still some basic requirements that should be satisfied before performing a calibration process because SCM is extremely sensitive to many factors, such as system configuration, environment change and tip difference.

Firstly, since parasitic capacitance is a part of the electrical measurement system [28] and has an effect on the capacitance detection system, the samples to be measured should be put in a similar (if not the same) position on the *x*-*y* stage with respect to the probe tip. In fact, it was found that the sample positioned at the edge of the stage should be preferred to minimize the parasitic capacitance between the SCM electrical module and the *x*-*y* stage [45]. Additionally, in our experiments, the measurements are done on the surface of the NWs sample in comparison with the cross sections of the staircase structure. In order to create a similar measurement configuration, a metallic sample holder was intentionally fabricated to reproduce the tip-sample *x*-*y* stage scene as much as possible. In the end, it is possible to reach a similar SCM capacitance sensor sensitivity for measurement on NWs sample and the staircase sample, as shown in Figure 3.17.

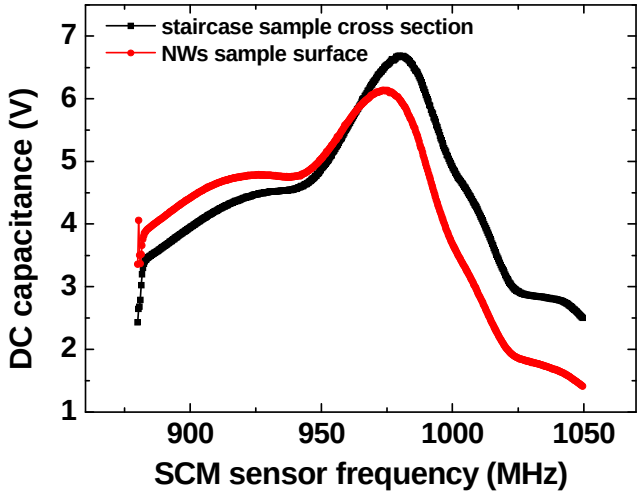

Figure 3.17: An example of the SCM sensor output as a function of frequency. Similar sensitivity of the capacitance sensor is observed for the two configurations in a certain range (around 1000 MHz).

Secondly, since it is normally impossible to perform measurements on different samples in a single tip scan (which would be far easier and more reliable for quantitative analysis), the measurements on the calibration sample and the studied sample of interest (NWs in this case) should be done one after another without any unnecessary delay in the same session using the identical probe tip. This arrangement intends to avoid any unwanted impact from the environment change and the system adjustment (laser alignment for example). Besides, the

use of exactly the identical tip is of significant importance because the tip plays an important role in the tip-sample capacitance formation and possible difference from tip to tip influences considerably the final SCM signal. Also, another reason why no delay is preferred between measurements on different samples is to avoid any evolution of the tip itself, especially tip wear, which is a problem encountered in almost all contact mode SPM measurements.

Thirdly, measurement condition should be kept in terms of system parameters, of which the most important are the amplitude and frequency of V_{ac} as well as capacitance sensor frequency. In an open loop measurement, the tip-sample capacitance variation is supposed to have a monotonic dependence on local carrier concentration for certain amplitude of V_{ac}, so V_{ac} has to be maintained for reasonable calibration performance. Maintenance of sensor frequency is to assure a similar sensitivity to the tip-sample capacitance change.

Finally is the choice of V_{dc}. To produce a maximum V_{ac}-induced variation of the tip-sample capacitance, SCM needs to operate in the depletion regime, the region corresponding to the largest slope in C-V curve and reflecting the flat band voltage. However, usually, the Fermi level differs for layers with different doping concentration thus leading to different flat band voltage for them with the tip. Therefore, the choice of V_{dc} matters to a large extent to yield reasonably a monotonic dependence of SCM signal on doping level. A wrong V_{dc} has been identified as one major cause of the contrast reversal (SCM signal amplitude increases with carrier density instead of decreasing) phenomenon in SCM. R. Stephenson and J. Smoliner *et al* [29, 46] studied this effect and suggested to use the V_{dc} corresponding to maximal SCM signal for the layer with lowest carrier concentration for SCM measurement to avoid contrast reversal. This is enough for qualitative analysis. Nevertheless, for quantitative analysis, it is no longer enough to just obtain a reasonable contrast for extracting the calibration curve, but maximal SCM signal values for each doping level should be utilized. For this reason, in our experiment, in order to construct a more reasonable calibration dataset, a series of V_{dc} are applied to obtain the maximal SCM signal value for each doping level as well as the NWs under investigation.

All the strategies above are intended to bring as much sense as possible for calibration process and they are supposed to be satisfied before any calibration analysis is conducted. Even so, there are still other uncontrollable factors that may have an impact on the measurement, such as topography change, possible tip wear depletion and system noise. In this work we would not deal with these potential problems in detail but instead focus on the calibration process for NWs. For all the results discussed below, these primary requirements have been satisfied during the SCM measurements. It is worth noting that while the laser light (wavelength of 670 nm corresponding to photon energy of 1.85 eV) in the AFM system has been found to play an important role in SCM in terms of minority generation on Si material (band gap 1.12 eV), it

doest not have an as large impact in ZnO due to its wide band gap (3.37 eV).

3.4.2 Calibration for NWs by SCM

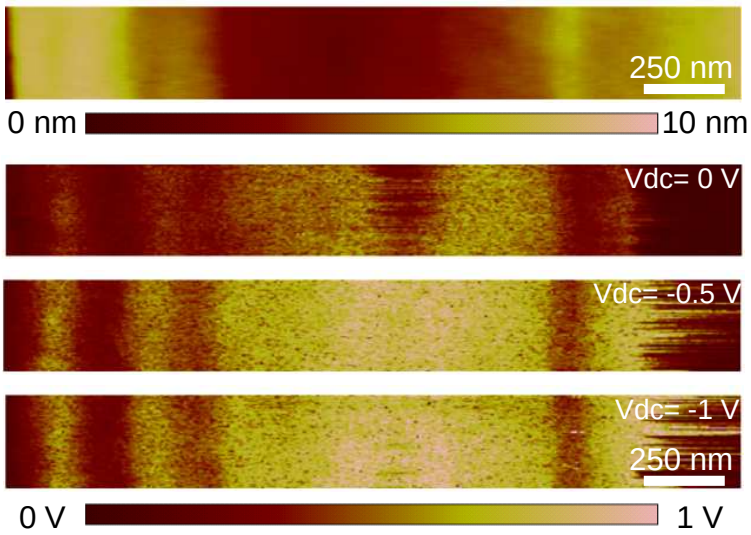

Figure 3.18: A group of SCM results on the second staircase structure with three V_{dc}: 0 V, -0.5 V, -1 V. Corresponding topography image is on the top. It is seen in general -0.5 V and -1 V V_{dc} produce brighter SCM data image indicating larger SCM data signal. Pt/Ir coated tip and 1000 mV V_{ac} were used. Sample surface is to the left.

Figure 3.18 shows a group of SCM results on the second staircase sample under three bias voltages, i.e. 0 V, -0.5 V, -1 V. They were collected continuously in the same area on the sample's cross section with an RMS roughness and height range of 1.97 nm and 6.88 nm, respectively. From the SCM data images, the difference of the SCM signal intensity as well as the contrast between layers with different doping levels can be observed. At the same time, evolution of the SCM signal intensity and relative contrast with V_{dc} can be noticed. This can be more clearly seen from the processed SCM data profile in Figure 3.19(a). Evidently, V_{dc}=-0.5 V and -1 V give larger SCM data for all the layers. Here no more V_{dc} is shown because a decrease of SCM data was noticed when trying another value and no 2D image was collected. This is under the consideration that as few scans as possible should be carried out between the different samples, in order to diminish the chance of tip wear and consequent change of tip geometry. From the SCM profiles, maximal SCM data value for each doping level can be extracted and be used to construct the calibration dataset in form of SCM data versus dopant density curve shown in Figure 3.19(b). This calibration curve is the base of

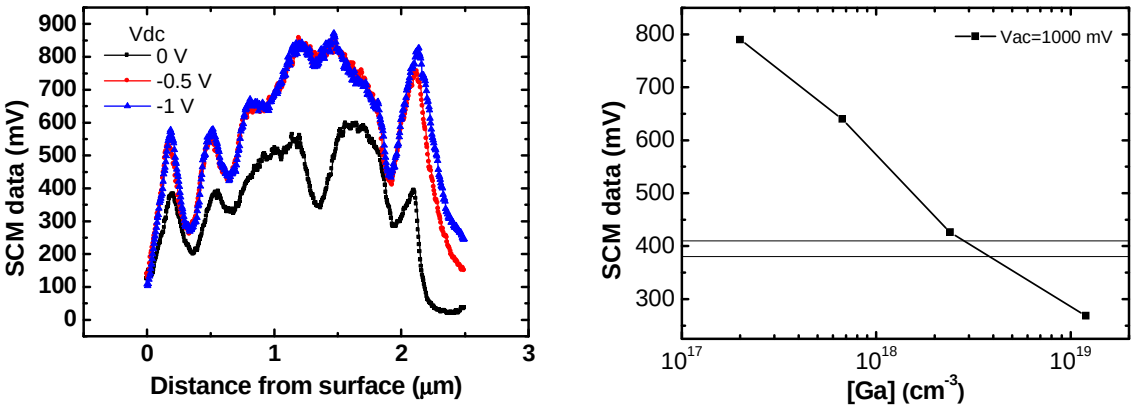

(a) (b)

Figure 3.19: (a) Averaged SCM data profiles corresponding to the three V_{dc} in Figure 3.18 to better present the influence of V_{dc} to the SCM data profile. Clearly, -0.5 V and -1 V V_{dc} produce larger SCM data for each doping level in the structure. (b) Largest SCM data values for each doping level were extracted from SCM data profiles to build the calibration curve. Two horizontal lines at 380 and 410 mV indicate the largest SCM data range for the NWs.

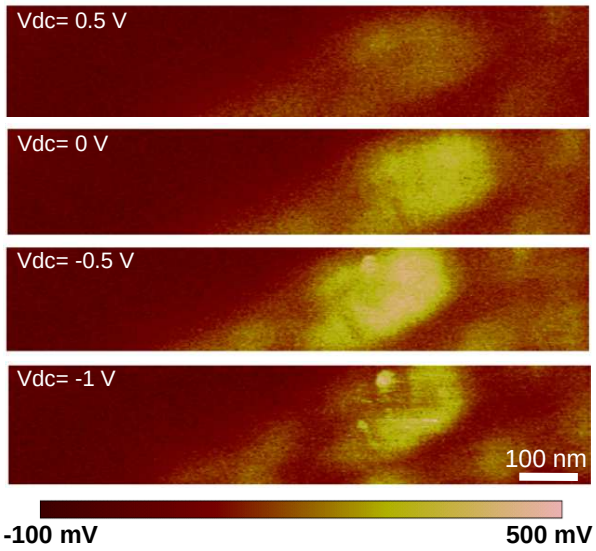

Figure 3.20: SCM data images of the CBD grown NWs sample under four V_{dc}: 0.5 V, 0V, -0.5 V, -1 V. Largest SCM data values in the range 300-400 mV were obtained at -0.5 V_{dc}. Measurements were done in the same session as the second staircase structure and identical tip together with same V_{ac} (1000 mV) were maintained. The spot which is most clearly seen in V_{dc}=-1 V image was due to topography change.

quantitative analysis for other structures.

Right after measurements on staircase sample, the CBD grown NWs sample was measured with the same system configuration. The results are displayed in Figure 3.20. Here, the largest SCM data was obtained under V_{dc}=-0.5 V and has a value range 380~410 mV. Through its comparison with the just established calibration curve, carrier concentrations between 2.9~3.9×10^{18} cm^{-3} is estimated for the investigated NWs.

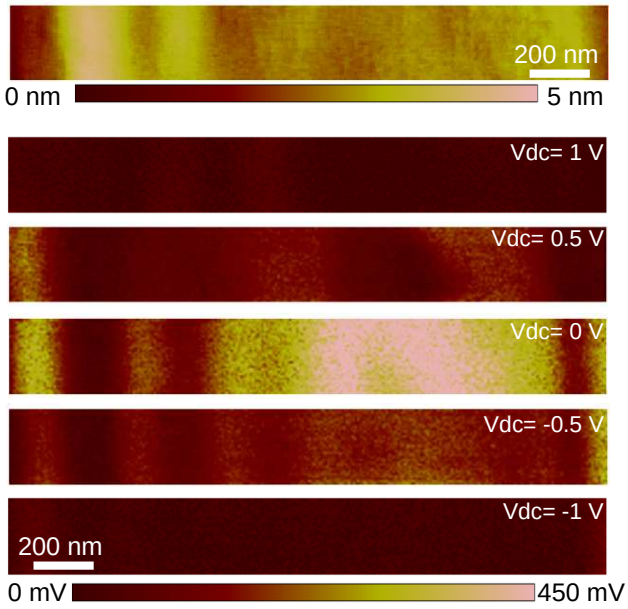

Figure 3.21: SCM results on the second staircase structure with five V_{dc}: 1 V, 0.5 V, 0 V, -0.5 V, -1 V. Corresponding topography image is on the top. Choice of V_{dc} affects the SCM image contrast and 0V V_{dc} produces brightest SCM data image. No-metal coated tip and 1000 mV V_{ac} were used. Sample surface is to the left.

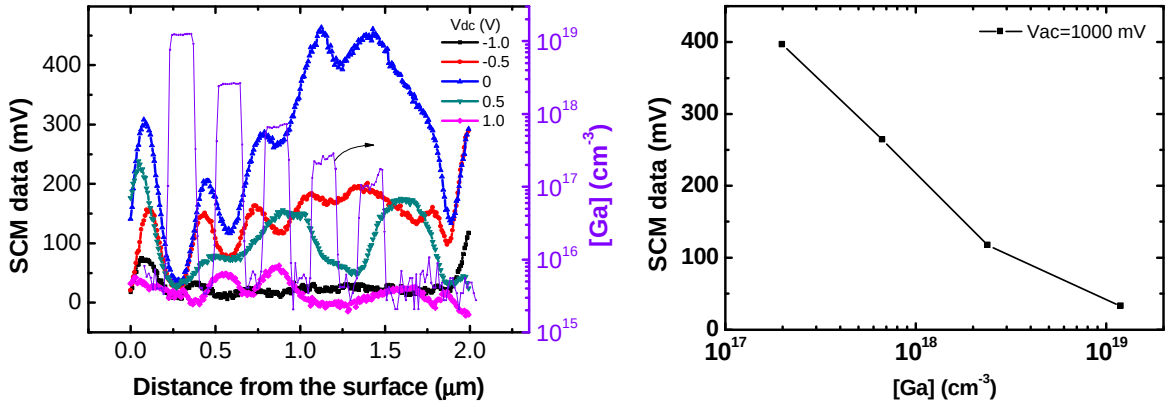

Figure 3.22: (a) Averaged SCM profiles under different V_{dc} corresponding to the results in Figure 3.21. Profile of largest SCM data was obtained under 0 V V_{dc}. (b) Established calibration curve from SCM profile at 0 V V_{dc}.

Another result is shown in Figure 3.21. The scanned region has an RMS roughness value of 0.57 nm and a height range of 4 nm resulted from simple cleavage. A tip without metal coating was used and five V_{dc} from -1 V to 1 V was applied. From the SCM data profiles as shown in Figure 3.22 (a), it is found that largest SCM data for almost all the layers was obtained at 0 V V_{dc}. Not surprisingly, a non-proper V_{dc} (1 V or 0.5 V) would destroy the monotonically increase of SCM data with decreasing doping level, demonstrating the importance of V_{dc} for correct analysis. From the SCM data profile corresponding to 0 V V_{dc},

the calibration curve is extracted and shown in Figure 3.22(b).

Subsequent measurements on the two NWs samples were carried out under several V_{dc} and the results with largest SCM data are shown in Figure 3.23. From the SCM images, the largest SCM data for CBD and MOCVD grown NWs are identified to be 100~120 mV and 120~140 mV (a little core-shell contrast), respectively. Then by calibration process, the carrier concentration inside the CBD and MOCVD grown NWs in this study are estimated to be 2.3~3.2×10^{18} cm^{-3} and 2~2.3×10^{18} cm^{-3}, respectively. Notice that the estimated residual carrier concentration for CBD grown NWs is on the same order of magnitude to that from the result presented before.

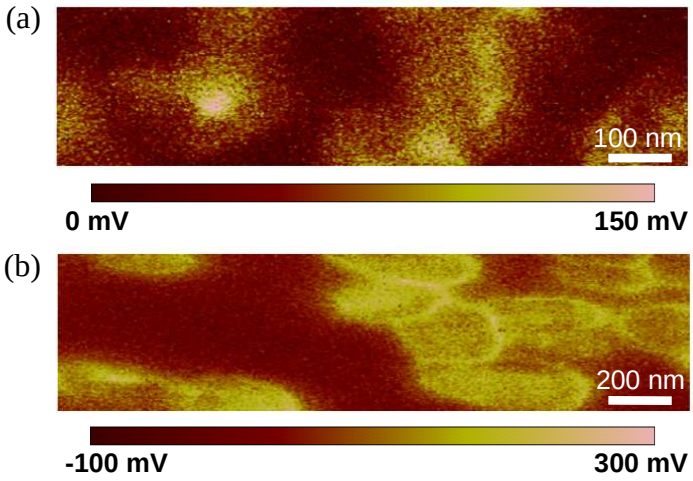

Figure 3.23: SCM data images corresponding largest SCM data values of (a) CBD grown NWs sample and (b) MOCVD grown NWs sample. SCM data for the two NWs sample are 100~120 mV and 120~140 mV, respectively.

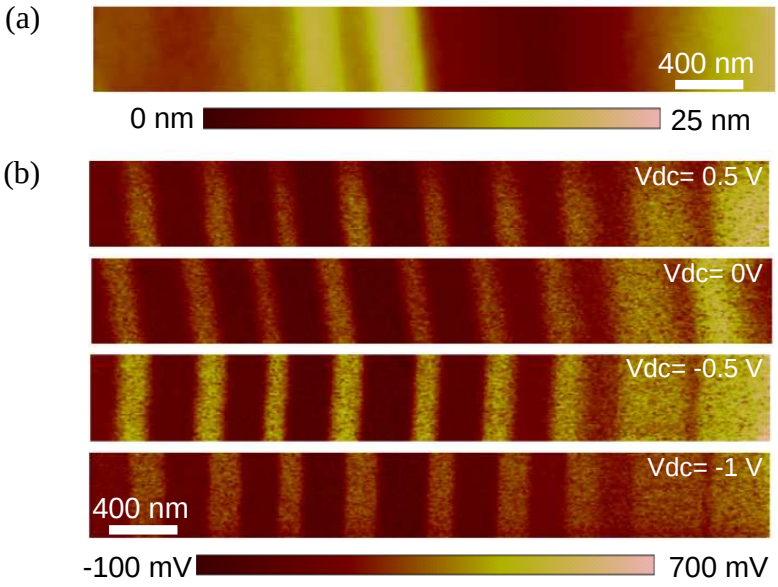

Figure 3.24: (a) AFM topography image. (b) SCM images on the first staircase structure with four V_{dc}: 0.5 V, 0 V, -0.5 V, -1 V. Brightest SCM data image correspond to -0.5 V V_{dc}. Co/Cr coated tip and 1000 mV V_{ac} were used. Sample surface is to the left.

One more result is shown in Figure 3.24. In this case, the first staircase structure was used for calibration purpose. RMS roughness and height range of the measured region are 4.7 nm and 18 nm, respectively. In this case, another metal coated tip (BESP tip from Bruker with Co/Cr coating) was used and it proved to work well. The layers with different Ga doping levels are well resolved in SCM data image which also exhibits a dependence on the applied V_{dc}. From the processed SCM data profiles (Figure 3.25 (a)), largest SCM data values corresponding to each Ga density can be extracted to build the calibration curve in Figure 3.25 (b). It is from this curve that a monotonic dependence of SCM data on the Ga doping level is clearly demonstrated.

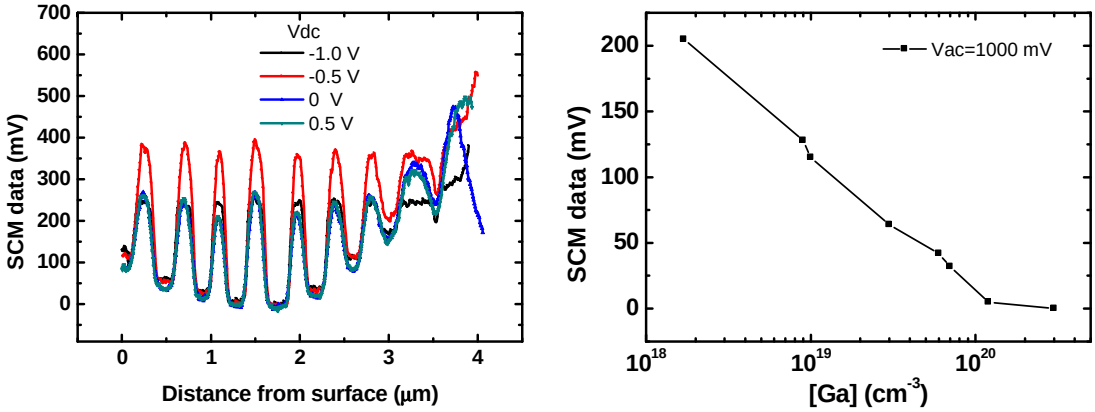

(a) (b)

Figure 3.25: (a) Averaged SCM profiles under different V_{dc} corresponding to the results in Figure 3.24. Largest SCM data profile was obtained under -0.5 V V_{dc}. (b) Established calibration curve from SCM profile at -0.5 V V_{dc}.

Then SCM was performed on the MOCVD grown NWs sample (Figure 3.26). A relatively small area was scanned to minimize any possible significant tip wear. It was found the SCM data signal was maximized with -1 V V_{dc} applied on the sample and has a value about 200 mV for the core and 350 mV for the shell of the NW. According to the calibration curve, carrier concentrations of 2×10^{18} and 7×10^{16} cm^{-3} for the core and the shell of the NW are estimated. This high residual carrier density is likely due to the diffusion of Al from the sapphire substrate [44] and/or the presence of hydrogen in the growth chamber and its possible incorporation during the growth, which can act both as shallow donors.

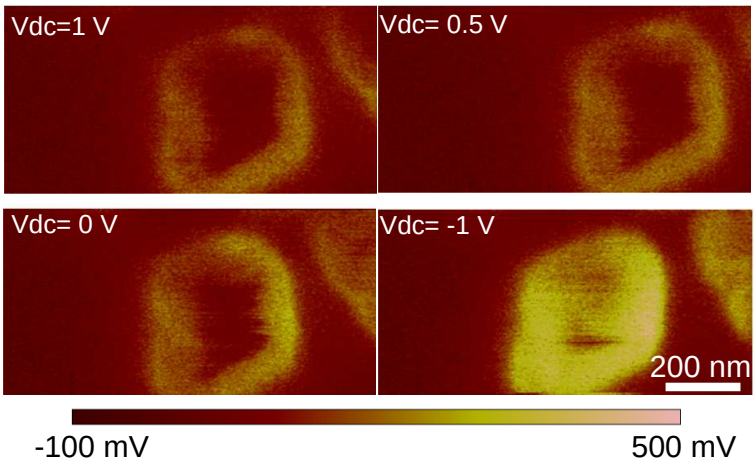

Figure 3.26: SCM data images under different V_{dc} of MOCVD grown NWs sample. SCM data signal was maximized with -1 V V_{dc}, in which case, SCM data values of 200 mV and 350 mV for the core and the shell of the NW, respectively, were obtained.

To conclude this part, measurements on the staircase structure and on the NWs sample were carried out satisfying the conditions required for calibration analysis. Then from the obtained SCM data images under a series of V_{dc}, calibration data/curve was established and calibration process was performed. As results, carrier concentrations were estimated to be about $3\pm1\times10^{18}$ cm^{-3} for the CBD and $2\pm0.3\times10^{18}$ for the MOCVD grown NWs.

3.4.3 Calibration for NWs by SCS

Previous section reported the results about determination of carrier concentrations inside the NWs sample through calibration method on base of SCM images. In addition, the quantitative analysis through calibration method can also be realized by SCS measurement. To do this, SCS curves on layers of different but known doping levels are collected and utilized to construct the calibration curve, then the SCS result on NWs are calibrated for quantification purpose. Compared with SCM, no tip scan is performed in SCS except when the tip needs to be relocated to another target position. This is likely to alleviate the tip wear problem.

Figure 3.27 shows the obtained SCS curves on the doped layers of the second staircase sample. Here various V_{ac} (250 mV, 500 mV, 1000 mV and 2000 mV) were applied for each layer to acquire the SCS curves. For each applied V_{ac}, the SCM data value experiences an evolution with the scan of V_{dc} and a larger V_{ac} leads to a higher SCM data peak in consequence of a wider modulated range in the C-V curve. Also, the V_{dc} position for SCM data peak is observed to be near 0 V, which is consistent with the optimal V_{dc} in normal SCM measurement. To establish a calibration curve, dependence of SCM data peak on the doping level is needed. This can be clearly seen in Figure 3.28, where SCM curves under same V_{ac} for different doping layers are depicted. On contrast to SCM measurement results under a

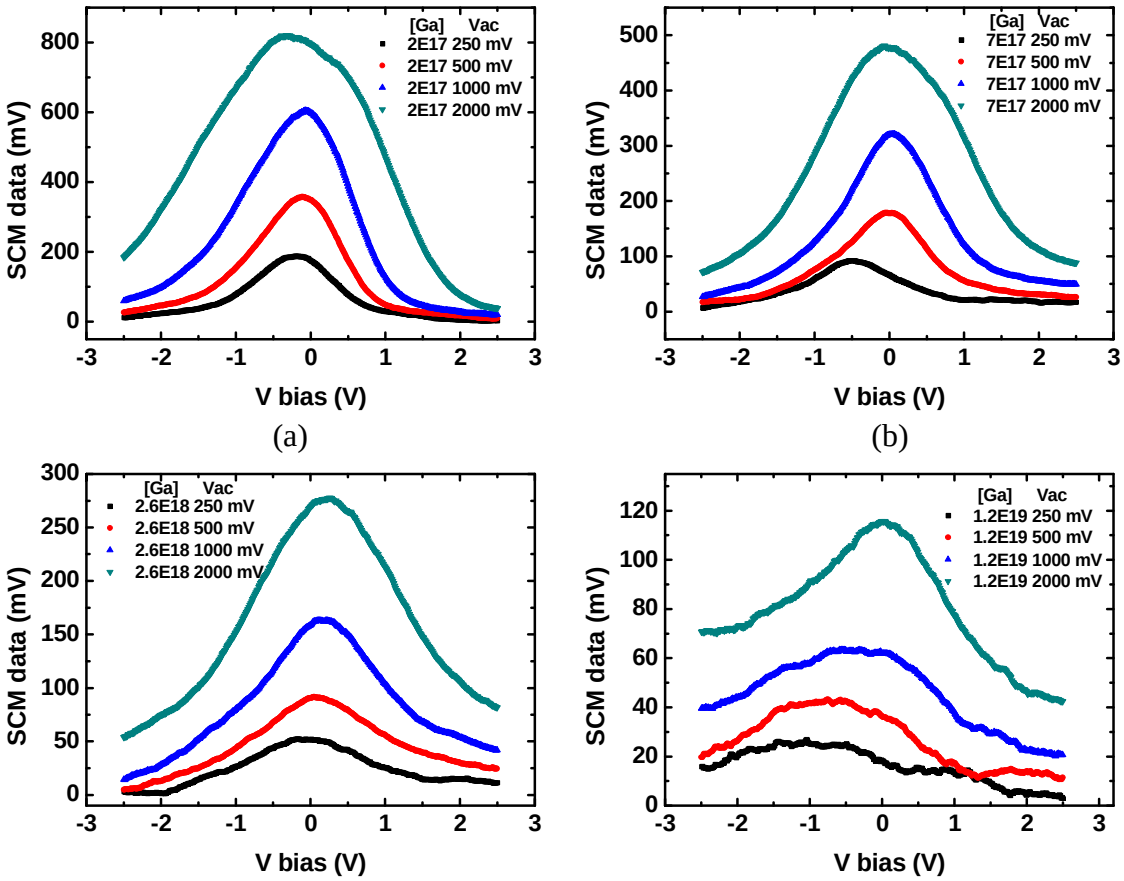

Figure 3.27: SCS curves on the four Ga doped layers with different V_{ac} amplitudes. Each figure corresponds to a certain layer. Ga density is indicated in each figure (unit: cm^{-3}). For each layer, a larger SCM data peak value is produced with a larger V_{ac}. Again, the V_{dc} position for SCM data peak is close to 0 V, consistent to the results from SCM measurements. Here, an ESP tip without metal coating was used with a smaller tip radius than the metal coated tip.

series of V_{dc}, SCS curves are more precise and appreciated for calibration curve construction. Calibration curves for each applied V_{ac} are presented in Figure 3.29(a). All of them have the potential for calibration analysis of other structures and it would be possible to compare their performance in the calibration process.

Under the same system condition, SCS curves were collected on the CBD grown NWs sample with the tip in contact with a NW under the same V_{ac} as the staircase sample (Figure 3.29(b)). Then SCM data peak values corresponding to each V_{ac} are extracted. They are indicated in Figure 3.29(a) as horizontal lines and compared with the respective calibration curve.

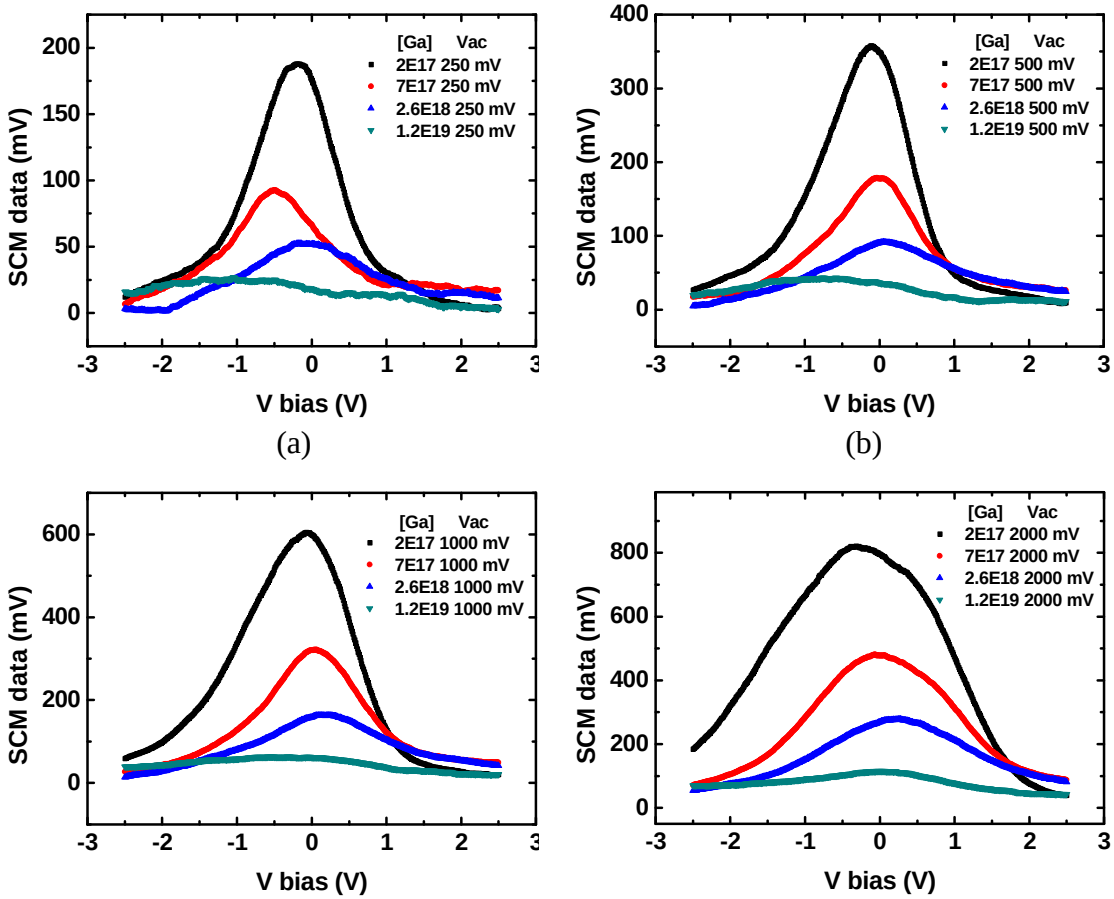

Figure 3.28: SCS curves on the four Ga doped layers with different V_{ac} amplitudes. Each figure corresponds to a certain used V_{ac}. Ga density is indicated in each figure (unit: cm^{-3}). For each V_{ac}, dependence of SCM data peak value on the Ga dopant concentration is seen and a calibration curve can be extracted.

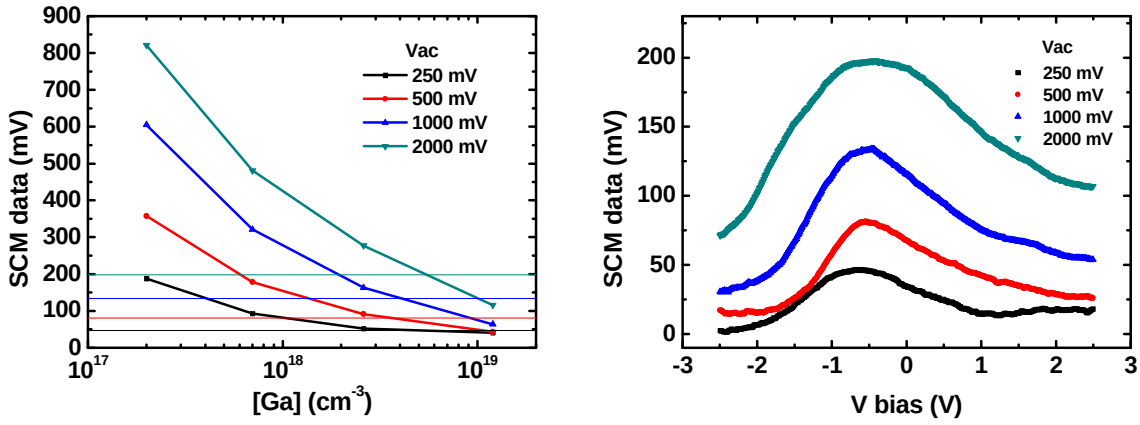

Figure 3.29: (a) Extracted calibration curves for each used V_{ac} and their comparison with corresponding SCM data value for the CBD grown NWs. Position of intersection point in X axis indicates the estimated value of carrier concentration in the NW. (b) SCS curves for a CBD grown NW collected in the same session. Conditions for the staircase sample were maintained.

Table 3.1: Estimated carrier concentration N_s for CBD grown NWs at different V_{ac} from calibration curve established based on SCS curves on the second staircase samples.

V_{ac} (mV)	250	500	1000	2000
Estimated Ns (cm^{-3})	5.3×10^{18}	3.5×10^{18}	4.0×10^{18}	5.5×10^{18}

Calibration results are listed in Table 3.1. It can be seen that similar results of carrier concentration for the NW are obtained except the case of 2000 mV V_{ac}. It is because under a larger V_{ac}, a wide range in the related C-V curve is detected, but the slope of the C-V does not maintain and can even lower to near 0 in the accumulation or deep depletion region. This is more the case for a lightly doping level, where a smaller voltage range is needed for the transition from accumulation to deep depletion regime. In other words, in SCM a relatively larger V_{ac} is required to achieve reliable signal to noise ratio, so even with V_{dc} equal to the flat band voltage, twice a V_{ac} is unlikely to double the SCM data signal, especially when large V_{ac} is used. This is exactly what we can see in Figure 3.29(b). For this reason, not too large V_{ac} is supposed to be used for quantitative analysis in SCM because it tends to finally overestimate the carrier concentration of the sample in study. Another reason for making use of not too large a V_{ac} is that the response area in the sample is enlarged when increasing the applied V_{ac}, this will enhance the tip-average effect and is better to be avoided for analysis of carrier profile with variation in a short distance. In our case, the similar values of estimated carrier concentration indicate the reasonability of using 1000 mV V_{ac}. The calibrated results for the CBD grown NW is also in good agreement with that obtained from normal SCM results.

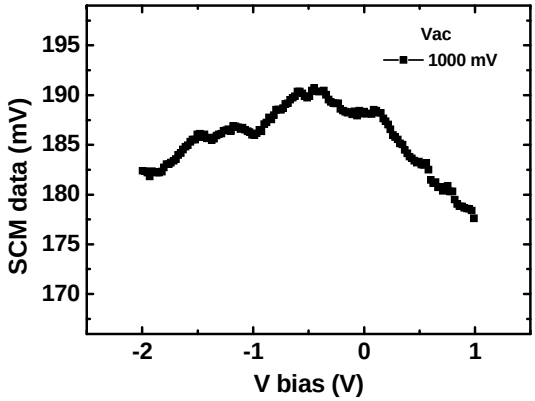

Figure 3.30: SCS curve on MOCVD grown NW with V_{ac}=1000 mV. An SCM data peak of 190 mV is observed.

SCS on the MOCVD NWs sample was also performed with a 1000 mV V_{ac} (Figure 3.30). An SCM data peak value of 190 mV was observed. This value, through its comparison with the calibration curve, indicates a carrier density inside the measured NW of about 2×10^{18} cm^{-3}, also in agreement with the result before.

3.5 Conclusion

This chapter reported the study of SCM for determination of carrier concentrations inside the NWs through calibration approach, which can be generalized to the study of other structures.

SCM was performed on the ZnO NWs structures after the sample preparation process. It was shown that the NWs in the SiO_2 matrix can be easily detected by SCM due to the V_{ac}-induced capacitance variation.

However, the results on the ZnO NWs alone are not enough for a quantitative analysis of the carrier concentration information of the NWs, which is the main objective of this study. To solve this problem, we employed calibration method to convert the SCM data for the NWs into carrier density.

Therefore, two ZnO:Ga multilayer staircase structures were grown by MBE. Ga was chosen as dopant because it acts an effective donor in ZnO. The two structures cover a Ga doping range from 1.7×10^{18} to 3×10^{20} cm^{-3} and from 1.7×10^{17} to 1.2×10^{19} cm^{-3}, separately. Before the calibration process, SCM was investigated on the two staircase sample. It was demonstrated that SCM is able to distinguish different doping levels for ZnO and a monotonic dependence of SCM data on the Ga density was observed for both samples. In addition, for a better interpretation of the SCM results, which in some cases give non-expected opposite polarity of SCM data signal, tip depletion effect was examined with help of a P doped Si multilayer structure. Obtained results show that a worn tip in loss of metal coating can bring about a misleading SCM signal polarity depending on the local carrier density of the sample as a result of tip depletion. Incorrect conclusion for conduction type may be drawn for carrier (of same conduction type as the tip, *n* or *p*) concentrations similar and higher than that of the used tip. Therefore, it is strongly suggested that great care be taken for the interpretation of SCM profile, especially where the sample is not fully known.

For a reasonable calibration of the SCM data for NWs, some basic requirements were clearly put forward for measurements on calibration sample (ZnO:Ga staircase structure here) and samples of interest (ZnO NWs here), including a similar SCM sensor sensitivity, measurements being done in the same session under same system conditions using the identical tip and extraction of optimal SCM data from SCM profiles collected under a series of V_{dc}. Finally, from the SCM measurements satisfying these requirements, calibration curves were constructed from results on staircase samples and the results on NWs were calibrated. Carrier concentrations about $3\pm1\times10^{18}$ cm^{-3} for the CBD grown NWs and $2\pm0.3\times10^{18}$ for the MOCVD grown NWs were estimated.

Besides calibration realization on the base of SCM measurements, SCS was also used to achieve this goal. From largest SCM data in SCS curves on different doping levels, calibration

curve was established and similar values of carrier concentration for the studied NWs were estimated, consistent with normal SCM measurements.

References:

[1] Williams, C. C. (1999). Two-dimensional dopant profiling by scanning capacitance microscopy. Annual review of materials science, 29(1), 471-504.

[2] Duhayon, N., Clarysse, T., Eyben, P., Vandervorst, W., & Hellemans, L. (2002). Detailed study of scanning capacitance microscopy on cross-sectional and beveled junctions. Journal of Vacuum Science & Technology B, 20(2), 741-746.

[3] Giannazzo, F., Raineri, V., Mirabella, S., Impellizzeri, G., Priolo, F., Fedele, M., & Mucciato, R. (2006). Scanning capacitance microscopy: Quantitative carrier profiling down to nanostructures. Journal of Vacuum Science & Technology B, 24(1), 370-374.

[4] Duhayon, N., Eyben, P., Fouchier, M., Clarysse, T., Vandervorst, W., Álvarez, D., *et al*. (2004). Assessing the performance of two-dimensional dopant profiling techniques. Journal of Vacuum Science & Technology B, 22(1), 385-393.

[5] Oliver, R. A. (2008). Advances in AFM for the electrical characterization of semiconductors. Reports on Progress in Physics, 71(7), 076501.

[6] McMurray, J. S., Kim, J., & Williams, C. C. (1997). Quantitative measurement of two-dimensional dopant profile by cross-sectional scanning capacitance microscopy. Journal of Vacuum Science & Technology B, 15(4), 1011-1014.

[7] Giannazzo, F., Goghero, D., Raineri, V., Mirabella, S., & Priolo, F. (2003). Scanning capacitance microscopy on ultranarrow doping profiles in Si. Applied physics letters, 83(13), 2659-2661.

[8] De Wolf, P., Geva, M., Hantschel, T., Vandervorst, W., & Bylsma, R. B. (1998). Two-dimensional carrier profiling of InP structures using scanning spreading resistance microscopy. Applied physics letters, 73(15), 2155-2157.

[9] Sumner, J., Oliver, R. A., Kappers, M. J., & Humphreys, C. J. (2008). Assessment of the performance of scanning capacitance microscopy for n-type gallium nitride. Journal of Vacuum Science & Technology B, 26(2), 611-617.

[10] Yin, H., Li, T., Wang, W., Hu, W., Lin, L., & Lu, W. (2009). Scanning capacitance microscopy investigation on InGaAs/InP avalanche photodiode structures: Light-induced polarity reversal. Applied Physics Letters, 95(9), 093506.

[11] Douheret, O., Maknys, K., & Anand, S. (2004). Scanning capacitance microscopy investigations of InGaAs/InP quantum wells. Thin solid films, 459(1), 67-70.

[12] Giannazzo, F., Musumeci, P., Calcagno, L., Makhtari, A., & Raineri, V. (2001). Carrier concentration profiles in 6H-SiC by scanning capacitance microscopy. Materials Science in Semiconductor Processing, 4(1), 195-199.

[13] Giannazzo, F., Raineri, V., Mirabella, S., Impellizzeri, G., & Priolo, F. (2006). Drift mobility in quantum nanostructures by scanning probe microscopy. Applied physics

letters, 88(4), 043117.

[14] Özgür, Ü., Alivov, Y. I., Liu, C., Teke, A., Reshchikov, M., Doğan, S., *et al*. (2005). A comprehensive review of ZnO materials and devices. Journal of applied physics, 98(4), 041301.

[15] Latu-Romain, E., Gilet, P., Chevalier, N., Mariolle, D., Bertin, F., Feuillet, G., ... & Chelnokov, A. (2010). Surface-induced p-type conductivity in ZnO nanopillars investigated by scanning probe microscopy. Journal of Applied Physics, 107(12), 124307.

[16] Krtschil, A., Dadgar, A., Oleynik, N., Bläsing, J., Diez, A., & Krost, A. (2005). Local p-type conductivity in zinc oxide dual-doped with nitrogen and arsenic. Applied Physics Letters, 87(26), 2105.

[17] Wang, B., Min, J., Zhao, Y., Sang, W., & Wang, C. (2009). The grain boundary related p-type conductivity in ZnO films prepared by ultrasonic spray pyrolysis. Applied Physics Letters, 94(19), 2101.

[18] Huang, Y., Williams, C. C., & Smith, H. (1996). Direct comparison of cross-sectional scanning capacitance microscope dopant profile and vertical secondary ion-mass spectroscopy profile. Journal of Vacuum Science & Technology B, 14(1), 433-436.

[19] Kopanski, J. J., Marchiando, J. F., & Lowney, J. R. (1996). Scanning capacitance microscopy measurements and modeling: Progress towards dopant profiling of silicon. Journal of Vacuum Science & Technology B, 14(1), 242-247.

[20] Huang, Y., Williams, C. C., & Wendman, M. A. (1996). Quantitative two-dimensional dopant profiling of abrupt dopant profiles by cross-sectional scanning capacitance microscopy. Journal of Vacuum Science & Technology A, 14(3), 1168-1171.

[21] Ko, H. J., Chen, Y. F., Hong, S. K., Wenisch, H., Yao, T., & Look, D. C. (2000). Ga-doped ZnO films grown on GaN templates by plasma-assisted molecular-beam epitaxy. Applied Physics Letters, 77(23), 3761-3763.

[22] Pearson, W. B. (1972). Crystal chemistry and physics of metals and alloys, Wiley, New York, 76

[23] Kato, H., Sano, M., Miyamoto, K., & Yao, T. (2002). Growth and characterization of Ga-doped ZnO layers on a-plane sapphire substrates grown by molecular beam epitaxy. Journal of Crystal Growth, 237, 538-543.

[24] Sadofev, S., Kalusniak, S., Schäfer, P., & Henneberger, F. (2013). Molecular beam epitaxy of n-Zn(Mg)O as a low-damping plasmonic material at telecommunication wavelengths. Applied Physics Letters, 102(18), 181905.

[25] Taïnoff, D., Al-Khalfioui, M., Deparis, C., Vinter, B., Teisseire, M., Morhain, C., & Chauveau, J. M. (2011). Residual and nitrogen doping of homoepitaxial nonpolar m-plane ZnO films grown by molecular beam epitaxy. Applied Physics Letters, 98(13), 131915.

[26] Sumner, J., Oliver, R. A., Kappers, M. J., & Humphreys, C. J. (2008). Assessment of the performance of scanning capacitance microscopy for n-type gallium nitride. Journal of Vacuum Science & Technology B, 26(2), 611-617.

[27] Buh, G. H., Kopanski, J. J., Marchiando, J. F., Birdwell, A. G., & Kuk, Y. (2003). Factors influencing the capacitance-voltage characteristics measured by the scanning capacitance microscope. Journal of applied physics, 94, 2680-2685.

[28] Kopanski, J. J., Marchiando, J. F., Rennex, B. G., Simons, D., & Chau, Q. (2004). Towards reproducible scanning capacitance microscope image interpretation. Journal of Vacuum Science & Technology B, 22(1), 399-405.

[29] Smoliner, J., Basnar, B., Golka, S., Gornik, E., Löffler, B., Schatzmayr, M., & Enichlmair, H. (2001). Mechanism of bias-dependent contrast in scanning-capacitance-microscopy images.Applied Physics Letters, 79(19), 3182-3184.

[30] Chang, M. N., Hu, C. W., Chou, T. H., & Lee, Y. J. (2012). Contrast distortion induced by modulation voltage in scanning capacitance microscopy. Applied Physics Letters, 101(8), 083503.

[31] Zavyalov, V. V., McMurray, J. S., & Williams, C. C. (1999). Advances in experimental technique for quantitative two-dimensional dopant profiling by scanning capacitance microscopy. Review of scientific instruments, 70(1), 158-164.

[32] O'Malley, M. L., Timp, G. L., Timp, W., Moccio, S. V., Garno, J. P., & Kleiman, R. N. (1999). Electrical simulation of scanning capacitance microscopy imaging of the pn junction with semiconductor probe tips. Applied physics letters, 74(24), 3672-3674.

[33] http://www.brukerafmprobes.com/

[34] Edwards, H., Ukraintsev, V. A., San Martin, R., Johnson, F. S., Menz, P., Walsh, S., ... & Chang, M. C. (2000). pn-junction delineation in Si devices using scanning capacitance spectroscopy. Journal of Applied Physics, 87(3), 1485-1495.

[35] Bowallius, O., Anand, S., Nordell, N., Landgren, G., & Karlsson, S. (2001). Scanning capacitance microscopy investigations of SiC structures. Materials Science in Semiconductor Processing,4(1), 209-211.

[36] Edwards, H., McGlothlin, R., San Martin, R., Elisa, U., Gribelyuk, M., Mahaffy, R., ... & Ukraintsev, V. A. (1998). Scanning capacitance spectroscopy: An analytical technique for pn-junction delineation in Si devices. Applied physics letters, 72(6), 698-700.

[37] Giannazzo, F., Goghero, D., Raineri, V., Mirabella, S., Priolo, F., Liotta, S. F., & Rinaudo, S. (2004). Simulation of scanning capacitance microscopy measurements on ultranarrow doping profiles in silicon. Journal of Vacuum Science & Technology B,22(1), 394-398.

[38] Degen, A., & Kosec, M. (2000). Effect of pH and impurities on the surface charge of

zinc oxide in aqueous solution. Journal of the European Ceramic Society, 20(6), 667-673.

[39] Moore, J. C., Kenny, S. M., Baird, C. S., Morkoç, H., & Baski, A. A. (2009). Electronic behavior of the Zn-and O-polar ZnO surfaces studied using conductive atomic force microscopy. Journal of Applied Physics, 105(11), 6102.

[40] McNamara, J. D., Ferguson, J. D., Foussekis, M., Ruchala, I., Reshchikov, M. A., Baski, A. A. *et al*. (2011, January). Surface Characterization of Ga-doped ZnO layers. In MRS Proceedings (Vol. 1315, pp. mrsf10-1315). Cambridge University Press.

[41] Fan, J. C., Sreekanth, K. M., Xie, Z., Chang, S. L., & Rao, K. V. (2013). p-Type ZnO materials: Theory, growth, properties and devices. Progress in Materials Science, 58(6), 874-985.

[42] Kohan, A. F., Ceder, G., Morgan, D., & Van de Walle, C. G. (2000). First-principles study of native point defects in ZnO. Physical Review B, 61(22), 15019.

[43] Van de Walle, C. G. (2000). Hydrogen as a cause of doping in zinc oxide. Physical Review Letters, 85(5), 1012.

[44] Brochen, S., Lafossas, M., Robin, I. C., Ferret, P., Gemain, F., Pernot, J., & Feuillet, G. (2014). Residual and intentional n-type doping of ZnO thin films grown by metal-organic vapor phase epitaxy on sapphire and ZnO substrates. Journal of Applied Physics, 115(11), 113508.

[45] Ligor, O. (2010). Reliability of the scanning capacitance microscopy and spectroscopy for the nanoscale characterization of semiconductors and dielectrics (Doctoral dissertation, Doc'INSA-INSA de Lyon).

[46] Stephenson, R., Verhulst, A., De Wolf, P., Caymax, M., & Vandervorst, W. (1998). Contrast reversal in scanning capacitance microscopy imaging. Applied physics letters, 73(18), 2597-2599.

Chapter 4

Carrier profiling on ZnO NWs by SSRM

The investigation together with the application of SCM on ZnO nano-scaled structures for carrier profiling objective have been reported in chapter 3 and quantitative determination of carrier concentrations inside ZnO NWs by calibration method was carried out. Besides SCM, scanning spreading resistance microscopy (SSRM) represents another widely studied and applied AFM-based technique for electrical characterization including 2D dopant/carrier profiling at the nanometer scale [1-5]. Compared with SCM, SSRM has proved an advantage of far less sensitivity to surface preparation owing to the stable contact between the tip and the sample [5]. Furthermore, SSRM possesses a more extensive dynamic range (10^{14}-10^{20} cm^{-3} for Si) with constant sensitivity and a high spatial and dopant gradient resolution [5]. This chapter, by performing SSRM measurements on the samples studied before (ZnO NWs and ZnO:Ga multilayer staircase structures), deals with the application of SSRM for 2D dopant/carrier profiling in ZnO nanostructures, with the aim to quantitatively determine the carrier concentration inside the ZnO NWs.

4.1 Introduction

The principle of SSRM has been described in chapter 2. During the scan of the conductive tip on the sample of interest with a DC bias (V_{bias}) between them, the total measured resistance is the sum of a number of terms, including the tip-sample barrier resistance ($R_{barrier}$), the spreading resistance (R_s), the back contact resistance (R_{bc}), the bulk resistance of the sample (R_{bulk}) and the tip resistance (R_{tip}). Normally, R_{bulk} and R_{bc} are neglectable compared with other terms when a good back contact can be formed. Typical R_{tip} for standard, commercially available conductive diamond coated Si probe is ~3 kΩ, which is considered as the main reason for the saturation of SSRM resistance in the case of very low resistivity (highly doped) Si materials [4].

In the ideal scenario of SSRM, where a perfect ohmic contact between the tip and the sample is made with negligible surface states, the measured resistance is dominated by the spreading resistance part R_s, which is intimately linked (directly proportional) to the local resistivity of the sample (ρ) through the Maxwell's equation $R=\rho/(4a)$ (assuming a circular ohmic contact), where a represents the tip radius [6]. If the contact radius a becomes smaller than the mean free path of the electrons in the sample, the local spreading resistance is adjusted and described by Sharvin's law ($R=4\rho\lambda/(3\pi a^2)$), with λ being the electron mean free path [7]. Then

from the equation of resistivity $\rho = 1/(qn\mu_n + qp\mu_p)$, where μ is the carrier mobility and n and p are the carrier concentration for holes and electrons, respectively, the effective carrier concentration can be determined.

Since its introduction, SSRM has been studied and applied primarily on Si-based structures and devices for carrier/dopant profiling purpose. A large dynamic range of dopant concentration (10^{14}-10^{20} cm^{-3}) has been demonstrated (for both *n*- and *p*-type Si) [5]. Regarding its spatial resolution, progress has been made during the development of this technique in terms of tip fabrication as well as measurement condition. While 10-20 nm and sub-5 nm resolution are typical for the use of conventional diamond-coated probes and full diamond tips in air, respectively [8-9], spatial resolutions down to 1 nm have been demonstrated for the measurements in vacuum ($<1\times10^{-5}$ Torr) [10-11]. Then the study of SSRM has been extended to other semiconductor materials such as Ge [12], SiGe [13], SiC [14-15], InP [16-17], GaAs [17], GaN [18]. It has been found that while a small V_{bias} (50-500 mV) permits to obtain quantitative results on Si and Ge, relatively large values of V_{bias} (1-5 V) are required in the case of GaAs and InP. Concerning the measured resistance dependence on the polarity of the applied bias for these two materials, reasonable explanation for the corresponding current transport properties was given by modeling of tip-sample contact based on a Schottky energy-band structure in the study of compound semiconductors [17]. For example, in the case of GaAs, the Fermi level is known to pin near the midgap of GaAs, so although SSRM data can be obtained with either polarity, only one bias polarity (positive or negative sample bias for *n*- or *p*- GaAs, respectively) produces SSRM results showing quantitative correlation with dopant density from SIMS. In contrast, for InP, the Fermi level is pinned near the conduction-band edge, which explains why quantitative SSRM profiles can be obtained with either bias polarity for *n*-type InP [17].

However, to our knowledge, detail study of SSRM has not been performed on ZnO, with only few cases on ZnO nanostructures investigation [19-20]. In the following, SSRM application on the ZnO NWs and multilayer staircase structure with the goal of carrier/dopant profiling will be reported with the attempt of quantitative analysis of carrier concentration for the NWs.

For information, in cases without further introduction, standard commercial conductive diamond (B doped) Si tips were used (DDESP-10 type from Bruker). The tip is coated with 100 nm thick B-doped diamond layer, leading to a nominal tip radius of 150 nm [21]. Typical spring constant of the probe cantilever is in the range 20~200 N/m with a nominal value of 80 N/m [21]. All the measurements were conducted in ambient environment.

4.2 Tip-ZnO contact characteristics

The performance of SSRM is fundamentally determined by the electrical characteristics of the tip-sample contact. Many factors can play a crucial role in determining the tip-sample interaction behaviour including but not limited to the type of material, the tip resistance, tip geometry (tip radius) and the doping level of the semiconductor. In reality, the measured resistance in SSRM is calculated from $R=V_{bias}/I$, with I the current flowing through the sample. On the one hand, this formula is only correct if the I-V characteristic of the tip-sample contact obeys the ohm's law, which is not always observed. For highly doped materials (Si for instance), ohmic model is still applicable as the effect of surface states is negligible and the energy barrier is transparent. In contrast, for lowly doped materials, ohmic contact behaviour no longer holds and current rectifying effect occurs, which represents a major cause of the deviation from expected dependence of SSRM resistance on the sample resistivity [12, 22]. On the other hand, as discussed before, for analysis in SSRM, to reach the information of resistivity (and carrier concentration) necessitates the measured resistance being dominated by the local spreading resistance. Both these considerations highlight the importance of acknowledge about the I-V properties of the tip-sample system. Mostly, given a certain tip and a material, the tip force shows a considerable impact on the measured resistance in the SSRM imaging. The necessary tip force on the sample for stable contact depends on the sample surface condition as well as the sharpness of the tip. Typically, for SSRM on Si in ambient condition using conventional diamond-coated Si probes, a tip force higher than 15 μN is usually needed to penetrate the native oxide layer covering the silicon surface and to transform the Si area underneath the tip into a metallic β-tin phase [23]. Similar phase transformation is also observed for Ge while a tip force ~2 μN is enough for successful SSRM mapping. Similarly, SSRM study on compound semiconductors was carried out with a typical tip force in the range 2~5 μN, except that crystal phase transformation was not addressed therein [17]. So, to start the investigation, the impact of tip force on the measured resistance and the contact I-V behaviour were studied.

4.2.1 Determination of tip force

The tip force on the sample, F_{tip}, is related to the deformation of the used cantilever by $F_{tip}=k\times d$, where k and d are the spring constant and the deflection of the cantilever, respectively. Among them, the value of cantilever spring constant can be evaluated from the thermal tune process [24]. As for the deflection of the cantilever, in the AFM system, it is expressed in the unit of V and its sensitivity to vertical displacement can be calculated from the ramp curve (force-displacement curve) after tip engagement. A representative ramp curve

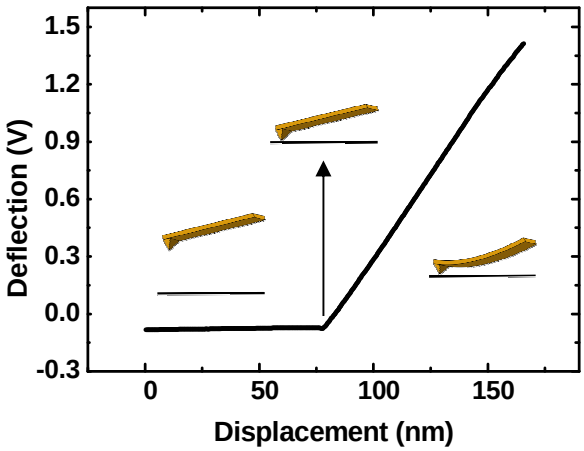

Figure 4.1: Force curve with the tip on a ZnO sample. Deflection sensitivity can be calculated from the linear part of the curve after tip contact with the sample. The three inset graphs indicate the tip's positions relative to the sample before contact, starting contact and pressing on the sample.

is shown in Figure 4.1. From the linear part between 75 nm and 150 nm, the deflection sensitivity of the cantilever to its deformation can be calculated to be Δdeflection/Δdisplacement=57.8 nm/V. Then for a certain used deflection setpoint, the applied F_{tip} on the sample can be calculated.

4.2.2 Resistance-force curve

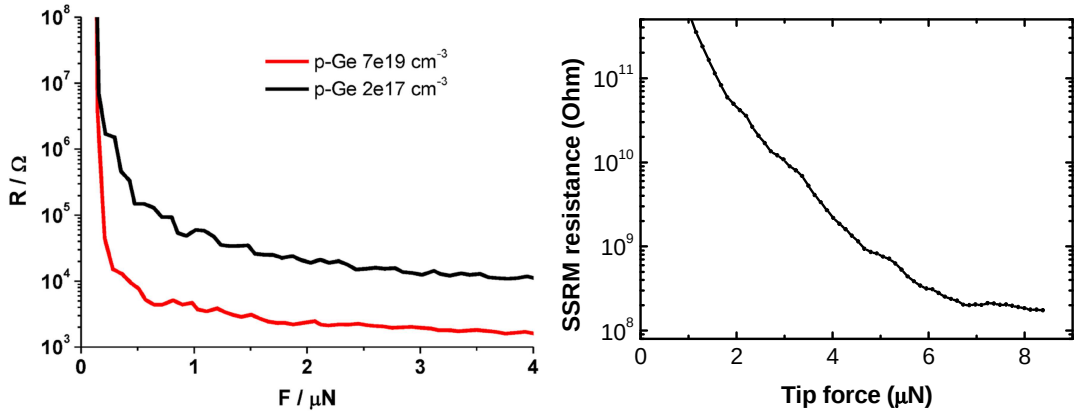

(a) (b)

Figure 4.2: (a) Resistance-force curves measured on *p*-type Ge. The drop in resistance between 0.5 and 2 μN indicates the phase transformation towards the metallic-like β-tin phase. A bias of +500 mV was applied to the sample, while the tip was electrically grounded. (Schulze, A. *et al* [12]) (b) Resistance-force curves a ZnO bulk material (Zn-face) with a carrier concentration in the order of 10^{17} cm^{-3}. Applied voltage on the sample was -2 V.

In SSRM, the tip-sample contact can be considered as a nano-indentation whereby a small volume of sample material is pressed by the probe tip for mechanical as well as electrical

contact. For instance, during the detailed study on Si and Ge, the measured SSRM resistance was found to be significantly dependent on the applied tip force to the sample material. Taking Ge for example, Figure 4.2(a) shows representative resistance-force curves using a conductive diamond coated tip on two *p*-type Ge layers with concentrations of 7×10^{19} and 2×10^{17} cm^{-3}, respectively [12].

At low forces (similar to the case of Si [25]), dopant dependence can hardly be observed. As the force increases (0.5~2 μN), the resistance drops several orders of magnitude, and the resistance becomes a clear measure of the carrier concentration. With further increasing forces (above 2 μN), a slower continuous decrease of the resistance can be observed, consistent with the assumed increase in contact radius *a*, resulting from the larger indentation. In the work of reference [12], the sharp decrease of resistance between 0.5~2 μN was explained by the formation of the β-tin phase underneath the probe with a large enough pressure, typically in the order of ~10 GPa, as in the case of Si. This pressure-induced phase transformation from the diamond cubic structure to the β-tin structure has been experimentally studied in different works [26-28].

Similarly, in this thesis work, the force dependence of the SSRM resistance was investigated on a ZnO bulk sample (with a carrier concentration in the order of 10^{17} cm^{-3}). A -2 V voltage was applied on the sample while the tip was electrically grounded and the resistance was recorded with the tip pressing on the sample with steadily increasing tip force. As shown in Figure 4.2(b), the measured SSRM resistance also undergoes a continuous decrease as the tip force increases. Note that the much larger resistance values obtained for the ZnO sample can be partly attributed to the smaller carrier mobility (electron in this case) compared with that for the Ge sample, although there can be other contributing factors such as the tip difference and measurement condition. Here, the decrease of the resistance with increasing tip force is worth being discussed. Unlike Si and Ge being of diamond cubic structure, ZnO possess a hexagonal crystal structure, which may play an important role determining its characteristics during mechanical deformation in a nano-indentation event [29]. In fact, from the literature, many conventional nano-indentation studies have been performed on ZnO. While different force loading characteristics from Si were observed, slip of dislocations has been identified as the only physical mechanism responsible for plastic deformation of ZnO and no evidence for pressure-induced phase transformation has been revealed by transmission electron microscopy and Raman spectroscopy studies during the indentation processes [30-33]. However, the indentation process in AFM operation (tens of nm tip radius and tip force at μN order) can differ from those in conventional nano-indentation experiments (μm indenter radius and indenter force at mN order) and pressure-induced phase transformation can not be completely ruled out [29]. A number of experimental measurements and theoretical

calculations [34-38] have shown that the wurtzite (B4) structure will transform into a cubic rocksalt (B1) structure at the pressure of ~9 GPa and the B1 structure has a narrower band gap ~2.45 eV (experimental value) [39-40]. Thus, here as the first explanation we attribute the reduction of resistance to possible phase transformation and created defect states. More studies are necessary concerning this problem.

4.2.3 I-V characteristic at different tip forces

Besides resistance-force investigation, another approach to examine the tip-sample contact properties is to collect I-V curves under different tip forces. This can be achieved under spectroscopy mode in both SSRM and C-AFM measurements. The tip is located at a specific position on the sample and I-V curves are recorded by scanning the V_{bias}. Figure 4.3(a) illustrates recorded I-V curves with tip forces between 0.44 to more than 12 μN on the same ZnO substrate as in Figure 4.2(b). It is seen that under a tip force less than 8 μN, current rectifying behaviour can be identified while a more symmetric behaviour is observed with tip force larger than 10 μN. This is consistent with results in Figure 4.2(b) where the measured resistance at reverse bias (+1 V on the sample) approaches that at -1 V with increasing tip force. Note that the parts near 0 V in the I-V curves are not shown because the resistances are not correctly measured due to the effect of the amplifier's response in SSRM detector (opposite-sign SSRM data output for opposite-sign V_{bias}). The result on another ZnO substrate is shown in Figure 4.3 (b). In this case, the carrier concentration (*n*-type) is in the mid 10^{16} cm^{-3} range and measurements were done in C-AFM mode. Also, a trend from Schottky I-V characteristic at low tip forces to ohmic-like behaviour at relatively high tip forces can be noticed. Moreover, a smaller "threshold" tip force is required to observe ohmic-like I-V curve in comparison to the previous substrate. Although the impact of tip difference may exist, the reduction of necessary tip force is believed to correlate with the higher carrier concentration in the sample.

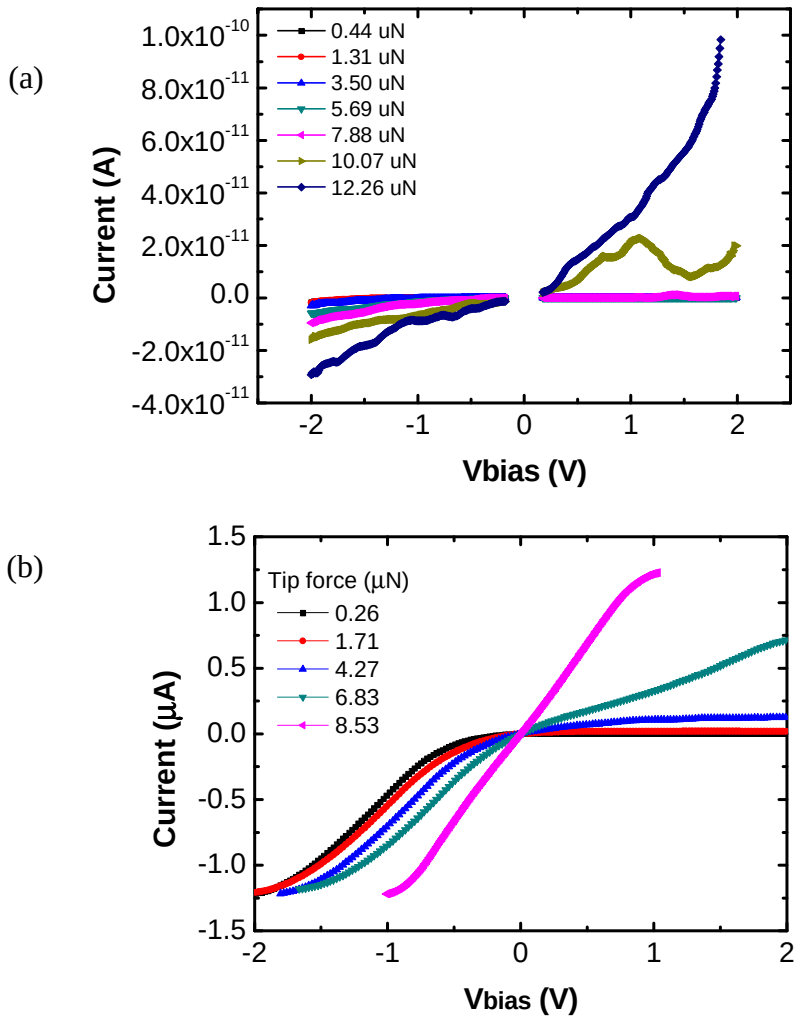

Figure 4.3: (a) I-V curves on the cross section of a ZnO substrate (O face) with a ~10^{14} cm^{-3} carrier concentration under varying tip forces between 0.44 and 12.26 μN in SSRM measurements. (b) I-V curves on the cross section of a ZnO substrate(m-face) with carrier concentration ~mid 10^{16} cm^{-3} under varying tip forces between 0.26 and 8.53 μN in C-AFM measurements. Evolution of the I-V characteristic can be noticed with increasing tip force. Bias voltage is applied on the sample while the tip is electrically grounded.

4.3 SSRM on ZnO NWs

As shown in Chapter 2, after the planarization process, the surface roughness of the NWs sample is acceptable for performing SSRM measurements. Same ZnO NWs samples as in SCM were studied, i.e. CBD grown and MOCVD grown NWs. For both samples, backside electrical contacts were made using large area silver paste on the substrate and also on the top of NWs [41-42].

4.3.1 CBD grown NWs

Figure 4.4 (a) and (b) show two SSRM images on the CBD grown ZnO NWs sample

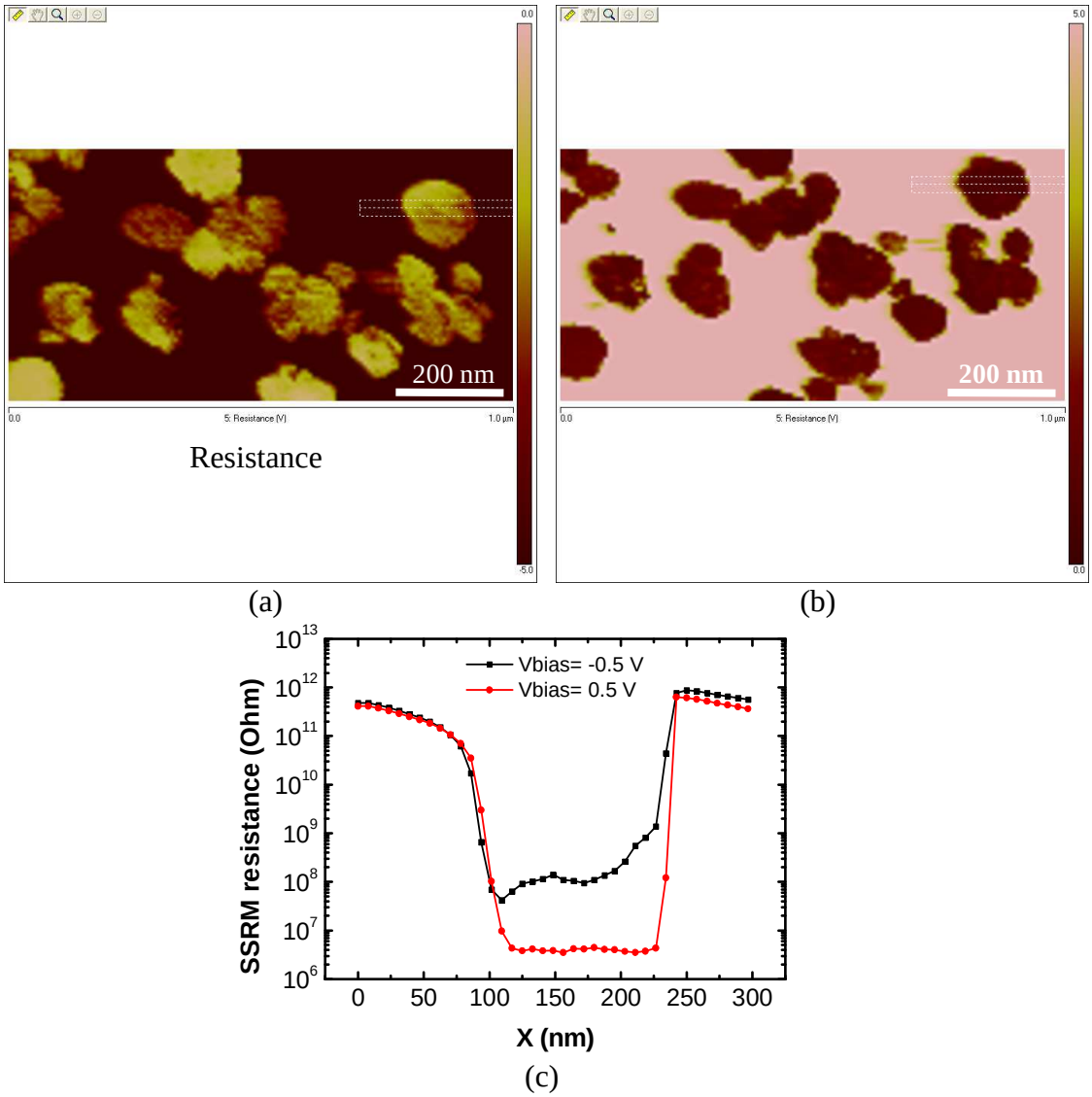

Figure 4.4: (a) SSRM image on an area of CBD grown NWs sample with -0.5 V V_{bias}. (b) SSRM image on almost same area as (a) with +0.5 V V_{bias}. (c) Averaged SSRM resistance profiles of the indicated rectangles in (a) and (b) for comparison. +0.5 V V_{bias} gives smaller resistance for NWs than -0.5 V V_{bias}. Applied tip force for the two images was ~1.68 μN.

collected one after another at the bias voltage of -0.5 V and 0.5 V, respectively. Note that for a negative V_{bias}, a larger SSRM data value corresponds to a smaller measured resistance and vice versa for a positive V_{bias}. In this way, it is seen that the SiO_2 matrix as insulating material gives rise to very large resistances and semiconducting ZnO NWs are well detected under both V_{bias} with opposite directions. For a better comparison of the two images, we compared the measured resistance on a specific NW. Averaged resistance profiles of the area indicated by the rectangles are given in Figure 4.4(c). What can be noticed is that as reduced resistances are recorded for ZnO NWs compared with SiO_2, a positive V_{bias} (0.5 V on the sample) yields smaller resistances than that of a negative one. What's more, the measurements were done at a tip force of ~1.68 μN, where a good electrical contact occurs already. A possible explanation

for these results is the following: as we know, the electron affinity of a semiconductor depends on both the material and its doping level. For highly doped material, the effect of surface states would be negligible and the barrier height with a metal tends to reduce even to zero, leading to the fact that the ohmic contact model is still applicable. So this result implies that the investigated NWs possess a relatively high residual carrier concentration. In a word, it is good news to be able to obtain such contact behaviour at a low tip force and we preferred to use positive bias for further measurements.

4.3.2 MOCVD grown NWs

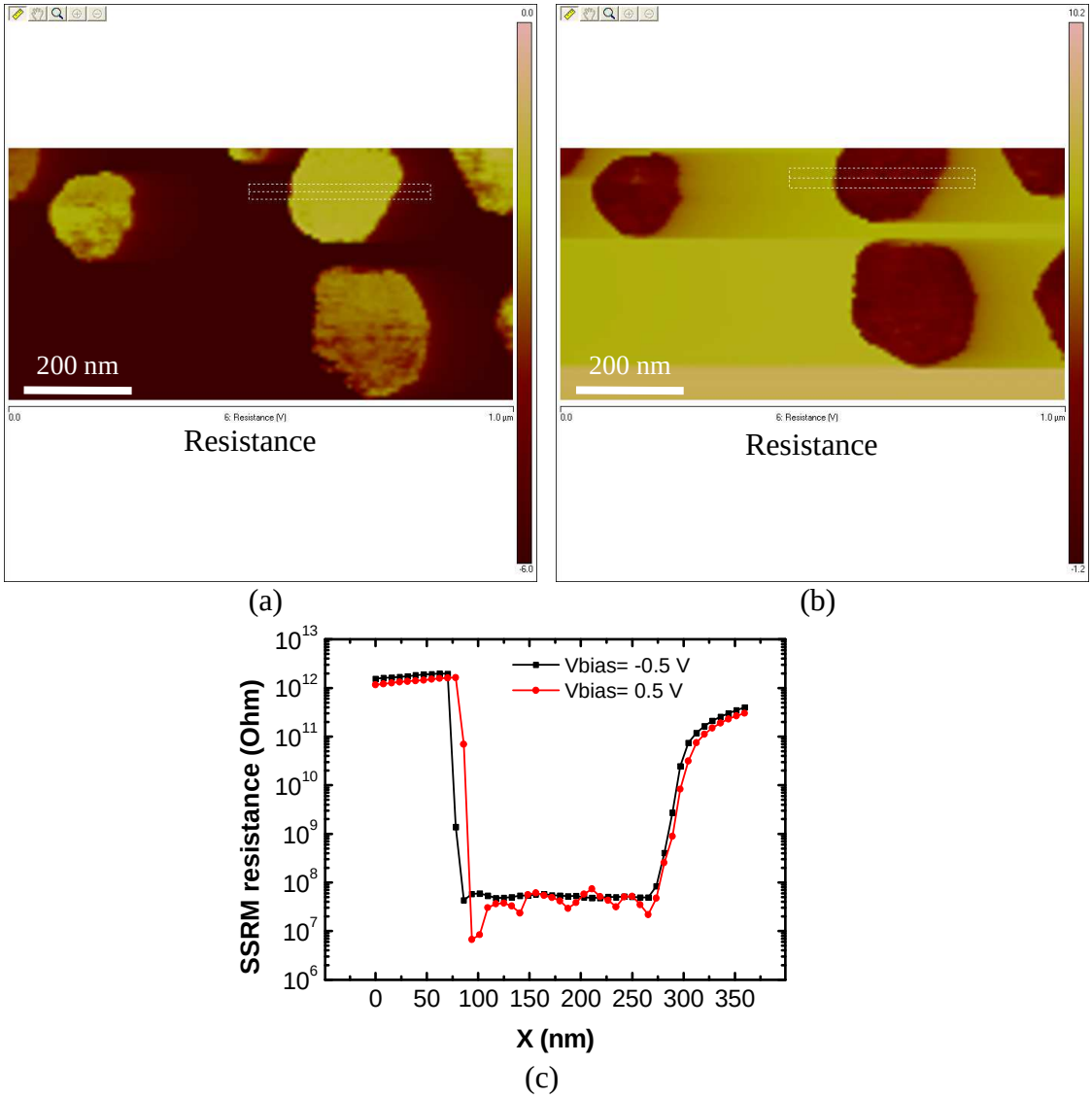

Figure 4.5: (a) SSRM image on an area of MOCVD grown NWs sample with -0.5 V V_{bias}. (b) SSRM image on the same area as (a) with +0.5 V V_{bias}. (c) Averaged SSRM resistance profiles of the indicated rectangles in (a) and (b) for comparison. Applied tip force for the two images was ~1.68 μN.

Two SSRM images of MOCVD grown NWs sample are shown in Figure 4.5(a) and 4.5(b),

corresponding to a V_{bias} of -0.5 V and 0.5 V, respectively. The applied tip force was also ~1.68 μN. As expected, the NWs are clearly resolved in SSRM under both V_{bias}. Furthermore, from a direct comparison of the measured resistance profile on a NW (indicated by the rectangles), it is found that the two V_{bias} produce similar SSRM resistance, indicating an ohmic-like contact between the tip and ZnO NWs during the scan. In addition, unlike in SCM where core-shell contrast is noticed [see page 52], here in SSRM, no evident core-shell difference is recorded. According to this result, it appears that the carrier density inside the NWs exhibits homogeneity. In contrast, topographical variation is found to impact the measured resistance in a way that a smaller resistance is likely to be obtained as the tip scans to a higher region on the NWs. This may be due to a scan-induced larger shear force, lowering the contact resistance. This effect underlines the importance of a more appropriate surface in terms of roughness.

4.3.3 Quantification of SSRM measurement

Like the analysis in SCM, no difficulty was encountered for SSRM to image the ZnO NWs in SiO_2 matrix and corresponding resistance can be recorded. Nevertheless, the same practical issue of quantification analysis of the results still arises for resistivity/carrier profiling purpose. To this end, one method is to model the tip-sample electrical contact and trying to determine straightly the investigated local resistivity or free carrier density. Assuming the resistance is dominated by the local spreading resistance, which is determined by the carrier concentration (doping level), carrier mobility as well as the contact radius, to achieve the assessment of dopant/carrier density requires the knowledge of contact radius of the tip-sample system. Actually, from a strict electrical point of view, the contact radius should be referred as electrically effective contact radius. As has been studied on silicon [27], its value is determined by the size of the induced metallic like β-Sn pocket in the mechanical tip-sample contact and can be much smaller than the geometrical radius of the probe tip (illustrated in Figure 4.6), making it extremely difficult for straightforward determination of the resistivity or carrier density from the resistance result on samples of interest. For materials without phase transformation, the electrical contact radius is related to the size of the nanocrystallite in the diamond film coating.

Another concern lies on the assumption of local spreading resistance dominance of the measured value. As discussed before, in practice, the barrier resistance, being dependent on the surface states and doping level, can play a role especially for relatively low doping material. For tip resistance (typical value of 3 kΩ for conductive diamond coated tip), it is considered as a major reason for the saturation of SSRM resistance for highly doped region in

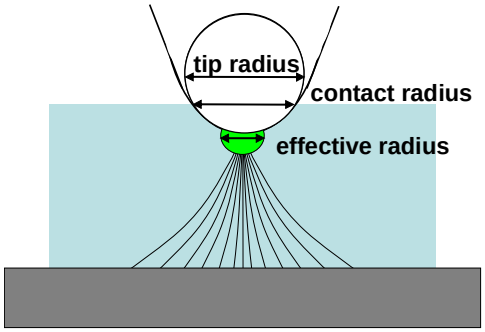

Figure 4.6: Illustration of electrically effective radius being different from tip radius and mechanical contact radius in SSRM measurement (for Si and Ge).

the case of Si when the spreading resistance decreases to the same order of magnitude as the tip resistance. This is no longer a serious problem for ZnO considering the much lower carrier mobility for this material than Si in normal cases [43], resulting in a much larger spreading resistance than that of the tip. This fact will allow a higher dynamic upper limit of detection in the highly doped range of ZnO than Si. Bulk resistance, usually negligible in SSRM imaging, may become a more influencing factor in the case of NWs structure. A simple estimation of the body resistance of a NW is made with an assumption of radially and axially homogeneous conduction. The body resistance of a NW is expressed as

$$R_{NW} = \frac{\rho l}{A} = \frac{4l}{\pi n q \mu d^2} \tag{4-1}$$

Where l and d are height and diameter of the NW respectively, A is area of the NW's cross section, n the carrier concentration and μ carrier mobility. For a NW with d of 100 nm, l of 1 μm, n of 10^{17} cm^{-3} and μ of 50 $cm^2/(V•s)$, its body resistance will be ~ 6.37×10^6 Ω. This is already a very large resistance value and is potentially to be comparable with the spreading resistance, especially for NWs with smaller diameter and larger length.

To go a bit further, in order to achieve better accuracy, particularly for samples containing significant variation in resistivity, it becomes necessary to consider the current flowing paths through a non-uniformly doped sample. For example, if we consider a measurement taken on a high-resistivity region close to a boundary with a region of much lower resistivity, then one would expect that much of the current flowing from the tip might follow a path through the lower resistivity material, and this would reduce the measured resistance. In effect, the measured resistance at any particular point is not exclusively determined by the carrier concentration at that point, but by the entire surrounding carrier profile. This issue was explored by P. de Wolf *et al* [3], who used finite element simulations to assess the current paths in inhomogeneous samples and the effect of the inhomogeneity on the measured resistance and details and be found therein.

Since it is almost impossible to know the value of electrically effective radius in SSRM imaging, again, the use of experimental calibration curve is chosen for quantitative analysis in the aim of carrier profiling.

4.4 SSRM on ZnO:Ga staircase structures

The same calibration samples, i.e. ZnO:Ga multilayer staircase structures, were used to investigate SSRM on different dopant density levels and obtain SSRM data for calibration curves.

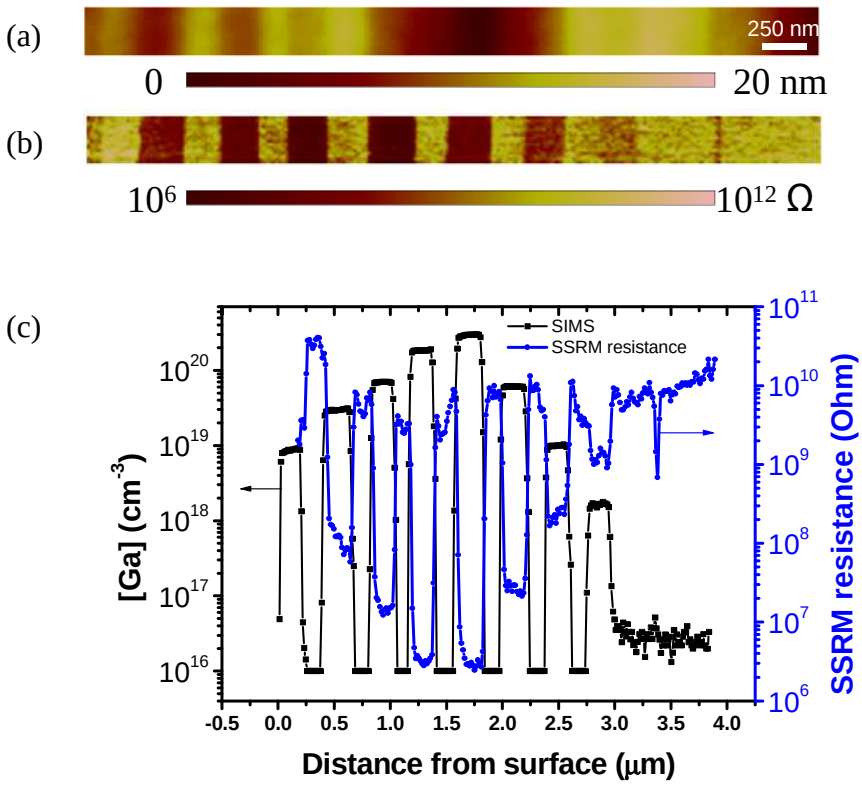

Figure 4.7: (a) Topography image of the measured cross sectional area on staircase structure A. RMS roughness value is 4.16 nm. (b) SSRM data image of the area with V_{bias}=0.5 V and a tip force of ~1.83 μN. (c) Averaged SSRM resistance profile plotted with Ga density profile from SIMS. Clearly, all the imaged ZnO:Ga layers are resolved with a good agreement between result from SSRM and SIMS. Sample surface is to the left.

Figure 4.7 (a) and (b) show the result of SSRM measurement on the heavily Ga doped ZnO staircase structure sample. The investigated area (Figure 4.7(a)) has an RMS roughness value of 4.16 nm. For electrical imaging, a tip force of ~1.83 μN and a V_{bias} of 0.5 V were employed. As can be seen in Figure 4.7(b), the ZnO:Ga layers are unambiguously resolved by SSRM. Darker stripes corresponding to lower SSRM resistances are Ga doped layers while brighter ones indicates nid ZnO layers resulting in larger measured resistances. Besides, the interface between the nid ZnO buffer layer and the ZnO substrate is reflected by the sharp downward

peak at 3.38 µm. In addition, more abrupt borders in SSRM than those in SCM measurements (Figure 3.13 on page 65) can be noticed between the Ga doped and nid ZnO layers. It is noted that the lateral step of the tip scan was ~8 nm for the SCM measurement in Figure 3.13 and ~16 nm for the SSRM measurement in Figure 4.7. This demonstrates that SSRM is able to offer a higher spatial resolution than SCM. To check the capability of SSRM to distinguish the layer in possession of various dopant concentrations, the comparison of averaged SSRM resistance profile with the Ga density profile from SIMS is performed as shown in Figure 4.7 (c). In this figure, it is evident that for all the imaged area, a higher Ga concentration produces a lower SSRM resistance, meaning a good agreement between results from the two techniques. What's more, the four layers with [Ga] from 6×10^{19} to until 3×10^{20} cm^{-3} are well distinguished without evident saturation phenomenon. This proves the correctness of the discussion before about a higher upper limit of the dynamic range in SSRM for ZnO than Si. This agreement demonstrates the potential of SSRM being an adaptable tool for high dopant-level profiling in ZnO material.

For this sample, it has been found that a low force (~1.5 µN) is enough to obtain stable results of SSRM due to the relative softness of ZnO in comparison with Si (Mohs hardness: 4.5 versus 7), very similar to the case of InP [16]. In fact, we have noticed that a force higher than 4 µN already scratch strongly the sample surface preventing from producing an acceptable image in terms of resolution and noise level. Besides, loss of expected contrast between layers with different Ga densities occurs when a voltage higher than 3 V is applied (Figure 4.8), indicating a deteriorated spatial resolution for imaging ZnO nanostructures.

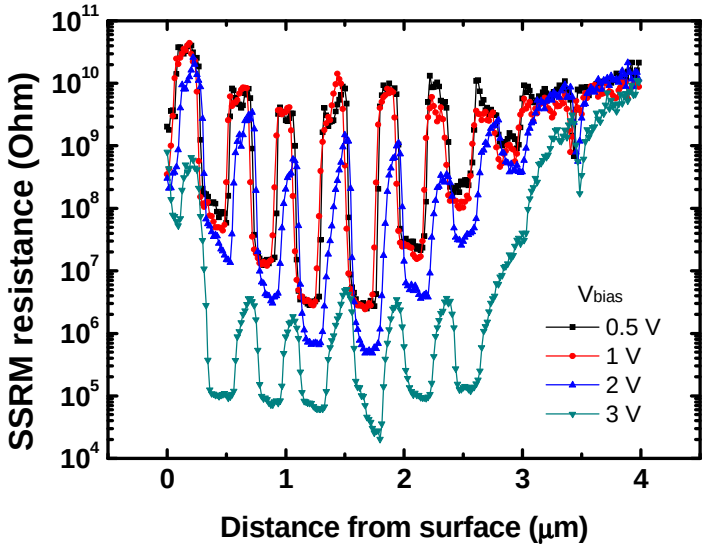

Figure 4.8: SSRM data profiles under different V_{bias} of 0.5 V, 1 V, 2 V and 3 V. For the first three V_{bias}, contrasts between the doped layers can be obtained. In comparison, for 3 V V_{bias}, the contrasts between the most heavily doped 6 layers are almost lost. Applied tip force was ~1.83 µN.

A result of SSRM on the second staircase structure sample is shown in Figure 4.9. RMS roughness of the measured area is about 0.97 nm. For this sample, a larger V_{bias} was needed to obtain SSRM data contrast of different layers. From Figure 4.9(b), the two layers with highest Ga density and the interface between ZnO buffer layer and ZnO substrate at ~1.68 μm from the surface are resolved while no clear contrast is seen for other layers. This is better seen by comparing the SSRM data profile with that of Ga density shown in Figure 4.9(c). Agreement between SSRM and SIMS exists for the nearest two doped layers from surface. Although no spatially resolved contrast is obtained for other doped layers, the general trend of increasing SSRM resistance with decreasing Ga density can still be noticed. Keeping the current flowing paths in mind, it is worth pointing out that the measured resistance for the nid layer at 0.3 μm, which shows an unexpected small value, is affected by the surrounding two doped layers. More accurate results can be obtained by reducing the tip radius or beveling the sample.

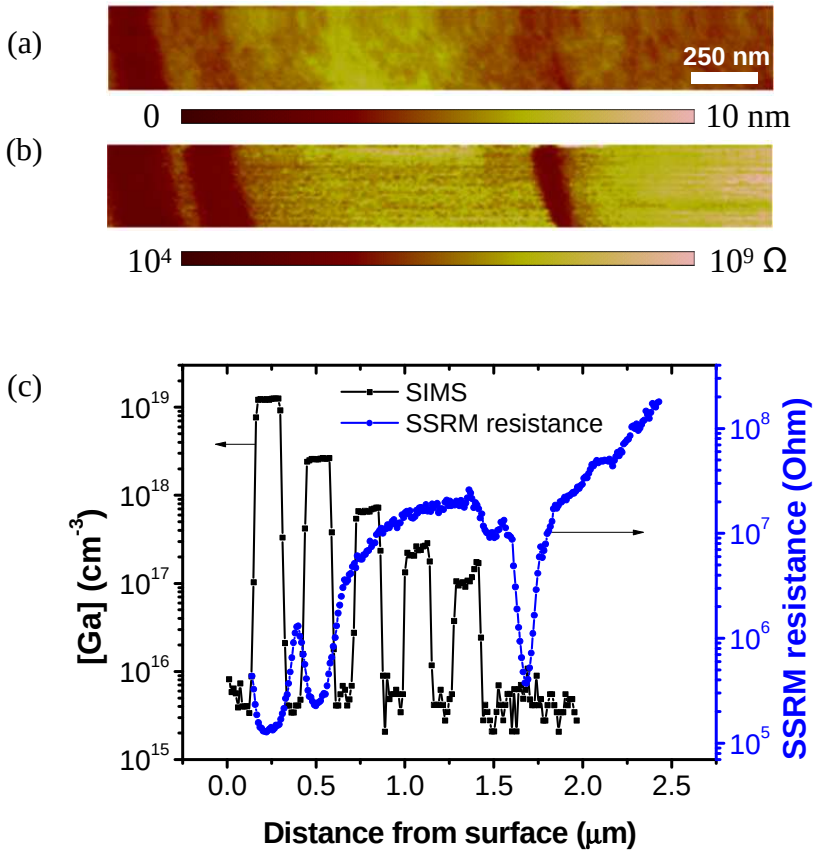

Figure 4.9: (a) Topography image of the measured area on staircase structure B. RMS roughness value is 0.97 nm. (b) SSRM data image of the area with V_{bias}=4 V and a tip force of ~1.68 μN. (c) Averaged SSRM resistance profile plotted with Ga density profile from SIMS. Sample surface is to the left.

4.5 Determination of carrier concentration in NWs

Following the discussion before, calibration method is employed for quantitative analysis of the SSRM results on ZnO NWs. In the last section, the ability of SSRM to differentiate ZnO

regions with varying doping level has been demonstrated on the staircase structure. From the SSRM resistance profile on ZnO:Ga staircase structure, calibration curve is able to be constructed. Then, the carrier concentration inside the NWs can be estimated by simply calibrating their SSRM values with the established calibration curve.

For reasonable and reliable calibration procedure as possible, identical probe tip and measurements conditions need to be maintained for staircase sample and the sample to be studied. Nevertheless, SSRM is not as sensitive as SCM and based on the discussion in section 4.2, the most important two parameters to be kept are the tip force and the V_{bias}.

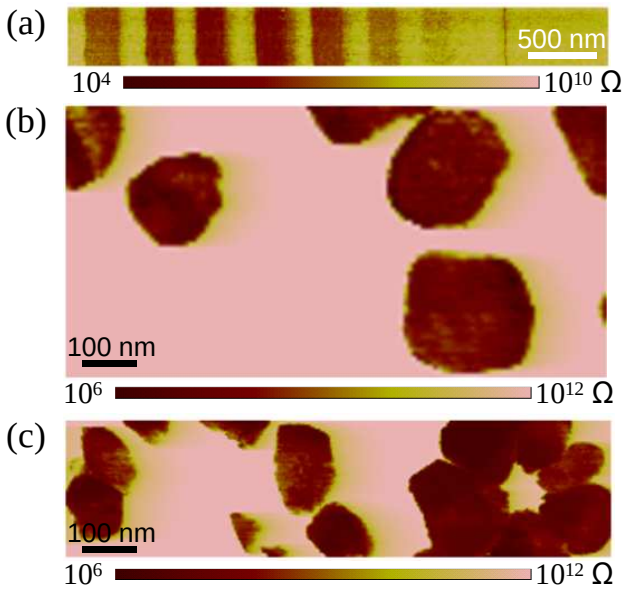

Figure 4.10: SSRM imaging on (a) cross section of the heavily doped ZnO:Ga staircase structure (surface is to the left), (b) MOCVD grown ZnO NWs and (c) CBD grown ZnO NWs. 1 V V_{bias} and 2 μN tip force were used for all measurements.

Figure 4.10 shows the SSRM images on a staircase structure of ZnO:Ga and the two NWs samples. They were obtained using the same tip under same measurements condition of 1 V V_{bias} and 2 μN tip force. Here, the Ga-doped layer near the top surface of the sample was not reached in order to protect the tip from falling at the side of the sample and breaking down. Of course, this problem can be solved by growing a relatively thick capping layer on the sample surface.

Similar to the analysis in the previous section, comparison between SSRM resistance profile and [Ga] density profile is done as shown in Figure 4.11(a). Apparently, the measured resistance undergoes a monotonic dependence of carrier density inside the layer for the whole [Ga] range, with resistance values being 4×10^7 and 7.5×10^5 Ω for [Ga] of 1.7×10^{18} and 3×10^{20} cm^{-3}, respectively. As can be expected, in this figure the nid layers as well as the substrate produce resistances larger than the doped counterparts.

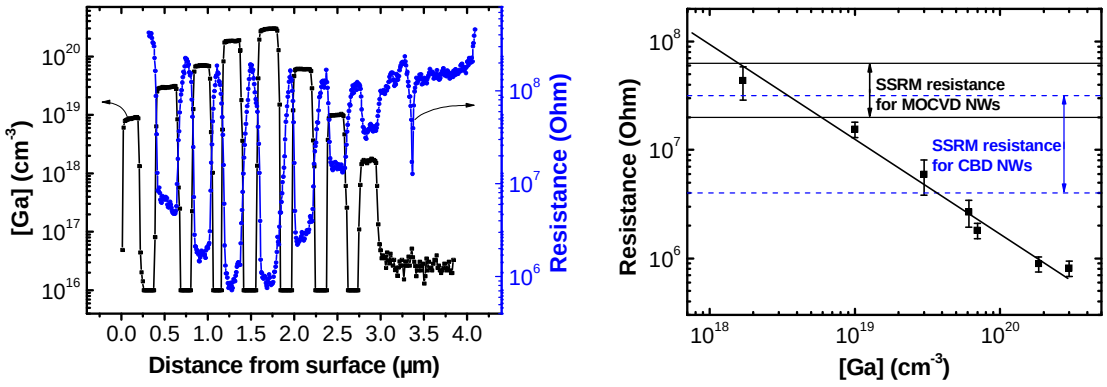

(a) (b)

Figure 4.11: (a) Averaged SSRM resistance profile of the result in Figure 4.10 on staircase structure plotted with [Ga] concentration profile from SIMS. (b) Calibration curve (resistance versus [Ga]) extracted from (a). In addition, range of SSRM resistance for MOCVD and CBD grown ZnO NWs are indicated by horizontal lines. Their intersections with the calibration curve give an idea of the range order of the carrier concentration in NWs, assuming similar electron mobility like in the staircase epi-layers.

On the base of result from the staircase structure, calibration curve is constructed and shown in Figure 4.11(b). An approximate linear correlation between the SSRM resistance and dopant concentration from SIMS is observed for the entire doping range of the sample (1.7×10^{18} to 3×10^{20} cm^{-3}). The deviation of resistance from linear fitting may be related to the contribution of contact barrier resistance between the diamond tip and the sample as well as differences in electron mobility between layers. For example, the electron mobility in the 1.7×10^{18} cm^{-3} doped layer is likely to have a higher value compared with the more heavily doped counterparts, thus producing a smaller resistance than expected for identical mobility. Further more, as the first application of this calibration curve, we estimated quantitatively the residual carrier concentration, like in SCM analysis, in the nid ZnO layers. From the SSRM profile in Figure 4.11(a), the SSRM resistance corresponding to the nid ZnO layers is near 2×10^{8} Ω. Assuming that this measured total SSRM resistance is still dominated by the local spreading resistance part, from its comparison with the established calibration curve, a carrier concentration about 3.5×10^{17} cm^{-3} is estimated. However, this process did not consider the carrier mobility difference between the doped and nid ZnO. In fact, SSRM measures the resistance which is linked to the local sample resistivity determined by both carrier density and carrier mobility through the equation $\rho=1/qn\mu_n$. Due to the presence of much less impurities, the electron scattering mechanism is largely reduced for these nid layers, so they have a larger value of electron mobility [44], which according to the study in reference [44] reaches >400 cm^2/Vs, about 8 times higher than the heavily doped layers. Thus, by taking into account this mobility difference, the residual carrier concentration for nid ZnO layer in the

measured staircase structure is estimated to be around 4.4×10^{16} cm^{-3}. This value is in good accord with the analysis result from SCM measurement, demonstrating the applicability of calibrated SSRM method.

From the SSRM images of NWs collected under same condition using the identical probe tip, we determine the SSRM resistance range for the MOCVD and CBD grown NWs being from 2×10^7 to 6.3×10^7 Ω and from 4×10^6 to 3.1×10^7 Ω, respectively. Regarding the carrier mobility, for MOCVD ZnO NWs here, from another work based on four probe measurements on ZnO nanowires grown in a similar condition [45], it was found that the conduction in the nanowires with similar diameters was dominated by the cores of them, showing a bulk-like conduction behavior with an electron mobility around 100 $cm^2/(V•s)$. This value is ~2 times higher than the typical Hall mobility for highly doped ZnO:Ga layers [43]. Then by taking this electron mobility difference into account, the residual carrier concentration inside the ZnO nanowires of study can be estimated to be between 10^{18} and 3×10^{18} cm^{-3}, which is consistent with the result obtained from four probe measurements [45]. Furthermore, this result is in good agreement with that obtained from SCM analysis in Chapter 3, demonstrating the good performance of SSRM in carrier/dopant profiling operation.

For CBD grown NWs, a lower resistance range is observed. If we assume a similar carrier mobility of them to the ZnO:Ga layers, a carrier concentration between 3.4×10^{18} and 3.5×10^{19} cm^{-3} is estimated. Although differences exist, this range covers the estimated value from SCM measurements. Since there is no result from other electrical characterization techniques on these NWs, it is difficult to assess the quality of this result. However, the calibration process has been demonstrated being a feasible approach for quantitative analysis of carrier profiling in ZnO NWs structure.

In the previous analysis, the assumption that the measured resistance is always dominated by the local spreading resistance was made. Here we discuss two issues that can deviate the reality from this assumption. First is about the bulk resistance R_b. Its contribution in bulk-like structure is negligible since the current spreads into a large volume. In contrast, in the NW geometry, the current must flow down the NW axis and can not spread in all directions, it is possible that R_b becomes important. In section 4.3.3, we have estimated R_b of ~ 6.37×10^6 Ω for a NW with diameter of 100 nm, height of 1 μm, n of 10^{17} cm^{-3} and μ of 50 $cm^2/(V•s)$. According to Equation (4-1), for n of 10^{18} cm^{-3}, R_b will be ~ 6.37×10^5 Ω. From the measurement on the NWs samples, the total resistance is much larger than this value, indicating the assumption that the NWs body resistance is negligible still works. Second is the deviation from the assumed ohmic tip-sample contact.

In real cases, this deviation occurs as a result of the Schottky-like contact characteristics affected by the sample's doping level as well as its surface states. For semiconductors, in

highly doped regime, the induced sharp band bending facilitates carrier field emission through the thin energy barrier producing a low-resistance contact, so the effect of surface states is negligible and the fact that the ohmic contact model is still applicable [46-48]. As the doping concentration decreases, a reduction in tunneling current transmission happens as the surface energy barrier widens and the impact of surface states is increasing depending on the materials and surface treatment. For most III-V covalent semiconductors such as GaAs and InP, the Fermi-level at the interface is pinned in a narrow energy range by intrinsic or extrinsic interface states within the band gap [49], resulting in the fact that the barrier height with metals is almost independent of the metal work function [50]. On the contrary, most of II-VI semiconductors have unpinned Fermi levels [51]. Consequently, ohmic contact can be formed based on the values of the metal work function and semiconductor electron affinity. Regarding ZnO, it resides at the borderline between covalent and ionic semiconductors. Thus, formation of ohmic contacts to ZnO with low contact resistance can be realized by reducing the barrier height and/or increasing the ZnO doping density. In this study, the measurements on the ZnO NWs have revealed a similar resistance for forward and reversal bias voltages (a smaller resistance at reversal bias than at forward bias for CBD ZnO NWs sample). Also, the staircase sample used for calibration is heavily doped, which favorites an ohmic-like contact. Under these considerations, we believe that the calibration process is applicable in this study. Nevertheless, we point out that more studies on the tip-ZnO contact properties are of interest for a better understanding of it and a better performance of SSRM.

4.6 Conclusion

This chapter has reported the study about quantitatively determining carrier density inside ZnO NWs through calibration method. Since SSRM requires a stable electrical contact between the tip and sample, hence a large force, B-doped conductive diamond probe tip is in regular use. The electrical properties of conductive diamond tip-ZnO contact were investigated with varying tip force on ZnO substrates with low carrier concentrations. It was found that the measured resistance decreases with increasing tip force. While Schottky contact is formed at low tip force, symmetric I-V characteristic is observed at large tip force. Possible mechanism is discussed and with no doubt further study on this issue is needed.

From SSRM on ZnO NWs samples, in accordance with expectation, the NWs were unambiguously detected in the SiO_2 matrix due to their large difference of conduction properties. For conversion of SSRM resistance to carrier concentration, due to the almost impossibility to know the parameters in modeling SSRM, calibration method was taken again, similar to that in SRP technique. Same calibration samples in chapter 3 were made use of. SSRM on the heavily doped ZnO:Ga staircase structure clearly and correctly resolves all the

doped layers with [Ga] between 1.7×10^{18} and 3×10^{20} cm^{-3}. A monotonic dependence of SSRM resistance on the Ga density was revealed, showing a good agreement between the SSRM and SIMS characterization. In contrast, it required a large V_{bias} to obtain reasonable SSRM resistance profile for the lightly doped staircase structure, probably due to the existence of Schottky barrier. Nevertheless, the obtained results on staircase structures demonstrate SSRM being an approach for 2D dopant/carrier profiling in ZnO nanoscale structure.

For reliable calibration analysis, measurements on the ZnO:Ga staircase structure and on the ZnO NWs were carried out under same conditions employing the same probe tip. As results, calibration curve, i.e. SSRM resistance versus carrier density, was established on the base of SSRM result and SIMS result on the ZnO:Ga staircase structure. Because SSRM is sensitive to local resistivity rather than just carrier concentration, carrier mobility should be taken into account. In the end, SSRM resistances of NWs were compared with the calibration curve, and residual carrier density of $1\sim3\times10^{18}$ cm^{-3} was estimated for MOCVD grown NWs, which is consistent with both results from four probe measurement and from SCM analysis in this thesis work. In this way, the feasibility of SSRM for 2D carrier/dopant profiling in ZnO nanostructures is demonstrated.

References:

[1] De Wolf, P., Clarysse, T., Vandervorst, W., Snauwaert, J., & Hellemans, L. (1996). One- and two-dimensional carrier profiling in semiconductors by nanospreading resistance profiling. Journal of Vacuum Science & Technology B, 14(1), 380-385.

[2] Clarysse, T., Caymax, M., De Wolf, P., Trenkler, T., Vandervorst, W., McMurray, J. S., ... & Neubauer, G. (1998). Epitaxial staircase structure for the calibration of electrical characterization techniques. Journal of Vacuum Science & Technology B, 16(1), 394-400.

[3] De Wolf, P., Clarysse, T., & Vandervorst, W. (1998). Quantification of nanospreading resistance profiling data. Journal of Vacuum Science & Technology B, 16(1), 320-326.

[4] Eyben, P., Xu, M., Duhayon, N., Clarysse, T., Callewaert, S., & Vandervorst, W. (2002). Scanning spreading resistance microscopy and spectroscopy for routine and quantitative two-dimensional carrier profiling. Journal of Vacuum Science & Technology B, 20(1), 471-478.

[5] Eyben, P., Denis, S., Clarysse, T., & Vandervorst, W. (2003). Progress towards a physical contact model for scanning spreading resistance microscopy. Materials Science and Engineering: B, 102(1), 132-137.

[6] R. Holm. (1979). Electric Contacts: Theory and Application, 11-16, (Springer, Berlin)

[7] Sharvin, Y. V. (1965). A Possible Method for Studying Fermi Surfaces. Soviet Journal of Experimental and Theoretical Physics, 21, 655.

[8] De Wolf, P., Stephenson, R., Trenkler, T., Clarysse, T., Hantschel, T., & Vandervorst, W. (2000). Status and review of two-dimensional carrier and dopant profiling using scanning probe microscopy. Journal of Vacuum Science & Technology B, 18(1), 361-368.

[9] Alvarez, D., Hartwich, J., Fouchier, M., Eyben, P., & Vandervorst, W. (2003). Sub-5-nm-spatial resolution in scanning spreading resistance microscopy using full-diamond tips. Applied physics letters, 82(11), 1724-1726.

[10] Zhang, L., Tanimoto, H., Adachi, K., & Nishiyama, A. (2008). 1-nm spatial resolution in carrier profiling of ultrashallow junctions by scanning spreading resistance microscopy. Electron Device Letters, IEEE, 29(7), 799-801.

[11] Hantschel, T., Demeulemeester, C., Eyben, P., Schulz, V., Richard, O., Bender, H., & Vandervorst, W. (2009). Conductive diamond tips with sub‐nanometer electrical resolution for characterization of nanoelectronics device structures. physica status solidi (a), 206(9), 2077-2081.

[12] Schulze, A., Verhulst, A. S., Nazir, A., Hantschel, T., Eyben, P., & Vandervorst, W. (2013). A comprehensive model for the electrical nanocontact on germanium for scanning spreading resistance microscopy applications. Journal of Applied Physics, 113(11), 114310.

[13] Giannazzo, F., Raineri, V., Mirabella, S., Impellizzeri, G., & Priolo, F. (2006). Drift

mobility in quantum nanostructures by scanning probe microscopy. Applied physics letters, 88(4), 043117.

[14] Osterman, J., Hallén, A., & Anand, S. (2002). Carrier profiling of Al-doped 4H-SiC by scanning spreading resistance microscopy. Applied physics letters, 81, 3004.

[15] Giannazzo, F., Roccaforte, F., & Raineri, V. (2007). Acceptor, compensation, and mobility profiles in multiple Al implanted 4H-SiC. Applied Physics Letters, 91(20), 2104.

[16] De Wolf, P., Geva, M., Hantschel, T., Vandervorst, W., & Bylsma, R. B. (1998). Two-dimensional carrier profiling of InP structures using scanning spreading resistance microscopy. Applied physics letters, 73(15), 2155-2157.

[17] Lu, R. P., Kavanagh, K. L., St J, D. W., Kuhl, A., SpringThorpe, A. J., Griswold, E., ... & Streater, R. (2001). Calibrated scanning spreading resistance microscopy profiling of carriers in III–V structures. Journal of Vacuum Science & Technology B, 19(4), 1662-1670.

[18] Fraser, I. S., Oliver, R. A., Sumner, J., McAleese, C., Kappers, M. J., & Humphreys, C. J. (2007). Compositional contrast in AlxGa1-xN/GaN heterostructures using scanning spreading resistance microscopy. Applied surface science, 253(8), 3937-3944.

[19] Børseth, T. M., Christensen, J. S., Maknys, K., Hallén, A., Svensson, B. G., & Kuznetsov, A. Y. (2005). Annealing study of Sb+ and Al+ ion-implanted ZnO. Superlattices and microstructures, 38(4), 464-471.

[20] Latu-Romain, E., Gilet, P., Chevalier, N., Mariolle, D., Bertin, F., Feuillet, G., ... & Chelnokov, A. (2010). Surface-induced p-type conductivity in ZnO nanopillars investigated by scanning probe microscopy. Journal of Applied Physics, 107(12), 124307.

[21] https://www.brukerafmprobes.com

[22] Schulze, A., Hantschel, T., Eyben, P., Verhulst, A. S., Rooyackers, R., Vandooren, A., ... & Vandervorst, W. (2011). Observation of diameter dependent carrier distribution in nanowire-based transistors. Nanotechnology, 22(18), 185701.

[23] Eyben, P., Mody, J., Vemula, S. C., & Vandervorst, W. (2008). Impact of the environmental conditions on the electrical characteristics of scanning spreading resistance microscopy. Journal of Vacuum Science & Technology B, 26(1), 338-341.

[24] Hutter, J. L., & Bechhoefer, J. (1993). Calibration of atomic force microscope tips. Review of Scientific Instruments, 64(7), 1868-1873.

[25] De Wolf, P., Snauwaert, J., Clarysse, T., Vandervorst, W., & Hellemans, L. (1995). Characterization of a point-contact on silicon using force microscopy‐supported resistance measurements. Applied physics letters, 66(12), 1530-1532.

[26] Pharr, G. M., Oliver, W. C., & Clarke, D. R. (1990). The mechanical behavior of silicon during small-scale indentation. Journal of electronic materials, 19(9), 881-887.

[27] Mylvaganam, K., Zhang, L. C., Eyben, P., Mody, J., & Vandervorst, W. (2009).

Evolution of metastable phases in silicon during nanoindentation: mechanism analysis and experimental verification. Nanotechnology, 20(30), 305705.

[28] Ruffell, S., Bradby, J. E., & Williams, J. S. (2006). High pressure crystalline phase formation during nanoindentation: Amorphous versus crystalline silicon. Applied physics letters, 89(9), 091919.

[29] Kucheyev, S. O., Bradby, J. E., Williams, J. S., Jagadish, C., & Swain, M. V. (2002). Mechanical deformation of single-crystal ZnO. Applied Physics Letters, 80(6), 956-958.

[30] Bradby, J. E., Kucheyev, S. O., Williams, J. S., Jagadish, C., Swain, M. V., Munroe, P., & Phillips, M. R. (2002). Contact-induced defect propagation in ZnO. Applied physics letters, 80(24), 4537-4539.

[31] Basu, S., & Barsoum, M. W. (2007). Deformation micromechanisms of ZnO single crystals as determined from spherical nanoindentation stress–strain curves. Journal of Materials Research, 22(09), 2470-2477.

[32] Jian, S. R. (2010). Mechanical responses of single-crystal ZnO. Journal of Alloys and Compounds, 494(1), 214-218.

[33] Juday, R., Silva, E. M., Huang, J. Y., Caldas, P. G., Prioli, R., & Ponce, F. A. (2013). Strain-related optical properties of ZnO crystals due to nanoindentation on various surface orientations. Journal of Applied Physics, 113(18), 183511.

[34] Desgreniers, S. (1998). High-density phases of ZnO: Structural and compressive parameters. Physical Review B, 58(21), 14102.

[35] Molepo, M. P., & Joubert, D. P. (2011). Computational study of the structural phases of ZnO. Physical Review B, 84(9), 094110.

[36] Amrani, B., Chiboub, I., Hiadsi, S., Benmessabih, T., & Hamdadou, N. (2006). Structural and electronic properties of ZnO under high pressures. Solid state communications, 137(7), 395-399.

[37] Saeed, Y., Shaukat, A., Ikram, N., & Tanveer, M. (2008). Structural and electronic properties of rock salt phase of ZnO under compression. Journal of Physics and Chemistry of Solids, 69(7), 1676-1683.

[38] Karzel, H., Potzel, W., Köfferlein, M., Schiessl, W., Steiner, M., Hiller, U., ... & Schwarz, K. (1996). Lattice dynamics and hyperfine interactions in ZnO and ZnSe at high external pressures. Physical Review B, 53(17), 11425

[39] Segura, A., Sans, J. A., Manjon, F. J., Munoz, A., & Herrera-Cabrera, M. J. (2003). Optical properties and electronic structure of rock-salt ZnO under pressure. Applied physics letters, 83(2), 278-280.

[40] Kuang, F. G., Kuang, X. Y., Kang, S. Y., Zhong, M. M., & Mao, A. J. (2014). A first principle study of pressure-induced effects on phase transitions, band structures and elasticity

of zinc oxide. Materials Science in Semiconductor Processing, 23, 63-71.

[41] Wang, Z. L. (2009). ZnO nanowire and nanobelt platform for nanotechnology. Materials Science and Engineering: R: Reports, 64(3), 33-71.

[42] Wang, Z. L., & Song, J. (2006). Piezoelectric nanogenerators based on zinc oxide nanowire arrays. Science, 312(5771), 242-246.

[43] Sadofev, S., Kalusniak, S., Schäfer, P., & Henneberger, F. (2013). Molecular beam epitaxy of n-Zn (Mg) O as a low-damping plasmonic material at telecommunication wavelengths. Applied Physics Letters, 102(18), 181905.

[44] Makino, T., Segawa, Y., Tsukazaki, A., Ohtomo, A., & Kawasaki, M. (2005). Electron transport in ZnO thin films. Applied Physics Letters, 87(2), 022101.

[45] Bugallo, A. D. L., Donatini, F., Sartel, C., Sallet, V., & Pernot, J. (2015). Metallic core conduction in unintentionally doped ZnO nanowire. Applied Physics Express, 8(2), 025001.

[46] Eyben, P., Denis, S., Clarysse, T., & Vandervorst, W. (2003). Progress towards a physical contact model for scanning spreading resistance microscopy. Materials Science and Engineering: B, 102(1), 132-137.

[47] Lu, R. P., Kavanagh, K. L., St J, D. W., Kuhl, A., SpringThorpe, A. J., Griswold, E., ... & Streater, R. (2001). Calibrated scanning spreading resistance microscopy profiling of carriers in III-V structures. Journal of Vacuum Science & Technology B, 19(4), 1662-1670.

[48] Brillson, L. J., & Lu, Y. (2011). ZnO Schottky barriers and Ohmic contacts. Journal of Applied Physics, 109(12), 121301.

[49] Spicer, W. E., Chye, P. W., Skeath, P. R., Su, C. Y., & Lindau, I. (1979). New and unified model for Schottky barrier and III–V insulator interface states formation. Journal of Vacuum Science & Technology, 16(5), 1422-1433.

[50] Mead, C. A. Ohmic Contacts to Semiconductors, edited by B. Schwartz (Electrochemical Society, New York, 1969), 1-16.

[51] Brillson, L. J., & Lu, Y. (2011). ZnO Schottky barriers and Ohmic contacts. Journal of Applied Physics, 109(12), 121301.

Chapter 5

Macroscopic characterization of collective ZnO NWs

Besides the development of SCM and SSRM for carrier profiling implementation at nanometer scale, conventional macroscopic technique has also been used on large area of collective ZnO NWs immerged in dielectric matrix. Toward this end, Schottky diode at the macroscopic scale was fabricated on ZnO NWs assemblies and electrically characterization was done by performing I-V and C-V measurements. In this chapter, carrier profiling using standard space charge zone technique for collective NWs is carried out and difference of its results from that obtained in SPM (SCM/SSRM) analysis is discussed.

5.1 Sample preparation

Similar as in SCM and SSRM, CBD grown and MOCVD grown ZnO NWs are prepared. The NWs structures have undergone the identical planarization process as those in SPM measurements: first insulating SiO_2 matrix is dip-coated to fill the gaps between NWs and to provide mechanical support for eventual metal contact; then CMP is carried out to remove the SiO_2 on the top of NWs and result in a proper surface flatness. As a matter of fact, it is after the planarization procedure that the original NWs sample was cleaved into two pieces for separate SPM and macroscopic measurements. So we consider the two pieces of each sample having same properties including residual carrier concentration. Prior to metal deposition, the sample surface is cleaned in organic solvents (acetone, trichloroethylene and methanol), rinsed in de-ionized water and blown dry with nitrogen. Then the Pt metal contacts were fabricated on a group of ZnO NWs by electron beam deposition (EBD) approach at a pressure of 2×10^{-6} mbar. The contacts were deposited as circular dots with a diameter of 0.5 mm and 1 mm for CBD grown and MOCVD grown NWs samples, respectively. For CBD NWs sample, backside electrical contact was made using large area silver paint on the n-Si substrate. For MOCVD NWs on sapphire substrate, the back contact was formed by large area silver paint on the top of NWs from the front side of the sample [1-2]. The schematic diagram and actual images of Pt/ZnO NWs Schottky diodes are shown in Figure 5.1.

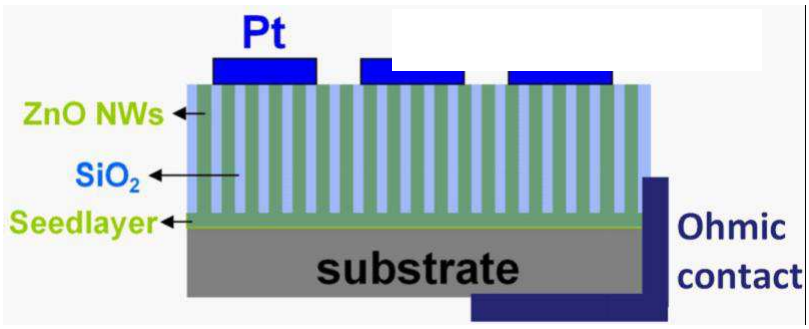

(a)

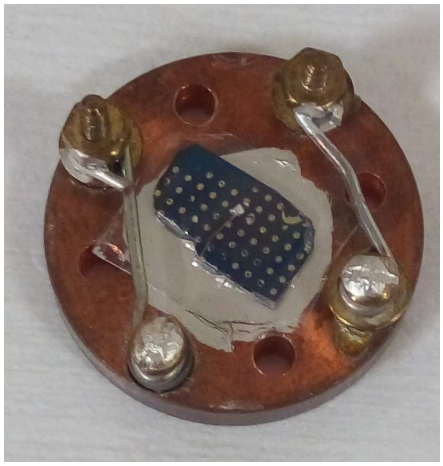

(b)

(c)

Figure 5.1: (a) Schematic diagram of Pt/ZnO Schottky diode. Fabricated Pt/ZnO Schottky diode on (b) CBD grown NWs sample and (c) MOCVD grown NWs sample after mounting for electrical characterization measurement.

Unlike electrical characterization on bulk materials, the deposited metal area does not represent effective metal contact with the NWs structure due to the existence of the insulating material SiO_2 filled in between the NWs. For the analysis of results from I-V and C-V measurements, effective diode area instead of metal electrode area should be used for extracting diode parameters especially for carrier depth profile. In this view, the NWs area ratio to the total contact area needs to be determined and it is not easy to obtain an accurate value. Inspired by SPM characterization approach, we attempted to estimate the active NWs area ratio by SSRM measurement, in which case only the active NWs are imaged. An example is shown in Figure 5.2. However, the analyzed result is believed to be largely overestimated primarily due to the tip averaging effect in SSRM measurement. So we turned to SEM observation which is usually used for NWs density and area estimation in the literature. Finally, NWs area ratio of 14% and 19% were evaluated for CBD and MOCVD grown samples, respectively (Figure 5.2(d) and Figure 5.2(f)).

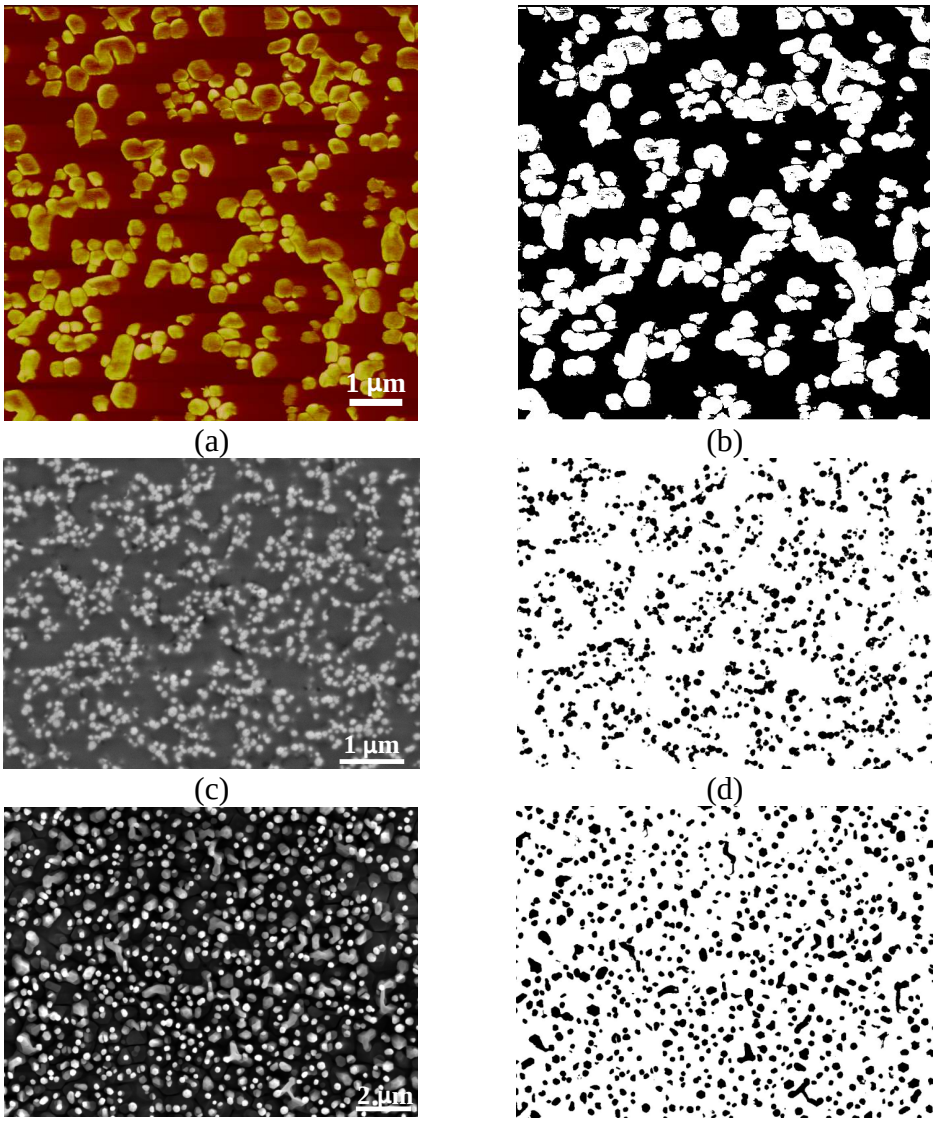

Figure 5.2: (a) SSRM image on an area of 8 µm×8 µm on MOCVD grown NWs sample. Active NWs are revealed. (b) Processed binary SSRM image by ImageJ software for estimation of active NWs ratio being ~37%. (c) An SEM image of CBD ZnO NWs. (d) Processed binary SSRM image by ImageJ software for estimation of active NWs ratio being ~14%. (e) An SEM image of MOCVD ZnO NWs. (f) Processed binary SSRM image by ImageJ software for estimation of active NWs ratio being ~19%.

5.2 I-V characteristics

Figure 5.3 (a) shows the typical room temperature I-V characteristics of Pt metal contact on collective CBD grown NWs. A current rectifying behavior is observed with an on/off ratio of 28 at +2V and -2 V. According to thermionic emission theory introduced in section 2.2, the current in such a Schottky diode can be expressed as

$$I = I_s\left[\exp\left(\frac{q(V-IR_s)}{\eta kT}\right)-1\right] \tag{5-1}$$

where I_s is the saturation current, R_s is the series resistance, k is the Boltzmann constant, T is the absolute temperature, q is the elementary electric charge, V is the applied voltage, and η is the ideality factor. The saturation current I_s is given as

$$I_s = AA^*T^2 \exp\left(-\frac{q\Phi_B}{kT}\right) \tag{5-2}$$

where A is the NWs area estimated from SEM observation, A^* is the effective Richardson constant (32 $Acm^{-2}K^{-2}$ for n-ZnO), and Φ_B is the Schottky barrier height.

From Equation (5-1), the ideality factor is determined to be 9.6. The higher ideality factor value reveals a poor quality of the junction probably caused by the presence of an interfacial layer or surface states and indicates that the transport mechanism is no longer dominated by thermionic emission. From Equation (5-2), the barrier height is found to be 0.60 eV, which is comparable with the results in the literature [3-5].

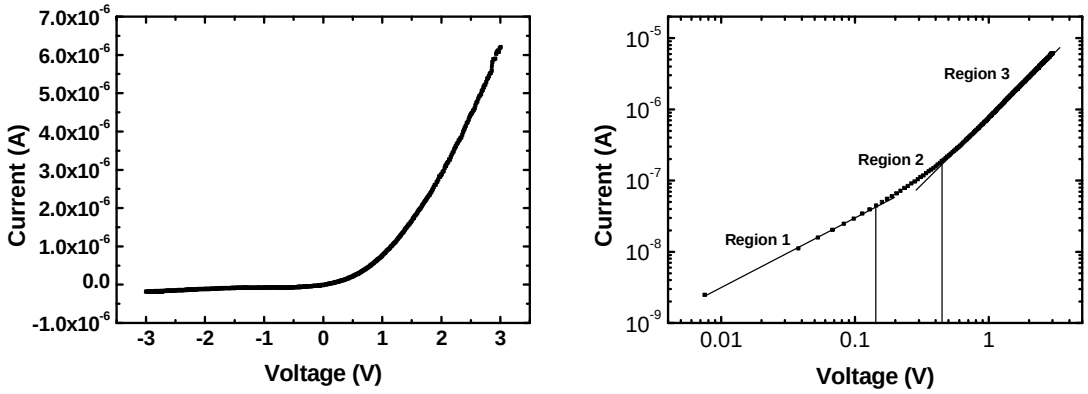

Figure 5.3: (a) Typical room temperature current-voltage characteristics for Pt/(CBD grown ZnO NWs) Schottky diode. (b) Log-log plot for the I-V data in (a).

To understand the charge transport mechanisms which control the junction behavior, the I-V characteristics in Figure 5.3(a) is redrawn on a log-log scale as presented in Figure 5.3(b). The logarithmic plot of the I-V characteristics shows three distinct regions, indicating different conduction mechanisms in each region. At low voltages (region 1) an ohmic-like conduction is dominant as the current exhibits a linear dependence on the voltage. This indicates tunneling being the dominant charge transport mechanism. As voltage increases (region 2), the current increases exponentially with a relationship of I~exp(cV). The ideality factor (9.6) is determined in this region and the dominant transport mechanism is recombination in the space charge region. Finally, in region 3, the current follows a power law ($I \sim V^2$), indicating a space-charge limited current (SCLC) transport mechanism, and this mechanism could be controlled by the presence of traps within the band gap of the ZnO NWs [6-7].

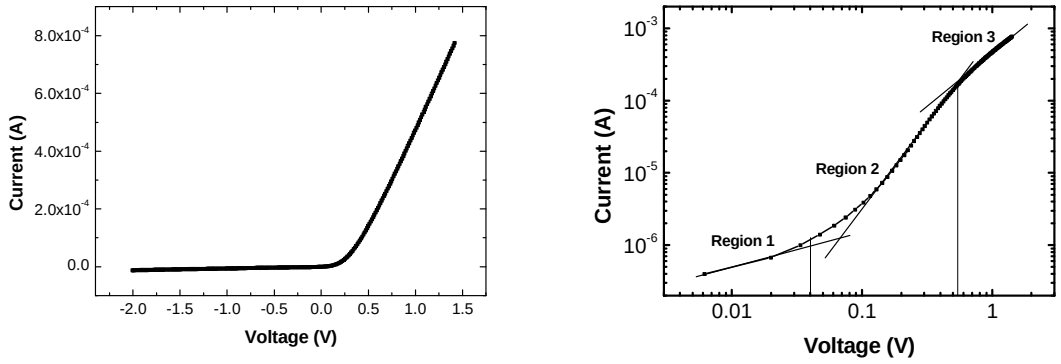

(a) (b)

Figure 5.4: (a) Typical room temperature current-voltage characteristics for Pt/(MOCVD grown ZnO NWs) Schottky diode. (b) Log-log plot for the I-V data in (a).

Figure 5.4 (a) shows the typical I-V characteristics of Pt metal contact on collective MOCVD grown NWs at room temperature. As can be seen, a Schottky contact is formed and the diode exhibits a rectifying on/off ratio of 87.5 at +1 V and -1 V. Using equation (5-1) and (5-2), the ideality factor and Schottky barrier height are determined to be 2.9 and 0.58 eV, respectively. In Figure 5.4(b) shows the forward I-V characteristics in log-log scale. Similar current behavior to the diode on CBD ZnO NWs is observed. The smaller value (2.9) of ideality factor compared with that for CBD NWs (9.6) indicates a Schottky diode of better quality. It is likely to correlate with the less interfacial defects as a consequence of the MOCVD growth process.

5.3 C-V characteristics and carrier profiling

C-V measurements were performed using a PhysTech HERA-DLTS system on the fabricated Schottky diodes. From the C-V characteristics in Figure 5.5(a) and using Equation (2-15), carrier concentration for the CBD grown sample is calculated to be 7×10^{16} cm^{-3}. Similarly, C-V result on the collective MOCVD grown NWs (see Figure 5.5(a)) gives a carrier density about 4×10^{16} cm^{-3}. During the calculation, relative dielectric constant ε_s=8.5 for ZnO was used [8].

The results from macroscopic C-V measurement are compared with those obtained from SCM and SSRM. As shown in Table 5.1, a considerable difference in carrier concentrations for the NWs between the C-V and SPM (SCM and SSRM) measurements can be noticed. The value of carrier densities from C-V profiling on collective NWs is about one order of magnitude lower than those obtained from SPM measurement. This fact again demonstrates that macroscopic and microscopic electrical properties can significantly differ from each other [9-10]. In order to understand the source responsible for this inconsistency, a discussion in detail about the C-V measurement on collective NWs structure is done.

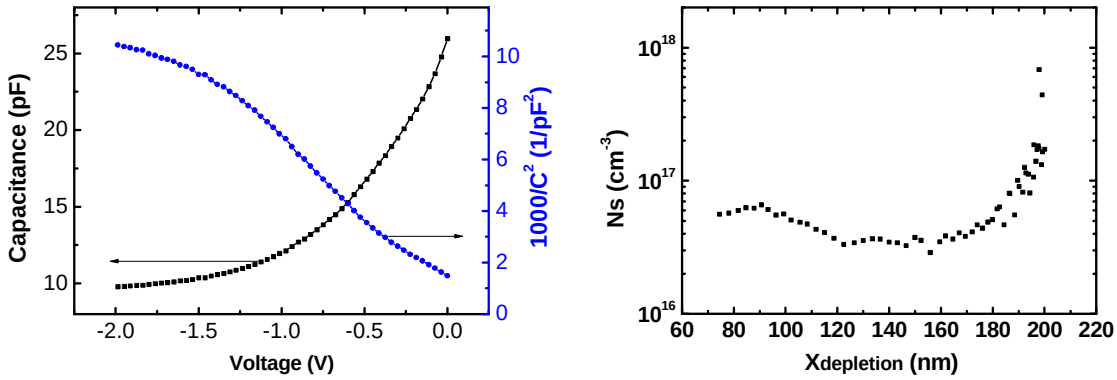

(a) (b)

Figure 5.5: (a) C-V reverse-biased characteristics of Pt/(CBD grown ZnO NWs) Schottky diode. (b) Calculated carrier depth profile giving carrier density 7×10^{16} cm^{-3}.

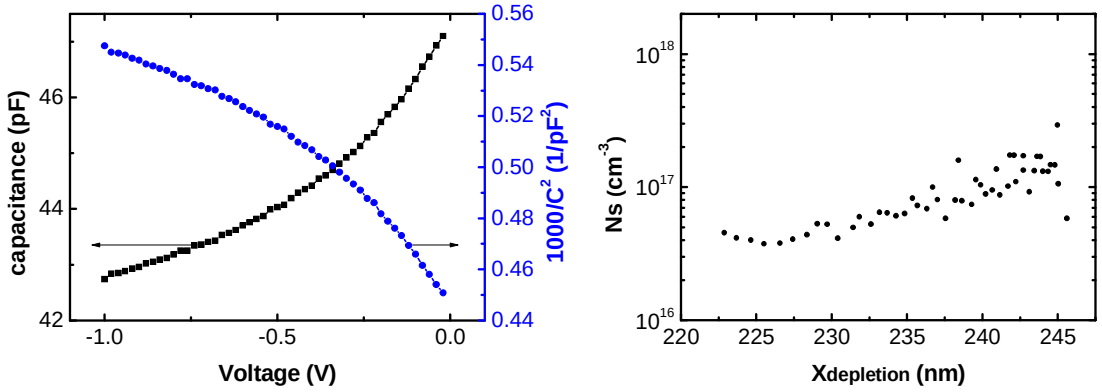

(a) (b)

Figure 5.6: (a) C-V reverse-biased characteristics of Pt/(MOCVD grown ZnO NWs) Schottky diode. (b) Calculated carrier depth profile giving carrier density ~4×10^{16} cm^{-3}.

Table 5.1: comparison of carrier concentration obtained from C-V profiling with those from SCM and SSRM characterization. (Unit: cm^{-3})

	C-V profiling on collective NWs	SCM result	SSRM result
CBD grown NWs	7×10^{16}	~3×10^{18}	/
MOCVD grown NWs	4×10^{16}	~2×10^{18}	1~3×10^{18}

5.4 Discussion of C-V profiling on collective NWs

C-V measurement on collective NWs structure is different from that on bulk materials mainly because of its non-uniformity in terms of carrier density, as a result of the gap between NWs and the introduction of the dielectric filling material. As a first assumption, we consider no difference of carrier density inside the NWs, in consistency with the estimation of active NWs area by SEM observation. In this case, two features of C-V characterization on collective

NWs can be remarked. One is that it is likely to produce a larger series resistance due to the cross sectional surface of the structure which can be very small. Another is that the introduction of SiO_2 matrix should bring an additional capacitance to the electric circuit.

5.4.1 Influence of R_s

Usually in C-V profiling, a diode behaving as a simple capacitor defined by the depletion capacitance is assumed. In reality, the diode has a leakage current and series resistance and the equivalent circuit is shown in Figure 5.7.

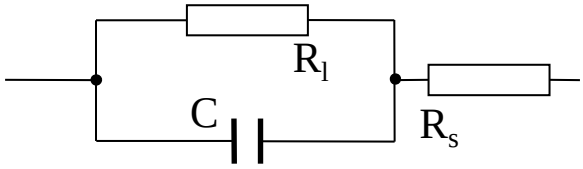

Figure 5.7: Equivalent circuit of a Schottky diode taking into account the leakage current and series resistance. *C* is the real depletion capacitance.

By circuit analysis, the measured (apparent) capacitance C_m can be written as [11]

$$\frac{C_m}{C}=\left[\left(1+\frac{R_s}{R_l}\right)^2+(\omega CR_s)^2\right]^{-1} \tag{5-3}$$

where ω is the frequency of the AC voltage. With $R_s \neq 0$, C_m will be less than C due to both series resistance and parallel conductance and is dependent upon frequency. In almost all cases, $R_s << R_l$ exists, thus we have

$$\frac{C_m}{C}=\left[1+(\omega CR_s)^2\right]^{-1} \tag{5-4}$$

So we have

$$\frac{dC_m}{dC}=\frac{1-(\omega CR_s)^2}{\left[1+(\omega CR_s)^2\right]^2} \tag{5-5}$$

Equation (2-15) can also be expressed as

$$N_s=-\frac{C^3}{q\varepsilon_s\varepsilon_0 A^2}\left(\frac{dV}{dC}\right) \tag{5-6}$$

In such a way, for the value of N_s deduced from measured C_m including effect of R_s (named as N_{sm}), we have

$$\frac{N_{sm}}{N_s}=\left(\frac{C_m}{C}\right)^3\frac{dC}{dC_m}=\frac{1}{1-(\omega CR_s)^4} \tag{5-7}$$

It shows that N_{sm} increases as ω, C or R_s increase, and that N_{sm} may change sign when ωCR_s=1. So the existence of a larger series resistance is likely to cause an overestimation of the carrier profile, especially under a low reverse bias where C is still large.

5.4.2 Influence of SiO_2 capacitance

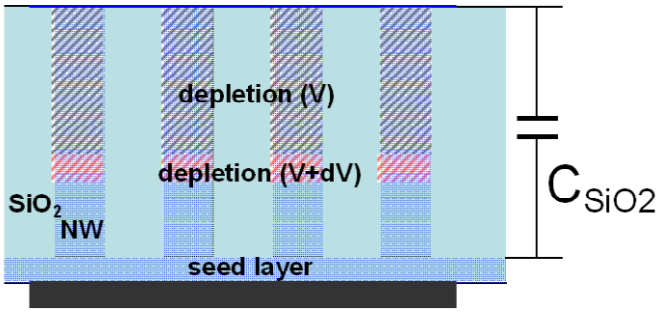

Figure 5.8: A simple model for C-V characterization on collective NWs structure taking into account the contribution of dielectric SiO_2 matrix.

Another factor signifying the difference of C-V profiling on between collective NWs and bulk sample is the additional capacitance introduced by the insulating material filling between the NWs. Although it should be considered during the analysis of C-V characteristics, no precise model has been established for the calculation of the capacitance of filling material [12]. Here, to perform a straightforward analysis, we use a simplest model by considering the SiO_2 part of capacitance (C_{SiO2}) being constant, i.e. irrespective with applied voltage (see Figure 5.8). In real cases, it is possible that C_{SiO2} shows a dependence on the voltage.

C_{SiO2} is in parallel with the depletion region capacitance. So we have

$$C_m=C_{NWs}+C_{SiO_2} \tag{5-8}$$

where C_{NWs} denotes the capacitance related to semiconductor NWs from depletion. Since C_{SiO2} is constant, we have

$$dC_m=dC_{NWs} \tag{5-9}$$

To highlight the influence of C_{SiO2}, we assume that R_s is negligible. Then by using Equation (5-6), relation between N_{sm} and N_s can be written as

$$\frac{N_{sm}}{N_s}=\left(\frac{C_m}{C_{NWs}}\right)^3=\left(\frac{C_{NWs}+C_{SiO2}}{C_{NWs}}\right)^3 \tag{5-10}$$

It can be seen that the existence of C_{SiO2} in excess in the circuit will result in a larger value of N_{sm} than N_s. The extent of the incorrectness depends on the ratio of C_{SiO2} to C_{NWs}. From this point of view, considering that $C_{SiO2}=\varepsilon_{SiO2}A_{SiO2}/d$, with d being the length of the NWs, it is suggested that a higher NWs area ratio and/or a larger NWs length is preferable for correct C-V profiling on collective NWs. Note that even if C_{SiO2} varies with external bias, Equation (5-10) holds for each voltage value. The larger C_{SiO2} compared with C_{NWs}, the more incorrect the Ns from C-V characteristics.

Figure 5.9 shows an example of the influence of additional capacitance on the carrier depth profile. Measurements were done on a bulk ZnO sample with and without additional capacitors. When only the depletion capacitance is measured, its value decreases from 280 pF at 0 V to 133 pF at -3 V and a carrier density of 2.8×10^{17} cm^{-3} is obtained, corresponding to its true value. Then measurements were done by adding an independent capacitor in the circuit in parallel to the sample. From Figure 5.9(b), the influence of the added capacitor can be noticed. A paralleled capacitor of a larger value results in a carrier density farther from its true value. Besides, as the depletion goes deeper, reduction of depletion capacitance enlarge the impact of paralleled capacitance on the measurement. This phenomenon can partly explain the abrupt increase of N_s with depletion depth in Figure 5.5(b).

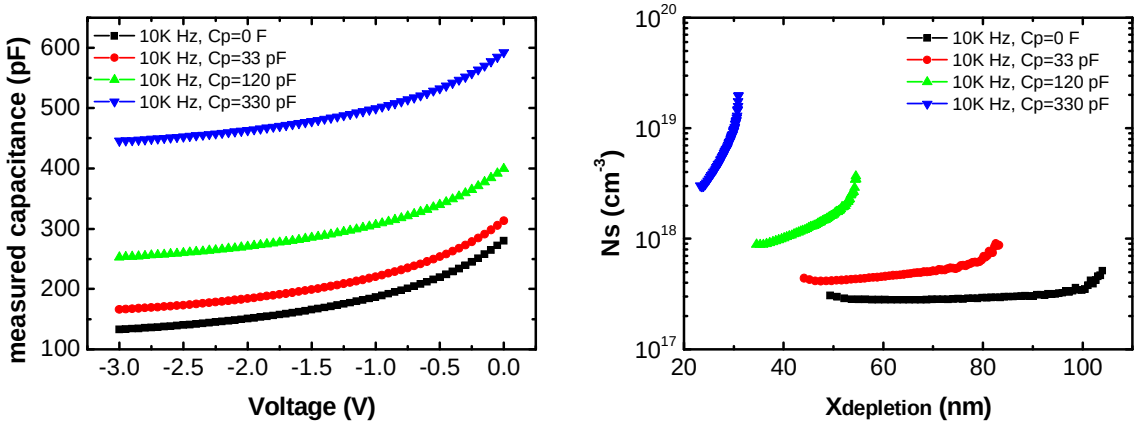

(a) (b)

Figure 5.9: C-V profiling on a ZnO bulk sample with capacitors of different capacitance values in parallel with the sample.

During the analysis above, the error of depletion width was not addressed since the focus was on the carrier density. It is worth pointing out that the error of measured capacitance from depletion capacitance is always accompanied by incorrectness of depletion width. Besides, deep states in the semiconductor material were not discussed. Simply, when the deep states are able to respond to the ac signal, they will produce an additional capacitance in the measurement and will have a similar effect as an external capacitor [13].

5.5 Discussion on the difference between microscopic and macroscopic results

From the discussion in last section, it was found that presence of R_s and/or C_{SiO2} tends to yield a carrier density N_{sm} higher than the true value of N_s. This does not explain the difference between microscopic and macroscopic results, where a smaller value of carrier density is obtained in macroscopic C-V measurements. So we have to consider other factors possibly responsible for this inconsistency. For example, errors may exist in the estimation of NWs area from SEM images. In the following, the reduction of active area in C-V characterization caused by surface-state-induced depletion effect is discussed.

As known, nanostructures are especially sensitive to surrounding conditions due to their large surface-to-volume ratio, making them ideal candidates for gas sensing and UV detecting applications. Regarding ZnO NWs, it has been found that in ambient condition, oxygen molecules adsorb on the ZnO surface and can capture electrons from inside the semiconductor [14-17], causing a surface charge depletion layer. In consequence of the surface-states-induced band bending effects, the depleted shell layer exhibits a lower carrier density hence a lower conductivity in comparison with the conductive core material. In effect, the effective cross section of the NW (A_{eff}) for current transport is smaller than its geometrical cross section (See Figure 5.10). For dielectric-integrated NWs assemblies, the surface charge induced by the surrounding dielectric can also significantly modify conduction mechanisms in NWs [18]. For example, under transmission electron microscopy (TEM) observation, a core-shell contrast in electron density has been revealed where the shell of the polymer-coated ZnO NWs has a weaker electron density than their cores [9]. In some cases, even *p*-type ZnO occurs as a result of significant band bending effect, as shown by SPM measurements [9]. Of course, the specific surface-induced depletion or accumulation phenomenon depends on the surrounding materials properties as well as the electrical properties of the NWs themselves. From Equation (2-15), calculated N_s has an inverse square relationship with the effective semiconductor area A_{eff}. In the previous analysis of C-V characteristics, A was evaluated from SEM images and homogeneous carrier density inside the NWs was assumed. According the discussion here, this can probably be not the real case. So we believe that the discrepancy between microscopic and macroscopic characterization results can be ascribed to the difference of geometrical NWs area from effective NWs area in C-V measurement.

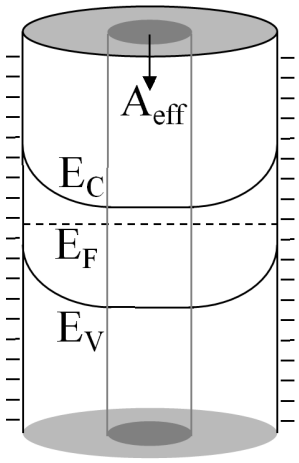

Figure 5.10: Schematic view of band bending for NW structure induced by surface negative charges. A depleted shell layer is produced reducing the effective cross section of the NW (A_{eff}).

However, although a smaller A_{eff} can be helpful to correlate the characterization results from SPM and C-V measurements, we should not take this for granted. In fact, if we consider that the much lower carrier density values obtained in C-V analysis (more than 40 time smaller than results from SCM/SRRM) is due to a smaller A_{eff}, then from the relationship $Ns \propto A_{eff}^2 \propto d^4$, the depleted width along the radial direction of the NWs should be significant, at least half of their diameter. This is unlikely the case simply because we did not observe a corresponding core-shell contrast in SSRM measurements for both NWs samples (See Figure 4.4 and 4.5). So we finally turned our attention to the theoretical model that has been used in C-V depth profiling.

Before we have used the classical Mott-Schottky model that was derived for semiconductor bulk material for C-V analysis, and typically the Equation (2-15) was taken into use to calculate the carrier density of the NWs where the depletion width is assumed to exhibit a linear dependence on the square root of the applied reverse voltage. However, the NWs structure where the NWs are separated from each other by the dielectric material represents a significantly different geometry. And this may introduce a considerable departure of its C-V characteristics from that in bulk sample. For example, the depletion width inside a single ZnO NW has been found to be linearly dependent on the applied voltage rather than its square root value (Figure 5.11) [19]. Furthermore, the NWs array geometry is likely to be essentially different from a single NW in respect of contact capacitance because the electric field distribution will be modified by the presence of other NWs. A discussion on this issue can be found in Ref [20, 21]. So we propose that the Mott-Schottky bulk model is no longer applicable to obtain the real carrier concentration of the NWs and a more reasonable analysis and interpretation of the C-V measurement results should be performed, which may eventually explain the difference or even achieve an agreement between microscopic and

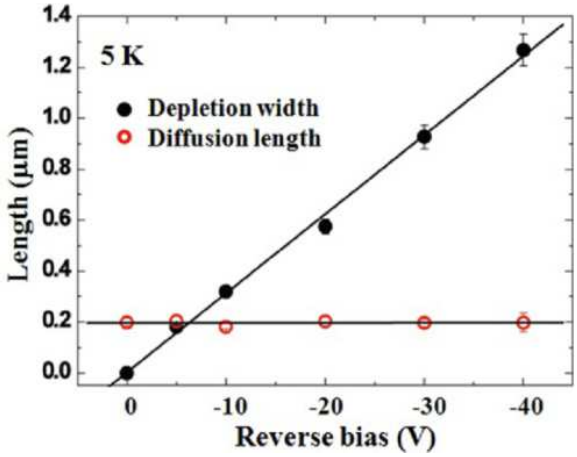

Figure 5.11: Diffusion length of the excitons and carrier depletion width in a ZnO NW as a function of the reverse bias condition. The values are obtained from the CL intensity profiles in CL measurement. Ref [19].

macroscopic characterization.

5.6 Conclusion

In this chapter, I-V measurement and C-V profiling were carried out on collective ZnO NWs samples. Pt contact was fabricated with the NWs by EBD method and Schottky contact behaviors have been observed for both CBD NWs and MOCVD NWs samples. From C-V characteristics, carrier concentrations were determined around 7×10^{16} cm^{-3} and 4×10^{16} cm^{-3} for CBD grown ZnO NWs and MOCVD grown ZnO NWs, respectively. This value is more than one order of magnitude lower than the results from SPM analysis. The big difference of results from C-V analysis and SPM analysis was discussed. After analyzing the impacts of large series resistance and the additional capacitance corresponding to SiO_2 matrix, in the end, the inconsistency between microscopic and macroscopic characterization results was partly attributed to the reduction of effective NWs area due to surface-state-induced depletion effect. Moreover, the inapplicability of classical C-V depth profiling model derived for bulk material was pointed out.

References:

[1] Wang, Z. L. (2009). ZnO nanowire and nanobelt platform for nanotechnology. Materials Science and Engineering: R: Reports, 64(3), 33-71.

[2] Wang, Z. L., & Song, J. (2006). Piezoelectric nanogenerators based on zinc oxide nanowire arrays. Science, 312(5771), 242-246.

[3] Ip, K., Heo, Y. W., Baik, K. H., Norton, D. P., Pearton, S. J., Kim, S., ... & Ren, F. (2004). Temperature-dependent characteristics of Pt Schottky contacts on n-type ZnO. Applied physics letters,84, 2835.

[4] Oh, M. S., Hwang, D. K., Lim, J. H., Choi, Y. S., & Park, S. J. (2007). Improvement of Pt Schottky contacts to n-type ZnO by KrF excimer laser irradiation. Applied Physics Letters, 91(4), 42109-42109.

[5] Endo, H., Sugibuchi, M., Takahashi, K., Goto, S., Sugimura, S., Hane, K., & Kashiwaba, Y. (2007). Schottky ultraviolet photodiode using a ZnO hydrothermally grown single crystal substrate.Applied physics letters, 90(12), 121906.

[6] Hussain, I., Soomro, M. Y., Bano, N., Nur, O., & Willander, M. (2012). Interface trap characterization and electrical properties of Au-ZnO nanorod Schottky diodes by conductance and capacitance methods. Journal of Applied Physics, 112(6), 064506.

[7] Klason, P., Nur, O., & Willander, M. (2008). Electrical characteristics and stability of gold and palladium Schottky contacts on ZnO nanorods. Nanotechnology, 19(47), 475202.

[8] Ye, J. D., Gu, S. L., Zhu, S. M., Liu, W., Liu, S. M., Zhang, R., ... & Zheng, Y. D. (2006). Electroluminescent and transport mechanisms of n-ZnO/p-Si heterojunctions. Applied Physics Letters, 88(18), 2112.

[9] Latu-Romain, E., Gilet, P., Chevalier, N., Mariolle, D., Bertin, F., Feuillet, G., ... & Chelnokov, A. (2010). Surface-induced p-type conductivity in ZnO nanopillars investigated by scanning probe microscopy. Journal of Applied Physics, 107(12), 124307.

[10] Krtschil, A., Look, D. C., Fang, Z. Q., Dadgar, A., Diez, A., & Krost, A. (2006). Local p-type conductivity in n-GaN and n-ZnO layers due to inhomogeneous dopant incorporation. Physica B: Condensed Matter, 376, 703-706.

[11] Blood, P., & Orton, J. W. (1992). The electrical characterization of semiconductors: majority carriers and electron states (Vol. 2). Academic Pr. 315-322

[12] Krunks, M., Dedova, T., Kärber, E., Mikli, V., Acik, I. O., Grossberg, M., & Mere, A. (2009). Growth and electrical properties of ZnO nanorod arrays prepared by chemical spray pyrolysis. Physica B: Condensed Matter, 404(22), 4422-4425.

[13] Blood, P., & Orton, J. W. (1992). The electrical characterization of semiconductors: majority carriers and electron states (Vol. 2). Academic Pr. 295-308

[14] Kind, H., Yan, H., Messer, B., Law, M., & Yang, P. (2002). Nanowire ultraviolet

photodetectors and optical switches.Advanced materials, 14(2), 158.

[15] Soci, C., Zhang, A., Xiang, B., Dayeh, S. A., Aplin, D. P. R., Park, J., ... & Wang, D. (2007). ZnO nanowire UV photodetectors with high internal gain. Nano letters, 7(4), 1003-1009.

[16] Fan, Z., Chang, P. C., Lu, J. G., Walter, E. C., Penner, R. M., Lin, C. H., & Lee, H. P. (2004). Photoluminescence and polarized photodetection of single ZnO nanowires. Applied Physics Letters, 85(25), 6128-6130.

[17] Schlenker, E., Bakin, A., Weimann, T., Hinze, P., Weber, D. H., Gölzhäuser, A., ... & Waag, A. (2008). On the difficulties in characterizing ZnO nanowires. Nanotechnology, 19(36), 365707.

[18] Yoon, J., Girgis, A. M., Shalish, I., Ram-Mohan, L. R., & Narayanamurti, V. (2009). Size-dependent impurity activation energy in GaN nanowires. Applied Physics Letters, 94(14), 142102.

[19] Hwang, J. S., Donatini, F., Pernot, J., Thierry, R., Ferret, P., & Dang, L. S. (2011). Carrier depletion and exciton diffusion in a single ZnO nanowire. Nanotechnology, 22(47), 475704.

[20] Rudaa, H. E., & Shik, A. (2004). Contact phenomena in nanowire arrays. Applied physics letters, 85(6), 1030.

[21] Achoyan, A., Petrosyan, S., Craig, W., Ruda, H. E., & Shik, A. (2007). Electron screening in nanostructures. Journal of applied physics, 101(10), 104308.

Chapter 6

Related applications of SCM/SSRM on ZnO based nanostructures

Many of the employed SPM techniques for the electrical characterization of semiconductors were originally developed in the aim of realizing two-dimensional (2D) dopant profiling with high-resolution, in order to accurately calibrate simulations of semiconductor processing schemes to improve their accuracy and aid in the design and development of nanoscale devices [1-2]. This is especially the cases of SCM and SSRM. Nevertheless, theses techniques have since their emergence also found a wide range of other applications such as assessment of electronic and optoelectronic devices, evaluation of dielectric films, characterization and analysis of defects in semiconductors as well as characterization on diverse nanostructures. Chapter 3 and Chapter 4 have reported the application of SCM and SSRM to carrier profiling at a nanometer scale, respectively. This chapter explores the capability of these two techniques to electrically characterizing ZnO-related material in other aspects by performing SCM/SSRM measurements on some specific ZnO-based nanostructures. For information, like the work presented before, without further mention, Pt/Ir coated Si tip and highly doped conductive diamond coated tip are used for SCM and SSRM measurements, respectively.

6.1 SCM/SSRM on ZnO:Sb film

Unlike Si being a material that can be "perfectly" grown with very low densities of extended defects such as dislocations, ZnO material (also GaN) may contain rather higher defect densities which can significantly impact its electrical properties. In the first case, we investigate the relation between the local electrical properties and extended defects in doped ZnO 2D films. In the effort of *p*-type ZnO realization in MADFIZ project, Sb doped ZnO film was grown by MOCVD method on r-plane sapphire substrate and ZnO substrate (in GEMAC). The doping concentration is higher than 10^{19} cm^{-3} as revealed by SIMS. From structural investigations under TEM, defects including dislocations and precipitation of Sb atoms are noticed in the grown film, as shown in Figure 6.1. In order to evaluate the impacts of these kinds of imperfection and elucidate the relationship between electronic behaviors and structural defects, examination of electrical properties including conductivity and dopant concentration with high spatial resolution will be helpful. Therefore SCM and SSRM are conducted on the film's cross section obtained from simple cleavage.

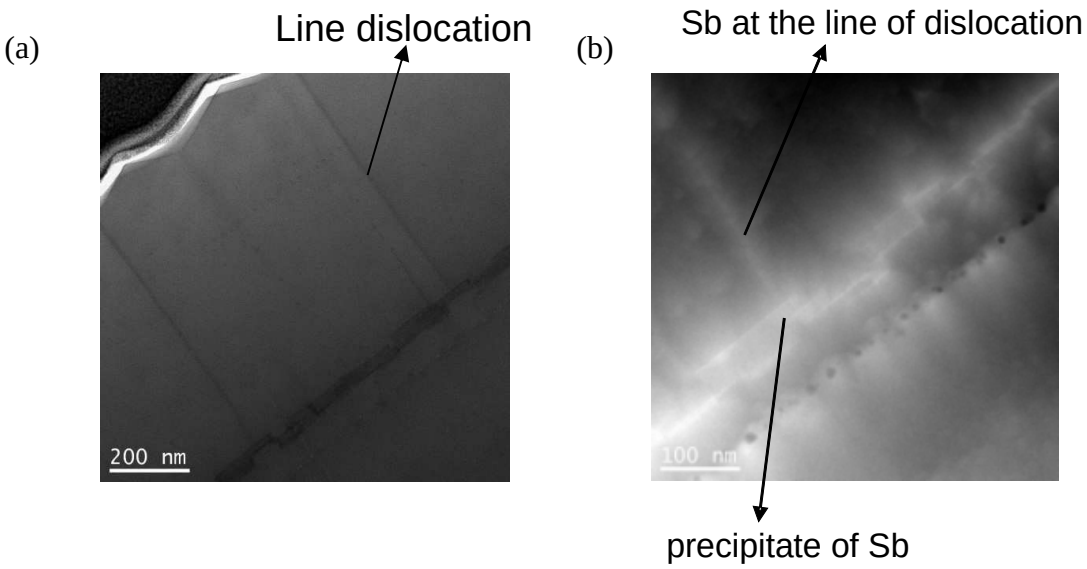

Figure 6.1: (a) and (b) TEM images on ZnO:Sb film grown on ZnO substrate by MOCVD. Dislocations and precipitate of Sb are observed as indicated by the arrows. (TEM images from Gilles Patriarche, LPN)

Simultaneously acquired topographic and SCM electrical images of ZnO:Sb films on sapphire are presented in Figure 6.2. It should be mentioned that the sample with sapphire substrate was chosen for SCM/SSRM investigation as a result of sample preparation problem. In Figure 6.2(a) the topographic features such as grain boundaries can be noticed. From SCM data image (Figure 6.2(b)), the 2D layer is identified as *n*-type and a contrast between grains bodies and boundaries is resolved. In general, brighter colors corresponding to higher SCM data amplitudes are correlated to the grain boundaries. In contrast, the grains, especially those possessing relatively large dimensions produce weaker SCM data signals appearing as darker colors (as indicated by the line profile). This implies a lower carrier density near the grains boundaries with respect to the grains bodies. Note that V_{dc} has been optimized on the base of a series of values to obtain the largest SCM signal. For clearness, the insulating sapphire substrate showing a slightly negative SCM data is due to the wear of the tip which is considered to be also responsible for the weak spatial resolution. The occurring noise for the three regions marked in Figure 6.2(c) can be attributed to the wear of the tip metal coating as analyzed in the Chapter 3 (section 3.3.2), where the tip depletion effect weakens the SCM response of the sample.

The SSRM result on the same sample is presented in Figure 6.3. A V_{bias} of -0.5 V and a tip force ~1.5 μN were applied on the sample. The interface of the sapphire substrate and the grown film can clearly be seen both in topography channel and SSRM data channel (SSRM data have been converted to SSRM resistance). In the SSRM resistance image, a darker color represents a larger measured resistance and a brighter color a smaller one. Assuming a similar

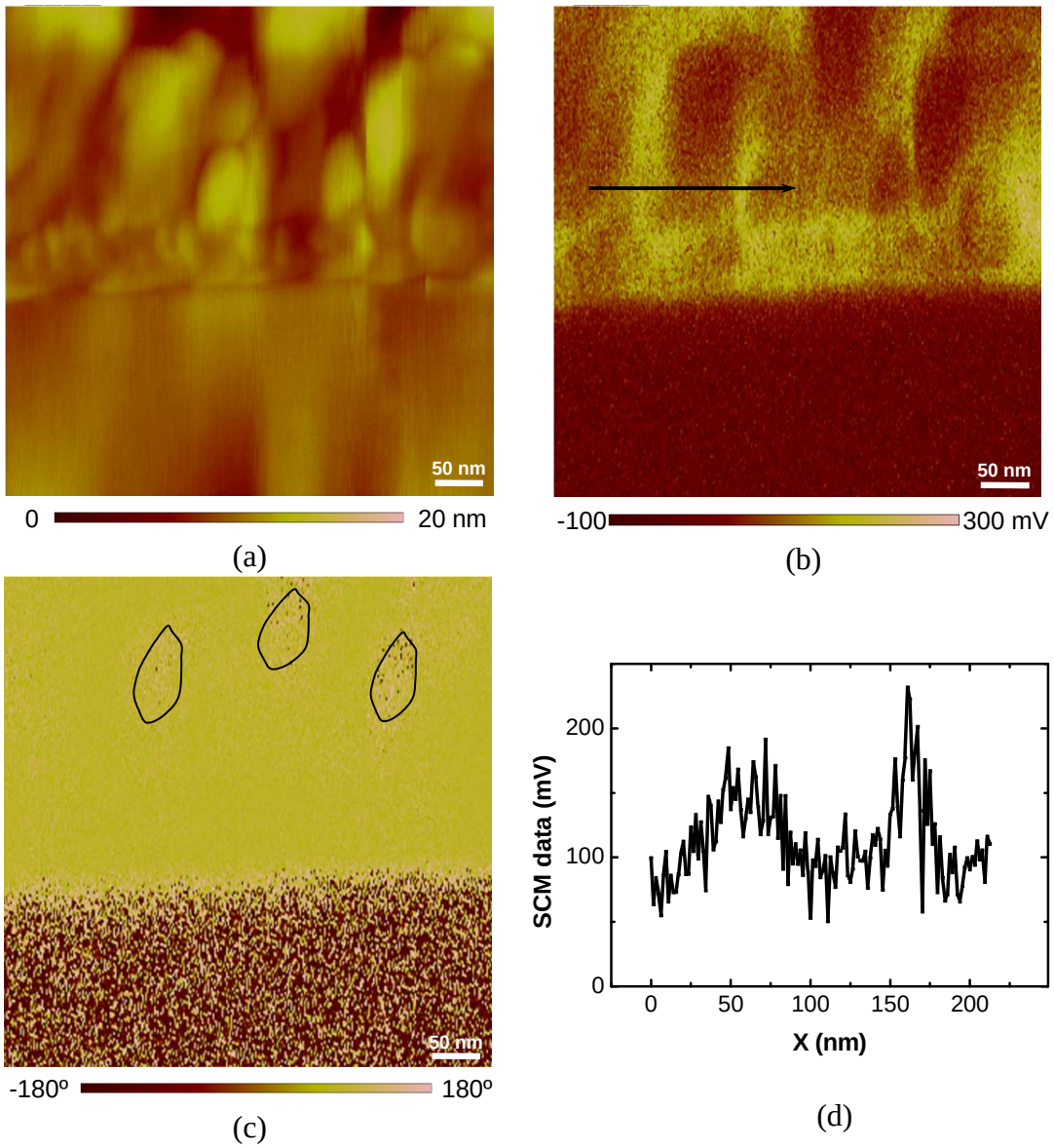

Figure 6.2: SCM result of an area of 500 nm × 500 nm on the cross section of a ZnO:Sb film. (a) Topography image. (b) SCM data image acquired at the same time. (c) SCM phase image. (d) Profile of the line indicated in (b) revealing a higher SCM amplitude for the grains boundaries than the grains bodies. Measurement condition: V_{ac}=1000 mV, V_{dc}=-1 V.

model of the tip-sample contact (resistance proportional to resistivity), it can be known that the grains boundaries exhibits a smaller conductivity with respect to the grain bodies. This phenomenon is in consistency with the result from SCM analysis. In addition, the result again shows that SSRM has a spatial resolution superior to SCM.

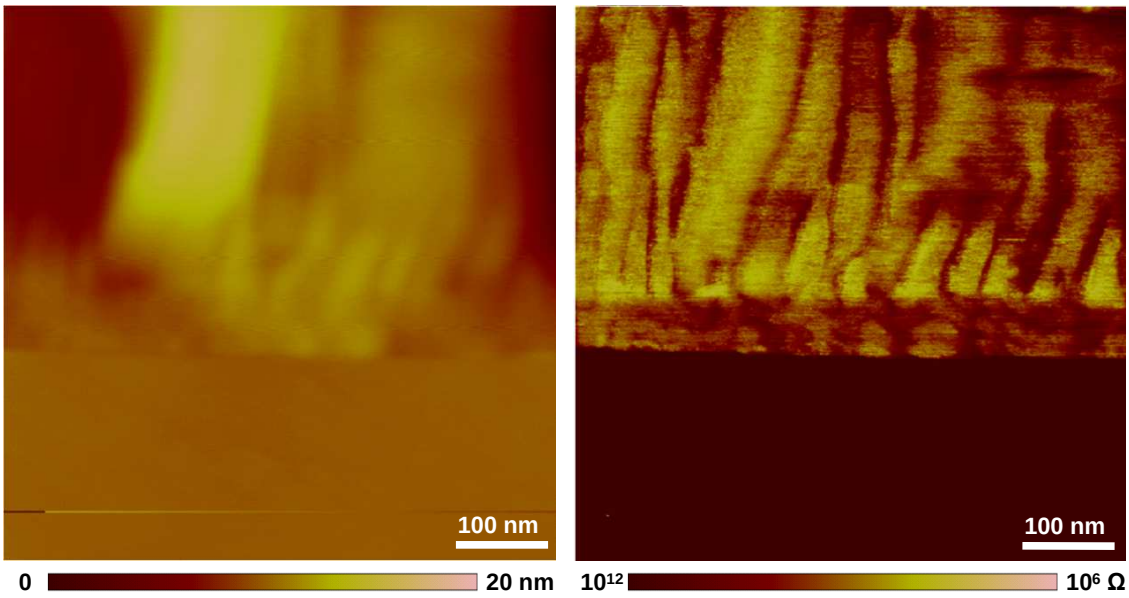

(a) (b)

Figure 6.3: SSRM result of an area of 500 nm × 500 nm on the cross section of the ZnO:Sb film. (a) Topography image. (b) SSRM data image recorded at the same time. A lower net carrier density is noticed for the grain boundaries and the near-substrate region. Measurement condition: F_{tip}~1.5 μN, V_{bias}=-0.5 V.

It is known that topographic variations can influence the electrical measurement through the variation of the tip-sample contact area, and thus SPM signal. So whilst the topographic features is able to provide an indication of grains and grain boundaries, significant care must be taken in interpreting electrical data on the purpose of demonstrating that the observed contrast in electrical images is genuinely related to the film's local electrical properties and not a consequence of changes in tip-sample interaction area. In some cases, the observed contrast between the grain boundaries and the grains could be reversed by varying the applied V_{dc}, hence ruling out topographic artifacts in the experiments [3]. In the case here, although a certain correspondence do exist between topography features and electrical contrast (both for SCM and SSRM), which usually exists in electrical SPM measurement, it is not the case for the entire imaged area. So we believe that the contrast in SCM and SSRM signal is correlated to the local electrical properties instead of topographically induced artifacts. For the area in the vicinity of substrate-epilayer interface (within ~50 nm distance from the interface), it shows an apparently larger SSRM resistance without significant topography features. This is likely to be related to the formation of gahnite ($ZnAl_2O_4$) at high temperature for the film growth.

During the efforts on reliable *p*-type doping of ZnO, special attention has been focused on the group-V elements (such as N, P, As, and Sb) due to the possibility of creating ZnO p-type conduction. P-type behavior has been reported by different research groups for Sb-doped ZnO (ZnO:Sb) [4-8]. In an attempt to explain the acceptor behavior of group V elements (As, Sb)

in ZnO, Limpijumnong *et al*. [9] proposed a model based on first-principle calculations. In this model, the large-size-mismatched group V dopant ions occupy Zn sites but form a complex with two spontaneously induced Zn vacancies. These As_{Zn}-$2V_{Zn}$ or Sb_{Zn}-$2V_{Zn}$ complexes create shallow acceptor levels and are responsible for *p*-type conductivity. However, Janotti and Van de Walle have pointed out that the formation of these complexes is unlikely from an energetic point of view, and entropic considerations argue against their formation because the complexes are comprised three constituents [10]. In the study of electrical behavior of Sb in ZnO:Sb layers doped in a wide concentration range (MBE grown method), H. Y. Liu *et al* found that electron concentration undergoes an initial increase with increasing Sb concentration indicating a donor behavior of Sb in ZnO. Nevertheless, a decrease in electron density was noticed for further increasing T_{sb} (higher Sb doping level) and it was explained by the formation of acceptor-type compensating defects involving Sb dopant on O sites (Sb_O) [11]. In a recent study of H. Liang *et al* [12], they reported *p*-type Sb doped ZnO films (MOCVD grown method) with low mole ratio of Sb precursor and a change of *p*-type to *n*-type as the Sb molar content increases further. These results reflect the complexity of Sb doping behavior in ZnO. In our case, an enrichment of Sb at the dislocations in the ZnO:Sb film has been revealed, which correlates to a reduction in net carrier density with respect to the grain bodies. We propose the explanation that the film is compensated (by either Sb_{Zn}-$2V_{Zn}$ or Sb_O) and the relatively lower carrier concentration near grain boundaries is due to a larger extent of the compensation in consequence of a higher Sb density.

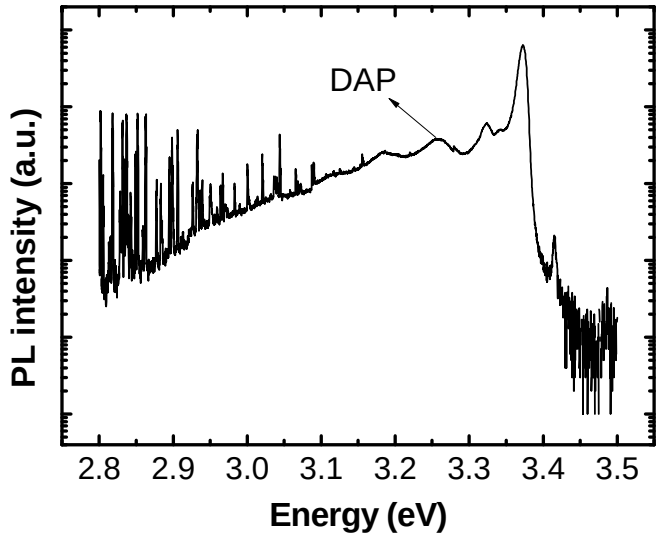

Figure 6.4: Low temperature (4.2 K) PL spectrum of ZnO:Sb film. (Measurement done by Alain Lusson at GEMAC)

Low temperature (4.2K) photoluminescence (PL) measurement was performed on the measured sample using a He-Cd laser with an excitation wavelength of 325 nm and the PL spectrum is shown in Figure 6.4. In addition to the band edge excitonic transitions usually

observed in ZnO (peaks at energy between 3.3 and 3.7 eV), the peak around 3.257 eV was identified as the transitions from donor-acceptor pair (DAP), indicating the existence of acceptors in the sample. This confirms the proposed explanation of formation of Sb-related acceptors in SCM/SSRM analysis.

6.2 SCM/SSRM on ZnO-based NWs--attempt of *p*-type doping

Although progress has been made, reliable and stable *p*-type ZnO still represents a crucial challenge in the opto-electrical field using ZnO. *p*-type doping is difficult to realize on ZnO bulk and thin films since ZnO exhibits naturally *n*-type conduction due to the presence of residual intrinsic defects and extrinsic impurities (Chapter 2). Recent works tend to demonstrate that the situation is quite different in the case of ZnO nanowires, and p-type doping could be more easily achieved. This is likely to be related to the high structural quality that can be achieved regardless of the substrate nature and the less impact of impurity out-diffusion from the substrate (Al from sapphire, Li from hydrothermal ZnO) on long nanowires than on thin 2D films. ZnO nanowires have been demonstrated to grow without extended defects (dislocations and stacking faults) on a variety of commonly used cheap and large-area substrates such as silicon, sapphire and glass [13-17].

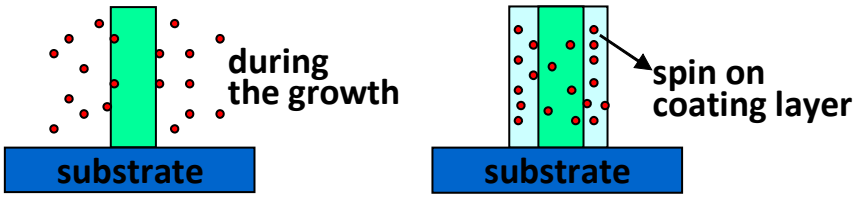

(a) (b)

Figure 6.5: Two mechanisms for the incorporation of doping impurities in ZnO NWs for obtaining *p*-type ZnO. (a) *In situ* doping in which case the impurities in gas phase are introduced in the growth process of the NWs. (b) *Ex situ* doping where a layer containing dopant atoms is spin-coated after the growth of non-doped ZnO NWs, followed by a thermal annealing process to induce the diffusion of impurities into the NWs.

Indeed it is noteworthy that *p*-type doping seems more easily attainable when ZnO nanostructures are involved instead of 2D layers or bulk crystals. As previously addressed, *p*-type ZnO and *p-n* ZnO homo-junctions have been realized by different groups. In the project that this thesis work takes part in, efforts have been done to obtain *p*-type ZnO NWs. For this purpose, two approaches were used for the incorporation of doping impurities in ZnO NWs, i.e. *in situ* doping and *ex situ* doping. In *in situ* doping case, the impurities in gas phase

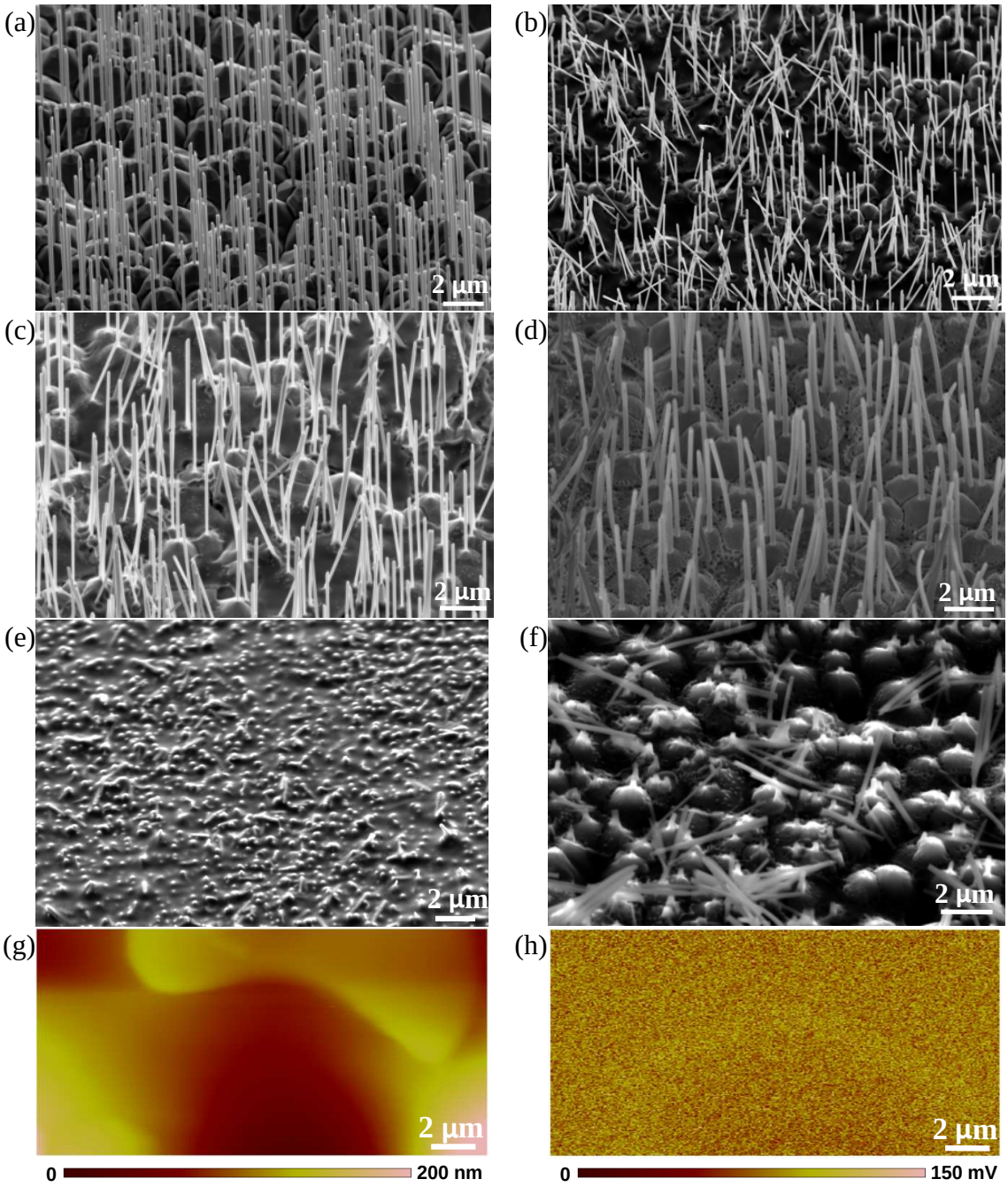

Figure 6.6: (a) Original grown non-doped ZnO NWs. (b) ZnO NWs sample after the spin-coating with the solution containing P impurities. (c) ZnO NWs sample after annealing process at 750 ºC to induce P diffusion into the NWs. (d) ZnO NWs sample after performing an etching process. (e) ZnO NWs sample after the planarization process of the NWs field. (f) Another area of the NWs sample before planarization process showing the damage on the NWs due to the previous processes. (g) Topography image of the area 10 µm × 5 µm in SCM measurement. (h) SCM image collected at the same time with the topography image. No contrast for ZnO NWs is observed.

are introduced in the growth process of the NWs by MOCVD. On the contrary, for *ex situ* doping, non-doped NWs are first grown (MOCVD), then a layer containing impurity atoms is spin-coated on the NWs, followed by a thermal annealing process to induce the diffusion of

impurities into the NWs. Finally, the grown NWs are investigated by different techniques and their electrical properties are studied by SCM/SSRM to detect possible *p*-type ZnO existence.

6.2.1 *Ex situ* doping: P doped ZnO NWs

Another approach to realize doping of ZnO NWs is to introduce the impurities after the growth of them. Figure 6.6(a)~(e) show the SEM images of the sample after each step including the growth of original non-doped NWs, spin-on-coating with P impurities, thermal annealing to activate diffusion of P into the NWs, O_2 etching, dip-coating of SiO_2 for planarization. While the original NWs show good structural quality, each step during the whole process tends to damage the overall NWs geography in terms of orientation and alignment. Also, large areas broken-down of the NWs were observed (an example in Figure 6.6(f)) before the planarization process which probably occurred during the previous process and long-journey transport. This has brought severe problem for the SCM/SSRM analysis on the sample making it very difficult even to observe contrast between the NWs and the SiO2 matrix due to significant absence of NWs vertical to the substrate. An example of SCM measurement is shown in Figure 6.6(g)-(h). No NWs were successfully imaged. What have been encountered highlights the importance of carefulness during the preparation of NWs sample to prevent them from breaking down, although in some technique process (etching for instance) it is not easy to avoid it.

6.2.2 *In situ* doping: ZnO/ZnO:Sb core-shell NWs

NWs having a ZnO/ZnO:Sb core-shell structure are studied. SEM images of the as grown non-intentionally doped ZnO core NWs are shown in Figure 6.7. The NWs exhibit a length about 3.7 μm and a diameter range 70~130 nm (Figure 6.7(a) and (b)). The shell layer growth of ZnO:Sb was carried out by adding Sb impurity in the growing process, which results in a similar length as the original NWs and an increased diameter in the range between 300 and 450 nm, as shown in Figure 6.7(c) and (d). The Sb density inside the shell layer is estimated to be around 6×10^{19} cm^{-3} according to the SIMS measurement on a 2D ZnO:Sb film that was grown in the chamber at the same time. The NWs field was planarized by the procedure presented before with SEM images in Figure 6.7(e) and (f). Then after a polishing process and forming backside metal contact, the core-shell NWs were characterized by SCM/SSRM.

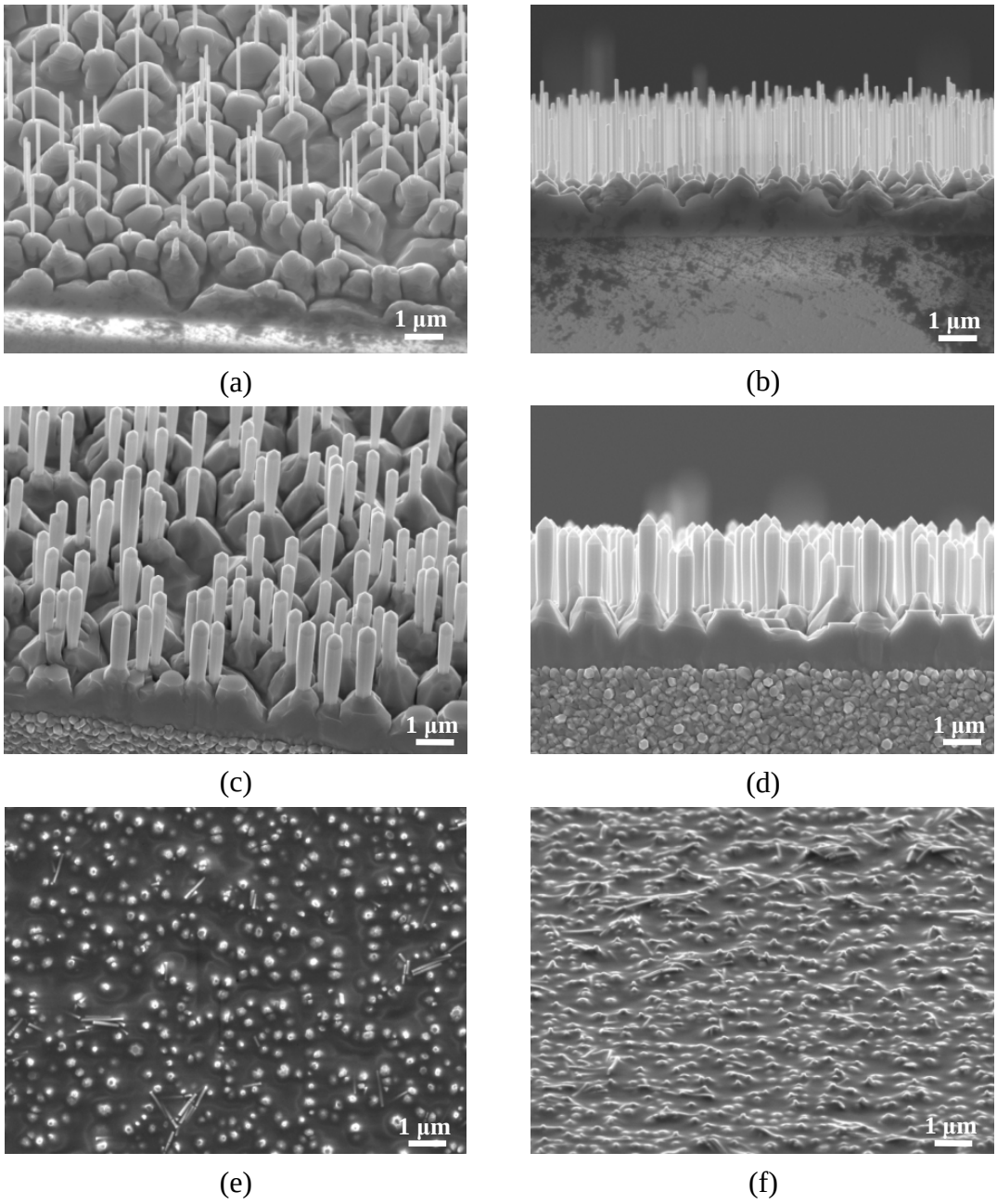

Figure 6.7: (a) and (b) Tilt view and side view of the as-grown ZnO core in SEM, respectively. (c) and (d) Tilt view and side view after the growth of the ZnO:Sb shell layer in SEM, respectively. (e) and (f) Top view and tilt view after the dip-coating process on the ZnO/ZnO:Sb core-shell NWs field. (a)~(d) were done in GEMAC.

Figure 6.8 shows the representative result of SSRM on the sample. From the topography image in Figure 6.8(a), the NWs can be recognized and the core of the NWs may also be identified appearing as bright dots at the center of them as a result of the polishing process. SSRM resistance image in Figure 6.8(b) was acquired simultaneously. Evidently a core-shell contrast is resolved indicating a difference in SSRM resistance during the tip scan between the ZnO core and the ZnO:Sb shell layer. In order to better see this contrast, a profile along the line indicated in Figure 6.8(c) is presented in Figure 6.8(d). It can be observed that the

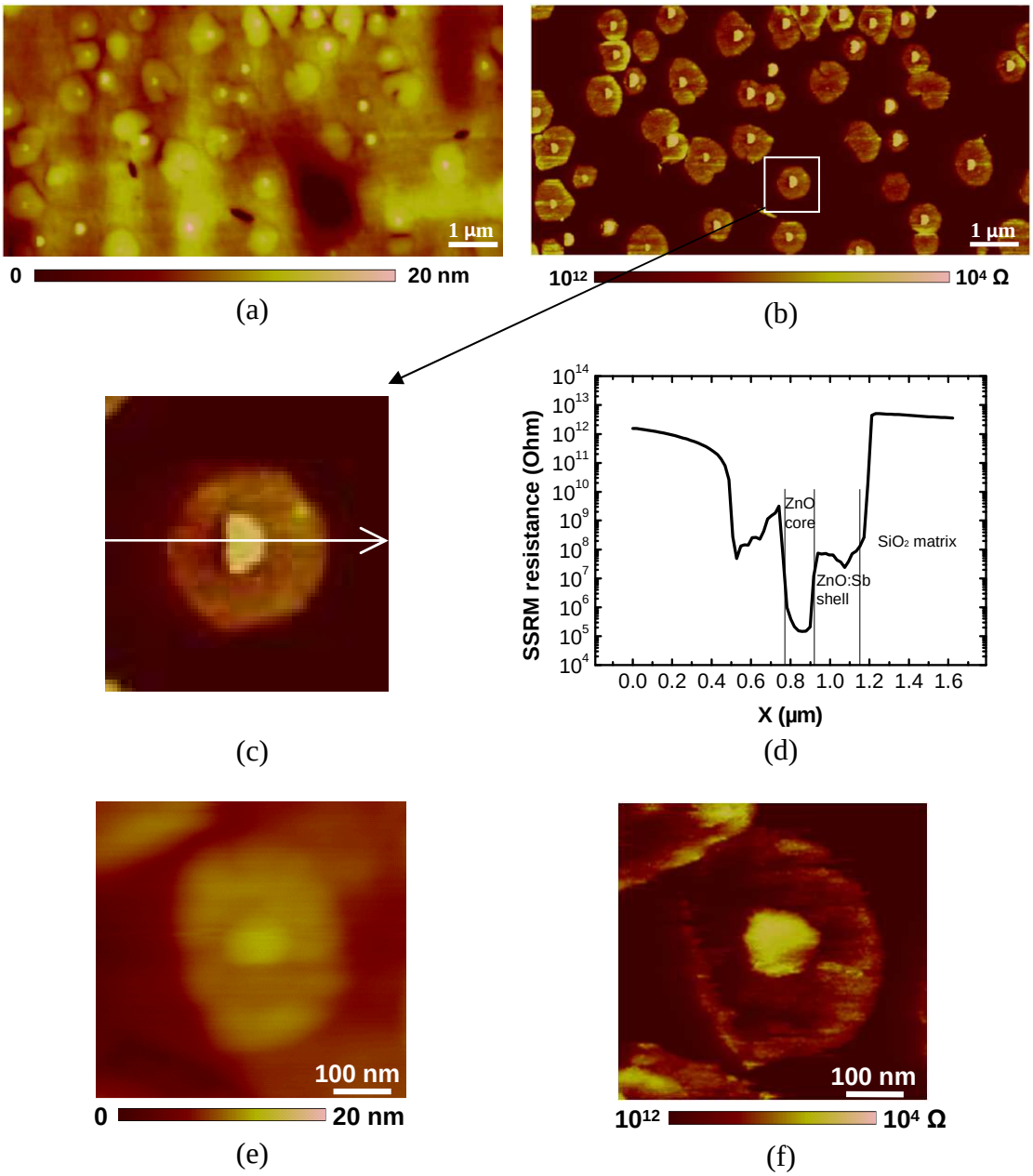

Figure 6.8: SSRM result of an area of 10 µm × 5 µm on the ZnO/ZnO:Sb core-shell NWs simple. (a) Topography image. (b) SSRM resistance image giving a contrast between the core of ZnO and shell of ZnO:Sb. (c) Zoomed in area of the rectangle in (b). (d) SSRM resistance profile of the arrowed line indicated in (c). For a single NW, the shell corresponds to a larger resistance than the core of the NW. F_{tip} of ~1.5 µN and V_{bias} of -3 V were used. (e) Topography AFM image after tip etching on the NW area to reduce the topographic features. (f) Corresponding SSRM resistance image still shows apparent core-shell difference, indicating the contrast correlating to electrical properties of the core and the shell. The image quality is not as good as before due to wear of the tip.

resistance for the core is near 3 orders of magnitude lower than the shell, indicating a much higher resistivity of the ZnO:Sb part in the NW. Note that the dimension of the low resistance part corresponds well with the diameter range of the as-grown ZnO NWs. In addition, a general correlation of topography contrast on NWs with that in electrical response can be

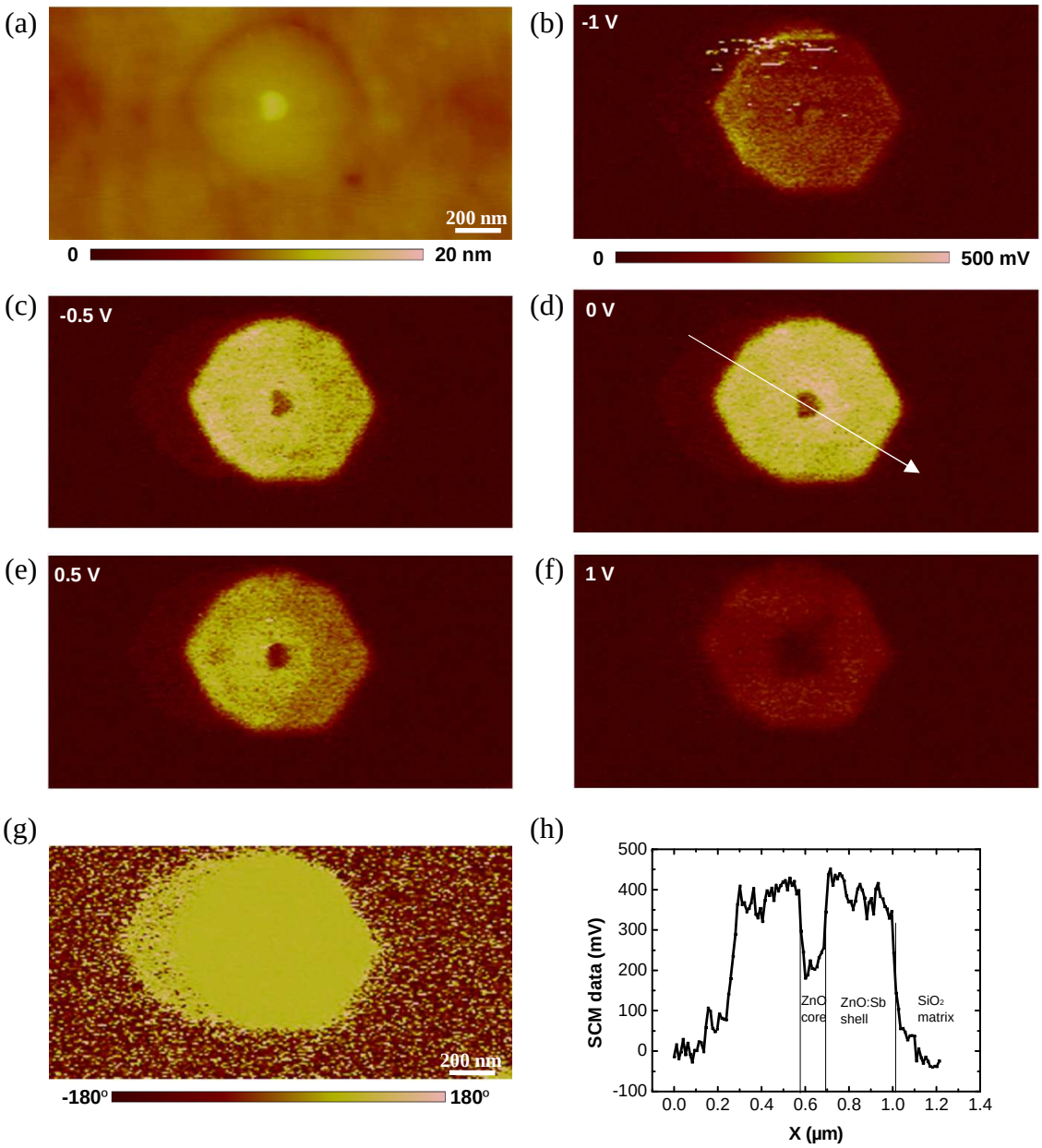

Figure 6.9: SCM results on a NW with ZnO/ZnO:Sb core-shell structure. Scan area: 2 μm × 1 μm. (a) Topography image with roughness RMS value ~0.87 nm. (b)-(f) SCM data image at a series of V_{dc} of -1 V, -0.5 V, 0 V, 0.5 V, 1 V. Core-shell contrast of SCM data is observed for certain V_{dc} and V_{dc}=0 V gives the strongest signal. (g) SCM data phase image. The NW is identified being of *n*-type conductivity. (h) SCM data profile along the line marked in (d).

noticed. In order to rule out the possibility of topography-change-induced contrast, larger forces can be applied on the NWs to enable a considerable etching effect and remove the difference in topography. This was done on a single NW, and the core-shell difference in resistance still exists after the disappearance of apparent topographic variation (Figure 6.8(e) and (f)), demonstrating the observed contrast in electrical image is genuinely related to the different electrical properties of the core and the shell from each other. This fact can also help to explain the absence of expected core-shell contrast for some NWs in Figure 6.8(b), which

is probably a consequence of the lack of exposure for the core material. It is worth pointing out that as the tip scans at a large force in SSRM, tip wear problem may become serious and consequently the contrast of the features (core-shell in this case) can be lost.

SCM was also performed with a V_{ac} of 1000 mV and a series of V_{dc}. Figure 6.9 presents the results on a single NW. The investigated area has a roughness of RMS value ~0.87 nm and the height difference between the core (bright dot at the center of Figure 6.9(a)) and the shell is less than 3 nm. SCM images under various V_{dc} between -1 and 1 V with a 0.5 V step are shown in Figure 6.9(b)-(f). For straightforward comparison, they share the same color scale of SCM data in Figure 6.9(b). As can be observed, the SCM response of the NW displays a dependence of V_{dc} and the strongest signal is obtained at V_{dc}=0 V where a clear core-shell contrast is observable. The darkness at the center corresponds to smaller SCM data amplitude indicating a higher free carrier density with respect to the shell layer. This conclusion is totally consistent with that from SSRM analysis, assuming similar carrier mobility for the two parts of the NWs. The profile of the line marked in Figure 6.9(d) is plotted in Figure 6.9(h), which better presents the significant decrease of SCM data when the tip scans across the core of the NW. Note that from the SCM data phase image in Figure 6.9(g), both the core and the shell of the NW is recognized as *n*-type. Although no direct calibration analysis was done for this sample, a simple estimation of the compensation effect can be made with the help of calibration curves established in Chapter 3. The largest SCM data obtained for the ZnO core and ZnO:Sb shell are ~235 mV and ~400 mV, respectively. Assuming that the core of NWs has similar residual carrier density to the MOCVD ZnO NWs studied in Chapter 3 (page 68), i.e. 2×10^{18} cm^{-3}, and that similar dependence of SCM data on the carrier density exists, then by comparing the SCM data results, the resulted carrier density after Sb doping in the ZnO:Sb shell layer is estimated to be around 3×10^{17} cm^{-3}, about one order of magnitude lower than the ZnO core without Sb doping.

The characterization of SCM/SSRM on the ZnO/ZnO:Sb core-shell structured NWs did not detect a *p*-type shell layer, which means no *p*-type ZnO was achieved for the grown NWs doped by Sb. However, the core-shell contrast was observed both in SCM and SSRM imaging. It has been found that the shell layer of ZnO doped by Sb possess a lower free carrier concentration in comparison with the nid ZnO core. So again it is reasonable to conclude that the shell layer is compensated by the forming of Sb-related acceptors. Although no *p*-type was realized, the results of SCM/SSRM definitely demonstrate the ability of both to characterize radial difference in ZnO NWs to study the local electrical properties.

Figure 6.10 shows the PL spectrum obtained on the same ZnO/ZnO:Sb core-shell structure that has been investigated. Typical band edge excitonic transitions of ZnO NW are seen between 3.3 eV and 3.37 eV. Although some peaks are observable between 3.2 eV and 3.3 eV,

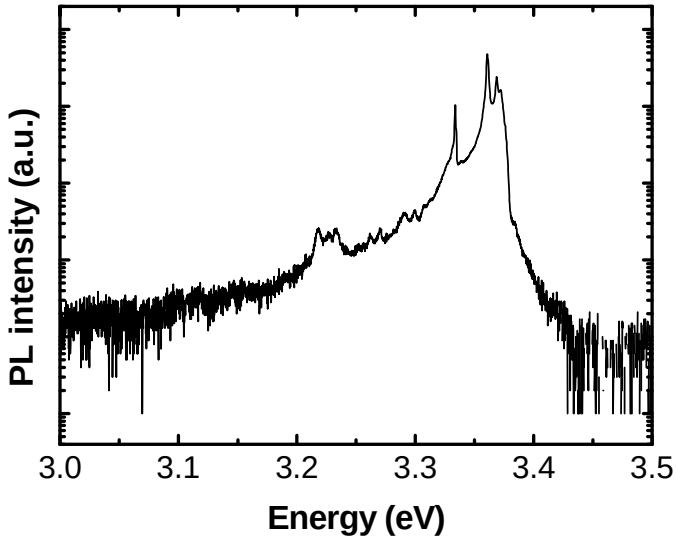

Figure 6.10: Low temperature (4.2 K) PL spectrum of the ZnO/ZnO:Sb core-shell NWs. (Measurement done by Alain Lusson at GEMAC)

no clear evidence can be affirmed concerning the presence or the absence of a donor-acceptor transition in the spectrum. However, this does not rule out completely our hypothesis of doping compensation due to Sb-related acceptors as indicated by the SCM analysis.

6.3 SCM/SSRM on ZnO/ZnMgO core-multishell coaxial structures

One-dimensional (1D) semiconductor NWs heterostructures are potentially ideal functional components for nanometer-scale electronics and optoelectronics [18-21]. In particular, heteroepitaxial NW quantum structures with well-defined interfaces greatly increase the versatility and power of building blocks used in many nanoscale devices. Two types of NW quantum structures are possible, depending on the composition modulation along either the axial or radial direction of the NWs. NW quantum structures with composition modulation along the radial direction can be formed into coaxial NW quantum structures when the overlayers in the quantum structures are covered uniformly and homogeneously over the side walls. For these coaxial quantum structures, the carriers are confined to the quantum wells, resulting in the formation of low dimensional carrier gas and generating one or more well-defined bound states in the wells. One application of this quantum effect is that the wavelength of the emitted light can be tuned by controlling the thickness of the quantum well, and the characteristics of the light emitting device can also be significantly enhanced. In recent years, ZnO/ZnMgO NW quantum structures have attracted extensive research interest for their potential applications in electric and optoelectric fields [22-23]. In this section, we try to characterize ZnO/ZnMgO multishell NWs structure by SCM and SSRM.

SEM images of the studied NWs sample are shown in Figure 6.11. The NWs sample were grown on a c-plane ZnO substrate by MOCVD and consist of 6 growth layers, forming a

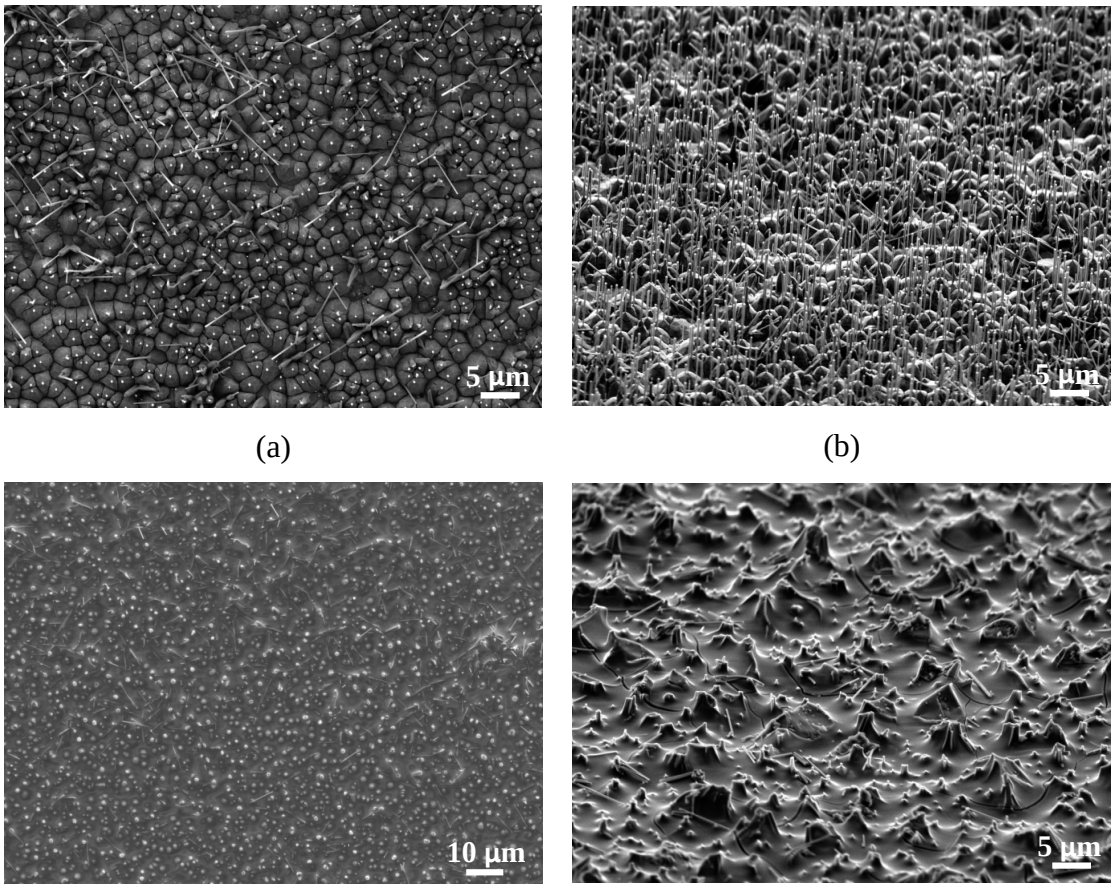

(a) (b)

(c) (d)

Figure 6.11: SEM images of the ZnO/ZnMgO multishell NWs. Top view (a) and tilt view (b) after the growth of NWs. Top view (c) and tilt view (d) after the dip-coating process.

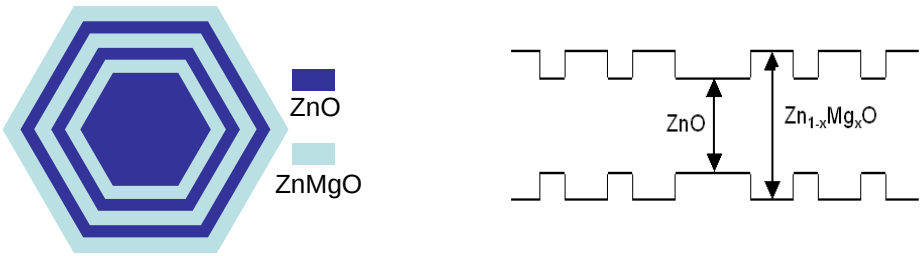

(a) (b)

Figure 6.12: (a) Illustration of the grown ZnO-based radial core-multishell NWs structure. (b) Band diagrams of the multishell structure.

3-period ZnO/ZnMgO coaxial structure, as illustrated in Figure 6.12(a). For original grown core ZnO NWs, diethylzinc (DEZn) and nitrous oxide (N_2O) were used as Zn and oxygen precursors, respectively. The ZnO NWs were grown at 850 ºC and the total reactor pressure was maintained at 50 torr. ZnO and $Zn_{1-x}Mg_xO$ (x=0.13) shells surrounding previously grown ZnO NWs were performed still using DEZn but a different oxygen source, O_2, and a lower temperature process, i.e. 450-500°C. Bismethylcyclopentadienyl-magnesium ((MCp2)Mg) was chosen as the Mg precursor, and the total reactor pressure was maintained at 30 torr.

These conditions allow a quasi-conformal coating over the entire nanowire. For all growth process, helium was used as carrier gas. Originally grown ZnO NWs have lengths ~9 μm and diameters about 130 nm. The ZnMgO and ZnO shell layers have thicknesses of ~15 nm and ~10 nm, respectively. ZnMgO has a wider band gap than ZnO. The band structure of the NWs structure is illustrated in Figure 6.12(b).

Low temperature PL spectrum on the NWs sample is given in Figure 6.13. The dominant emission peak at 3.36 eV corresponds to the neutral-donor bound excitons (D^0X) in ZnO. The ZnMgO layers produce emissions in the higher energy range around 3.55 eV.

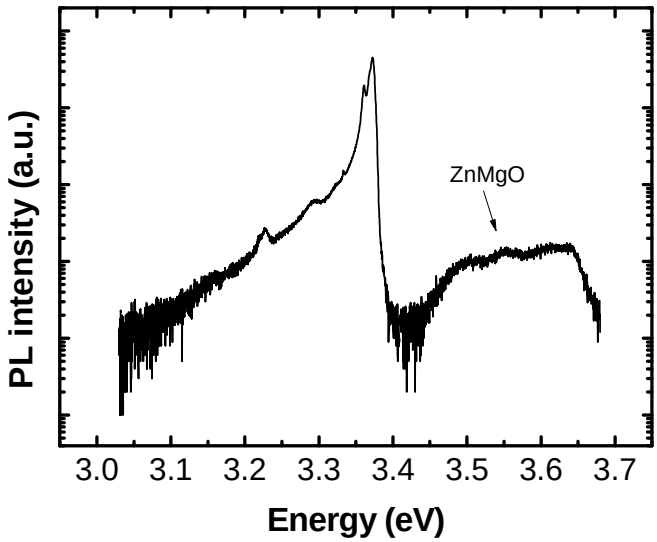

Figure 6.13: Low temperature (4.2 K) PL spectra of the 3-period ZnO/ZnMgO core-multishell NWs. (Measurement done by Alain Lusson at GEMAC)

After the planarization process, SCM and SSRM measurements were conducted on the NWs sample. Representative SCM results are presented in Figure 6.14. The topographical AFM image is given in Figure 6.14(a) where the NWs including their multishell structures are well distinguished. The height variation on the analyzed NW is within 4 nm. SCM data images were recorded at various V_{dc} of 0.5 V, -0.5 V, -1.5 V and are presented in Figure 6.14(b) to Figure 6.14(d). Evidently the NWs structure containing a ZnO/ZnMgO core-multishell structure is well detected with the contrast correlating to its material composition structure. Besides, the hexagonal form for each layer can be unambiguously observed. It is known that ZnMgO is a semiconductor having a wider band gap than ZnO. In the ZnO/ZnMgO heterostructure, due to the conduction band offset, ZnMgO layers act as quantum barriers while ZnO layers create quantum wells. A transfer of electrons from ZnMgO to ZnO will happen near the interface of the two materials, resulting in an accumulation in ZnO and the consequent depletion in ZnMgO in the aspect of electron carriers. An averaged SCM data profile using V_{dc}= -1.5V of the marked rectangle is shown in Figure 6.14(e). As expected, the ZnMgO layers can be identified as SCM data peaks indicating a lower carrier density while

the two ZnO shell layers produce SCM data downward peaks (dips) due to higher carrier concentrations inside them. From the SCM images at different V_{dc}, a dependence of SCM response of the NW structure on V_{dc} is noticeable. In particular, the core ZnO appears as bright contrast for 0.5 V V_{dc} and dark contrast for -1.5 V V_{dc}, suggesting a reversed contrast by varying V_{dc}. First of all this phenomenon helps us rule out the topography variation as the origin of SCM data contrast and proves a genuine correlation between the measured SCM data and the local electrical features. Nevertheless, carefulness should be taken in explaining this dependence on V_{dc}. For better analysis, the SCM data profiles for a region across the NW

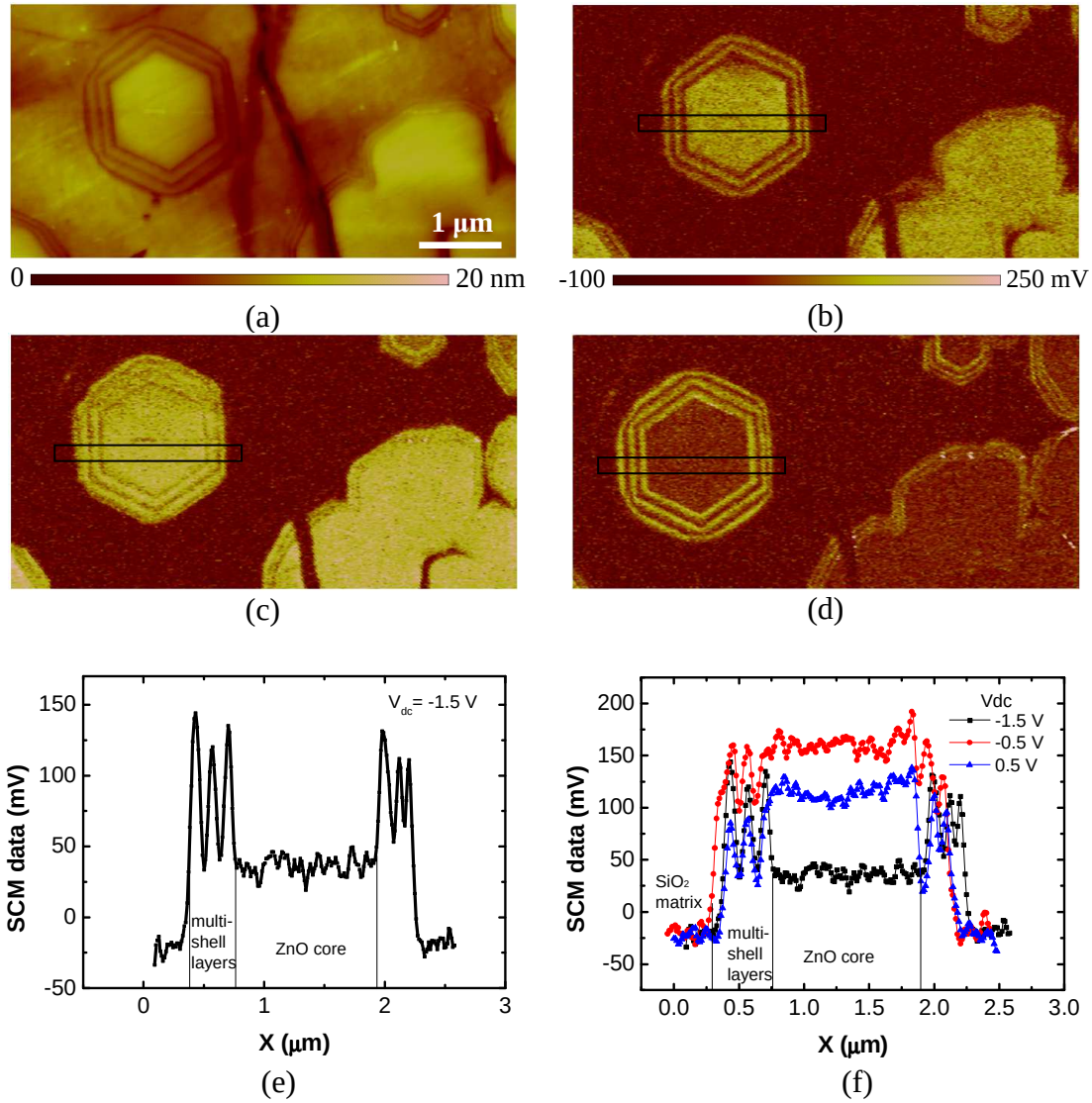

Figure 6.14: SCM measurement results on the ZnO/ZnMgO multishell NWs structure. (a) Topography image. (b)-(d) SCM data image at V_{dc} of 0.5 V, -0.5 V, -1.5 V. (e) Averaged SCM data profile of the rectangle indicated in (d). (f) Comparison of SCM data profiles obtained at different V_{dc} for a similar area marked in (b)-(d). Scanned area: 6 µm × 3 µm. V_{ac}=1000 mV was used. (c) and (d) share the same color scale in (b).

(indicated rectangles) under the three values of V_{dc} are plotted in Figure 6.14(f). It is seen that for V_{dc}=-1.5 V, the ZnO core produces smallest SCM data and all the five shell layers are

distinguishable in a way down peaks (dips) correspond to ZnO shell layers and peaks signify ZnMgO material. On the contrary, it is under -0.5 V V_{dc} that SCM data for all the layers reach their largest values. In this case, the firstly grown ZnMgO shell is not as clearly seen probably due to the effect of the ZnO core with the V_{dc} near the optimized value for its SCM signal. The dependence of SCM signal contrast for quantum well (2D) structure has been reported by F. Giannazzo *et al* [24-25] and O.Douheret *et al* [26]. It should be mentioned that the investigated NW exhibits a much larger dimension (~2 μm diameter) than expected from the

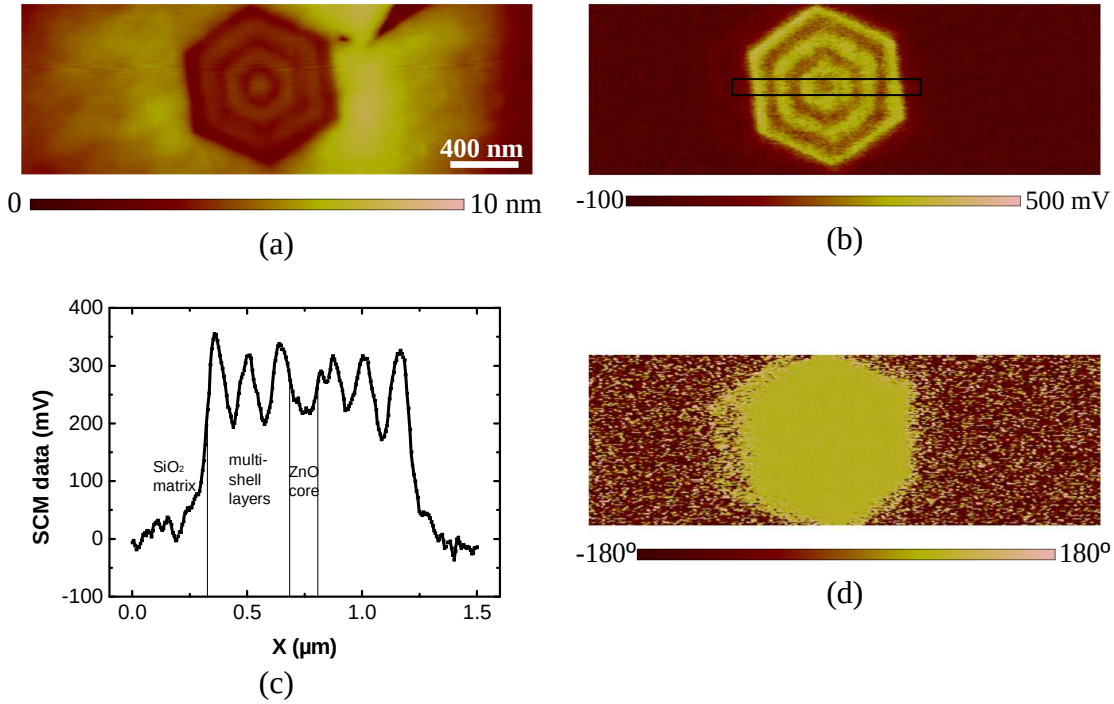

Figure 6.15: Another SCM result on the ZnO/ZnMgO multishell NWs structure. (a) Topography AFM image. (b) SCM data image on an individual NW with ZnO/ZnMgO multishell structure obtained with -1 V V_{dc}. (c) Averaged SCM data profile of the rectangle indicated in (b). (d) SCM data phase image. Scanned area is 3 μm × 1 μm. V_{ac}=1000 mV was used.

growth (~260 nm). Although a size distribution phenomenon may exist for the grown NWs, a possible reason is the polishing process reaching the base of the NWs. In addition, by noticing the other NWs being imaged by SCM exhibiting different shell thicknesses, SCM can also be used to investigate the difference in growth of the shell layers on NWs.

Another result on a NW with a smaller diameter is shown in Figure 6.15. Undoubtedly the intrinsic structure of the NW is clearly detected showing core-multishell contrast. In Figure 6.15(c), from the averaged profile of SCM data for the area marked in Figure 6.15(b), the comparison between SCM signal for ZnO (smaller SCM data) and ZnMgO (larger SCM data) layers is consistent with the previous analysis from an carrier density point of view. SCM data phase image in Figure 6.14 indicates all parts of the NW being of *n*-type conductivity.

Figure 6.16 shows typical SSRM result on the same NWs sample. Unsurprisingly, the NWs

are detected in both topography scans and SSRM resistance scans. A more evident contrast between different layers of the NWs is viewed in electrical channel (i.e. SSRM resistance image), revealing the variance of local electrical properties. Through a comparison of the SSRM image with previous SCM images, a difference in spatial resolution is again noticed. This occurs, even considering the larger tip radius (typically ~100 nm) in SSRM than in SCM (typically 20~30 nm), because the spatial resolution in SSRM imaging is mostly determined

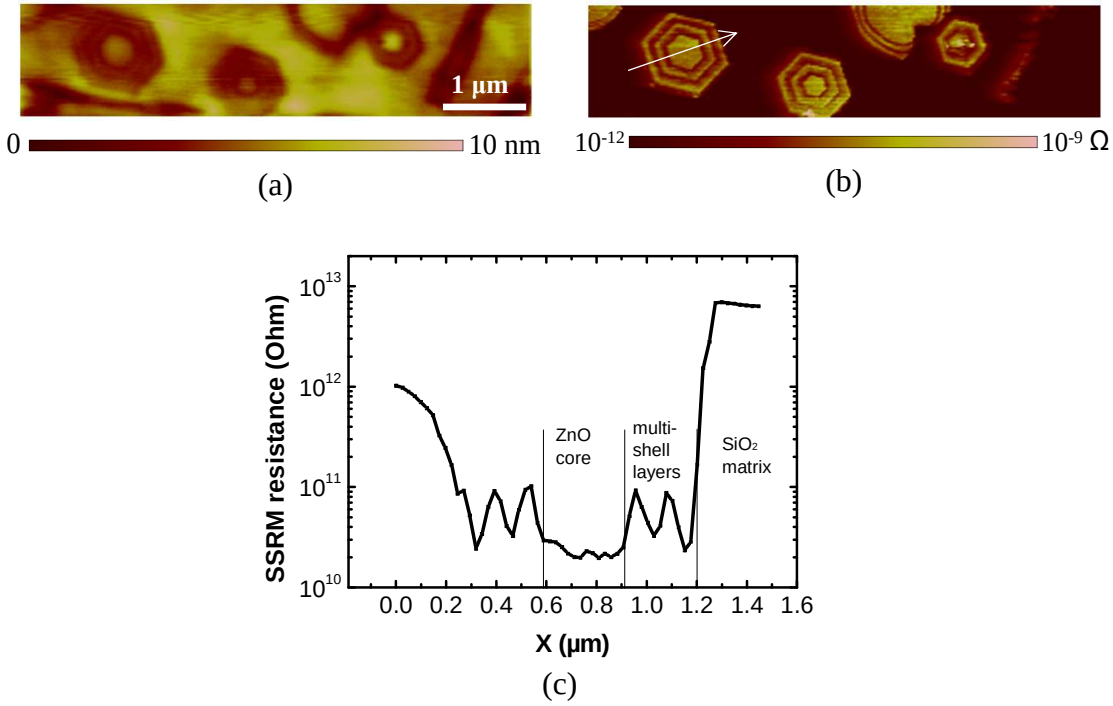

Figure 6.16: SSRM result on the ZnO/ZnMgO multishell NWs sample. (a) Topography image. (b) SSRM resistance image of the same region. (c) SSRM resistance profile along the arrow indicated in (b). Scanned area is 6 µm × 1.3 µm. V_{bias}= -2 V and F_{tip} ~1.5 µN were used.

by the effective radius of the tip-sample contact, which can be significantly smaller than that of the tip, while the spatial resolution in SCM depends more on the lateral distribution of the depletion region in the sample underneath the tip. A profile of SSRM resistance along the line across a NW in Figure 6.16(b) is plotted in Figure 6.16(c). It can be seen that the ZnO, as well as the ZnO shell layers are detected corresponding to smaller measured resistances during the scan in contrast to the ZnMgO layers. This is in consistency with the analyzed result from SCM. Another possible factor responsible for this difference in resistance is the discrepancy of carrier mobilities for different layers. Note that the resistance peak for outermost ZnMgO layer is not directly visible as a result of its coalesce with the measurement resistance outside the NW (on SiO_2 matrix).

6.4 Conclusion

The SCM/SSRM investigations on some ZnO-related nanostructures have been reported. For

ZnO:Sb film, it has been found that the areas adjacent to grain boundaries exhibit a reduction of net carrier density in comparison with the grain bodies. Considering an enrichment of Sb dopants at the grain boundaries, an effect of compensation of free carriers due to the formation of Sb related acceptors (Sb_{Zn}-$2V_{Zn}$ or Sb_O) has been proposed being responsible for the decrease of net carrier concentration. Regarding SCM/SSRM measurement on ZnO based core-shell structures, with the attempt of growing *p*-type ZnO through both *in situ* and *ex situ* approaches, although no *p*-type ZnO was detected, it is certainly without difficulty to detect the related core-shell contrast by the two techniques. Therefore, it is reasonable to say that SCM is able to confirm the local p conduction type inside NWs structure if it is successfully realized. Finally, SCM and SSRM were utilized to investigate ZnO/ZnMgO core-multishell structures. A relatively lower carrier concentration for ZnMgO layers with respect to ZnO layers is revealed and the result is consistent with the analysis on the different electrical properties of the two materials. Note that for all investigated samples a good agreement exists between SCM and SSRM measurements.

The study in this chapter demonstrates that SCM/SSRM are applicable and can be useful tools for electrical characterization on ZnO based nanostructures, especially for detection of local electrical properties inside ZnO related core-shell NWs structure. What's more, they can be used as complementary method to study the dopant behaviors in ZnO. We believe that further studies on more structures and in more detail are worth being carried out.

References:

[1] Oliver, R. A. (2008). Advances in AFM for the electrical characterization of semiconductors. Reports on Progress in Physics, 71(7), 076501.

[2] McMurray, J. S., Kim, J., Williams, C. C., & Slinkman, J. (1998). Direct comparison of two-dimensional dopant profiles by scanning capacitance microscopy with TSUPREM4 process simulation. Journal of Vacuum Science & Technology B, 16(1), 344-348.

[3] Visoly-Fisher, I., Cohen, S. R., & Cahen, D. (2003). Direct evidence for grain-boundary depletion in polycrystalline CdTe from nanoscale-resolved measurements. Applied physics letters, 82(4), 556-558.

[4] Chu, S., Lim, J. H., Mandalapu, L. J., Yang, Z., Li, L., & Liu, J. L. (2008). Sb-doped p-ZnO/Ga-doped n-ZnO homojunction ultraviolet light emitting diodes. Applied Physics Letters, 92(15), 152103.

[5] Mandalapu, L. J., Xiu, F. X., Yang, Z., Zhao, D. T., & Liu, J. L. (2006). p-type behavior from Sb-doped ZnO heterojunction photodiodes. Applied Physics Letters, 88(11), 112108.

[6] Chu, S., Zhao, J., Zuo, Z., Kong, J., Li, L., & Liu, J. (2011). Enhanced output power using MgZnO/ZnO/MgZnO double heterostructure in ZnO homojunction light emitting diode. Journal of Applied Physics, 109(12), 123110.

[7] Mandalapu, L. J., Yang, Z., Xiu, F. X., Zhao, D. T., & Liu, J. L. (2006). Homojunction photodiodes based on Sb-doped p-type ZnO for ultraviolet detection. Applied physics letters, 88(9), 092103.

[8] Aoki, T., Shimizu, Y., Miyake, A., Nakamura, A., Nakanishi, Y., & Hatanaka, Y. (2002). P-Type ZnO Layer Formation by Excimer Laser Doping. physica status solidi (b), 229(2), 911-914.

[9] Limpijumnong, S., Zhang, S. B., Wei, S. H., & Park, C. H. (2004). Doping by large-size-mismatched impurities: the microscopic origin of arsenic-or antimony-doped p-type zinc oxide. Physical review letters, 92(15), 155504.

[10] Janotti, A., & Van de Walle, C. G. (2009). Fundamentals of zinc oxide as a semiconductor. Reports on Progress in Physics,72(12), 126501.

[11] Liu, H. Y., Izyumskaya, N., Avrutin, V., Özgür, Ü., Yankovich, A. B., Kvit, A. V., ... & Morkoç, H. (2012). Donor behavior of Sb in ZnO.Journal of Applied Physics, 112(3), 033706.

[12] Liang, H., Chen, Y., Xia, X., Feng, Q., Liu, Y., Shen, R., ... & Du, G. (2015). Influence of Sb valency on the conductivity type of Sb-doped ZnO. Thin Solid Films.

[13] Geng, C., Jiang, Y., Yao, Y., Meng, X., Zapien, J. A., Lee, C. S., ... & Lee, S. T. (2004). Well-Aligned ZnO Nanowire Arrays Fabricated on Silicon Substrates. Advanced Functional Materials, 14(6), 589-594.

[14] Li, S. Y., Lee, C. Y., & Tseng, T. Y. (2003). Copper-catalyzed ZnO nanowires on silicon

(100) grown by vapor-liquid-solid process. Journal of Crystal Growth, 247(3), 357-362.

[15] Huang, M. H., Mao, S., Feick, H., Yan, H., Wu, Y., Kind, H., ... & Yang, P. (2001). Room-temperature ultraviolet nanowire nanolasers. Science, 292(5523), 1897-1899.

[16] Zhao, Q. X., Willander, M., Morjan, R. E., Hu, Q. H., & Campbell, E. E. B. (2003). Optical recombination of ZnO nanowires grown on sapphire and Si substrates. Applied Physics Letters, 83(1), 165-167.

[17] Yuan, H., & Zhang, Y. (2004). Preparation of well-aligned ZnO whiskers on glass substrate by atmospheric MOCVD. Journal of crystal growth, 263(1), 119-124.

[18] Lauhon, L. J., Gudiksen, M. S., Wang, D., & Lieber, C. M. (2002). Epitaxial core–shell and core–multishell nanowire heterostructures. Nature, 420(6911), 57-61.

[19] Goldberger, J., He, R., Zhang, Y., Lee, S., Yan, H., Choi, H. J., & Yang, P. (2003). Single-crystal gallium nitride nanotubes. Nature, 422(6932), 599-602.

[20] Park, W. I., Yi, G. C., Kim, M. Y., & Pennycook, S. J. (2003). Quantum confinement observed in ZnO/ZnMgO nanorod heterostructures. Advanced Materials, 15(6), 526-529.

[21] Bae, J. Y., Yoo, J., & Yi, G. C. (2006). Fabrication and photoluminescent characteristics of ZnO/Mg0.2Zn0.8O coaxial nanorod single quantum well structures.

[22] Jang, E. S., Bae, J. Y., Yoo, J., Park, W. I., Kim, D. W., Yi, G. C., ... & Ohtsu, M. (2006). Quantum confinement effect in ZnO/Mg0.2Zn0.8O multishell nanorod heterostructures.

[23] Kim, C., Park, W. I., Yi, G. C., & Kim, M. (2006). Formation and photoluminescent properties of embedded ZnO quantum dots in ZnO/ZnMgO multiple-quantum-well-structured nanorods. Applied physics letters, 89(11), 113106.

[24] Giannazzo, F., Raineri, V., La Magna, A., Mirabella, S., Impellizzeri, G., Piro, A. M., ... & Liotta, S. F. (2005). Carrier distribution in quantum nanostructures by scanning capacitance microscopy. Journal of applied physics, 97(1), 14302-14302.

[25] Giannazzo, F., Raineri, V., Mirabella, S., Impellizzeri, G., Priolo, F., Fedele, M., & Mucciato, R. (2006). Scanning capacitance microscopy: Quantitative carrier profiling down to nanostructures.Journal of Vacuum Science & Technology B, 24(1), 370-374.

[26] Douheret, O., Maknys, K., & Anand, S. (2004). Scanning capacitance microscopy investigations of InGaAs/InP quantum wells. Thin solid films, 459(1), 67-70.

Chapter 7

General conclusion

The demand of high-spatial-resolution 2D mapping of the electrical properties of semiconductors (especially Si) devices has motivated remarkably the developments of novel AFM-based electrical scanning probe techniques. SCM and SSRM have been applied on many semiconductor materials and are recognized to be suitable techniques due to their nanoscale spatial resolution and wide doping range. This thesis work has been devoted to the application of the two important SPM techniques for electrical characterization of ZnO NWs structures at nanoscale. In view of the challenging problem of ZnO *p*-type doping, a particular objective of this work was to realize quantitatively carrier profiling for the studied ZnO NWs. As results, it has been shown that SCM and SSRM have the potential to be utilized to investigate electrical properties of ZnO NWs structures in terms of carrier concentration. We believe that these investigation approaches can be well generalized to other semiconductor materials and specifically for NWs.

Two kinds of ZnO NWs, namely CBD grown and MOCVD grown NWs, have been investigated. First of all, a planarization procedure was developed to allow the SPM measurements on the NWs field (in Chapter 2). It primarily consists of two steps: dip-coating of SiO_2 sol-gel to encapsulate the quasi vertical NWs and CMP + cleaning processes to expose the top of the NWs as well as attain a smooth sample surface. Monitoring of the samples situation was done by SEM and tapping AFM to make sure that the surface roughness is suitable for subsequent SPM measurements.

The characterization of the ZnO NWs using SCM was reported in Chapter 3. While the NWs embedded in SiO_2 matrix can be detected without difficulty, special efforts were dedicated to the quantification of the measurement results. Calibration method was employed. Two homo-epitaxial ZnO:Ga multilayer staircase structures containing Ga density ranges from 1.7×10^{17} to 1.2×10^{19} cm^{-3} and from 1.7×10^{18} to 3×10^{21} cm^{-3} grown by MBE were used as calibration samples. It has been shown that SCM is able to successfully distinguish all the doped layers with reasonable contrast, demonstrating its capability for carrier profiling in the doped range. In this process, the important effect of V_{dc} choice was highlighted on the rational construction of calibration curve. Finally, from measurements on the NWs and calibration sample under a series of V_{dc} and in the same condition, calibration analysis was performed for SCM and SCS. As results, residual carrier densities $\sim3\pm1\times10^{18}$ and $\sim2\pm0.3\times10^{18}$ cm^{-3} for

CBD and MOCVD NWs were estimated, respectively. For MOCVD NWs, the result is in good agreement with that from another study carried out by 4-point probe measurements. Additionally in this chapter, the influence of tip depletion effect on the SCM signal polarity inversion and identification of sample's carrier type was investigated, which showed that the wear of tip's metal coating may bring about misleading result in the recognition of sample's conduction type.

In the application of SSRM on carrier profiling for ZnO NWs (Chapter 4), First the conductive diamond coated tip/ZnO contact characteristics were studied in terms of its dependence on the tip force and bias voltage. It was found that under certain large tip forces, the I-V characteristics of the tip/ZnO contact exhibit ohmic-like behaviour. In the course of quantitative analysis for the NWs, the contribution of NWs body resistance to the total measured resistance was estimated and it showed that the total resistance is still dominated by the local spreading resistance in the calibration process. In the end, the calibration curve was established for determining the residual carrier density in the NWs. By taking into account the mobility difference between ZnO:Ga layers and the ZnO NWs, a carrier density range of $1\sim3\times10^{18}$ cm^{-3} was estimated, in good agreement with SCM result.

In addition to characterization at a microscopic level, conventional technique C-V profiling was utilized to study the macroscopic electrical properties of collective ZnO NWs. With the NWs area ratio being estimated from SEM observation, carrier concentrations at the level of 7×10^{16} cm^{-3} and 4×10^{16} cm^{-3} were found for the CBD and MOCVD ZnO NWs, respectively. The source of this difference between microscopic and macroscopic results was discussed and the error of effective NWs contact area due to both preparation process and NWs surface depletion effect was assigned as the major cause.

The last part of this thesis investigated the potential of SCM and SSRM to characterize some other ZnO-related nanostructures. First, on a MOCVD grown ZnO film doped by Sb, a lower electron carrier density was revealed for the grain boundaries in comparison with the grain bodies, which can be ascribed to an compensation effect due to Sb-related acceptor formation. Then in the attempt of ZnO *p*-type doping by Sb, ZnO/ZnO:Sb core-shell structured NWs were elaborated to fabricate possible radial ZnO *p*-*n* junction. Although no *p*-type was attained for the ZnO:Sb shell layer, a core-shell contrast is clearly visualized both in SCM and SSRM, revealing a lower carrier concentration and lower conductivity for the ZnO:Sb shell layer with respect to the ZnO core. Finally, SCM/SSRM measurements demonstrated the potential of the two techniques on characterizing ZnO based core-shell NWs structures by spatially resolving different layers inside the ZnO/ZnMgO core-multishell coaxial heterostructures.

Several possible aspects in continuing the present work are following:

Firstly, all the measurements in this work have been done in ambient atmosphere. Since it has been demonstrated on Si structures that SPM characterization abilities can be largely enhanced in vacuum, improved results would be expected by performing the measurements under vacuum condition. This will help to better distinguished local characteristics inside the NWs structure. In addition, further reducing the topography features of the sample surfaces in the SPM measurements is likely to be helpful for obtaining improved results. In this regard, the employment of a better polishing process such as focused ion beam may be appreciated except that its effect on the sample of interest should be considered.

Secondly, in SSRM, the tip-ZnO contact characteristics have shown a dependence on the tip force. No related report on this phenomenon was found in the literature. Considering ZnO being a different material from Si, it is worth further investigated to achieve a full understanding.

Thirdly, in respect of characterizing the semiconductor NW at the macroscopic level, while a deeper understanding of the C-V measurement on collective NWs structure is needed to address its difference from conventional bulk material, other macroscopic techniques such as DLTS may be potentially helpful in characterizing the NWs as well as correlating the their electrical properties at the macroscopic level and at the microscopic level.

Finally, based on the obtained results, it is believed that applications of SCM and SSRM can be well extended to more ZnO based nanostructures and other semiconductor NWs structure. In particular, regarding the ZnO *p*-type doping problem, the two techniques have shown their capabilities of allowing direct characterization doping effect in comparison with non-doped ZnO, which is very useful for comparing and understanding the doping mechanisms. Considering the fact the complexity of ZnO doping problem, it is suggested that more delicate structures can be investigated by SCM and SSRM in addressing this issue. For example, on the road to *p*-type ZnO, multilayer structure, whether in form of 2D films or 1D NWs structures can be readily characterized by the two techniques to detect their conduction type and free carrier concentrations and identify the preferred conditions for *p*-type ZnO doping condition.

Scientific contributions

Journal publications :

L. Wang, J. Laurent, J. M. Chauveau, V. Sallet, F. Jomard, and G. Brémond. "Nanoscale calibration of n-type ZnO staircase structures by scanning capacitance microscopy". Applied Physics Letters, 107(19), 192101, 2015.

L. Wang, J. M. Chauveau, R. Brenier, V. Sallet, F. Jomard, C. Sartel, and G. Brémond. "Access to residual carrier concentration in ZnO nanowires by calibrated scanning spreading resistance microscopy". Applied Physics Letters, 108(13), 132103, 2016.

L. Wang, S. Guillemin, J. M. Chauveau, V. Sallet, F. Jomard, R. Brenier, V. Consonni and G. Brémond. "Characterization of carrier concentration in ZnO nanowires by scanning capacitance microscopy". Phys. Status Solidi C, 1–5, 2016.

L. Wang, B. Gautier, A. Sabac and G. Brémond. "Investigation of tip-depletion-induced fail in scanning capacitance microscopy for the determination of carrier type". Ultramicroscopy, in submission, Mar 10, 2016.

L. Wang, V. Sallet, C. Sartel and G. Brémond. "Cross-section imaging and p-type doping assessment of ZnO/ZnO:Sb core-shell nanowires by scanning capacitance microscopy and scanning spreading resistance microscopy". Nano Letters, in submission, May 4, 2016.

L. Wang, V. Sallet and G. Brémond. "SCM and SSRM investigation on ZnO/ZnMgO core-multishell coaxial heterostructure". Applied Physics Letters, in preparation.

Conferences participated:

L. Wang, G. Brémond. "Caractérisation du dopage dans les nanofils de ZnO par microscopie à sonde locale". GDR nanofil, Toulouse, France, Octobre 29-31, 2014. Oral presentation.

L. Wang, J. Laurent, A. Sabac, J.M. Chauveau, V. Sallet, F. Jomard, C.Sartel, R. Brenier and G. Brémond. "Characterization of doping by Scanning Capacitance Microscopy and C(V) technique in ZnO nanowires for optoelectronic application". 17th International Conference on II-VI Compounds and Related Materials. Paris, France, September 13-18, 2015. Oral presentation.

L. Wang, S. Blanc, M. Pouzet, A. Descamps–Mandine, R. Brenier and G. Brémond. "Electrical Assessment of doping in ZnO nanowires by Scanning Probe Microscopy". E-MRS SPRING MEETING, Strasbourg, France, May 27-31, 2013. Poster presentation.

L. Wang, J. Laurent, A. Descamps–Mandine, J.M. Chauveau, V. Sallet, R. Brenier and G. Brémond. "Characterization of Doping in ZnO Nanowires for Optoelectronics Applications by Scanning Probe Microscopy". 17th forum of scanning probe microscopy, Montauban,

France, Mars 17-21, 2014. Poster presentation.

L. Wang, J. Laurent, D. Albertini, P..Hamoumou, J.M. Chauveau, V. Sallet, F. Jomard, R. Brenier and G. Brémond. "Caractérisation du dopage de nanofils de ZnO par SCM et par la méthode de capacité-tension (C-V) pour des applications optoélectroniques", 17th forum of scanning probe microscopy, Troyes, France, Mars 21-25, 2015. Poster presentation.

L. Wang, J. Laurent, A. Descamps, J. M. Chauveau, V. Sallet, R. Brenier and G. Brémond. “Characterization of Doping in ZnO Nanowires for Optoelectronics Applications by Scanning Probe Microscopy”. Annual meeting of atomic force microscope (AFM) users. Lyon, France, November 20-21, 2013. Poster presentation.

G. Brémond, S. Guillemin and **L. Wang**. "ZnO nanowires for optoelectronics". ELyT lab Workshop, Zao To-o-gatta, Japan, February 17-20, 2013. Invited presentation.

G. Brémond, **L. Wang** and J. Laurent. "Assessment of doping profiles in semiconductor nanowires by scanning probe microscopy". 5th International Conference on Nano Structures SElf-Assembly, Marseille, France, July 7-11, 2014. Invited presentation.

UNIVERSITÉ DE LYON

INSA INSTITUT NATIONAL DES SCIENCES APPLIQUÉES LYON

FOLIO ADMINISTRATIF

THESE DE L'UNIVERSITE DE LYON OPEREE AU SEIN DE L'INSA LYON

NOM : WANG
(avec précision du nom de jeune fille, le cas échéant)

DATE de SOUTENANCE : 28/04/2016

Prénoms : LIN

TITRE : Carrier profiling of ZnO nanowire structures by scanning capacitance microscopy and scanning spreading resistance microscopy

NATURE : Doctorat

Numéro d'ordre : 2016LYSEI031

Ecole doctorale : Matériaux de Lyon

Spécialité : Matériaux

RESUME :Based on atomic force microscope (AFM), scanning capacitance microscopy (SCM) and scanning spreading resistance microscopy (SSRM) have demonstrated high efficiency for two dimensional (2D) electrical characterizations of Si semiconductors at nanoscale and then have been extensively employed in Si-based structures/devices before being extended to the study of some other semiconductor materials. However, ZnO, always a representative of high potential semiconductor material, being considered as a promising candidate for future devices in many areas, especially in opto-electronic area, has rarely been addressed. Recently, extensive research interests have been attracted by ZnO NWs for future devices such as LED, UV laser and sensor. Therefore, a good understanding of electrical properties of the NWs is needed. In this context, this thesis work is dedicated to the 2D electrical characterization of ZnO NWs with the focus of carrier profiling on this kind of nanostructure in the effort to turn them into p-type doping. For this purpose, a planarization process has been developed for the NWs structure in order to obtain an appropriate sample surface and to perform SCM and SSRM measurements on cross-section on the top of the NWs. For quantitative analysis, Ga doped ZnO multilayer staircase structures were disigned and measured serving as calibration samples. Finally, residual carrier concentrations (nid) inside the CBD and MOCVD grown ZnO NWs are determined to be around 3×10^{18} cm^{-3} and 2×10^{18} cm^{-3}, respectively. The results from SCM and SSRM characterization have been compared with that from macroscopic C-V measurements on collective ZnO NWs and the differences are discussed in term of NWs active surface. In addition to carrier profiling on NWs structure, applications of SCM and SSRM on some other ZnO-based nanostructures are also investigated including ZnO:Sb films, ZnO:nid/ZnO:Sb core-shell NWs structure, ZnO/ZnMgO core-multishell coaxial heterostructures, pointing out the interest of such nanoscale carrier profiling techniques for 1D nanostructures.

MOTS-CLÉS : scanning capacitance microscopy; scanning spreading resistance microscopy; ZnO nanowires; p-type ZnO

Laboratoire (s) de recherche : Institut des Nanotechnologies de Lyon

Directeur de thèse: Georges BREMOND

Président de jury : Brice GAUTIER

Composition du jury :

M. Brice GAUTIER	Professeur des Universités	INSA LYON	Président
M. François BERTIN	Docteur, HDR	CEA-Leti	Rapporteur
M. Pierre EYBEN	Docteur, Senior Scientist	IMEC	Rapporteur
M. Daniel ALQUIER	Professeur des Universités	Université de Tours	Examinateur
M. Vincent SALLET	Docteur, Chargé de recherche	CNRS-UVSQ	Examinateur
M. Georges BREMOND	Professeur des Universités	INSA LYON	Directeur de thèse